June 5, 2023

Theoretical Insights of Defects in Modulating Functional Properties of Various Advanced Energy Materials

Deepika Gill

Indian Institute of Technology Delhi

Hauz Khas, New Delhi 110016

February 2023

Theoretical Insights of Defects in Modulating Functional Properties of Various Advanced Energy Materials

Deepika Gill

Indian Institute of Technology Delhi

Hauz Khas, New Delhi 110016

February 2023

Dedicated to my parents and supervisor

Certificate

This is to certify that the thesis entitled "**Theoretical Insights of Defects in Modulating Functional Properties of Various Advanced Energy Materials.**" being submitted by **Deepika Gill**, to the Indian Institute of Technology Delhi, for the award of the degree of **Doctor of Philosophy** in Physics is a record of bonafide research work carried out by her under my supervision and guidance. She has fulfilled the requirements for the submission of the thesis, which to the best of my knowledge has reached the required standard. The material contained in the thesis has not been submitted in part or full to any other University or Institute for the award of any degree or diploma.

Prof. Saswata Bhattacharya
Thesis Supervisor
Department of Physics,
Indian Institute of Technology Delhi,
Hauz Khas, New Delhi 110016, India.
Date:.......
Place: New Delhi

Acknowledgments

First and foremost, I would want to take this chance to convey my sincere thanks to Professor Saswata Bhattacharya, who oversaw my thesis, for his unwavering support, wise counsel, tolerance, and inspiration. He enabled me to begin my studies in the same way that parents enable their newborn to take their first steps. I owe him a great deal of gratitude for our stimulating conversations about physics, research techniques, leadership qualities, philosophy, and a variety of other topics. These discussions have not only improved my understanding of physics but have also helped me develop into a well-rounded and inquisitive individual. He gave me considerable support and inspired bravery when things became difficult, and I owe him a great deal. He has always been an inspiration to me because of his contagious energy, love of physics, dynamic personality, and drive to achieve great things. He consistently believed in my talents, which inspired me to pursue a career in research, for which I am really grateful. I appreciate the thoughtful questions and ideas from Professors B. K. Mani, N. M. Anoop Krishnan and J. P. Singh, who make up the remainder of my student research committee in addition to my adviser. DISCERE group members Shikha Saini, Pooja Basera, Ekta Arora, Manish Kumar, Arunima Singh, Manjari Jain, Preeti Bhumla, Sajjan Sheoran, Ankita Phutela, Sanchi Monga, Ruman Moulik, Riya Gupta, Shantanu Pathak have my deepest gratitude for their assistance during my doctoral studies. I have had several enjoyable conversations with them on physics. I'm also appreciative to my other team members, Professors K. K. Pant, Sreedevi Upadhyayula, and Sameer Sapra, and Priyesh Yadav, Dr. Arindam Modak, and Dr. Sachin Tomar for our productive conversations and collaborations. I appreciate all the resources provided by the Indian Institute of Technology Delhi in New Delhi for my research efforts and travel funding. I'd like to express my gratitude to the University Grants Commission (UGC) for providing money for my study. I also thank the Council of Scientific Industrial Research (CSIR) for helping me out financially by paying for my travel. I am very appreciative of my family since without their unwavering support it would not have been able to complete this thesis. I will always be grate-

ful to my parents for their unending love and blessings. I might not be who I am now without their wishes, motivation, and emotional support. Each of my victories or setbacks was felt by them as their own. Last but not least, I humbly thank the Almighty for bestowing upon me five senses and undying love.

Thank you!

Deepika Gill

Deepika Gill

Abstract

The necessity to switch to renewable energy sources has become critical due to the world's increasing energy demands and the depletion of fossil fuel reserves. The answer to the current problem is to use renewable energy sources, which are economical, ecologically responsible, and abundant in nature. Advanced solid-state materials that are utilized to solve environmental problems have attracted a lot of scientific interest. The three kinds of innovative energy materials—solid-state electrolyte materials for all-solid-state batteries, perovskite materials for solar cells and optoelectronic devices and catalysts for H_2 production and bio-mass conversion are the core topics of this thesis. The most widely used kind of energy storage in both autos and portable gadgets is the lithium-ion battery. Its use in large-scale energy applications is hindered by the usage of flammable liquid electrolytes. The use of solid-state electrolytes in place of liquid electrolytes, as in all-solid-state batteries, improves battery design and assures safety. LISICON oxide-based materials are been explored as solid-state electrolytes since they are easy to synthesize and environmentally friendly. However, they exhibit poor ionic conductivity at room temperature. Hence, we look at the impact of point defects on the ion transport properties, namely Li-vacancy, substitution at the P site with Si, Ge and Al. We do ab-initio molecular dynamics (AIMD) simulations to determine the diffusional characteristics of the pristine and defected materials. We explain how the point defects play a pivotal role in modifying the ion transport properties in oxide-based solid state electrolytes. On the other hand in optoelectronics, lead halide perovskites have become an effective compound semiconductor replacement for traditional solar materials. The materials in this class have a good optical band gap, long carrier diffusion length, high charge carrier mobility, and low cost of production. However, their widespread use is constrained by worries about the toxicity of lead and intrinsic instability. As an alternative to conventional lead halide perovskites, several derivatives of these have been proposed. Double perovskites like $Cs_2M(I)M(III)X_6$ (M = metal, X = halogen) and layered hybrid perovskites have been developed in an effort to combat toxicity and instability. However, these lead-free halide double perovskites and layered hybrid perovskites do not demonstrate the same efficiency as that of lead halide perovskites. Therefore, we do point defects in these materials to improve their stability, electronic and optical properties. Since double perovskites and layered hybrid perovskites do not meet all the criteria and lack at some points, we focus on a new type of inorganic layered type perovskite i.e., Ruddlesden Popper phases of chalcogenides. Here, we study the polaronic and excitonic effects with the number of perovskites units in a layer. To address optical features such as dielectric function, absorption spectra, exciton binding energy, and polaronic effects in perovskites, we use a robust methodological approach that combines many layers of theories into a single multi-scale simulation. Density functional theory (DFT) is used in this thesis work to predict the ground-state properties, ab initio atomistic thermodynamics is used to predict thermodynamic stability, many-body perturbation theory (GW, BSE, and model-BSE) is used to predict excited-state properties, the Wannier-Mott approach is used to calculate the exciton binding energy and exciton lifetime, and density functional perturbation theory (DFPT) is used to determine the exciton lifetime. Lastly, engineering an effective and optimized catalyst is the ultimate objective of research in heterogeneous catalysis. This is because there are many different catalytic processes. Consider what restricts the usefulness of current catalysts as a useful technique for finding acceptable catalysts. Understanding the intended functionality at an atomistic level is crucial for the development and logical design of catalytic materials. In this thesis, we study role of O-vacancy on the surface of the catalyst in facilitating the dissociation of the SO_3 which is the most endothermic reaction step in the S-I cycle for H_2. We also study the effect of surrounding ligands on the catalytic activity of the single-atom-Ru in partial hydrogenation of the xylose/glucose into useful sweeteners, which are popular in medical as well as industrial areas.

सार

ऊर्जा की बढ़ती मांग और जीवाश्म ईंधन भंडार की कमी के कारण अक्षय ऊर्जा स्त्रोतों पर स्विच करने की आवश्यकता महत्वपूर्ण हो गई है। वर्तमान में इसका एकमात्र उपाय नवीकरणीय ऊर्जा स्त्रोतों का उपयोग करना है, जो किफायती, पारिस्थितिक रूप से जिम्मेदार हो, और प्रकृति में प्रचुर मात्रा में पाए जाते हो। उन्नत ठोस-राज्य सामग्री जिनका उपयोग पर्यावरण की ऊर्जा सम्भंदित समस्याओं को हल करने के लिए किया जाता है, जिस कारण ये वैज्ञानिक शोध का केंद्र बने हुए है। तीन प्रकार की नवीन ऊर्जा सामग्री -सभी ठोस-राज्य बैटरी के लिए ठोस-राज्य इलेक्ट्रोलाइट सामग्री, सौर सेल/ऑप्टोइलेक्ट्रॉनिक उपकरणों के लिए पेरोसाइट सामग्री, और H_2 उत्पादन और जैव-द्रव्यमान रूपांतरण के लिए उत्प्रेरक, इस थीसिस के मुख्य विषय हैं। मोबाइल और डिजिटल डिवाइस में सबसे व्यापक रूप से इस्तेमाल किया जाने वाला ऊर्जा भंडारण और पोर्टेबल गैजेट लिथियम-आयन बैटरी है। ज्वलनशील तरल इलेक्ट्रोलाइट्स की उपस्थिति ने उनके बड़े पैमाने पर व्यावसायीकरण में बाधा उत्पन्न की है। तरल इलेक्ट्रोलाइट्स की जगह ठोस-अवस्था इलेक्ट्रोलाइट्स का उपयोग, जैसा कि सभी ठोस-राज्य बैटरी में होता है, बैटरी डिजाइन में सुधार करता है और सुरक्षा का आश्वासन देता है। LISICON ऑक्साइड-आधारित सामग्री को ठोस-अवस्था इलेक्ट्रोलाइट्स के रूप में खोजा गया है क्योंकि वे संश्लेषित करना आसान है और पर्यावरण के अनुकूल है। हालांकि, वे खराब आयनिक चालकता प्रदर्शित करते हैं कमरे के तापमान पर। इसलिए, हम आयन परिवहन गुण पर बिंदु दोष के प्रभाव को देखते हैं, अर्थात् Li-रिक्ति, Si, Ge और Al के साथ P साइट पर प्रतिस्थापन। हम प्राचीन और दोषपूर्ण सामग्री की विसारक विशेषताओं को निर्धारित करने के लिए आणविक गतिकी (AIMD) सिमुलेशन की हैं। हम समझाते हैं कि कैसे बिंदु दोष ऑक्साइड-आधारित ठोस अवस्था इलेक्ट्रोलाइट्स में आयन परिवहन गुण संशोधित करने में महत्वपूर्ण भूमिका निभाते हैं। वहीं दूसरी ओर ऑप्टोइलेक्ट्रॉनिक्स में, लेड हैलाइड पेरोसाइट्स एक प्रभावी यौगिक सेमीकंडक्टर बन गए हैं, जो परंपरागत सौर सेल सामग्री को प्रतिस्थापित कर सकता है। ये सामग्री अच्छे ऑप्टिकल बैंड का प्रदर्शन करती हैं अंतराल, लंबी वाहक प्रसार लंबाई, उच्च चार्ज वाहक गतिशीलता, और उत्पादन की कम लागत। हालांकि, सीसा की विषाक्तता और आंतरिक अस्थिरता ने उनके बड़े पैमाने पर व्यावसायीकरण में बाधा डाली है। पारंपरिक लेड हलाइड पेरोसाइट्स के विकल्प के रूप में कई पेरोसाइट्स प्रस्तावित किए गए हैं। $Cs_2M(I)M(III)X_6$ (M = धातु, X = हलोजन) जैसे डबल पर्कोसाइट्स और स्तरित संकर पर्कोसाइट्स विषाक्तता और अस्थिरता से निपटने

के प्रयास में विकसित किए गए हैं। हालाँकि, ये लेड-फ्री हैलाइड डबल पर्कोव्साइट्स और लेयर्ड हाइब्रिड पर्कोव्साइट्स करते हैं उच्च शक्ति रूपांतरण दक्षता का प्रदर्शन नहीं करते हैं, जैसा कि लेड हैलाइड पेरोसाइट्स के रूप में होता है। प्रदर्शन नहीं करते। इसलिए, उनकी स्थिरता, इलेक्ट्रॉनिक और ऑप्टिकल गुणों में सुधार करने के लिए हम ऐसी सामग्रियों में दोषों की भूमिका का अध्ययन करते हैं। जैसा डबल पर्कोव्साइट्स और लेयर्ड हाइब्रिड पर्कोव्साइट्स सभी मानदंडों को पूरा नहीं करते हैं और कुछ में कमी है, हम एक नए प्रकार के अकार्बनिक स्तरित प्रकार के पेरोसाइट पर ध्यान केंद्रित करते हैं, जैसे कि चाकोजेनाइड रुडल्सडेन पॉपर पेरोव्स्काइट्स। यहां, हम एक परत में पेरोसाइट इकाइयाँ की संख्या के साथ पोलरोनिक और एक्साइटोनिक प्रभावों का अध्ययन करते हैं। परावैद्युत फलन, अवशोषण जैसी प्रकाशीय विशेषताओं, स्पेक्ट्रा, एक्सिटोन बाइंडिंग एनर्जी, और पेरोसाइट्स में पोलरोनिक प्रभाव का अध्ययन के लिए हम एक मजबूत पद्धति का उपयोग करते हैं, जो सिद्धांतों की कई परतों को एक बहु-स्तरीय अनुकरण में जोड़ता है। Density functional theory (DFT) का उपयोग इस थीसिस कार्य में जमीन-राज्य गुणों की भविष्यवाणी करने के लिए किया जाता है, *ab initio* Molecular dynamics का उपयोग थर्मोडायनामिक स्थिरता की भविष्यवाणी करने के लिए किया जाता है, many body Perturbation theory (GW, BSE, and model-BSE) उत्साहित राज्य गुणों की भविष्यवाणी करने के लिए प्रयोग किया जाता है, Wannier-Mott दृष्टिकोण का उपयोग एक्सिटोन बाइंडिंग एनर्जी और एक्साइटन लाइफटाइम की गणना के लिए कियाजाताहै, और घनत्व कार्यात्मक गड़बड़ी सिद्धांत (DFPT) का उपयोग एक्साइटन जीवनकाल को निर्धारित करने के लिए किया जाता है। अंत में, इंजीनियरिंग में एक प्रभावी और अनुकूलित उत्प्रेरक अनुसंधान का अंतिम उद्देश्य है। ऐसा इसलिए है क्योंकि कई अलग-अलग उत्प्रेरक प्रक्रियाएं हैं। विचार करना स्वीकार्य खोजने के लिए एक उपयोगी तकनीक के रूप में वर्तमान उत्प्रेरक की उपयोगिता को क्या प्रतिबंधित करता है उत्प्रेरक। विकास के लिए एक परमाणु स्तर पर इच्छित कार्यक्षमता को समझना महत्वपूर्ण है और उत्प्रेरक सामग्री का तार्किक डिजाइन। इस थीसिस में, हम O-रिक्ति की भूमिका का अध्ययन करते हैं जो SO_3 के वियोजन को सुविधाजनक बनाने में उत्प्रेरक की सतह पर महत्वपूर्ण भूमिका निभाता है। SO_3 का वियोजन, H_2 उत्पादन के लिए S-I चक्र में सबसे अधिक एंडोथर्मिक चरण है।हम Ru एकल परमाणु की उत्प्रेरक गतिविधि पर आसपास के लिगेंड की भूमिका का भी अध्ययन करते हैं, जिसका उपयोग जाइलोज/ग्लूकोज के हाइड्रोजनीकरण के लिए जाइलिटोल/सोर्बिटोल में किया जाता है, जो चिकित्सा और उद्योगों में मांग में हैं।

List of Publications

1. **D. Gill**, M. Kumar, P. Basera, S. Bhattacharya “Understanding the ionic diffusivity in (meta)stable (un)doped solid state electrolyte fromfirst- principles: A case study of LISICON" J. Phys. Chem. C 124, 17485 (2020).
2. **D. Gill**, P. Bhumla, M. Kumar, S.Bhattacharya “High-throughput screening for band gap engineering by sub lattice mixing of $Cs_2AgBiCl_6$ from first- principles" J. Phys. Mater. 4, 025005 (2021).
3. **D. Gill**, A. Singh, M. Jain, S.Bhattacharya “Exploring Exciton and Polaron Dominated Photophysical Phenomena in RuddlesdenPopper Phases of $Ba_{n+1}Zr_nS_{3n+1}$ (n = 1-3) from Many Body Perturbation Theory" J. Phys. Chem. Lett. 12, 6698 (2021).
4. **D. Gill**, G. Yadav, S. Bhattacharya “Sn/Ge Substituted in ($(C_nH_{2n-1}NH_3)_2PbI_4$; n=3-6): An Emerging 2D Layered Hybrid Perovskites with Enhanced Optoelectronic Properties" J. Phys. Chem. C 2022 126 (32), 13957-13966.
5. S. Tomar, **D.Gill**, K. Kondamudi, S. Upadhayula, S. Bhattacharya “SO_3 decomposition over silica modified b-SiC supported $CuFe_2O_4$ catalyst: Effects of Si treated support and Fe-O-vacancy-Cu on catalyst activity” Nanoscale 14, 6876 (2022).
6. A. Modak, **D. Gill**, A. Mankar, V. Bhasin, C. Nayak, K. K. Pant, S. Bhattacharya “Ru-Single Atom Decorated Ordered Mesoporous Polymer for High Yield Synthesis of Sugar Alcohols under Microwave Conditions" Nanoscale 14, 15875 (2022).
7. P. Yadav, **D. Gill**, S. Khurana, R. S. Lamba, S. Bhattacharya, S. Sapra “Enhanced Luminescence and Interstitial Site Mn^{2+} Doping in Two-Dimensional Na-In Halide Perovskite" J.Phys.Chem.C accepted.
8. M. Kumar, A. Singh, **D. Gill**, S. Bhattacharya “Optoelectronic Properties of Chalcogenide Perovskites from Anybody Perturbation Theory" J. Phys. Chem. Lett. 12, 5301

(2021).

9. M. Jain, **D. Gill**, P. Bhumla, S. Bhattacharya “Theoretical Insights of Excitonic in Lead Bromide Perovskites" Apple. Phys. Lett. 118, 192103 (2021).

10. P. Bhumla, **D. Gill**, S. Sheoran, S. Bhattacharya “Origin of Rashba Spin- splitting and Strain Tunability in Ferroelectric Bulk $CsPbF_3$" J. Phys. Chem. Lett. 12 (39), 9539-9546.

11. P. Basera, A. Singh, **D. Gill**, S. Bhattacharya “Capturing Excitonic Effects in Lead Iodide Perovskites from Many-Body Perturbation Theory" J. Mater. Chem. C 9 (47), 17113-17123.

12. M. Jain, **D. Gill**, S. Monga and S. Bhattacharya “Theoretical evaluation of oxynitride, oxyfluoride and nitrofluoride perovskites with promising photon absorption properties for solar water splitting” arXiv:2301.04335.

13. A. Modak, **D. Gill**, K. Sharma,V. Bhasin,K. K. Pant, S. N. Jha,D. Bhattacharyyac and S. Bhattacharya“Hydrogenolysis of biomass-derived xylose to xylitol and 1,2-diols under microwave condition by hydroxylated Ru single-atom on phosphine-modified silica” to be submitted.

Contents

List of Figures

CHAPTER 1

Introduction

1.1 Why advanced energy materials?

Advanced energy materials have gained considerable momentum especially for their use as energy harvesting materials to meet the growing energy demands of 21^{st} century.Over 80% of the world's energy requirements are supplied by the combustion of fossil fuels, which enhance global warming and has hazardous effects on the our environment. Moreover, these non-renewable fossil fuels will eventually be exhausted due to worldwide high energy demand and high combustion rate. To meet the continuous advancement of the human society, new cheap, clean, compact and renewable sources of energies are required [2, 3, 4, 5]. Many such materials including battery materials, solar cells, organic and inorganic photovoltaics, hydrogen production/storage, water splitting and photocatalysis, piezo-electricity materials, thermoelectrics, etc are being studied and a lot of research is being done to make these materials reliable for on-board applications [3, 6, 7]. The invention of spectroscopy, followed by various characterization techniques for the noble advanced energy materials allowed one to investigate size, phase distribution, composition/element distribution and correlate the changes in the physical properties and characteristic properties with the defects and imperfections in the materials. By the end of 20^{th} centuary, the theoretical studies through computational simulations became an ultimate tool to study the size, structure, configuration, electronic properties, physical properties, excited state properties, defects, and various fundamental properties for various applications of the materials. However, even after so many attainments in the comutational studies, there are a lot of challenges in studing the effects of defects on the fundamental properties and defects in advanced energy materials.

1.2 A brief introduction to imperfection or defects in solids

Any deviation in the microscopic region of a regularly arranged atomic crystal is defined as an imperfection or defect in solids. Figure 1.1 shows the dimensional spans of various types of defects in solids. Based on the dimensional ranges, crystalline defects are generally classified into four groups, which are as follow

- Atomic point defect (zero-dimensional defect)
- Line defect (one-dimensional defect)
- Interfacial defect (two-dimensional defect)
- Volume defect (three-dimensional defect)

This thesis is oriented toward atomic point defects and their effects on the functional properties of advanced energy materials. Further, atomic point defects are categorized into vacancies, self-interstitial atoms, substitutional atoms and interstitial impurity atoms. Missing of an atom from its lattice site results into a vacancy defect (intrinsic defect). Such defects mainly occur at high temperature due to frequent exchange of atomic positions among the atoms and leave behind empty spaces. On the other hand, when an extra atom occupies the interstitial void, it is called self-interstitial defect (intrinsic defect). Note that vacancy and self-interstitial defects are also known as intrinsic defect as no foreign atom is involved in such defects. A substitutional defect occurs when an atom of different type than bulk system occupies the lattice site of one of the atom of the bulk system. If this foreign atom occupies the interstitial position or void in the bulk system, then this is an interstitial defect. Interstitial defect is possible only when the size of the interstitial impurity atom is smaller than free space or void present in the bulk matrix lattice. Here, substitutional and interstitial defects are of extrinsic type as they occurs due to the presence of foreign atoms in the system.

1.3 Thermodynamics of defects

Defects increase the energy of crystals i.e., they are energetically unfavorable. However, the presence of defects increase the entropy of the crystal i.e., they are entropically fovorable. As two processes are going in parallel in the system. According to thermodynamic relation

$$\triangle \mathrm{G} = \triangle \mathrm{H} - \mathrm{T} \triangle \mathrm{S} \tag{1.1}$$

For any feasible reaction, $\triangle$G must be negative, hence, entropy must increase. Let us consider a system consisting of N atoms and n vacancies (point defect), then using Boltzmann equation [8] the configurational entropy is given by

$$\triangle \mathrm{S} = k_{\mathrm{B}} ln\omega \tag{1.2}$$

where $\omega = \frac{\mathrm{N!}}{(\mathrm{N-n})!\mathrm{n!}}$, is the total number of possible configurations for the arrangement of the atoms in the system. If we imagine an ideal system, having no defects i.e., n=0 or ω=1. Using above equation, $\triangle$S = 0. Hence, from thermodynamic equation 1.1, is not reduced. It emphasizes that in practical world, the perfect crystal is not possible and defects are inevitable in the crystals.

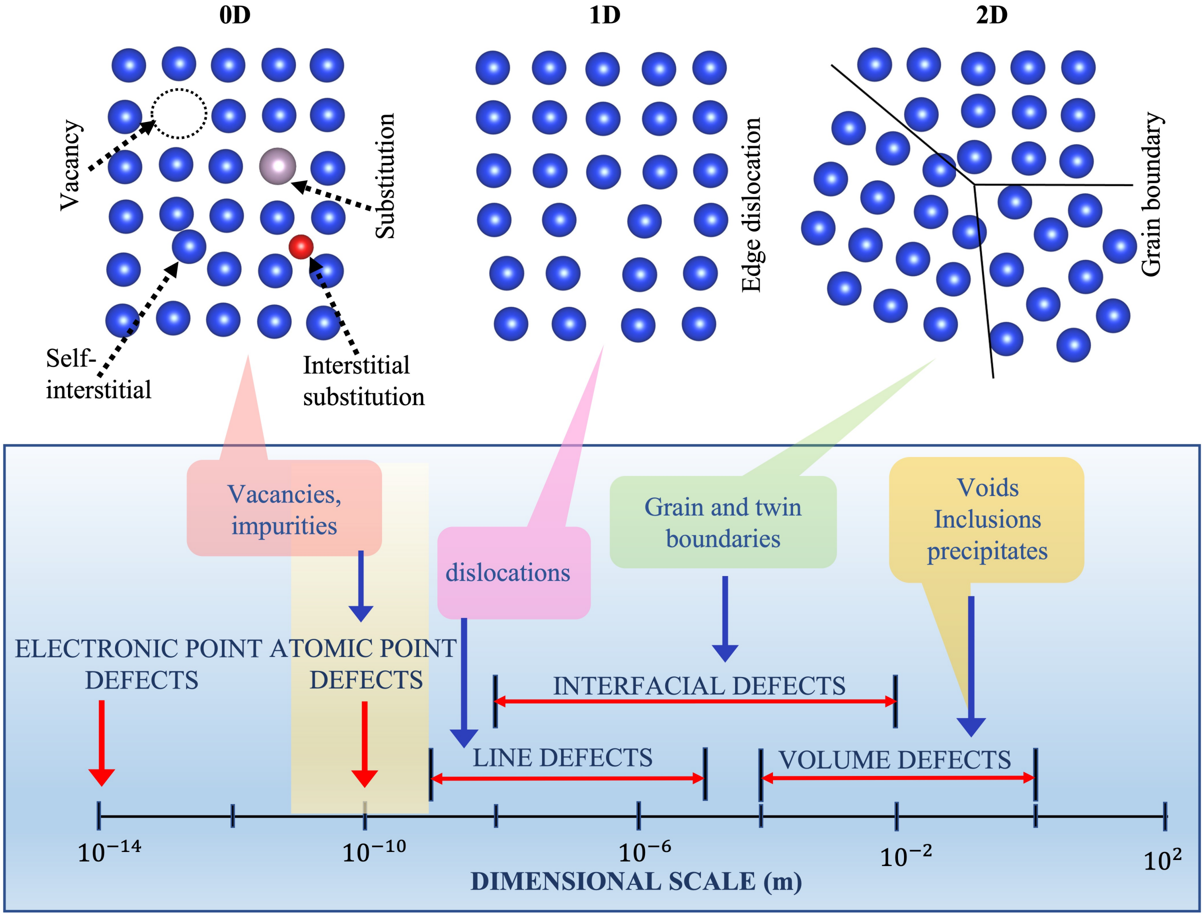

Figure 1.1: Diagrammatic representation of surface defects such as flaws at grain boundaries, edge dislocations, and point defects such as vacancies, substitutions, and interstitial defects.

1.4 Solid solutions

In extrinsic defects which are associated with the impurities or dopants in the system, which either occupy the interstitial site or substitute the native atom of the lattice system. When the dopant concentration rises above ≥ 0.1-1 %, the system is referred to as a solid solution instead of a doped system. However, both these terminologies are interchangeable. Basically, a crystal with variable concentration is known as solid solution. As in case of doped systems, the solid solutions are also of two types (i) substitutional solid solution and (ii) interstitial solid solution. If the introduced atom or ion replaces the atom or ion of the parent system, then it is known as substitutional solid solution. On the other hand, in interstitial solid solution, the species being introduced occupies the interstitial site or void in the parent system.

1.5 The Hume-Rothery Rules for the Solid Solution

In engineering materials, the substitutional solid solutions are more common among the solid solutions. Let us consider the parent system as the solvent and the atom or ion is being introduced as the solute. In the case of an interstitial solid solution, the solute will go into an interstitial site or position if it is very much smaller in size than that of the solvent atom. Whereas the substitutional solid solution depends on various rules known as the Hume-Rothery rules for solid solutions. These rules are as follows:

Ionic radius: This rule says that the ionic radii of solute and solvent atoms must lie with in the range of 15% of each other is given by the following equation:

$$\left| \frac{r_{solvent} - r_{solute}}{r_{solvent}} \right| \leq 0.15 \tag{1.3}$$

The ionic radius is important because of two reasons. First, if the atomic size of the solute is a very small in comparison to the solvent, it will always be an interstitial solid solution rather than a substitutional solution. The second reason, is if the size of the solute is too large, then the lattice strain effects caused by the solute atom will hinder its solubility. That is introducing a too-large or too-small solute at the lattice site of solvent will always cause strain in the lattice (see Figure 1.2) and the substitutional solid solution will not be possible.

Similar crystal structure: According to this rule to have appreciable solubility of the

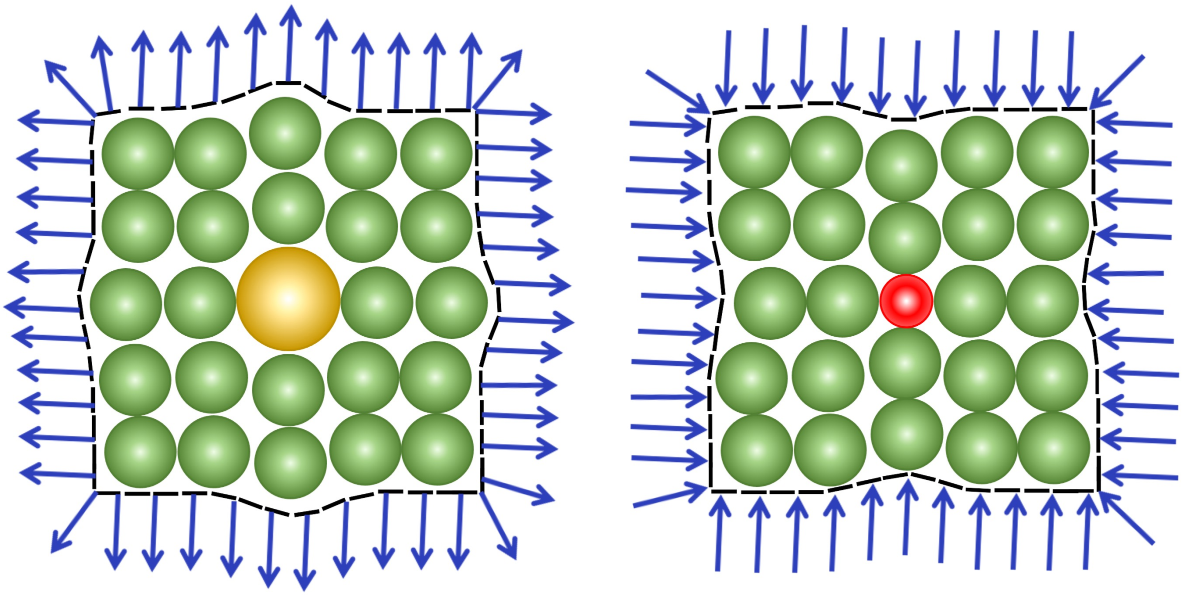

Figure 1.2: Schematic presentation of strain in the lattice on doing substitutional point defect.

solute in the solvent, both the elements should exhibit similar crystal structure. However, there are some exceptions to this rule. For example: Iron and Cromium both exhibit BCC stable crystal structures and their solid solution stainless steel is also BCC. However, on adding Ni (that exhibits stable FCC crystal structure) in excess, the new solid solution is thermodynamically more stable in FCC phase rather than BCC.

Electronegativity: Electronegativity (χ) difference between solute and solvent atoms should be small. If the electronegativity difference is large, it results in a strong attraction between two atoms. Therefore, they will make compounds instead of solution and the system will tend to be regular instead of random. On the other hand, entropy prefers the random arrangement of the atoms. Hence, as long as electronegativity difference is such that entropy is a dominating factor, the obtained system will form a solution rather than a compound. Using this criterion, on the Pauling scale, to have a solid solution, the maximum electronegativity difference is about 0.3.

$$\left|\frac{\chi_{solvent} - \chi_{solute}}{\chi_{solvent}}\right| \leq 0.3 \tag{1.4}$$

Valencies: The atoms should possess similar valency, i.e., the number of electrons in the valence shell should be same. In other words, if the elements belong to the same group of the periodic table the solubility will be maximum.

1.6 Properties affected or controlled by the by point defects

The presence of defects or imperfections in the crystal influences many crystal properties.Such properties which are being controlled or modified by the defects or crystal imperfections are as follows:

- The electrical conductivity of semiconductors is entierly controlled by the point defects.
- The thermal or electrical conductivity of the metals decreases with increase in point defects.
- Atomic diffusion and ionic conductivity can be accelerated immensely by point defects.
- Point defects can have a strong effect on the luminescence or color properties of the host crystal.
- Imperfections or defects also control the mechanical and plastic properties of the host crystal.

Here, we have provided an example to show the effect of the defect in solid-state materials on one of the systems that we have studied in our research work (see Figure 1.3). In Figure 1.3(a), we have shown a perfect crystal ($Cs_8Ag_4Bi_4Cl_{24}$) and its electronic and optical properties using the partial density of states (pDOS) and absorption plot, respectively. Whereas in the lower panel of this Figure, we have shown the optimized structure of the defective system ($Cs_3Ag_3AuBi_4Cl_{24}$), which is obtained by substituting Au at the Ag site i.e. substitutional point defect. The electronic and optical properties of this defective crystal are also shown in the same panel. A noticeable effect of the point defect can be seen on comparing the electronic and optical properties of pristine and defective systems. This shows how one can modulate the properties of the solid system by doing defects.

1.7 Role of point defects in advance energy materials

The point defects, either intrinsic or extrinsic, play a crucial role in modulating the functional properties of the solid crystals. Since defects require energy to be formed, therefore, they can be considered energy storage units in solid systems. In energy applications, defects play a central role as they affect the physical properties and have a decisive impact on the performance

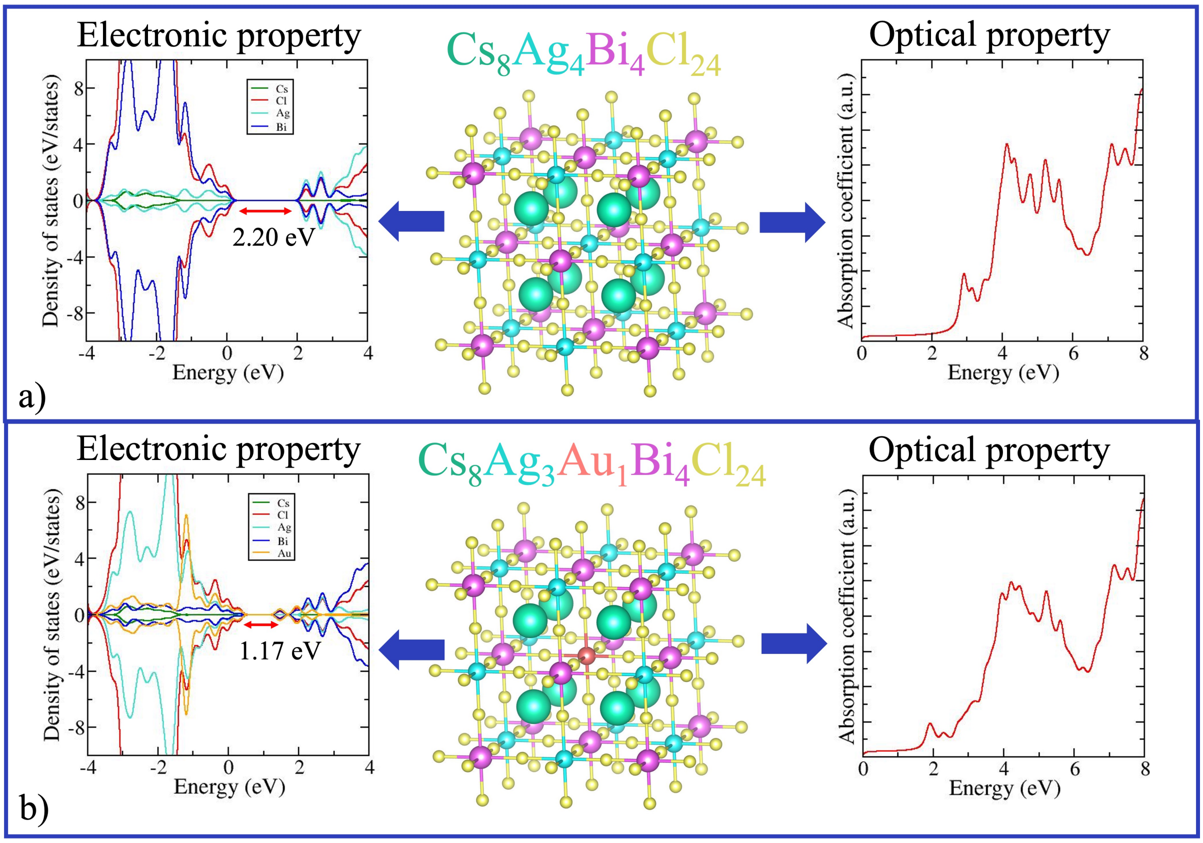

Figure 1.3: Partial density of states and absorption spectra of (a) pristine ($Cs_8Ag_4Bi_4Cl_{24}$) and (b) defected $Cs_8Ag_3Au_1Bi_4Cl_{24}$ double perovskites along with respective optimized geometries.

of the advanced energy materials (see Figure 1.4). Various properties like diffusion of ions, mechanical properties, electronic properties, and optical properties in semiconductors can be controlled by the different amount of doping or defects in the materials. A marvelous example of the effect of point defects is observed in semiconductors, where even a small concentration of defect can bring a large change in the electrical conductivity [295]. Therefore, characterization and controlling of defects are pivotal in solid materials. Experimentally characterization and identification of defects is a strenuous procedure, thus other techniques are required to perform this task. In this regard, first-principles calculations have emerged as a powerful tool to investigate the defects in various materials. In this race, for defect calculations, Density functional theory (DFT) which is based on the first principles approach has emerged as the most popular and reliable method among world wide research groups. Under the framework of DFT, we have attempted to understand the role of point defects in various materials which are directly or indirectly related to energy. In our present thesis, we have focused on various perovskite materials which include inorganic bulk/layered perovskites, hybrid layered perovskites, LISICON-based oxide materials and catalysts.

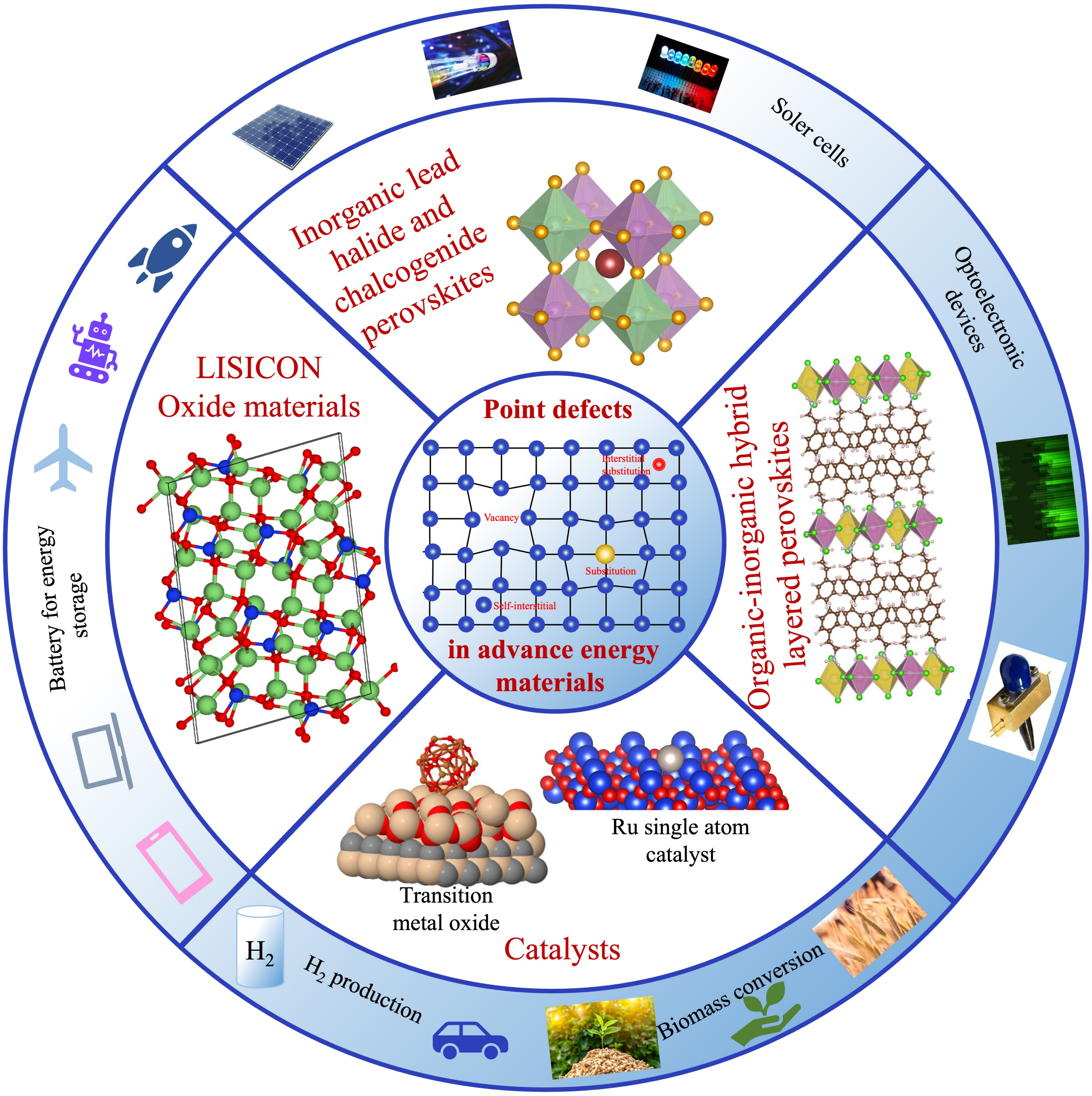

Figure 1.4: Schematic illustration of point defects in different energy materials viz., LISICON, perovskites, catalysts and their applications in automobile, electronic devices, solar cells, and optoelectronic devices, H_2 production and biomass conversion.

1.8 Problems and Challenges

When considering defects in semiconductors, the convergence of supercell size and a dependable exchange-correlation functional are the main challenges. To minimize defect-defect interactions, prior investigations frequently reported very low dopant concentrations. High doping concentrations can be attained, nonetheless, even when employing periodic boundary conditions to calculate system defects the supercell needs to be large enough for this function in order to prevent erroneous interactions between images. Interactions might have an impact on the defect levels, formation energies, and transition levels, which would lead to inaccurate results. Supercell size expansion may also bring attention to the problem of electrostatic interaction, particulary in charged defects in semiconductors. Even for established semiconductors like Si or Ge, high and adequate control over doping is still a hot topic of research [9]. Controlled doping is necessary because even semiconductors with acceptable inherent properties cannot be utilised in device applications if the material's conductivity is not under our control. From an experimental standpoint, this is a challenging endeavor, but advances in computational techniques allow us to use first-principles simulations to comprehend and manage the defects. Understanding the electrical and optical characteristics depends on the trustworthy exchange-correlation (ϵ_{xc}) functional. The ϵ_{xc} functional, which must be meticulously studied in light of the electron's self-interaction error and spin-orbit coupling (SOC) effect, has never been simple to understand at the theoretical level (e.g. DFT [10, 11]). Researchers are encouraged to employ straightforward GGA (PBE) functionals for this system since, in a select few circumstances, their contributions cancel one another and the bandgap agrees with the experimental values, such as MAPbI_3 [12, 13, 14, 15]. However, employing the PBE ϵ_{xc} [16, 17] functional would result in completely inaccurate defect formation energy, transition levels, and defect levels of neutral as well as charged defects due to the improper placements of the valence band maximum (VBM) and conduction band minimum (CBm).

In light of this, hybrid functionals have become a potent method to get around these problems. The ground state electronic structure is computed with extreme accuracy using DFT and hybrid functionals. However, GW+BSE calculations must be done for the best results in order to capture optical and excitonic effects in semiconducting materials. The schematic picture demonstrates the difficulties and many approaches one must take in order to record the electronic, optical, and excitonic characteristics as well as the thermodynamic stability of any system (see Figure 1.5). The dependability of the computational technique is mostly determined by comparing theoretical results with experimental data. Additionally, it gives theory the ability to comprehend and analyze the outcomes of experiments while also predicting the characteristics that may be subsequently explained by experiments.

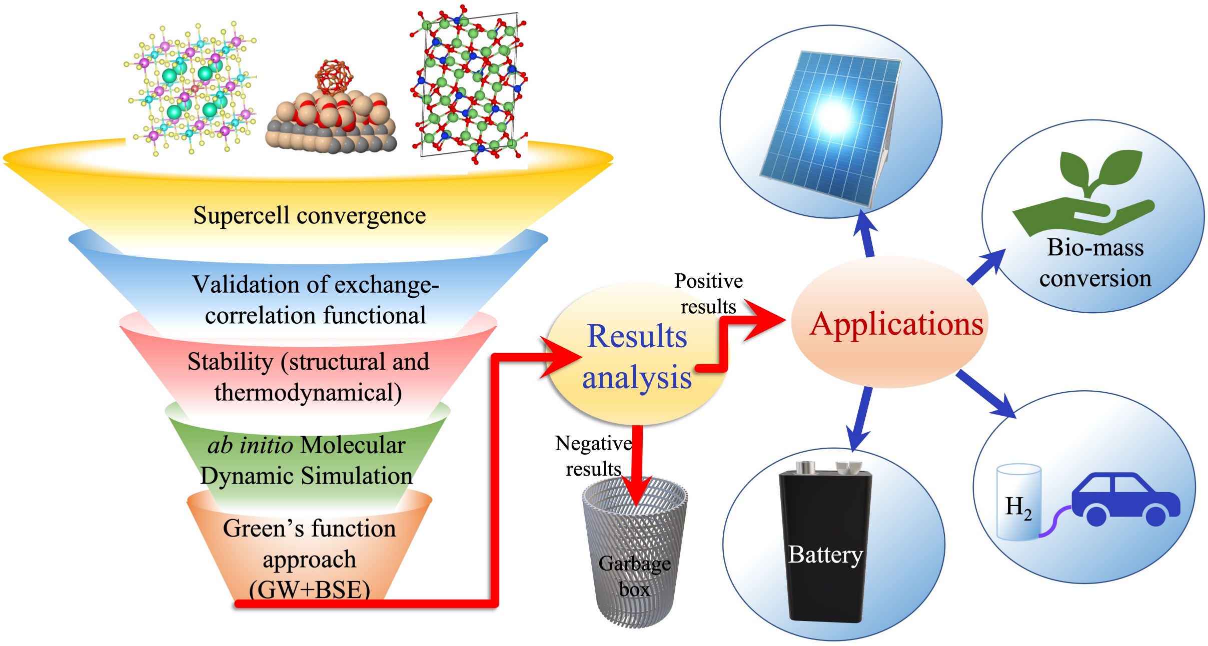

Figure 1.5: Schematic illustration of various energy materials as input, and several challenges and steps to be followed to have accurate prediction of the electronic, ion transport, optical properties and thermodynamic stability for their application in different energy fields.

1.9 A short overview

- **Chapter 2 :** The theoretical approach used in this work is presented in this chapter. We have briefly introduced to first-principles-based DFT, which is used to analyze the structural and electrical characteristics of different advanced energy materials. The GW approximation, and the BSE method, two MBPT techniques that are helpful in comprehending optical aspects including excitonic parameters, are also discussed. To determine the thermodynamic stability and dynamic diffusion of the ions in a system, a brief description of AIMD is also presented.

- **Chapter 3** : In this chapter, we have investigated the relationship between ionic diffusion and dopants/defects in LISICON, a potential solid-state battery (SSB) material. We have firstly computed the formation energies of various defects in LISICON using density functional theory (DFT) to identify the thermodynamically stable configurations. According to our findings, the most stable defects are those that retain charge neutrality. The diffusion and ionic conductivity of Li-ions have then been investigated using an AIMD simulation on (meta)stable (un)doped systems. We have examined the amplitude of vibration, tracer diffusivity, ionic conductivity, jump rate, charge density, and activation barrier for both pristine and point-defect samples after assessing the results of our AIMD simulation to gain insight into the synergistic impact of point defects. To get insight into the synergistic impact of point defects, we have compared the amplitude of vibration, tracer diffusivity, ionic conductivity, jump rate, charge density, and activation barrier for both pristine and defective systems. The jumps between various planes are strikingly dissimilar, which results in anisotropy in the ionic conductivity of LISICON. Since there are fewer interplanar leaps in bc planes, its ionic conductivity is constrained in that direction. We have also demonstrated that point defects, such as Li-vacancy and replacement at Si-sites with other elements, such as P, Ge, and Al, can increase the limited jump rate at ambient temperature.

- **Chapter 4** : In this chapter, we have offered a thorough theoretical analysis of how sublattice mixing can change the band gap of $Cs_2AgBiCl_6$ in this work. To improve the optical characteristics of $Cs_2AgBiCl_6$, M(I) is substituted at Ag-sites, M(II) at Ag- and Bi-sites concurrently, and M(III) at Bi-sites in a range of concentrations. DFT is used to produce a high-throughput screening by carrying out hierarchical calculations. We begin by doing extensive pre-screening on a large number of configurations using the GGA ϵ_{xc} functional (PBE), and the successful candidate structures are then further examined using hybrid DFT with HSE06. For a more precise knowledge of the excited state attributes, use the later ϵ_{xc} functional. It should be noted that the impact of SOC is always taken into account in the aforementioned computations (namely, PBE or HSE06). Due to the presence of heavy metal atoms, this step is essential for determining the precise band gap and band-edge locations of these systems. We have started with 64 separate sets of the metal combinations M(I), M(II), and M(III), respectively. First, the Goldschmidt tolerance factor and octahedral factor are used to determine structural stability. It is important to remember that perovskites cannot develop only on the basis of structural stability. Therefore, the enthalpy of breakdown per atom (H_D) is determined in order to confirm the material's thermodynamic stability. Then, in order to identify an effective solar cell absorber, we have calculated the spectroscopic limited maximum efficiency (SLME) of all the stable configurations with direct band gaps.

- **Chapter 5** : In the current work, we have investigated how the development of mixed perovskite structures can lower the concentration of Pb and increase solar cell performance by utilizing Ge/Sn substitution and Pb-vacancy (Pb). For this, we have first comprehensively benchmarked and verified the exchange and correlation (ϵ_{xc}) functionals inside the DFT framework to ensure that the findings are not influenced by the same artifacts. Then, using the calculated formation energy, we have looked into the thermodynamic stability and the structural stability using the Goldschmidt tolerance factor and octahedral factor. After that, we have looked at the stable configuration's electrical and optical characteristics. Finally, in order to assess their theoretical maximum efficiency as prospective solar cell materials, we have estimated exciton binding energy, electron-phonon coupling strength, and the spectroscopic limited maximum efficiency (SLME).

- **Chapter 6** : In this chapter, we have studied excitonic properties and polaron properties in Ruddlesden-Popper Phases of chalcogenide perovskites. Exciton generation has a significant impact on the charge separation characteristics of optoelectronic materials. Hence, one key excitonic parameter is the exciton binding energy (E_B), a term used to describe optoelectronic applications. Performance of solar cells is dependent on the percentage of the free-charge carriers which were created as a result of the thermal dissociation of excitons into electrons and holes. Additionally, polaron theory has been applied to explain a variety of photophysical phenomena. It has been proposed that polaronic effects play a significant impact in the carrier transport and excitation dynamics.

- **Chapter 7** : In this chapter, we have shown the role of point defects and surrounds on the catalytic performance of $CuFe_2O_4$ and Ru-single-atom, respectively. The S-I cycle involves several reactions, the most endothermic of which is SO_3 dissociation. For SO_3 dissociation, $CuFe_2O_4$ is spread over treated or untreated SiC. Here, we have investigated the impact of O-vacancy in enhancing the catalytic activity of the $CuFe_2O_4$ catalyst using a DFT technique. Next, we have studied the catalytic activity of Ru-single-atoms surrounded by different ligands. Due to their unique electrical characteristics, atomically dispersed metal-single-atoms have emerged as a frontier in solid catalysis. Even though metal-single-atoms have had considerable success in solid catalysis, it is still difficult to convert biomass using metal-single-atoms because of insufficient metal-support contacts and poor yield. In our research, we have theoretically studied the influence of various ligands around single Ru-atoms on the catalytic activities of the single Ru-atoms in the partial hydrogenation of xylose/glucose into useful sweeteners.

- **Chapter 8 : Conclusion**

  This chapter wraps up the research reported in the thesis and gives a quick overview of next initiatives.

CHAPTER 2

Theoretical methodology

2.1 Computer simulation

A computer simulation is a bunch of programs running on an assembly of CPUs to simulate an abstract model. It uses the mathematical description of the real system and this mathematical description consists of a set of equations to depict the functional relationships within the real system. In recent times, computer simulation has become an integral part of research in various fields such as mathematics, chemistry, physics, medical science, biology, economics, social science, psychology and engineering science. Simulation has become a powerful tool to explore new technologies and their innovations. Moreover, they can be used to estimate the performance of analytically complex systems of interest under a wide range of circumstances. Hence, apart from the theory and experiments, computer simulation has evolved as the third pillar of science and technology. The sustainable and steady enhancement in the comprehensive knowledge of algorithms, and the invention of fast computers, enable us to tackle the problems related to time and length scale in complicated systems. Multi-scale simulations incorporate a wide range of the length scale starting from the electronic, all the way to meso/micro/macro-scale and time scale from picosecond, all the way to days/months/years. Computational simulations act as an alternative for examing experiments which are not feasible in the laboratories due to various reasons. Hence, computational simulation act as a bridge between analytical theory and experiment. Moreover, computer simulation has evolved so much that it allows one to examine the functioning of entire system even the role of a tiny the entity that is influencing the system. Thus, a new interdisciplinary research area has been established by computational simulation, which is known as "Computational Material Science". In physics, the material properties and the material behavior under several environmental circumstances can be determined using multi-scale simulations. Here, multiscale simulation refers to the technique or practice of simulation in which information from different methods at different scales or levels is used simultaneously to describe a model system on one level gathering information from other levels. Here, different levels are distinguished as (i) molecular dynamic model (accounts for the information of individual atoms explicitly), (ii) quantum mechanical model (information about the electrons are included), (iii) meso-scale, which incorporates the information about the group of atoms or molecules, (iv) continuum models, where material exhibit continuous state instead of discrete states, (v) device model corresponds to an analytical model that emerged based on the substantial amount of theoretical and experimental results. Here, each level exhibits a particular time and length scale as shown in Figure 2.1. Multi-scale simulation plays a crucial role in computational material engineering to determine the various properties and to understand the behavior of the system utilizing elementary knowledge of the atomic structure. Computational methods can be used to determine several properties of materials viz. ground state properties, band gaps, vibrational spectra, optical spectra, and charge densities. Hence, based on different phenomena the aforementioned methodologies can be implemented to determine the properties of a material one is interested in. In the present thesis work, employing first principles electronic structures methods, we have performed simulations to study the effect of point defects on functional properties of the various distinct advanced energy materials (LISICON, Perovskites, catalysts). The outline of our theoretical framework is as follows: To have a basic idea of the first principles, first, a brief description of the first-principle has been provided. Here, we have explained how the quantum mechanical description is governed by Schrödinger equation can be used to determine the properties of the condensed materials. We then discuss the origin behind the density functional theory (DFT) which is governed by the Hohenberg-Kohn paradigm. Further, various exchange-correlation functionals have been categorized based on their approximations. For excited state properties, we highlight the beyond DFT methodologies which include Green's function approaches, in particular, GW and BSE. Lastly, we provide a brief introduction to *ab initio* Molecular Dynamic (MD) simulation, which is used to understand the dynamic motions of the atoms in the condensed material.

2.2 First principles calculation

Any theoretical calculation which is based on the basic laws of physics, and established science is said to be "First-principles calculations". Such calculations noway make hypotheticals such

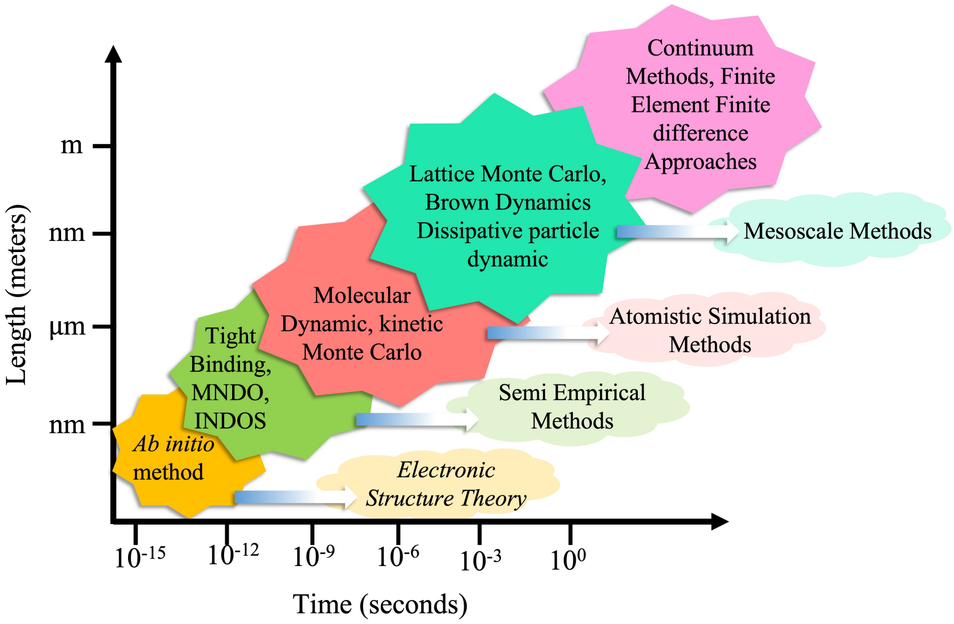

Figure 2.1: Multi-scale simulation in different length and time scales.

as empirical models or parameter fitting. Quantum mechanics, which is the fundamental theory of physics used to describe the characteristic or fundamental properties of atoms or molecules at the electronic level, comes under the first principles calculation. The whole world surrounding us consists of condensed matter. The state of matter where it gets condensed to the lowest energy to form a stable system that is made up of atoms/molecules is termed as condensed matter. Generally, condensed matter exists in liquid or solid phases. The building entity of condensed matter i.e., an atom is comprised of the positively charged nucleus which is surrounded by a negatively charged electron cloud. The interactions among the fundamental constituents of the atoms decide the nature of bonding (viz. covalent, ionic, chemical or molecular) among the atoms of condensed matter. Hence, all the physical properties or physics of a condensed matter eventually evolved from the interactions of these fundamental constituents. Therefore, to understand all the complex physical phenomena, accurate modeling of these basic interactions is a big challenge. Here, it should be noted that since this basic interaction is due to two entity (viz. nucleus and electron), the physics that describe this interaction is simple quantum mechanics. The main challenge comes when the number of atoms in the condensed matter increases, the numerical formulation becomes more complicated.

In 1928 Paul Dirac (a famous scientist of quantum mechanics said "*The fundamental physical laws necessary for the mathematical treatment of a large part of physics and the whole of chemistry are thus completely known, and the difficulty lies only in the fact that application of*

these laws leads to complicated equations which are too complex to be solvable”)
Thus, to deal with the many-body problem, the focus of the ongoing exploration in this realm is to develop efficient and precise theoretical and computational techniques.

2.3 Introduction to many body physics: A theoretical framework

The main goal of many-body physics is to study the mutual interactions among the quantum particles of a many-body system. By solving the basic fundamental equation i.e., the Schrödinger equation, the various properties of a many-body particle system can be determined. However, as the number of quantum particles increases in the many-body system, solving the Schrödinger equation analytically becomes impracticable except for a few simple systems such as a harmonic oscillator, H-atom or He-atom, etc. From the theoretical point of view, numerically the solution of any real system is feasible. However, due to the restricted speed and finite memory of the computers, the numerical solution is not possible for a system that consists of a large number of electrons. When determining the exact solution to a specific problem becomes extremely complex or computationally challenging, the normal strategy that is used is to replace the problem with a new problem that is in its approximation. Such that solution to a new problem is feasible and is slightly different from the original. The difference between the two is considered as a perturbation to exactly solvable problem and the approach is termed as perturbation theory. Hence, the quantitative result of many body system is an approximate solution, which is further improved by doing corrections to the approximate value. The first approximation that is used to tackel the many body problem is Born-Oppenheimer approximation [18],where the motion of the electron and nucleus can be decoupled owing to heavier mass of the nucleus, hence the total wavefunction can be written as a product of the nucleus and electron wavefunction. Though this approximation reduces the complication of the many body problem to some extent, the electron-electron interaction remains a big challenge. In 1927, D.R. Hartree introduced an approximation to solve the many body problem, according to this approximation each electron move under an effective central potential due to nucleus and other electrons. Therefore, all the electrons can be treated as independent entity and total wavefunction of the many body system can be considered as a product of wavefunctions of the of individual electron. His work sets a stage for various numerical calculations still in use today. The biggest draw back of this approximation is that the symmetric wavefunction proposed by Hartree does not satisfy Pauli's exclusion principles. According to Pauli's principle, two fermions can't exist in one state. Therefore, the nature of the many-body wavefunction should be antisymmetric. Later, in 1930, Fock came up with an antisymmetric determinant wavefunction [19] for many-body problems, which satisfies Pauli's principle that each electron is described by a distinguished wavefunction. This approach is known as Hartree Fock (HF) method. This approximation adds a new additional term i.e., exchange interaction term (or electron exchange term) between the electrons having the same spin in the Schrödinger equation. Though this approximation improves the total energy and successfully defines the geometries, since it neglects the correlation term, it fails to predict the physical and chemical properties of the materials. In 1960, Coulson, to account for the correlation term, considered a linear combination of Slater determinants instead of single determinant. Later, to consolidate exchange and correlation interactions, various methods have been proposed viz. Møller-Plesset (MP) perturbation theory, Coupled Cluster (CC) methods, Configuration Interaction (CI), Quantum Monte-Carlo (QMC) methods, and multiconfiguration self-consistent field (MCSCF). These approaches are often known as "beyond Hartree Fock" method. Although, aformentioned methods improve the calculations, still these methods suffer substantial drawback due to the "exponential wall", means exponential increment in the computational cost with the number of particles in a system. Hence, it is a computationally very expensive task even for a system with few number of atoms. Therefore, in order to develop a method which incorporates the electron correlation effect and easily deal with larger systems (viz. consist of hundreds, thousands of atoms etc.), nowadays, for electronic structure calculation, DFT has evolved as a most powerful technique and widely used methodology.

The DFT is based upon two fundamental theorems provided by the Hohenberg and Kohn [10]. The main motive of these theorems is to formulate DFT as exact methodology for a many body system consisting of interacting particles. According to these theorems many properties of the system can be written as a function of the electron density, which includes the total energy. This energy will be minimum if the density is an exact ground state density of many-body interacting system. Later in, 1965, Kohn and Sham, proposed that ground state density of a real interacting many body system can be replaced by an auxiliary non-interacting system. To incorporate the exchange and correlation effects within approximation, it considers an auxiliary hamiltonian (with usual kinetic energy term) and an effective local potential. The incorporation of the exchange-correlation energy as a functional of the density of electrons is the fundamental remark of Kon-Sham approach. For quantitative calculations on realistic problems, this approach is widely used to understand the ground state properties. To understand particle behavior at the quantum level, DFT is a marvelously exemplary approach. The crucial point of the DFT is that all the properties of the many-body system can be described as a functional of the ground state density; where the density is the scalar function of the position of the electrons and comprised of all the details of the system. If it is possible to derive an accurate or exact relation between the density of the electrons and the energy, the DFT will give an accurate value. However, for many cases, DFT results are surprisingly accurate even if one takes into account the simplest approximation used to derive the relation between the electron density and the energy. The DFT has achieved great popularity in the field of computational theory due to its ability to describe the ground state properties with a good balance between the electronic structure description and computational cost. However, it should be noted that DFT gives result at 0K and an unparalleled approach for the ground state properties, but fails to describe the excited state properties. Hence, to predict the excited state properties, beyond DFT approaches such as *ab initio* many-body perturbation theory (viz. GW approximation and the Bethe-Salpeter equation (BSE) are efficient methods. Further, to study the dynamic properties of the many-body system, ab initio molecular dynamics is an established approach. To determine the minimum energy path for any reaction mechanism, the Nudge elastic band (NEB) [20] method is being used.

2.4 Wavefunction

In quantum physics, the mathematical description of any quantum state of a system as a function of momentum, time, position, and spins is known as a wavefunction. Generally, the Greek letter psi (Ψ) is used to describe a wavefunction, e.g., ($\Psi(\mathbf{r}_1, \mathbf{r}_2, ...\mathbf{r}_i, ...; \mathbf{R}_1, \mathbf{R}_2, ...\mathbf{R}_l, ...)$), where $\mathbf{r}_i$ and $\mathbf{R}_l$ correspond to the position of the i^{th} electron and l^{th} nucleus, respectively of the system. Using wavefunction, we can determine the probability of finding the electron at an instant at a particular position. Subsequently other properties like momentum, kinetic energy, etc. can be determined. To be physically acceptable, a wavefunction must satisfy the following necessary conditions:

1. It must be single-valued

2. It and all its first-order derivatives must be continuous everywhere
3. It must be square integrable.
4. It must vanish at infinity for a finite system
5. It must be finite everywhere

Once wavefunction Ψ is known for a system, then one can calculate the expectation value of any physical quantity. Notably, the eigenvalue of an observable must be a real number. For example, the expectation value of the E having operator $\hat{H}$ is given below:

$$E = \frac{\int\int ... \int \Psi^*(\mathbf{r}_1, \mathbf{r}_2, ...\mathbf{r}_N)\hat{H}\Psi(\mathbf{r}_1, \mathbf{r}_2, ...\mathbf{r}_N)d\mathbf{r}_1 d\mathbf{r}_2 ...d\mathbf{r}_N}{\int\int ... \int \Psi^*(\mathbf{r}_1, \mathbf{r}_2, ...\mathbf{r}_N)\Psi(\mathbf{r}_1, \mathbf{r}_2, ...\mathbf{r}_N)d\mathbf{r}_1 d\mathbf{r}_2 ...d\mathbf{r}_N} \tag{2.1}$$

Dirac bra and ket notation is another convenient way of writing the expectation value:

$$E = \frac{\langle\Psi|\hat{H}|\Psi\rangle}{\langle\Psi|\Psi\rangle} \tag{2.2}$$

We use normalized wavefunction, i.e., $\langle\Psi|\Psi\rangle = 1$. Note that, Ψ does not exhibit any physical meaning. However, the square $|\Psi(\mathbf{r}_1, \mathbf{r}_2, ...\mathbf{r}_N)|^2$ gives the probability of finding one electron at $\mathbf{r}_1$ and another one at $\mathbf{r}_2$, and so forth. We can understand this normalization with an example. Let us consider a system consisting of a single electron, then $|\Psi(\mathbf{r})|^2 d\mathbf{r}$ conveys the probability of finding the electron at point $\mathbf{r}$ within a small volume $d\mathbf{r}$. Now if the wavefunction is normalized, then its integration over all the space must be equal to 1, which means the probability of

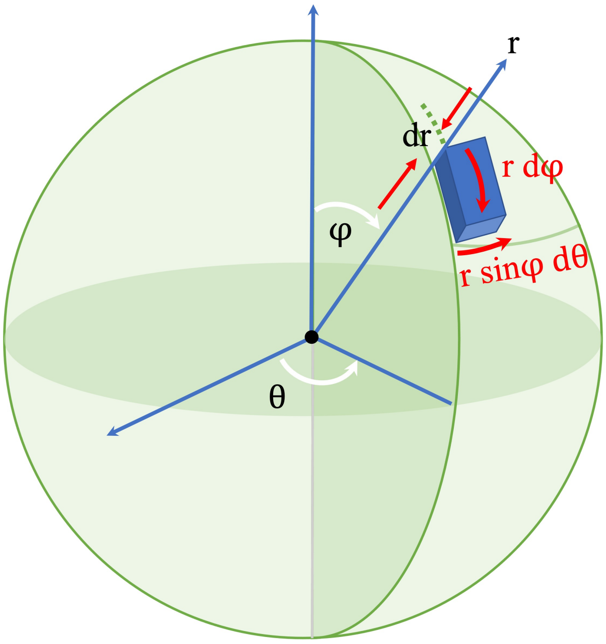

Figure 2.2: The polar coordinates of a spherical symmetric system

finding the electron is 1 and it is 100% sure that the electron lies somewhere within complete space.

$$\int \Psi(\mathbf{r})^*\Psi(\mathbf{r})d\tau = \int_0^{\pi}\int_0^{2\pi}\int_0^{\infty} \Psi(\mathbf{r})^*\Psi(\mathbf{r})\mathbf{r}^2 sin\theta d\mathbf{r} d\theta d\phi = 1 \qquad (2.3)$$

2.5 Time independent Schrödinger equation

In quantum mechanics, the wavefunction of a quantum system is governed by the Schrödinger equation which is a linear differential equation. For a many-body system, the physical or chemical properties can be determined at the microscopic level by solving time independent Schrödinger equation.

$$\hat{H}\Psi(\mathbf{r}_1, \mathbf{r}_2, ...\mathbf{r}_i, ...; \mathbf{R}_1, \mathbf{R}_2, ...\mathbf{R}_l, ...) = E\Psi(\mathbf{r}_1, \mathbf{r}_2, ...\mathbf{r}_i, ...; \mathbf{R}_1, \mathbf{R}_2, ...\mathbf{R}_l, ...) \qquad (2.4)$$

In the above equation, $\hat{H}$ (pronounced as Hamiltonian) is an operator corresponding to the total energy (viz. kinetic and potential energy). For a many-body system, the total energy (E) of a system can be determined by constructing many-body Hamiltonian $\hat{H}$. Note that throughout the following sections, atomic-units $\hbar$ = 1, m$_e$ = 1, e = 1, and $4\pi\epsilon_0$ are used. The general form of many-body hamiltonian is:

$$\hat{H} = -\frac{1}{2}\sum_i \nabla_i^2 - \sum_{i,l}\frac{Z_I}{|\mathbf{r}_i - \mathbf{R}_I|} + \frac{1}{2}\sum_{i\neq j}\frac{1}{|\mathbf{r}_i - \mathbf{r}_j|} - \sum_I \frac{1}{2M_I}\nabla_I^2 + \frac{1}{2}\sum_{I\neq J}\frac{Z_I Z_J}{|\mathbf{R}_I - \mathbf{R}_J|} \qquad (2.5)$$

where $\mathbf{r}_i$ and $\mathbf{R}_I$ correspond to the position of i^{th} electron and I^{th} nucleus, respectively. Z_I is the atomic number of the I^{th} atom. ∇_i^2 characterizes the Laplacian operator. $|\mathbf{r}_i - \mathbf{R}_I|$ denotes the distance between the I^{th} nucleus and the i^{th} electron, whereas, $|\mathbf{r}_i - \mathbf{r}_j|$ corresponds to the distance between the i^{th} and j^{th} electron. $|\mathbf{R}_I - \mathbf{R}_J|$ is the distance between the I^{th} and J^{th} nucleus. In Equation 2.5, the first and fourth terms are the kinetic energy of the electron and nucleus, respectively. The second term corresponds to the potential energy due to the Coulomb attraction between the electrons and nuclei. The third and fifth terms are the potential energies due to Coulomb repulsion between electrons and nuclei, respectively. In cartesian coordinates $|\mathbf{r}_i - \mathbf{r}_j|$ and $|\mathbf{r}_i - \mathbf{R}_I|$ can be written as follows:

$$|\mathbf{r}_i - \mathbf{r}_j| = \sqrt{(x_i - x_j)^2 + (y_i - y_j)^2 + (z_i - z_j)^2}$$

$$|\mathbf{r}_i - \mathbf{R}_I| = \sqrt{(x_i - X_I)^2 + (y_i - Y_I)^2 + (z_i - Z_I)^2}$$

Equation 2.5 can be written in a more comprehensive form:

$$\hat{H} = \hat{T}_e + \hat{V}_{ext} + \hat{U}_{ee} + \hat{T}_{nucl} + \hat{U}_{nucl} \qquad (2.6)$$

where $\hat{T}_e$ denotes the kinetic energy of electrons.

$\hat{V}_{ext}$ denotes the potential energy due to the Coulomb interaction between the electrons and nuclei.

$\hat{U}_{ee}$ is the potential energy due to electrostatic repulsion among electrons.

$\hat{T}_{nucl}$ corresponds to the total kinetic energy associated with the nuclei.

$\hat{U}_{nucl}$ is the potential energy due to interaction among nuclei.

However, as the system becomes larger (i.e, consisting of the large number of quantum particles), the number of variables becomes large and solving the Schrödinger equation becomes impracticable. Tremendous efforts have been done in search of practicable approximations to reduce the complexity of the Schrödinger equation. In this regard, the Born-Oppenheimer approximation, which considers the dynamics of electrons and nuclei, was revolutionary in simplifying the Schrödinger equation.

2.6 Born-Oppenheimer approximation

In 1927, Born and Oppenheimer came up with first approximation for the first level of simplification of Schrödinger equation. According to Born-Oppenheimer approximation, since the mass of electrons in comparision to the nuclei is negligible (mass of a proton is 1836 times that of the electron). Hence, the velocity of the nuclei will be much slower than that of electrons, for the same quantity of kinetic energy. In consequence, without any lapse of time, the electrons adjust their ground state w.r.t. any change in the position of the nuclei. Here, using parametric approach, the motion of the nuclei can be considered as static w.r.t. the electrons and the dynamics of electrons and nuclei can be treated distinctly. Mathematically, we can decouple the total wavefunction as a product of individual wavefunctions of the electrons and nuclei.

$$\begin{aligned} \Psi_{total} &= \psi_{electronic} \times \psi_{nuclear} \\ \Psi(\mathbf{r}_1, \mathbf{r}_2, ..., \mathbf{R}_1, \mathbf{R}_2, ...) &= \psi(\mathbf{r}_1, \mathbf{r}_2, ...; \mathbf{R}) \times \psi(\mathbf{R}_1, \mathbf{R}_2, ...) \end{aligned} \tag{2.7}$$

The wavefunction of the electron (i.e., $\psi(\mathbf{r}_1, \mathbf{r}_2, ...; \mathbf{R})$) parametrically depends on the nuclear position (R). Thus, R can be suppressed for stationary nuclei. While solving many-body hamiltonian, we can omit the nuclear kinetic energy term ($\hat{T}_{nucl}$) and another term that is due to ion-ion electrostatic interaction. After solving electronic ground state energy, we can calculate the nuclear energy terms (viz. $\hat{T}_{nucl}$ and $\hat{U}_{nucl}$) and add these energies to electronic ground state energy to have the total ground state energy of the system. The simplified form of the electronic

Hamiltonian for the many-body system is:

$$\hat{H}_{el} = \hat{T}_e + \hat{V}_{ext} + \hat{U}_{ee} \tag{2.8}$$

The above electronic Hamiltonian can be written as:

$$\hat{H}_{el} = \sum_{i=1}^{N} \hat{h}_i + \hat{U}_{ee} \tag{2.9}$$

Here, $\hat{h}_i = -\frac{1}{2}\nabla_i^2 + \hat{v}_i$, which depends on the position of the i^{th} electron. $\hat{U}_{ee}$ depends simulataneously on the position of two electrons. Now solution of the Schrödinger equation for this new simplified Haliltonian can be written as follows:

$$\hat{H}_{el}\psi_e(r_i, \sigma_i) = E_e\psi_e(r_i, \sigma_i) \tag{2.10}$$

Though the Born-Oppenheimer approximation reduces the dimensionality of the many-body wavefunction, still to obtain an exact solution one needs to deal with 3N number of variables for a system consisting of N electrons owing to electron-electron interaction ($\hat{U}_{\text{ee}}$). Hence, it is still impractical to solve the Schrödinger equation and further approximations are required to evaluate the electron-electron interaction terms accurately.

2.7 Wavefunction based approximation

The fundamental quantity that we need to determine to solve the Schrödinger equation is the many-electron wavefunction. To have a correct form of the wavefunction, one needs to apply the most common strategy i.e., first guess a wavefunction and then apply the variational principle. According to variation principle, the expectation value of energy E is calculated using this guess wavefunction is either equal to the ground state energy E_0 or greater than the E_0.

$$E = \frac{\left\langle \Psi|\hat{H}|\Psi \right\rangle}{\langle \Psi|\Psi \rangle} \geqslant E_0 \tag{2.11}$$

Notably, $E = E_0$ is satisfied only if the wavefunction belongs to actual ground state i.e. $\Psi = \Psi_0$.

2.8 The Hartree approximation

In 1984, Hartee provided an independent-electron picture [21, 22], which considers that all electrons are independent of each other and do not interact individually, but each electron interacts with an averaged density of the electrons. According to this approximation, the N electron wavefunction, Ψ can be written as a product of the individual single electron wavefunctions ($\phi_i(\mathbf{r}_i)$):

$$\Psi_{\mathbf{r}_1,\mathbf{r}_2,...\mathbf{r}_N} = \phi_1(\mathbf{r}_1)\phi_2(\mathbf{r}_2)...\phi_N(\mathbf{r}_N) \tag{2.12}$$

The density corresponding to each electron can be determined as follows:

$$\rho_i(\mathbf{r}) = |\phi_i(\mathbf{r})|^2 \tag{2.13}$$

Hence, the aggregate electron density for all the electrons present in the system is:

$$\rho_{total}(\mathbf{r}) = \sum_{i=1}^{N} \rho_i(\mathbf{r}) = \sum_{i=1}^{N} |\phi_i(\mathbf{r})|^2 \tag{2.14}$$

The density of the electron with which k^{th} electron interacts can be written as:

$$\rho^k(\mathbf{r}) = \rho_{total}(\mathbf{r}) - \rho_k(\mathbf{r}) = \left(\sum_{i=1}^{N} \rho_i(r)) - |\phi_k(\mathbf{r})|^2\right) = \sum_{i=1,i\neq k}^{N} |\phi_i(\mathbf{r})|^2 \tag{2.15}$$

Notably, here we have excluded the k^{th} electron from the density term with which the k^{th} electron interacts. Now the interaction of an electron located at **r** with the rest electrons can be written as:

$$\hat{g}_k(\mathbf{r}) = \int \rho^k(\mathbf{r}')\frac{1}{|\mathbf{r}-\mathbf{r}'|}d\mathbf{r}' \tag{2.16}$$

Hence, the electron-electron interaction term can be written as:

$$\hat{U}_{ee} \approx \sum_{i=1}^{N} \hat{g}_i(\mathbf{r}) \tag{2.17}$$

Still, there is a discrepancy due to the double count of the interaction term, which we will correct later. Now, $\hat{H}_{el}$ can be written as a single electron operator and many-electron Schrödinger equation can be simplified into N-independent single electron equations:

$$\hat{H}_{el} \approx \sum_{i=1}^{N}\left(-\frac{1}{2}\nabla_i^2 + \hat{v}_i + \hat{g}_i(\mathbf{r})\right) \tag{2.18}$$

$$\left(-\frac{1}{2}\nabla_i^2 + \hat{v}_i + \hat{g}_i(\mathbf{r})\right)\phi_i(\mathbf{r}) = \epsilon_i\phi_i(\mathbf{r}) \tag{2.19}$$

ϵ_i correspond to the i^{th} electron energy. As an initial step, first, we consider an approximate orbital ϕ_i which belongs to the simplest system i.e., H atom. Using these orbitals, $\hat{g}_i(\mathbf{r})$ Hartree potential is obtained and subsequently, N equations of single particle Schrödinger equations are solved to have new ϕ_i's. Here, we consider these new ϕ_i's better than the previous ϕ_i. In the next iteration, we consider these new orbitals as starting points. We iterate until no further improvements or changes are observed between two consecutive iterations. (see Figure 2.3) i.e. self-consistent field orbital is converged. Using these converged orbitals the, many-body wavefunction Ψ is constructed, which is further used to obtain total ground state energy E, which is the expectation value of the Hamiltonian $\hat{H}_{el}$. Note that, the total energy E may not be equal to the sum of the energies of the individual orbitals (ϵ_i). Further, using the variational principle approach, the ground state wavefunction is obtained. Mathematically the variational principle is as follows:

$$\frac{\langle\Psi|\hat{H}|\Psi\rangle}{\langle\Psi|\Psi\rangle} \geq E_0 \tag{2.20}$$

Here, E_0 is the ground state energy of the system. In general, the electron-electron Coulomb interactions are counted twice, once when we calculate for ϕ_i and ϵ_i and the second time when we solve for new $\phi_i^{'}$ and $\epsilon_i^{'}$. Therefore, the accurate total energy is:

$$E = \sum_{i=1}^{N} \epsilon_i - \sum_{i=1}^{N-1} \sum_{j=i+1}^{N} J_{ij} \tag{2.21}$$

where, J_{ij} correspond to the Coulomb integrals i.e., the interaction between i$^{\text{th}}$ and j$^{\text{th}}$ electrons, which is defined as follows:

$$J_{ij} = \int\int \frac{\rho_i(\mathbf{r}_1)\rho_j(\mathbf{r}_2)}{|\mathbf{r}_1 - \mathbf{r}_2|} d\mathbf{r}_1 d\mathbf{r}_2 = \int\int |\phi_i(\mathbf{r}_1)|^2 \frac{1}{|\mathbf{r}_1 - \mathbf{r}_2|} |\phi_j(\mathbf{r}_2)|^2 \, d\mathbf{r}_1 d\mathbf{r}_2 \tag{2.22}$$

Though Hartree's approach works well with simple systems and can be considered the foundation for the various approximations to solve many-body problems efficiently. However, the main drawback of the Hartree approach is that its wavefunction is symmetric and does not satisfy Pauli's exclusion principle.

2.9 The Hartree-Fock approximation

After a few years, Fock [23] introduced a new term i.e., exchange energy term, and in the same year, independently Slater[24] proposed a similar solution. Both worked on the modification of the Hartree independent particle approach and product wavefunction. They suggested a single determinant theory for many-body wavefunction instead of product wavefunction used in independent particle approach. Since an elelctron is a fermion, hence two electrons can not exist simultaneously in the same state. Therefore, the wavefunction of the many-electron system must be antisymmetric under the exchange of electrons.

$$\hat{P}_{1,2}\Psi(\mathbf{r}_1, \mathbf{r}_2, ...\mathbf{r}_N) = -\Psi(\mathbf{r}_2, \mathbf{r}_1, ...\mathbf{r}_N) \tag{2.23}$$

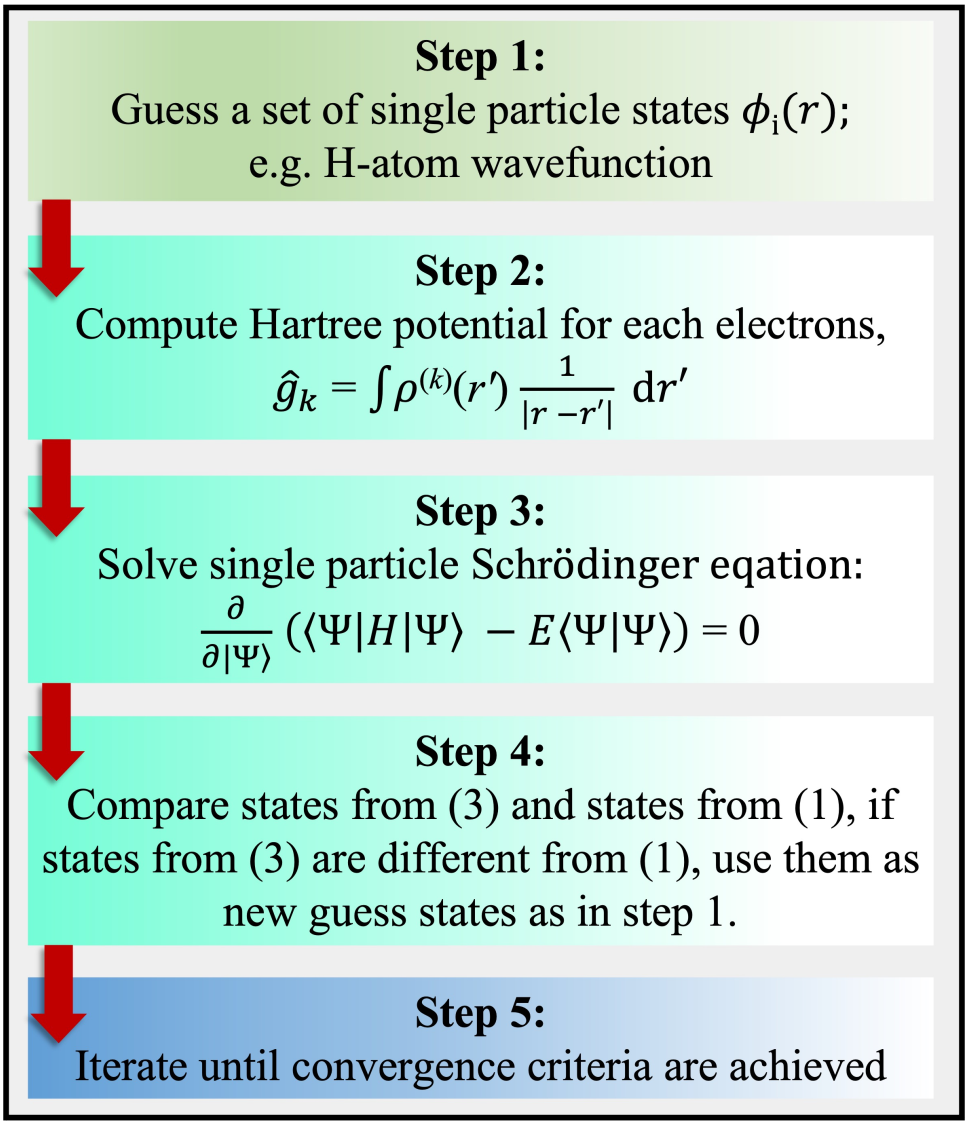

Step 1:
Guess a set of single particle states $\phi_i(r)$;
e.g. H-atom wavefunction

Step 2:
Compute Hartree potential for each electrons,
$$\hat{g}_k = \int \rho^{(k)}(r') \frac{1}{|r - r'|} \, dr'$$

Step 3:
Solve single particle Schrödinger eqation:
$$\frac{\partial}{\partial |\Psi\rangle} \left(\langle \Psi | H | \Psi \rangle - E \langle \Psi | \Psi \rangle \right) = 0$$

Step 4:
Compare states from (3) and states from (1), if states from (3) are different from (1), use them as new guess states as in step 1.

Step 5:
Iterate until convergence criteria are achieved

Figure 2.3: Schematic flowchart of Hartree method for solving the many electron system.

here, $\hat{P}_{1,2}$ corresponds to the parity operator. The negative sign established that if any two or more electrons occupy the same state and violate Pauli's exclusion principle, then eventually the total wavefunction will be reduced to zero. In Hartree-Fock approach, the wavefunction of N interacting electrons is associated with a single Slater determinant. Where a Slater determinant is elucidated as a linear combination of all products of single electron wavefunctions obtained after employing all possible combinations and permutations of the electrons. However, this way of presentation of N electron wavefunction would be very tedious. To overcome this, Slater recommended a more convenient way to represent the wavefunction, where a wavefunction is represented as a single antisymmetric Slater determinant, and matrix elements of this determinant are single electron states.

$$\Psi(\mathbf{r}_1, \mathbf{r}_2, ...\mathbf{r}_N) = \frac{1}{\sqrt{N!}} \begin{vmatrix} \phi_1(\mathbf{r}_1) & \phi_2(\mathbf{r}_1) & ... & \phi_N(\mathbf{r}_1) \\ \phi_1(\mathbf{r}_2) & \phi_2(\mathbf{r}_2) & ... & \phi_N(\mathbf{r}_2) \\ \phi_1(\mathbf{r}_3) & \phi_2(\mathbf{r}_3) & ... & \phi_N(\mathbf{r}_3) \\ . & . & . & . \\ . & . & . & . \\ . & . & . & . \\ \phi_1(\mathbf{r}_N) & \phi_2(\mathbf{r}_N) & ... & \phi_N(\mathbf{r}_N) \end{vmatrix} \tag{2.24}$$

To have a better understanding, let us consider an example of a two-electron system:

$$\Psi(\mathbf{r}_1, \mathbf{r}_2) = \frac{1}{\sqrt{2}} \begin{vmatrix} \phi_1(\mathbf{r}_1) & \phi_2(\mathbf{r}_1) \\ \phi_1(\mathbf{r}_2) & \phi_2(\mathbf{r}_2) \end{vmatrix} = \frac{1}{\sqrt{2}}[\phi_1(\mathbf{r}_1)\phi_2(\mathbf{r}_2) - \phi_2(\mathbf{r}_1)\phi_1(\mathbf{r}_2)] \tag{2.25}$$

Now on interchanging the labels of these two electrons, the obtained wavefunction is:

$$\Psi(\mathbf{r}_2, \mathbf{r}_1) = \frac{1}{\sqrt{2}} \begin{vmatrix} \phi_1(\mathbf{r}_2) & \phi_2(\mathbf{r}_2) \\ \phi_1(\mathbf{r}_1) & \phi_2(\mathbf{r}_1) \end{vmatrix} = \frac{1}{\sqrt{2}}[\phi_1(\mathbf{r}_2)\phi_2(\mathbf{r}_1) - \phi_2(\mathbf{r}_2)\phi_1(\mathbf{r}_1)] \tag{2.26}$$

$$\Psi(\mathbf{r}_1, \mathbf{r}_2) = -\Psi(\mathbf{r}_2, \mathbf{r}_1) \tag{2.27}$$

Now if we assume a situation when both the electrons exhibit the same spin-orbital i.e. $\phi_1 = \phi_2 = \phi$, we procure:

$$\Psi(\mathbf{r}_2, \mathbf{r}_1) = \frac{1}{\sqrt{2}} \begin{vmatrix} \phi(\mathbf{r}_2) & \phi(\mathbf{r}_2) \\ \phi(\mathbf{r}_1) & \phi(\mathbf{r}_1) \end{vmatrix} = \frac{1}{\sqrt{2}}[\phi(\mathbf{r}_2)\phi(\mathbf{r}_1) - \phi(\mathbf{r}_2)\phi(\mathbf{r}_1)] = 0 \tag{2.28}$$

This results in the wavefunction and probability of finding such electrons being zero. Finding a suitable wavefunction determinant that minimizes the system energy for the interacting Hamiltonian is termed as Hartree-Fock method. Figure 2.4 shows the flowchart which summarizes the various steps involved in Hartree-Fock method. Notable, Slater's determinant obeys the Pauli's principle. When any two rows of the determinant are same, it results in zero, which means no two electrons can exist in the same state simultaneously. On interchanging any two rows of the determinant, the sign changes and if any one row or column is zero, the determinant will be zero. This incorporates a new exact term i.e., $electron\ exchange$ in the Hartree method. However, electron-electron Coulomb correlation energy is neglected which is the difference between exact energy and Hartree-Fock energy ($E_{corr.} = E_{exact} - E_{HF}$) of the system.

It plays a pivotal role to delineate the chemical and physical properties of solid-state systems which consists of atoms or molecules. Hence, to account for correlation energy, many correlated approaches have been proposed which consider multi-determinant wavefunctions for example CI, CC, MP2, MP4 and QMC methods. Although these methods are rather accurate, still computationally immensely expensive. Hence, a more scrupulous approach is required to deal with interacting many-body systems. In this regard, the DFT allows one to solve the many electron problems by balancing the computational cost and accuracy.

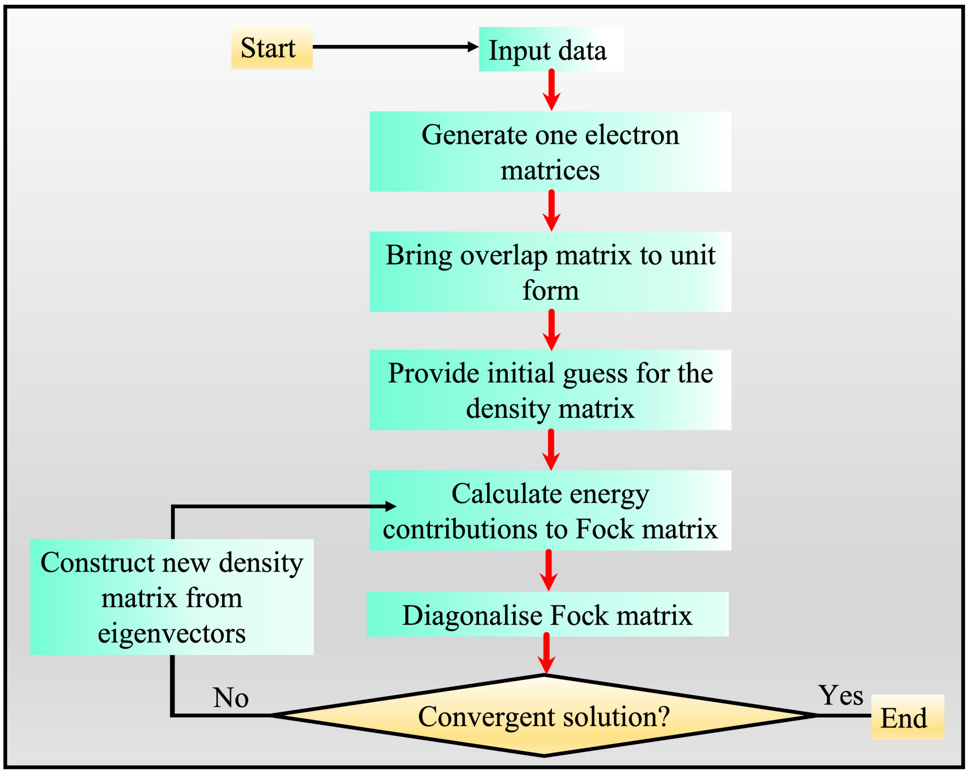

Figure 2.4: Schematic flowchart of Hartree-Fock method for many-body system.

2.10 Functional

A function of function is known as a functional. It means that the argument of a functional is a function and when we apply a functional on a function it yields an output. Let us consider f is a function of x and F is the functional of f then in general notation, it will be written in square brackets as $F[f] = a$. Like functions can have derivatives. Similarly derivatives of the functionals are also possible that is defined as:

$$\partial F[f] = F[f + \partial f] - F[f] = \int \frac{\partial F}{\partial f(x)} \partial f(x) dx \tag{2.29}$$

Notably, the derivatives of the functional exhibit similar properties as that of conventional derivatives of the functions.

2.11 Density Functional Theory

Density functional theory (DFT), like its name is the theory which is centralized on the electron density and widely used in the computational study of material science, condensed matter physics and chemistry. To describe the ground state properties of the materials, it has been widely accepted. Unlike other wavefunction approaches, the key point of the DFT is that it considers the electron density which abundantly reduces the degree of freedom of N particle system from 3N to 3. As density always possesses 3 degree of freedom independent of the number of atoms in the system. This enables the solution of Schrödinger equation tractable for an interacting system consisting of hundreds or thousands of atoms. In 1927, Thomas and Fermi proposed the Thomas-fermi model that is also based on electron density approach instead of the wavefunction. Whereas in 1964, Hohenberg and Kohn, established the foundation of the modern DFT. In 1998, Walter Kohn won the Noble prize in Chemistry for his incredible contribution in fomulating the foundation of the DFT. In henceforth sections, we have described the evolution of DFT in more detail.

2.11.1 The Thomas-Fermi Model

To approximate the total energy of the system, the elementary approach is the Thomas-Fermi approach[25, 26] which assumes uniform electron density in an atom. The Thomas-fermi kinetic energy functional is a functional of local electron density which is written as follows:

$$T_{TF}[\rho(\mathbf{r})] = \frac{3}{10}(3\pi^2)^{2/3} \int \rho^{5/3}\rho(\mathbf{r}) d^3\mathbf{r} \tag{2.30}$$

Note that local density approximation (LDA) uses the same expression. Incorporating all the energy terms due to other interactions, the total energy equation given by Thomas-Fermi approach is:

$$E^{TF}[\rho(\mathbf{r})] = \frac{3}{10}(3\pi^2)^{2/3} \int \rho^{5/3}\rho(\mathbf{r}) d^3\mathbf{r} - \int \frac{\rho(\mathbf{r})}{\mathbf{r}} d^3\mathbf{r} + \frac{1}{2}\int \frac{\rho(\mathbf{r}_1)\rho(\mathbf{r}_2)}{\mathbf{r}_{12}} d^3\mathbf{r}_1 d^3\mathbf{r}_2 \tag{2.31}$$

where, the second and third terms on the RHS correspond to the potential energy due to electron-nucleus interaction and the Hartree energy i.e. electron-electron interaction, respectively. Using variational principle, the electron density and hence, the total ground state energy can be obtained. However, inaccurate kinetic energy and non-inclusion of the exchange-correlation effects are termed out to be the major drawbacks of this approach. In 1930, Dirac[27] introduced a new term to incorporate the electron exchange term in the Thomas-Fermi model, this approach is known as Thomas-Fermi-Dirac model. However, the shell structure of the atoms is a crude approximation of this approach and gives inaccurate results for the molecular systems.

2.11.2 Hohenberg and Kohn Theorem

In 1964, Hohenberg and Kohn introduced two fundamental theorems which laid the foundation of DFT. According to these theorems, the electronic Hamiltonian can be expressed as a functional of the electron density $\rho(\mathbf{r})$[10, 11].

Theorem I: *For any many-body interacting system of particles in an external potential* $\hat{V}_{ext}(\boldsymbol{r})$*, the ground state electron density* $\rho(\boldsymbol{r})$ *is uniquely determined.* Therefore, full Hamiltonian can be determined from the ground state density and hence all the properties of the many-body interacting system such as potential energy, kinetic energy and total energy which are functional of the density $\rho(\mathbf{r})$ can be determined. For any N particle system, the electronic density is defined as follows:

$$\rho(\mathbf{r}) = N \sum_{\mathbf{s}_1} ... \sum_{\mathbf{s}_N} \int d\mathbf{r}_2 ... \int d\mathbf{r}_N |\Psi(\mathbf{r}_1, \mathbf{s}_1, \mathbf{r}_2, \mathbf{s}_2, ..., \mathbf{r}_N, \mathbf{s}_N)|^2 \tag{2.32}$$

where $\mathbf{r}_i$ and s_i denote the spatial and spin coordinates of the electrons.

$$N = \int \rho(\mathbf{r}) d\mathbf{r} \tag{2.33}$$

Here, electron density ($\rho(\mathbf{r})$) corresponds to the probability of finding the electron at the position $\mathbf{r}$. Integration of the $\rho(\mathbf{r})$ over the entire space determines the total number of electrons in the system. Once the electron density is determined in a many-body system then almost all the properties can be obtained in a more convenient way than employing the wavefunction approach.

Proof I: Let us consider there exist two potentials $\hat{V}_{ext}(\mathbf{r})$ and $\hat{V}^{'}_{ext}(\mathbf{r})$ for electron density $\rho(\mathbf{r})$ and obviously, they exhibit two distinct Hamiltonians, $\hat{H}_{el}$ and $\hat{H}^{'}_{el}$, respectively. The distinct Hamiltonians give rise to two different wavefunctions Ψ and $\Psi^{'}$, respectively. Now the expectation values of the ground state energy for two potentials $\hat{V}_{ext}(\mathbf{r})$ and $\hat{V}^{'}_{ext}(\mathbf{r})$ are:

$E_0 = \langle\Psi|H|\Psi\rangle$ and $E_0^{'} = \langle\Psi^{'}|H^{'}|\Psi^{'}\rangle$, respectively. If we assume that the ground state is nondegenerate. Then using variational wavefunction, for potential $\hat{V}_{ext}(\mathbf{r})$, wavefunction Ψ determines the minimum energy i.e., E_0 and energy will be always higher for other wavefunctions:

$$E_0 = \langle\Psi|H|\Psi\rangle < \langle\Psi^{'}|H|\Psi^{'}\rangle \tag{2.34}$$

$$\langle\Psi^{'}|H|\Psi^{'}\rangle = \langle\Psi^{'}|H^{'}|\Psi^{'}\rangle + \langle\Psi^{'}|H - H^{'}|\Psi^{'}\rangle \tag{2.35}$$

$$E_0 < E_0^{'} + \int \rho(\mathbf{r})[\hat{V}_{ext} - \hat{V}_{ext}^{'}]d\mathbf{r} \tag{2.36}$$

Similarly, employing the variational principle on the second potential $\hat{V}_{ext}^{'}(\mathbf{r})$, we get:

$$E_0^{'} = \langle\Psi^{'}|H^{'}|\Psi^{'}\rangle < \langle\Psi|H^{'}|\Psi\rangle \tag{2.37}$$

$$\langle\Psi|H^{'}|\Psi\rangle = \langle\Psi|H|\Psi\rangle + \langle\Psi|H^{'} - H|\Psi\rangle \tag{2.38}$$

$$E_0^{'} < E_0 - \int \rho(\mathbf{r})[\hat{V}_{ext} - \hat{V}_{ext}^{'}]d\mathbf{r} \tag{2.39}$$

Now add Equations 2.36 and 2.39, and we obtain:

$$E_0 + E_0^{'} < E_0 + E_0 \tag{2.40}$$

here, Equation 2.40 is a contradiction, this infers that for a common ground state density two different potentials are not possible, hence the theorem is proved.

Theorem II: *According to this theorem, the universal functional of the energy (E[$\rho(\boldsymbol{r})$]) can be expressed in terms of the electron density $\rho(\boldsymbol{r})$ for an external potential $V_{ext}(\boldsymbol{r})$. The exact ground state enenrgy is the global minimum of the energy functional and the density for which this functional exhibits minimum enenrgy is the ground state density ($\rho_0(\boldsymbol{r})$).*

Proof II: As it is already proved above that the external potential $V_{ext}(\mathbf{r})$ is uniquely determined by the ground state density $\rho_0(\mathbf{r})$ and $V_{ext}(\mathbf{r})$ uniquely determines the wavefunction. Therefore, all observable properties which are functional of the $\rho_0(\mathbf{r})$ such as kinetic enenrgy can be determined uniquely. The total ground state energy E[$\rho(\mathbf{r})$] as a functional of the ground state density $\rho(\mathbf{r})$ can be defined as follows:

$$E[\rho] = T_e[\rho] + V_{ext}[\rho] + U_{ee}[\rho] \tag{2.41}$$

$$E[\rho] = \int \rho(\mathbf{r})\hat{V}_{ext}(\mathbf{r})d\mathbf{r} + F_{HK}[\rho] \tag{2.42}$$

where F_{HK} is a universal functional. Since, the potential energy and the kinetic energy operates only on the electron density and their analysis is independent of the systems, therefore, F_{HK} can be considered as a universal functional. As the ground state energy is uniquely determined by the ground state density. Therefore, the ground state energy can be written as a functional of exact ground state density which minimizes the energy functional:

$$E_0 = E[\rho_0(\mathbf{r})] \tag{2.43}$$

Using the variational theorem, for any electron density other than ground state density $\rho_0(\mathbf{r})$ will always give higher energy:

$$E_0 \leq E[\tilde{\rho}(\mathbf{r})] \tag{2.44}$$

However, there are some important issues with Hohenberg-Kohn Theorems, one of them is a v-representability problem. Here, v corresponds to the density. The density associated with a non-degenerate ground state with external potential (V_{ext}) is known as v-representable density. All densities are not v-representable as shown by Levy and Lieb [28, 29], which means densities are not associated with the external potential. There is always some probability that minimization of energy leads to some higher energy rather than ground state energy and never converges to actual ground state density. It should be noted that in Hohenberg-Kohn's theorems, we always start with a trial density to minimize the energy. Here, it is assumed that this trial density will remain v-representable, and its associated Hamiltonian $\tilde{\hat{H}}_{el}$ is used to obtain wavefunction $\tilde{\Psi}$ i.e., defined as follows: $\tilde{\rho} \rightarrow \tilde{\hat{H}}_{el} \rightarrow \tilde{\Psi}$. However, according to variational principle, for real electronic Hamiltonian $\hat{H}_{el}$ of the system, this wavefunction obtained from the trial density doesn't correspond to the ground state.

$$\langle\tilde{\Psi}|H|\tilde{\Psi}\rangle = E[\tilde{\rho}] \geq E[\rho_0] \equiv E_0 \tag{2.45}$$

here $\rho_0(\mathbf{r})$ corresponds to the accurate ground state density of the many-body system. The energy associated with the density $\rho(\mathbf{r})$ is minimized to obtain the ground state energy. Finally, the density corresponding to minimum energy is termed as the ground state density. While minimizing the energy functional, it is required that all densities used in the algorithm remain N-representable. Here, N-representability of density apprises that the density is derived from an antisymmetric wavefunction. To conduct a constrained minimization of the energy which obey the N-representability, the method of Lagrange's multipliers also known as Lagrange's method of undetermined multipliers can be a practicable. In this approach, the value of the constraints becomes zero once they are converged. The mathematical expression for the N-representablility is:

$$\text{constraint} = \int \rho(\mathbf{r})d\mathbf{r} - N = 0 \tag{2.46}$$

The constraints after multiplying with an undetermined constant (μ) are added to the functional obtained after the minimization.

$$E[\rho(\mathbf{r})] - \mu\left(\int \rho(\mathbf{r})d\mathbf{r} - N\right) \tag{2.47}$$

Further, the above expression is minimized:

$$\partial\left[E[\rho(\mathbf{r})] - \mu\left(\int \rho(\mathbf{r})d\mathbf{r} - N\right)\right] = 0 \tag{2.48}$$

The derivative of the functional,

$$\partial E = \int \frac{\partial E[\rho(\mathbf{r})]}{\partial\rho(\mathbf{r})}\partial\rho(\mathbf{r})d\mathbf{r}$$

Now interchanging the integral and differential signs, we have:

$$\int \frac{\partial E[\rho(\mathbf{r})]}{\partial\rho(\mathbf{r})}\partial\rho(\mathbf{r})d\mathbf{r} - \mu\int \partial\rho(\mathbf{r})dr = 0 \tag{2.49}$$

It determines the Lagrange multiplier value at the minimum.

$$\frac{\partial E[\rho(\mathbf{r})]}{\partial\rho(\mathbf{r})} - \mu = 0 \tag{2.50}$$

Using Equation 2.42, the Lagrange multiplier can be written in terms of external potential:

$$\mu = \frac{\partial E[\rho(\mathbf{r})]}{\partial\rho(\mathbf{r})} = \hat{V}_{ext}(\mathbf{r}) + \frac{\partial F_{HK}\rho(\mathbf{r})}{\partial\rho(\mathbf{r})} \tag{2.51}$$

From Equation 2.51, it is observed that the Lagrange multiplier (μ) exhibits a physical meaning. It is the chemical potential of the system. For a detailed description, refer to chapters 4 and 5 of Parr & Yang (1989). According to the aforementioned theorems, a many-body interacting system can be constructed with a unique functional of energy which mainly depends on the electron density. Additionally, this functional can be minimized to have ground state energy and electron density. However, there is no mathematical expression to express the universal functional F_{HK} which makes the solution of the Schrödinger equation a difficult task. Later, in 1965, using Hohenberg-Kohn theorems, Kohn and Sham [11] demonstrate a new framework to find the exact ground state density and the minimum energy of the system. In many-body electron problems, this method has been proven as a revolutionary success and is widely used for qualitative studies of realistic systems. Kohn and Sham to approximate the universal functional proposed that the ground state density of an interacting system can be replaced with the ground state density of a non-interacting auxiliary system. This method gives a set of individual particle equations which can be solved independently.

2.11.2.1 Kohn-Sham equations

In 1965, Kohn and Sham proposed an ingenious method to circumvent the problem associated with inaccurate explanations for kinetic energy. In this method, in place of the interacting system, we can consider a non-interacting system (or auxiliary system) that exhibits the same ground state density as that of the real system as shown in Figure2.5. The Hamiltonian of the single particle of this auxiliary system ($\hat{H}_{KS}$) consists of single particle kinetic energy and effective single particle potential energy term $V_{eff}(\mathbf{r})$. The expression for the Hamiltonian of a single particle of a non-interacting auxiliary system, generally known as Kohn-Sham equations is:

$$\hat{H}_{KS}\phi_i = \left[-\frac{1}{2}\nabla_i^2 + \hat{V}_{eff}(\mathbf{r})\right]\phi_i^{KS}(\mathbf{r}) = \epsilon_i\phi_i(r)^{KS} \tag{2.52}$$

the expression for the effective potential:

$$\begin{aligned}\hat{V}_{eff}(\mathbf{r}) &= \hat{V}_{ext}(\mathbf{r}) + \hat{V}_H(\mathbf{r}) + \hat{V}_{xc}(\mathbf{r}) \\ &= \sum_\alpha \frac{-Z_\alpha}{|\mathbf{R}_\alpha - \mathbf{r}|} + \frac{\rho(\mathbf{r}')}{|\mathbf{r}-\mathbf{r}'|}d\mathbf{r}' + \frac{\partial E_{xc}[\rho(\mathbf{r})]}{\partial\rho(\mathbf{r})}\end{aligned} \tag{2.53}$$

where $\hat{V}_H$ and $\hat{V}_{xc}$ correspond to the Coulomb potential from all the electrons (Hartree term) and the exchange-correlation potential, respectively. $\hat{V}_{xc}$ comprises many-body interaction terms due to electron-electron interactions which are excluded in the Hartree term. The Equation 2.52 resembles very much with Hartree-Fock method or is a more simplified version of Hartree-Fock method. Here, the Kohn-Sham operator doesn't rest upon the electron's index but rather upon ***r***. Hence, it remains common for all the electrons. From equation 2.52, we can obtain the Khon-Sham orbitals $\phi_i(\mathbf{r})^{KS}$, which can be used to determine the total electron density:

$$\rho(\mathbf{r}) = \sum_{i=1}^{N} |\phi_i^{KS}(\mathbf{r})|^2 \tag{2.54}$$

Once the electron density is known by employing the self-consistent cycles, further we can obtain the improved version of the $\hat{V}_{eff}(\mathbf{r})$. Here, we assume that initial electron density is

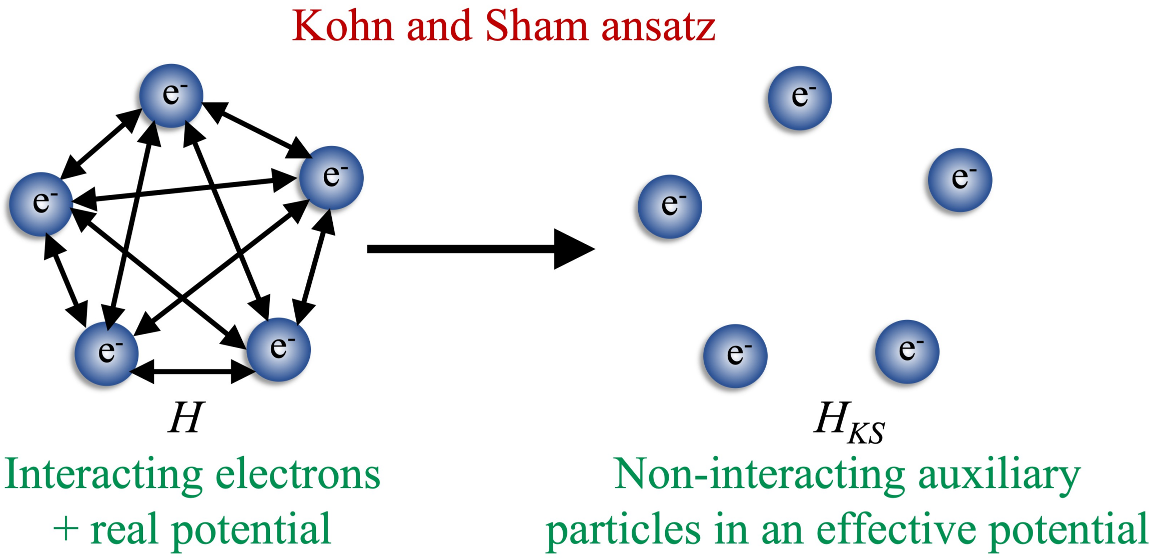

Figure 2.5: Schematic of the interacting and non-interacting electron systems possessing same ground density.

a superposition of all the atomic densities. Here, the spin-related effects are incorporated by considering both spin-up and spin-down densities and their sum is defined as total density, $\rho(\mathbf{r}) = \rho_{\uparrow}(\mathbf{r}) + \rho_{\downarrow}(\mathbf{r})$. The total energy can be evaluated using density:

$$E[\rho] = T_0[\rho] + \int [\hat{V}_{ext}(\mathbf{r}) + \hat{V}_H(\mathbf{r})]\rho(\mathbf{r})d\mathbf{r} + E_{xc}[\rho] \tag{2.55}$$

Here, orbitals are used to determine the associated kinetic energy $T_0[\rho]$ rather than density.

$$T_0[\rho] = \frac{1}{2}\sum_{i=1}^{N}\langle\phi_i^{KS}|\nabla_i^2|\phi_i^{KS}\rangle \tag{2.56}$$

and the Kohn -Sham effective potential can be written as:

$$V_{eff}[\rho] = \int \hat{V}_{eff}(\mathbf{r})\rho(\mathbf{r})d\mathbf{r} \tag{2.57}$$

Rest of energy terms are incorporated in $E_{xc}[\rho]$ such as:

1. Correlation energy term
2. Exchange energy term
3. To have a true kinetic energy term, which exactly matches the real system kinetic energy $T_e[\rho]$, it is required to add some quantity of the kinetic energy to $T_0[\rho]$.
4. Self-interaction correction emanated due to classical coulomb potential.

Starting with a trial electron density ρ(r) and effective potential $\hat{V}_{eff}(\mathbf{r})$, the Kohn-Sham single particle equations are solved employing a self-consistent approach. Note that the E_{xc} is the crucial term that needs to be determined accurately to have precise results of the methods based on Kohn-Sham equations.

2.11.3 Exchange and correlation energy

For the practical application of the Kohn-Sham equations, it is required to know the accurate formalism of the Kohn-Sham equations. However, no mathematical or analytical expression is known for the exchange and correlation (ϵ_{xc}) functional. To have an accurate formalism of this, since the beginning of DFT, various approximations have been proposed to have a suitable balance between the computational cost and the accuracy. Generally, these approximations have been classified into three categories: (1) based on localized density viz., local density approximation (LDA) [30] (2) based on semi-localized density viz. generalized gradient approximation (GGA) and meta-GGA, (3) based on non-localized density viz. hybrid and random phase approximation. In simplest approximation i.e., homogeneous electron gas approximation, it is assumed that electron density is homogeneous, hence exchange-correlation energy is a functional of the localized density. Therefore, local density approximation (LDA) is the elementary exchange-correlation functional to solve the Kohn-Sham equations [30]? In LDA approximation, it is assumed that as we go from one position to another, the electron density varies slowly, hence it can be considered localized. As the variation in the density is negligible, its derivative is nearly zero, hence, derivatives are not incorporated in this approximation. For spin polarization calculations, it is required to incorporate both spin up $\rho_{\uparrow}(\mathbf{r})$ and spin down $\rho_{\downarrow}(\mathbf{r})$ densities, which is called local spin density approximation (LSDA). Further, the exchange-correlation energy consists of two terms: correlation energy and exchange energy.

$$E_{xc}[\rho] = E_x[\rho] + E_c[\rho] \tag{2.58}$$

Exchange energy: The origin of this term lies in the Hartree-Fock method which considers the antisymmetric nature of the electronic wavefunction. As per Pauli's exclusion principle, no two electrons can occupy the same energy state, correspondingly, repulsive forces occur among the electrons which exhibit similar spin states. This repulsive force introduces a spatial separation between two electrons consequently, the coulomb interaction is reduced between electrons, which is known as exchange energy. Technically, this is the difference between Hartree-Fock energy and Hartree energy. The mathematical expression for the exchange energy term in the LDA, under the framework of the homogeneous electron gas, is [31].

$$E_x[\rho] = -\frac{9}{4}\alpha\left(\frac{3}{4\pi}\right)^{\frac{1}{3}} \int [\rho_{\uparrow}^{\frac{4}{3}}(\mathbf{r}) + \rho_{\downarrow}^{\frac{4}{3}}(\mathbf{r})]d\mathbf{r} \tag{2.59}$$

here, $\alpha = \frac{2}{3}$

Correlation energy: This term originated from the electron-electron coulombic interaction. Being negatively charged entities, the electrons always repel each other. A significant part of the correlation energy is contributed by the kinetic energy difference between the interacting and non-interacting systems ($T_e - T_0$). Numerically, this is the difference of the Hartree-Fock energy and the exact energy of the system:

$$E_c = E_{exact} - E_{HF} \tag{2.60}$$

The mathematical expression for the correlation energy is:

$$E_c[\rho] = \int \rho(\mathbf{r})\epsilon_c[\rho_{\uparrow}(\mathbf{r})\rho_{\downarrow}(\mathbf{r})]d\mathbf{r} \tag{2.61}$$

here $\epsilon_c[\rho_{\uparrow}(\mathbf{r})\rho_{\downarrow}(\mathbf{r})]$ corresponds to the correlation energy per entity (electron) of a uniformly distributed electron gas with uniform density $\rho(\mathbf{r})$, however, its analytical exact form is still unknown. Several efforts have been done to ameliorate the correlation energy using quantum Monte Carlo approach[32], and subsequent fitting of the results to analytical expansion. For a system that is close to homogeneous electron gas, the LDA functional works very well e.g. for metals, LDA gives quite accurate results. However, it fails in the case of the inhomogeneous system such as molecules, atoms, etc. Though it can be used to describe atomic structures, and vibrational and elastic properties of a wide range of systems, it cannot be used to determine binding energy, chemical bonds, bandgap, reaction enthalpy, and energy of activation barriers. Further, to improve the exchange-correlation energy, people have realized that homogeneous electron density is not sufficient to describe a system in which the electron density varies rapidly. Therefore, along with electron density, the electron gradient is been incorporated. This semi-local approximation is called generalized gradient approximation (GGA) [33, 34].The expression for the exchange-correlation energy as a functional of $\rho(\mathbf{r})$ and $\nabla\rho(\mathbf{r})$ is:

$$E_{xc}^{GGA}[\rho(\mathbf{r})] = \int \rho(\mathbf{r})\epsilon_{xc}^{GGA}(\rho(\mathbf{r}), |\nabla\rho(\mathbf{r})|)d\mathbf{r} \tag{2.62}$$

Although this approximation gives better results while calculating lattice constants and bond

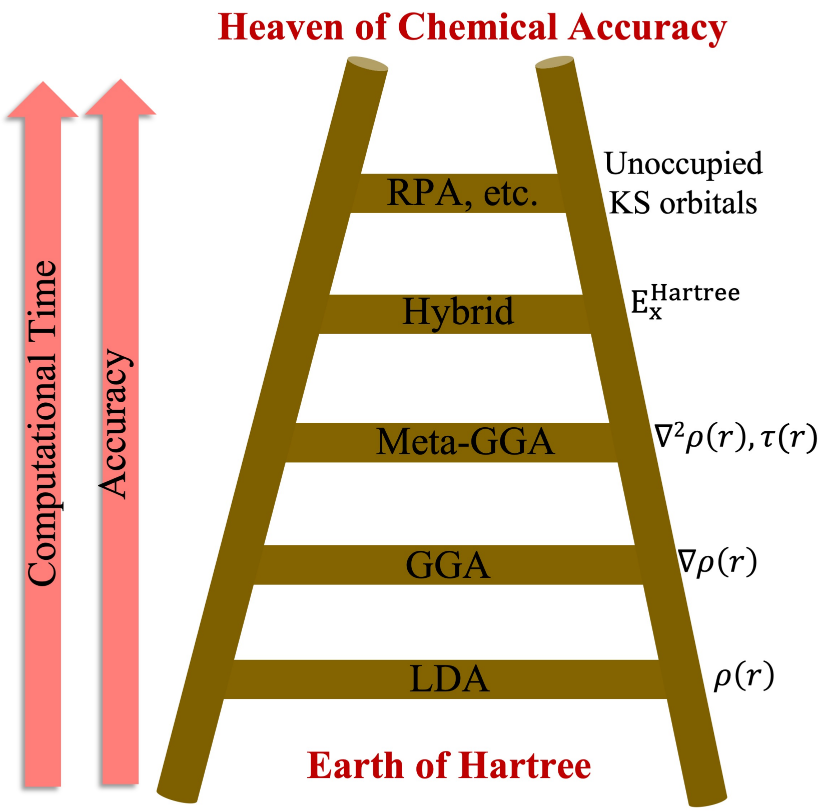

Figure 2.6: Jacob's ladder, illustrating the variation of the accuracy and the commputational cost with different exchange-correlation functionals.

lengths of most of the systems, it fails while dealing with the systems which consist of large atoms (or transition elements). In the following step, to improve the methodology, the forth-order gradient of density is been accounted for in the evolution of the exchange-correlation energy, which is known as meta-GGA functional. In this functional, to incorporate the fourth-order gradient of the density, the second derivative of the density i.e., Laplacian of the density is included and an additional degree of freedom via. the kinetic energy density $\tau(r)$. The under-estimation of the bandgap acts as a major drawback of these semi-local exchange-correlation functionals. These functionals fail to resolve the self-interaction error incorporated in the Hartree term, which results in a systematic error, where localization plays a pivotal role such as surfaces and the defects. To overcome this self-interaction error, a more advanced functional i.e., hybrid functional comes into existence, which improves the accuracy but with increased computational cost and time. Here, the hybrid functional is obtained by combining the fraction of the exact exchange from Hartree-Fock and the exchange-correlation energy from the local or semi-local terms. exact exchange from Hartree-Fock theory and the exchange-correlation energy that comes from the local or semi-local approximations [30]. By varying the fraction of exact exchange in hybrid functional, one can overcome the self-interaction error. Numerically, the exchange-correlation energy for the hybrid functional is written as:

$$E_{xc}^{hyb} = \alpha E_x^{HF} + (1-\alpha)E_x^{DFT} + E_c^{DFT} \tag{2.63}$$

here, α corresponds to the fraction of the exact exchange coming from Hartree-Fock and rest of the terms are from GGA or LDA fnctional. In hybrid functional approach, the Coulomb potential consists of two parts one viz. short range (SR) and long range (LR). All this makes the computation expensive. To overcome this problem, Heyd, Scuseria, and Ernserhof (HSE) [35] proposed that short-range terms can be used to compute the exact exchange term, whereas GGA or LDA functional can be used to describe the long range terms. To speed up the calculations, they used an error function.

$$\frac{1}{r} = \underbrace{\frac{1-erf(\omega r)}{r}}_{\text{SR}} + \underbrace{\frac{erf(\omega r)}{r}}_{\text{LR}} \tag{2.64}$$

where, ω corresponds to the screening parameter which describe the range of the interaction. The error function in its explicit form is defined as follows:

$$erf(\omega r) = \frac{2}{\sqrt{\pi}} \int_0^{\omega r} e^{-x^2} dx \tag{2.65}$$

Note that different values of the ω result in different functional. For example, if ω = 0, the long range terms will get vanished and full Coulomb potential will be described by the short range term. This HSE functional is termed PBE0 functional [36]. Whereas, at high values of ω, the short terms vanish and HSE functional becomes GGA or LDA approximation. In case of HSE06, the exchange-correlation energy is expressed as follows:

$$E_{xc}^{HSE} = \alpha E_x^{HF,SR}(\omega) + (1-\alpha)E_x^{PBE,SR}(\omega) + E_x^{PBE,LR}(\omega) + E_c^{PBE} \tag{2.66}$$

In the case of HSE calculation, the suggested default values of the α and ω are $\frac{1}{4}$ and 0.11 bohr^{-1} , respectively, which works very well in determining band gaps of the semiconductors and metallic systems. In our work also, we have used these values to have accurate band gap results. The variation of different exchange-correlation energy with respect to the computational time and accuracy are shown in Figure 2.6. In present thesis, semi-local (Perdew-Burke-Ernzerhof (PBE) version of GGA [33]) and non-local (HSE06, GW [37]) are been used.

The Kohn-Sham single particle equations are evaluated self-consistently, starting with the initially guessed electron density $\rho(\mathbf{r})$ and estimating the effective potential $V_{eff}(\mathbf{r})$. The flow

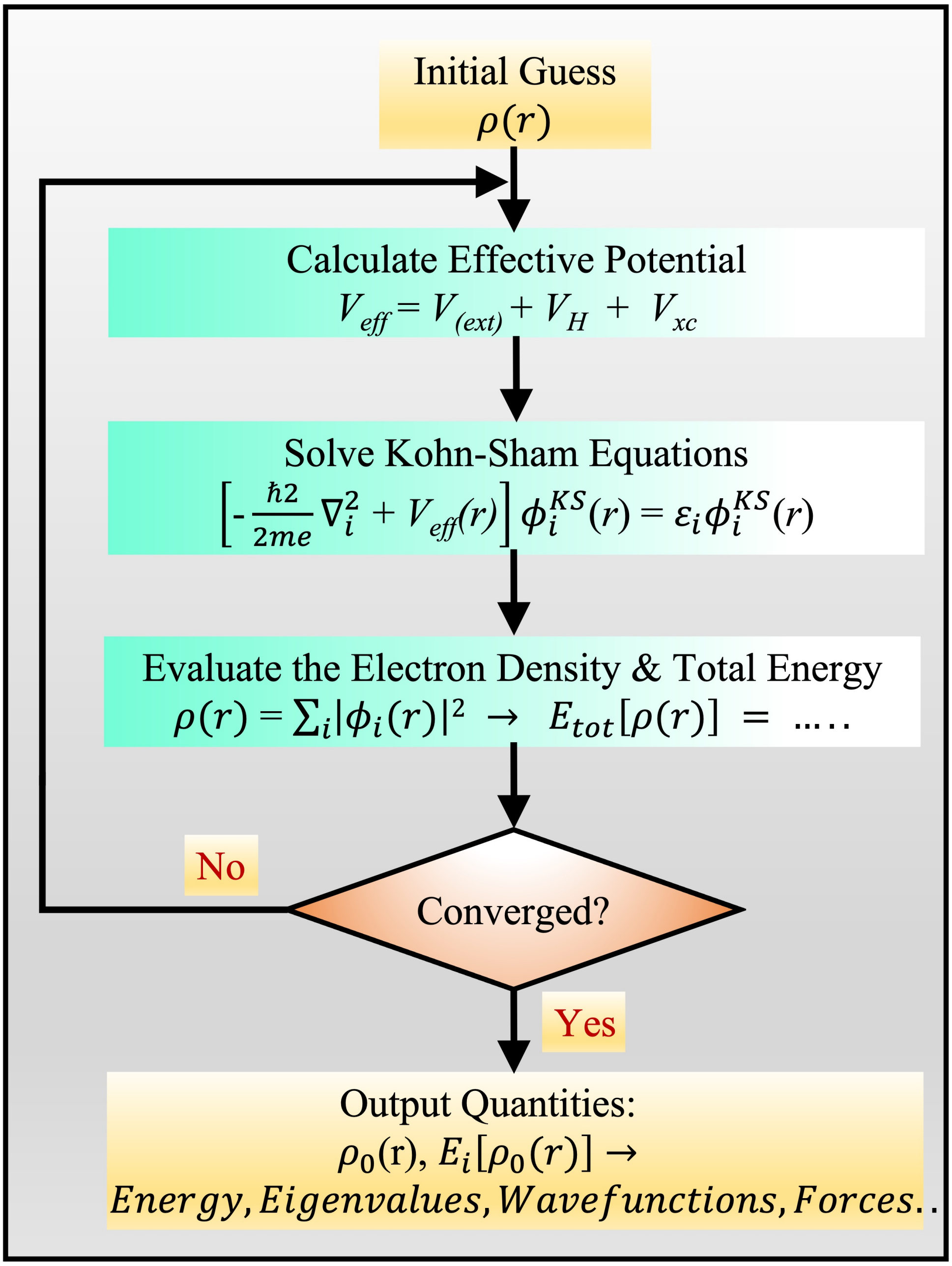

Figure 2.7: Flow-chart for the solution of the Kohn-Sham equations using self-consistent method.

chart to solve Kohn-Sham equations is encapsulated in Figure 2.7. Today, numerous codes are available to execute DFT calculations. In our thesis, we have employed VASP (Vienna *Ab initio* Simulation Package) code [38, 39, 40].

2.12 Basis set

A basis set is the set of basis functions, which are used to describe any electronic wave function. Any wave function used in Hartree-Fock or Density Functional Theory can be expanded as a set of basis functions. Hence, the practical way to solve electronic structure or Schrödinger equation is the basis set. While choosing the basis functions, one should take care of the following points:

> The basis function should be selected such that they build the accurate wavefunction or density along with practicable low computational cost. Notably, efficiency and accuracy of any theory depends largly on the accuracy of the basis functions. A basis set must be chosen such that it gives accurate results and on further increasing the number of basis set the results remain almost similar. While choosing a basis function, it must be ensured that it is capable in capturing all the basic physics. The basis sets must obey the Bloch boundary conditions in case of periodic systems (crystals).

The disadvantage of this method is that because the wavefunctions are fixed, it is challenging to predict the converged basis set. To overcome this problem, the energy dependent wavefunctions were considered in order to vary the number of wavefunctions. Here, we have provided a brief introduction of the plane wave basis sets, pseudopotential method and projector augmented wave (PAW) method. As our work is maily oriented around the periodic systems, hence we have chosen plane wave based approach which is quite popular for the electronic structure calculations of the periodic systems.

2.12.1 The Plane wave basis set

In the case of periodic systems, the Bloch theorem paves the path to solving the Schrödinger equation. Generally, the plane wave-based basis set is considered for periodic systems. The wavefunction which obeys the Bloch theorem in terms of the plane wave basis function can be written as follows:

$$\Psi_k(r) = u_k(\mathbf{r})e^{i\mathbf{k}.\mathbf{r}} \tag{2.67}$$

$$\rho(\mathbf{r}) \approx \sum_k |\Psi_k(\mathbf{r})|^2 \tag{2.68}$$

here, $u_k(r)$ corresponds to the basis set function which exhibits similar periodicity as that of the supercell.

$$u_k(\mathbf{r} + n_1\mathbf{a}_1 + n_2\mathbf{a}_2 + n_3\mathbf{a}_3) = u_k(\mathbf{r}) \tag{2.69}$$

where, n_1, n_2, and n_3 are the integers. Therefore, the Kohn-Sham equations can be solved independently for each value of **k**. Notable the space associated with **k** vector is the reciprocal space, which is also termed momentum space. Moreover, the values of **k** vectors are set such that they lie within the primitive cell, which is termed as the first Brillouin zone (BZ). Depending on the **k**-mesh, the BZ can be divided into different ways. In the present thesis, the Monkhorst-Pack grid has been employed [41]. Note that, a real space vector can be obtained by taking the reciprocal of a reciprocal lattice vector. Kohn-Sham orbitals can be further expressed as sum of the plane wave basis set:

$$u_{nk}(\mathbf{r}) = \sum_{\mathrm{G}} C_{nk,\mathrm{G}} e^{i\mathbf{G}.\mathbf{r}} \tag{2.70}$$

where **G** denotes the reciprocal lattice vectors. k and n represent the wavevector and the band index in the first Brillouin zone, respectively. The electronic wavefunctions are expanded in terms of plane wave basis set as follows:

$$\phi_{nk}(\mathbf{r}) = \sum_{\mathrm{G}} C_{nk,\mathrm{G}} e^{i(\mathbf{k}+\mathbf{G}).\mathbf{r}} \tag{2.71}$$

where, $C_{nk,\mathrm{G}}$ corresponds to the expansion coefficient and its value can be reduced by increasing $|\mathbf{G}|^2$. Hence, the infinite series in Equation 2.71 is truncated to include the plane waves up to a threshold value of the cutoff energy (E_{cut}). Therefore, in order to compute accurate and efficient ground state energy and density, one needs to perform a convergence test for E_{cut}.

$$\frac{|\mathbf{k}+\mathbf{G}|^2}{2} \leq E_{cut} \tag{2.72}$$

Note that, the number of plane waves (N_{PW}) required for the wavefunction expansion principally rely on E$_{cut}$:

$$N_{PW} = \frac{VE_{cut}^{\frac{3}{2}}}{6\pi^2} \tag{2.73}$$

here, V corresponds to the real space lattice volume. The advantages of choosing plane wave as the basis function are as follows:

1. On increasing the plane wave cutoff energy, the accuracy inceases.
2. In order to determine the plane wave coefficients, we can easily convert the real space quantities to reciprocal space quantities using several standard numerical techniques.
3. This method may be used for non-periodic systems that supercells can modify.

However, there are many drawbacks concomitanted with plane waves.

1. As in the vicinity of the nucleus, wavefunctions become random and strong, hence large number of plane waves are required near the core region.
2. It is impractical to perform plane wave calculations for entire electrons in the system.

2.12.2 Numeric atom-centred basis functions

In DFT, for cluster or molecular electronic structure calculations, the Numeric atom-centred orbitals (NAO) basis are quite popular due to their accuracy, compactness and fast convergence. The numeric form of localized basis function (NAO) in FHI-aims [42] is expressed as:

$$\phi_i(\mathbf{r}) = \frac{u_i(r)}{r} Y_{lm} \tag{2.74}$$

here, Y_{lm} corresponds to the spherical harmonics and $u_i(r)$ denotes the numerically tabulated radial part, which makes the basis functions flexible. $u_i(r)$ can be obtained by solving Schrödinger-like radial equation:

$$\left[-\frac{1}{2}\frac{d^2}{dr^2} + \frac{l(l+1)}{r^2} + v_i(r) + v_{cut}(r) \right] u_i(r) = \epsilon_i u_i(r) \tag{2.75}$$

here, potential $v_i(r)$ gives the information regarding the behavior of $u_i(r)$ (for example: it can be like Hydrogen, free-atom, free-ions,Gaussians, etc.). Whereas, the smooth decay of radial function is ensured by the confining potential $v_{cut}(r)$. Note that, the radial function must become zero outside the cutoff radius. As a result of this, the calculations do not get slow down because of peripheral tails of the function, which allows to develop the tightly packed element-dependent basis sets and that also retain the transferability. Moreover, all radial functions $u_i(r)$ remain strictly localized within the provided radius. In FHI-aims, in order to formulate the minimum basis set, for sherically symmetric atoms the numerical solutions of radial Schrödinger equation is used. Here, the minimum basis sets incorporate wavefunction oscillations surrounded by the nucleus, hence they enable all electron calculations greatly. To have guaranteed accurate convergence, it is preferred that all bigger basis sets consist of all minimal ones. In FHI-aims, the bigger basis sets are obtained by starting with the smaller ones and expanding them by adding basis functionals, which are imported from an immense pool of radial functions.

2.12.3 Plane wave pseudopotential method

Although tremendous efforts have been done to solve the Kohn-Sham equations, computationally obtaining a solution is still challenging, as it is required to have the information of N wavefunctions each one corresponding to the individual electron. Also, the core states are highly localized, as a result of this, in the core region of the atoms the valence wavefunctions

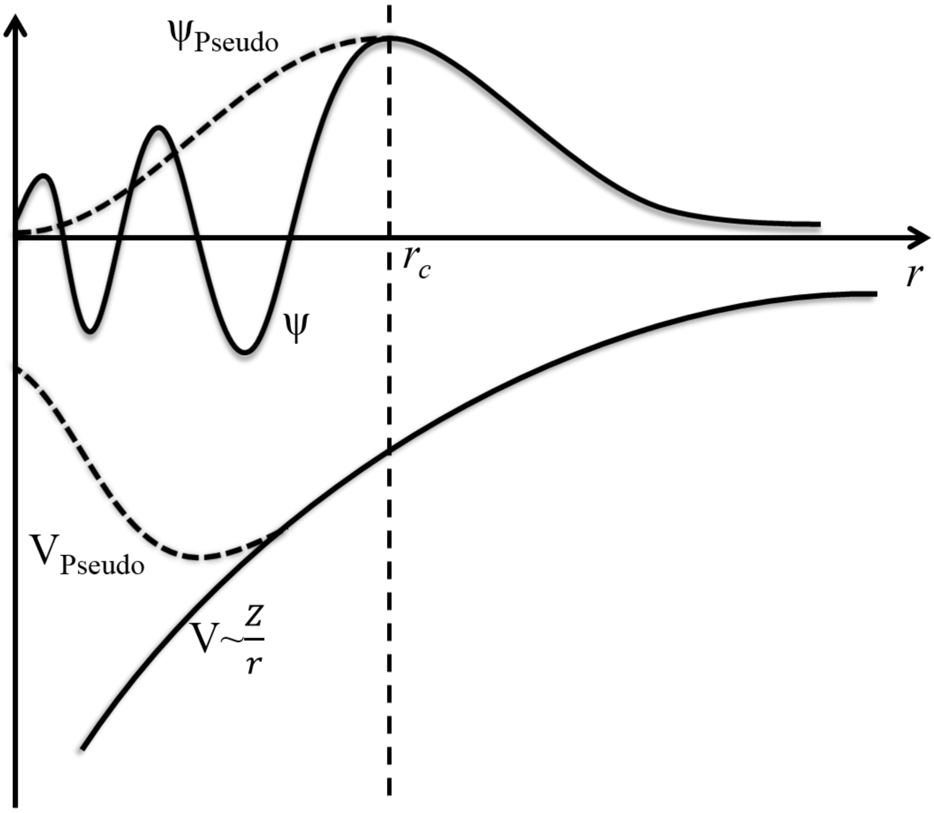

Figure 2.8: Schematic representation of all electron wavefunction (shown with solid line) and its corresponding pseudo wavefunction (shown with dashed line) and along with the respective external Coulomb potential and pseudopotential [1].

oscillate rapidly. This shows that the corresponding valence states exhibit high kinetic energy. Therefore, a large E_{cut} and a large number of plane waves are required to reproduce these fast oscillations, which makes the calculations computationally expensive. As most of the physical properties in the case of solids are mainly described by the valence electrons. The pseudopotential approximation can be employed to reduce the computational cost significantly. As in this approximation, the strong effect of core electron potential is not considered explicitly, it is replaced with an approximated pseudopotential (V_{Pseudo}). A core radius $\mathbf{r}_c$ is defined (as shown in Figure 2.8.), which separates the electron into core and valence electrons. The range of the $\mathbf{r}_c$ controls the softness and hardness of the pseudopotential. Large $\mathbf{r}_c$ leads to ultrasoft potential, whereas a small value of the $\mathbf{r}_c$ results in a hard pseudopotential. Below the $\mathbf{r}_c$, all electron real wavefunctions are also replaced by a set of pseudo wavefunctions (Ψ_{Pseudo}) [34, 30, 140]. Beyond the $\mathbf{r}_c$, the pseudopotentials wavefunction becomes indentical with the all the valence electron real wavefunction. One more privilege of the pseudopotential approach the relativistic effects can be easily incorporated into the potential without affecting the valence electron and treated as non-relativistic. In DFT, different types of pseudopotentials have been developed which are described in more detail below.

2.12.4 Norm-conserving pseudopotential

In 1979, Hamamm, Chiang, and Schlüter were the first who proposed Norm-conserving pseudopotential. Later, it was reformed by Bylander and Kleinman. It is more transferable than ultrasoft pseudopotentials due to its ability to conserve charge. The transferability rate is determined by the $\mathbf{r}_c$, value. A pseudopotential can be transferred to any chemical environment if $\mathbf{r}_c$, falls within the inert region. Outside of the inert region, the transferability is, however, diminished. In the latter scenario, the ultrasoft approximation is observed. It should be noted that ultrasoft pseudopotentials can also be made transferable, which is generated for the atom, and can also be applied to molecules or solids with a similar level of accuracy, but their execution is more challenging. Since the real and pseudo wavefunctions are equal outside the core region, as we explained in the previous section, this produces an identical charge density and further allows us to precisely calculate the exchange and correlation energies. Here, all electron wavefunction Ψ is equal to the norm for the pseudopotential wavefunction (Ψ_{Pseudo}).

$$\int_0^{\mathbf{r}_c} \mathbf{r}^2 \Psi^*_{Pseudo}(r)\Psi_{Pseudo}(r)d\mathbf{r} = \int_0^{\mathbf{r}_c} \mathbf{r}^2 \Psi^*(\mathbf{r})\Psi(\mathbf{r})d\mathbf{r} \tag{2.76}$$

This can be accomplished by utilizing a non-local pseudopotential, where each potential defines a different part of the pseudopotential's angular momentum. Additionally, it is possible to determine the ion's dispersion characteristics in various environments [43].

2.12.5 Vanderbilt Ultrasoft pseudopotential

In a pseudopotential system, it is difficult to handle elements with nodeless valence states. For these atoms, the pseudo and overall electron wavefunctions are almost identical. As electrons are confined in an ionic core area, a significant number of plane waves are required for a decent depiction of their wavefunction. As a result, the computations for such items are costly. Vanderbilt developed Ultrasoft pseudopotentials as a new kind of pseudopotential to solve this issue [44]. The norm-conserving constraint has been loosened for Ultrasoft pseudopotentials in order to minimise the size of the basis set. Only a tiny fraction of a wavefunction from the complete valence wavefunction is taken into account by this pseudopotential. This method aids in lowering the plane wave cutoff energy in the computations, which in turn lowers the cost of computation. Despite this, there are several disadvantages, including the following: (i) the difficulty in determining the Fourier representation of the Kohn-Sham equation, and (ii) the fact that the Bloch eigenstates are no longer orthonormal because of the norm-conserving requirement. To solve this issue, it is necessary to include an overlap matrix and turn the eigenvalue problem into a generalised eigen value equation, (iii) evaluate the density dependent non-local component of the pseudopotential, and (iv) assess extra terms in the force calculation. The pseudo wavefunctions in this technique are similar to all electron wavefunctions when $\mathbf{r} > \mathbf{r}_c$. Since wavefunctions (both pseudo and all electron) at $\mathbf{r} < \mathbf{r}_c$ are thought to be soft, this may be done by relaxing the norm-conservation condition. All electron wavefunctions are the same as pseudo wavefunctions.

2.12.6 Projector augmented-wave method (PAW)

The projector-augmented wave (PAW) approach was proposed by Peter Blöchl in 1994. This approach is based on the augmented wave techniques and the unified description of the ultra-soft pseudopotentials [45]. It recovers the wavefunction inside the core area while taking into account the whole electron wavefunction. The wavefunction is split into two sections in this method: (i) the augmentation area (a partial wave in a sphere surrounding the atom), and (ii) the interstitial region (outside the sphere). Because they must be orthogonal to the core states, valence wavefunctions tend to fluctuate quickly close to the ion cores. Since the wave function must be adequately described by numerous Fourier components (or extremely fine grids in grid-based approaches), dealing with this circumstance is challenging. This issue is resolved by the PAW approach by translating this quick oscillating wave. Two spaces i.e., the pseudo wavefunction and the true wavefunction are connected using the linear transformation operator (T):

$$|\Psi\rangle = T|\tilde{\Psi}\rangle \tag{2.77}$$

The following is the expression for the operator T:

$$T = 1 + T_0 \tag{2.78}$$

where T_0 operates in the atom's surrounding augmentation zone. In order to depict the all-electron partial waves and the pseudo partial waves, respectively, let's take into consideration a set of functions $|\phi_i\rangle$ and $|\tilde{\phi}_i\rangle$. Given that both wavefunctions are complete in the augmentation zone, the operator T is defined as follows:

$$|\phi_i\rangle = (1 + T_0)|\tilde{\phi}_i\rangle \tag{2.79}$$

We may infer from equation 2.79 that since T_0 only operates within the augmentation region, both all-electron and pseudo partial waves will be equivalent outside of it. In the augmentation region, the set of pseudo partial waves ($\tilde{\phi}_i$) is complete, hence, each pseudo wavefunction ($\tilde{\Psi}$) can be expressed in terms of the pseudo partial waves:

$$|\tilde{\Psi}\rangle = \sum_i c_i|\tilde{\phi}_i\rangle \tag{2.80}$$

where the expansion coefficients are c_i's. Then, T maps this pseudo wavefunction into:

$$T|\tilde{\Psi}\rangle = |\Psi\rangle = \sum_i c_i|\phi_i\rangle \tag{2.81}$$

The all-electron wavefunction can be found by subtracting equations 2.80 and 2.81, respectively:

$$|\Psi\rangle = |\tilde{\Psi}\rangle = \sum_i c_i(|\phi_i\rangle - |\tilde{\phi}_i\rangle) \tag{2.82}$$

The coefficients c_i should be linear functionals of $|\tilde{\Psi}\rangle$ because of the linear operator T. The s, p, and d-type projector functions examine the nature of the wavefunction. The scalar product with a constant function can be used to define the general form of a linear function. The symbol ($\langle\tilde{p}_i|$), which refers to a projector function, is used to denote this function. We can thus write:

$$c_i = \langle\tilde{p}_i|\tilde{\Psi}\rangle \tag{2.83}$$

The pseudo partial waves can provide the complete basis:

$$c_i = \langle\tilde{p}_i|\tilde{\phi}_j\rangle = \delta_{ij} \tag{2.84}$$

At this point, T, the projection operator, can be expressed as follows:

$$T = 1 + \sum_i [|\phi_i\rangle - |\tilde{\phi}_i\rangle]\langle\tilde{p}_i| \tag{2.85}$$

Any local operator O's expectation value can be expressed in terms of pseudo functions $\langle\tilde{\Phi}_i|\tilde{O}|\tilde{\Phi}_i\rangle$, here, $\tilde{O}$ corresponds to the pseudo operator:

$$\tilde{O} = T^{\dagger}OT = O + \sum_{ij} |\tilde{p}_i\rangle[\langle\phi_i|O|\phi_j\rangle - \langle\tilde{\phi}_i|O|\tilde{\phi}_j\rangle]\langle\tilde{p}_j| \tag{2.86}$$

The numerical solution to the many-body problem can be achieved by using these approximations. A limited number of plane waves can be used to represent the smooth pseudo wavefunctions. Furthermore, because these functions are the result of a radial function and a spherical harmonic, integrations for rapidly fluctuating partial waves may be carried out on a radial grid. In the present thesis, the PAW approach has been used for all the electronic structure calculations, which were carried out using the Vienna *Ab initio* Simulation Package (VASP) [38, 39, 40].

2.13 Introduction: Beyond DFT

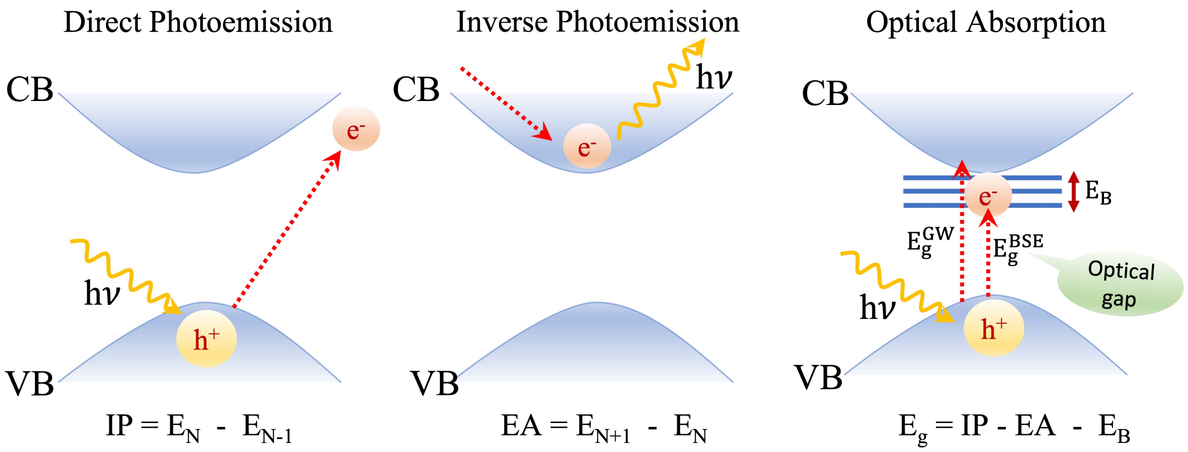

Figure 2.9: Photoemission and inverse photoemission spectroscopies along with optical band gap are shown schematically.

Density functional theory (DFT) is a popular technique for predicting the ground state characteristics of materials, such as energy, lattice parameters, force, mechanical strength, vibrations, etc. However, it entirely fails to identify the many-body system's excited state properties, such as the bandgap, optical spectra, and excitons. Therefore, it is necessary to move beyond the single particle framework in order to explain the system's excited state features. To get from a single particle to Landau's quasi-particle (QP) energies, which can be determined by experiments, is essential. These experiments, known as photoemission and inverse photoemission spectroscopies, involve adding and subtracting electrons from the system (see Figure 2.9). Similar to this, single particle calculations are used to determine QP energies. The many body perturbation theory (MBPT) uses Green's function techniques. It depicts how an electron's addition or removal spreads across the system. Similar to how difficult it is to solve the exchange-correlation term in DFT, the most challenging term in this is self-energy. Self-energy is energy dependent and non-local term. The lifespan of the particle and the propagation of the electron or hole from one place to another within the system are described, respectively, by the real and imaginary parts of self-energy. In the QP equation, the self-energy component is mentioned directly. The eigenstates and eigenvalues of the single-particle excitations must be ascertained in order to solve the eigen value issue that results from the solution of the quasi-particle equation. Self-energy computation is an extremely difficult problem. This technique, also known as the GW approach, where G and W denote the Green's function and a fully screened Coulomb potential, respectively.. It was initially proposed by Hedin in 1965. It is possible to deal with ionic states, excited states, and extended states with this approach since it is so powerful.

DFT orbitals serve as the starting point for GW computations. Initial G and W are afterward built. Depending on how G and W are updated, GW methodology can take many distinct forms. The most popular and straightforward technique is single-shot GW. For this kind of computation, a relevant starting point is crucial. Therefore, the initial starting point, or DFT orbitals is crucial for a single-shot GW. Bandgap is mostly delivered via the single shot GW technique in accordance with experimental data. However, GW has several real-world drawbacks, such as (i) high computational cost and (ii) enormous memory. This is because it requires a large number of unoccupied bands, as well as a large number of basis functions N. The electronic polarizability and the correlation portion of the self-energy operator must converge before the former may be used. In theory, it requires an endless number of bands, making it virtually impossible. The accurate prediction of the self-energy and the optical response function depends on the convergence of the number of unoccupied bands and the basis function N. Convergence of quasiparticle energies with respect to the number of basis functions N is challenging. This may be understood by using the example of ZnO, where a tiny system requires thousands of bands in order to provide findings that are highly converged [46]. Klimes *et al.* have proposed a correction approach based on finite basis set [47], to get over this problem, on the premise that quasiparticle energies converge in the ratio of $\frac{1}{\mathrm{N}}$ [48]. The GW method has been widely used to several insulators and semiconductors. There are two ways to calculate the energy and bandgaps of quasiparticles: The first technique is to calculate the QP energies with regard to the plane wave basis set N, cutoff energy, and quantity of k-points. Here, we compute the QP energies with increasing N, cutoff energy, and k-point counts, and then further verify convergence. Notably, we did not extrapolate our data in this case. Whereas, the QP energies are extrapolated to N → ∞ in case of the basis set corrected methodology used in the second method. In 1969, Hedin's study described the novel GW approximation, which was used to solve the many body problem. The development and remodelling in this region began a few years ago. The first work on the GW approximation was written by Hybertsen and Louie [49, 50]. Godby, Schlüter, and L.J. Sham employed this technique in 1980 for Si, GaAs, and AlAs in addition to diamond [51]. This thesis uses PBE and HSE06 to perform single shot GW calculations beginning with DFT orbitals.

2.14 GW method

A useful technique for predicting the ground state characteristics of both new and current materials is density functional theory (DFT). However, it falls short of describing the many-body system's excited state characteristics. Therefore, moving beyond the single particle technique is necessary to explore the system's excited state features. The photoemission and inverse photoemission spectroscopies, which involve adding and removing electrons from the system, are often used to analyze the electronic characteristics. The energies of electron addition and removal are not directly related to the energies of the Kohn-Sham orbitals by any theorem. Excited electrons are highly interacting particles in the photoemission or inverse photoemission process. The propagation of one electron being removed or added to the system is described by the single-particle version of Green's function. In the theory of many-body perturbations, the complex, non-local, and energy-dependent self-energy is used to define Green's function. The imaginary portion of the self-energy defines the lifespan of the particle, whereas the real portion of the self-energy explains the energy change of the electron/hole as it moves from one place to another in the system. The eigenfunctions and eigenvalues of the single-particle excitations are obtained by solving the quasiparticle equation [37, 52, 53]. The behavior of quasiparticles is described by the equation below:

$$(-\frac{\nabla^2}{2} + V_{ext} + V_H)\Psi_{QP}(r) + \int dr^{'}\Sigma_{xc}(r, r^{'}; \epsilon_{QP})\Psi_{QP}(r^{'}) = \epsilon_{QP}\Psi_{QP}(r) \tag{2.87}$$

The reference Hamiltonian is typically employed in the GW approach. The first input is a set of Kohn-Sham orbitals. The green function (G) Lehmann's (spectral) representation is as follows:

$$G(r, r^{'}; \epsilon) = \lim_{\eta \to 0^+} \sum_s \frac{\Psi_s(r)\Psi_s^*(r^{'})}{\epsilon - \epsilon_s + i\eta \mathrm{sgn}(\epsilon_s - \mu)} \tag{2.88}$$

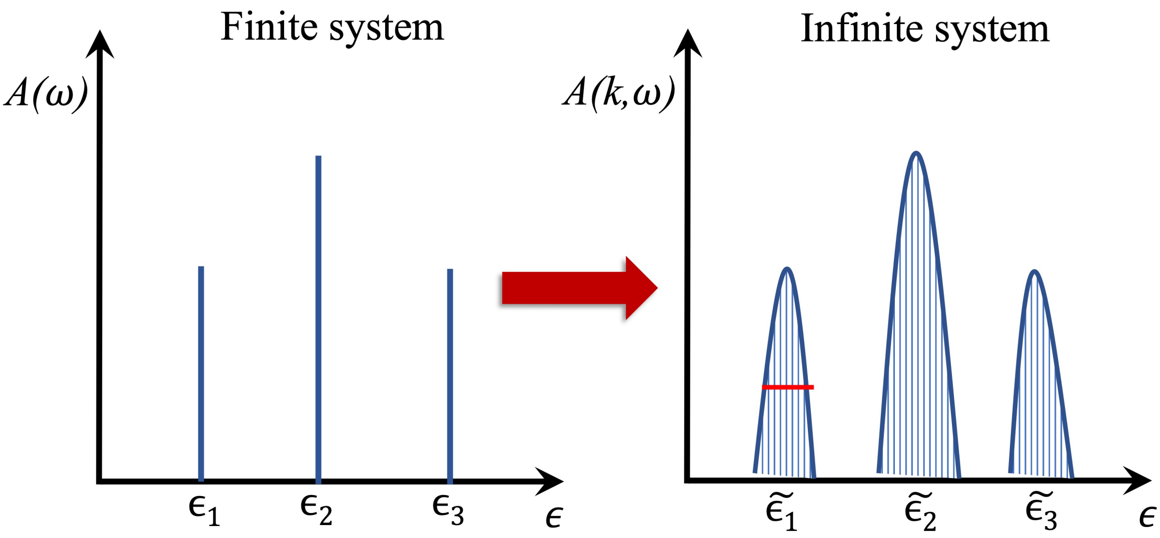

Figure 2.10: Spectral function representation for both interacting many particles and non-interacting single particle excitation.

where ϵ_s corresponds to the system's charged excitation energy for the N-electron system.

$$\epsilon_s = \begin{cases} E^{N+1} - E^N & \text{if } \epsilon_s > \mu \\ E^N - E^{N-1} & \text{if } \epsilon_s < \mu \end{cases}$$

The spectral function, which specifies all the probability to reach the final state, is defined by the imaginary portion of the Green's function.

$$A(\epsilon) = \frac{-1}{\pi} \int dr \lim_{r^{'} \to r} \text{Im}G(r, r^{'}; \epsilon) \tag{2.89}$$

$$A(\epsilon) = \text{Im}G_k(\epsilon) \approx \frac{Z_k}{\epsilon - (\epsilon_k + i\Gamma_k)} \tag{2.90}$$

The lifespan of an electron under electronic excitation is unlimited since it does not degrade. As a result, for each transition, we see a corresponding delta function. Contrary to this, the peak is seen with some widening in experimental measurements, as illustrated in Figure 2.10. This may be accounted for by the fact that several electrons, as opposed to just one, are excited throughout the process, and that each excitation contributes a delta function with closely spaced energetics. The result is a peak with a limited width. This peak, which is seen in the right panel of Figure 2.10, resembles a single particle, thus we named it a quasiparticle peak. As a result, we may infer the three essential components from the excited spectrum: quasiparticle energy (ϵ_k), defined as the distance between the peak's two points, inverse of life-time (Γ_k), and quasi-particle weight Z_k. Figure 2.11 shows how to see the quasiparticle from a different angle. An electron is ejected from the sample when it is exposed to light, and this electron leaves a hole behind. The negative charge will eventually screen out the positive charge as the system evolves with time. Consequently, a quasiparticle (QP), which we refer to as, is created when a hole and the charge around it combine and act as single entity. The QP will now flow through the system. Through screened Coulomb potential (W), the QP interacts with the rest of the system ineffectively. Within the context of the many-body perturbation theory, QP energies are assessed using Green's function methods, where polarisation and screening concepts are described. In particular, screening is been represented by the dielectric function,

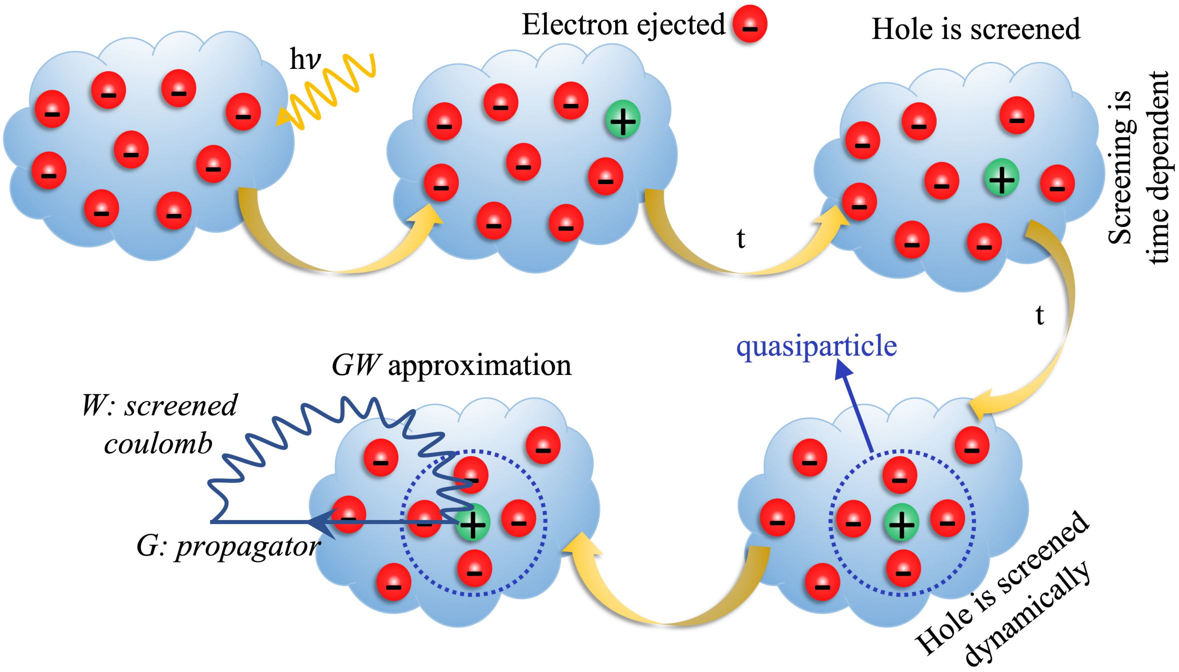

Figure 2.11: The illustration of the quasiparticle and noninteracting particle excitation peaks.

while polarisation is been translated to the polarisation response function. The interacting and non-interacting Green's functions make up the precise Green's function. The non-interacting function is assessed using DFT. The Dyson equation then links self-energy with non-interacting function to achieve complete interaction. Dyson's equation provides the following relationship between the interacting and non-interacting Green's functions:

$$G^{-1} = G_0^{-1} - \Sigma \tag{2.91}$$

The self energy is used to define the sum of all potential single scattering processes, and the Dyson equation is used to characterise all scattering processes during excitations. Notably, the remainder of the electrons attempt to adjust to the new state whenever one electron is added or withdrawn from the system, where the self energy plays a significant role. The other electrons repel a moving electron, which polarizes the potential and causes it to shift. It becomes difficult to calculate the self energy throughout the excitation phase since the system experiences an endless number of scatterings. Hedin put up a set of GW equations in 1965, and their self-consistent solution can give the precise self-energy of the interacting situation. Even for the most basic homogeneous electron gas system, the exact solution of Hedin's equations is not tractable. However, we can generate systematically improvable approximations if we are aware of the precise theory. The GW approximation is the most straightforward.

Hedin's Equations Exact solution:

$$P(12) = -i\int d(34)G(13)G(41^{+})\Gamma(342) \tag{2.92}$$

$$\Sigma(12) = i\int d(34)G(14^{+})W(13)\Gamma(423) \tag{2.93}$$

$$\Gamma(123) = \delta(12)\delta(13) + \int d(4567)\frac{\delta\Sigma(12)}{\delta G(45)}G(46)G(75)\Gamma(673) \tag{2.94}$$

$$W(123) = v(12) + \int d(34)W(13)P(34)v(42) \tag{2.95}$$

The following is the Dyson equation to connect Green's function (G) with the self-energy (Σ_{xc}):

$$G(12) = G_{KS}(12) + \int d(34)G_{KS}(13)\Sigma(34)G(42) \tag{2.96}$$

where G, P, Γ and Σ correspond to Green's function propagator, polarizability, vertex function and self-energy, respectively. The approach is unaffordable in terms of cost and memory requirements due to inclusion of derivative of self-energy w.r.t green's function in the vertex function. In order to make the equations solvable, the vertex adjustments are therefore disregarded in the GW approximation.

$$\Gamma(123) = \delta(12)\delta(13) \tag{2.97}$$

$$\begin{aligned}\Sigma &= iGW = \Sigma_x + \Sigma_c \\ &= iGv + iG(W - v)\end{aligned} \tag{2.98}$$

The random phase approximation (RPA) is used to derive the irreducible polarizability:

$$P(r,r^{'},\epsilon) = \frac{i}{2\pi}\int d\epsilon e^{i\omega\eta}G(r,r^{'},\epsilon+\epsilon^{'})G(r,r^{'},\epsilon) \tag{2.99}$$

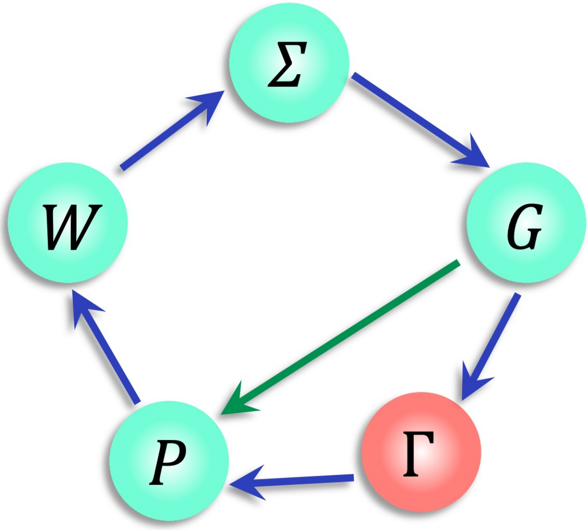

Figure 2.12: The pentagon of Hedin. In the GW approximation, the vertex function (Γ) is omitted.

One may determine the dielectric constant by:

$$\varepsilon(r,r^{'},\epsilon)=\delta(r-r^{'})-\int dr^{''}\frac{P(r,r^{''},t)}{|r^{''}-r^{'}|} \tag{2.100}$$

We can calculate W if the dielectric function (ε) is known. This explains how screened coulomb interactions allow the quasiparticle to interact with the rest of the system. The coulomb interaction under screening:

$$W(r,r^{'},t)=\int dr^{''}\frac{\varepsilon^{-1}(r,r^{''},t)}{|r^{''}-r^{'}|} \tag{2.101}$$

The self-energy may be calculated as follows using a GW approximation:

$$\Sigma^{GW}(r,r^{'},\epsilon)=-\frac{i}{2\pi}\int d\epsilon e^{i\epsilon\eta}G(r,r^{'},\epsilon+\epsilon^{'})W(r,r^{'},\epsilon) \tag{2.102}$$

Here, the screened interaction is represented by $W(r,r^{'},\epsilon)$, and Green's function $G(r,r^{'},\epsilon)$ serves as a propagator to explain the velocity of the quasiparticle. The energy that a quasiparticle experiences as a result of being present is known as self-energy. It is an energy contribution that the particle itself has caused. Knowing all the components allows us to solve the equation 2.87 to calculate the quasiparticle energies. By using the quasi-particle equation, the GW self-energy can be used to perturbatively correct the DFT/HF eigenvalues: The quasi-particle energies are assessed perturbatively on top of a prior DFT, hence the GW approach is quite dependent on the calculations for the starting point.

$$\epsilon_i^{QP}=\epsilon_i^{KS}-\langle\psi_i^{KS}|V_{xc}^{KS}-\Sigma_c^{GW}(\epsilon_i^{QP})-\Sigma_x|\psi_i^{KS}\rangle \tag{2.103}$$

The correlation component of the self-energy GW is represented by Σ_c^{GW}, where Σ_x stands for the exact-exchange operator. The exchange-correlation potential of the previous DFT computation is represented by V_{xc}^{KS}, and its associated eigenvalues and eigenvectors are ϵ_i^{KS} and ψ_i^{KS}, respectively. The most popular approach is the single-shot G_0W_0, which determines the band gap or fundamental gap well in agreement with the experimental findings [51, 54].

2.15 Bethe-Salpeter Equation (BSE)

The one particle Green's function can be used to explain the propagation of a single electron or hole. Similar to this, higher-order Green's function governs the propagation of two or more particles. The interaction between the electron and the hole that forms following excitation is particularly important in neutral excitations (for example, optical absorption, and electron energy loss and inelastic X-ray scattering). The term "excitons" refers to these electron-hole pairs. The Bethe-Salpeter equation takes into account the effort to solve the electron-hole interaction. Together, Bethe and Salpeter were able to determine the equation of motion for the two particle Green's function in 1951 [55, 56]. Later, Sham et al. updated it for the exciton, which is an interaction between electrons and holes [57, 58]. Baym and Kadanoff in 1961 [59] suggested an exact formula. Strinati then applied the Baym and Kadanoff theory and utilized the GW technique and BSE to compute the excitons [60]. Onida expanded on Strinati's strategy in 1995 to explain the excitons on the sodium tetramer [61]. It is now possible to undertake the GW and BSE computations to unravel the optical spectra due to recent advancements in computer resources and technology [62]. Figure 2.9 depicts the schematic depiction of bandgap fluctuation using various approaches (DFT, GW and BSE). Strinati's work is followed by the BSE equation, which connects the interacting four-point correlation function L to the non-interacting four-point correlation function L_0. BSE is defined as follows:

$$\begin{aligned} L\left(12;1'2'\right) = L_0\left(12;1'2'\right) + \textstyle\int d(3456) L_0\left(14;1'3\right) \\ \times K(35;46) L\left(62;52'\right) \end{aligned} \tag{2.104}$$

The electron-hole correlation function and the electron-hole interaction kernel are denoted by the symbols $L\left(12;1'2'\right)$ and $K(35;46)$.

$L_0\left(12;1'2'\right) = G_1(1,2')G_1(2,1')$

Free electron-hole pairs with K=0 are represented by the pair $G_1(1,2')G_1(2,1')$ (without interaction). Position, spin, and time coordinates are functions of the variables in equation 2.104. L is a function of two creation time variables and two annihilation time variables. The four time variables in this situation are reduced to two time independent variables since we assume simultaneous creation and annihilation. Equation $L_0\left(12;1'2'\right)$ that depends on time is transformed into equation $L_0\left(12;1'2';\omega\right)$ that depends on energy. The energy space is currently the subject of all debates.

Assume that the electron and the hole quasiparticle both provide the one-particle Green's function G_1, but that there is no interaction between the two (electron and hole). In light of this, the non-interacting correlation function L_0 can be expressed as:

$$\begin{aligned} L_0\left(12,1'2';\omega\right) =& i\sum_{v,c}\left[\frac{\psi_c\left(\mathbf{x}_1\right)\psi_v^*\left(\mathbf{x}_1'\right)\psi_v\left(\mathbf{x}_2\right)\psi_c^*\left(\mathbf{x}_2'\right)}{\omega-\left(E_c-E_v\right)}\right. \\ & \left.-\frac{\psi_v\left(\mathbf{x}_1\right)\psi_c^*\left(\mathbf{x}_1'\right)\psi_c\left(\mathbf{x}_2\right)\psi_v^*\left(\mathbf{x}_2'\right)}{\omega+\left(E_c-E_v\right)}\right] \end{aligned} \tag{2.105}$$

where, respectively, v and c represent the total sum of the occupied hole and unoccupied electron states. It should be noted that the denominator should also contain adequate imaginary infinitesimals; however, for convenience of illustration, we have not done that here.

Let's now assume that the electron and the hole are interacting. Consequently, the equation for the interacting electron-hole correlation function L is as follows:

$$\begin{aligned} L\left(12,1'2';\omega\right) = i\sum_{S}&\left[\frac{\chi_S\left(\mathbf{x}_1,\mathbf{x}_1'\right)\chi_S^*\left(\mathbf{x}_2',\mathbf{x}_2\right)}{\omega-\Omega_S}\right. \\ & \left.-\frac{\chi_S\left(\mathbf{x}_2,\mathbf{x}_2'\right)\chi_S^*\left(\mathbf{x}_1',\mathbf{x}_1\right)}{\omega+\Omega_S}\right] \end{aligned} \tag{2.106}$$

Here, the term S stands for the correlated electron-hole states, which are a linear combination of a number of v and c states, while the term Ω_S stands for the excitation energies.

The form of the electron-hole amplitudes is:

$$\chi_S\left(\mathbf{x},\mathbf{x}'\right) = -\left\langle N,0\left|\psi^\dagger\left(\mathbf{x}'\right)\psi(\mathbf{x})\right|N,S\right\rangle \tag{2.107}$$

Next, we change the continuous position variables to reflect the single-particle wave functions of the electron and hole states. The modified version of the electron-hole amplitudes is as follows:

$$\chi_S\left(\mathbf{x},\mathbf{x}'\right) = \sum_{v}^{\text{occ}}\sum_{c}^{\text{empty}} A_{vc}^S\psi_c(\mathbf{x})\psi_v^*\left(\mathbf{x}'\right) + B_{vc}^S\psi_v(\mathbf{x})\psi_c^*\left(\mathbf{x}'\right) \tag{2.108}$$

We have two summations in reference equation 2.108. One run covers the occupied states (v) while the second run covers the c unoccupied states. Notably, we have not seen any product combinations that had either two occupied vv states or two empty cc states. After the substitution of Eq. 2.105, 2.106, 2.108 in the BSE Eq. 2.104. The obtained final eigenvalue equation is as follows:

$$\begin{aligned}(E_c - E_v) A^S_{vc} + \textstyle\sum_{v'c'} K^{AA}_{vc,v'c'}(\Omega_S) A^S_{v'c'} \\ + \textstyle\sum_{v'c'} K^{AB}_{vc,v'c'}(\Omega_S) B^S_{v'c'} = \Omega_S A^S_{vc}, \\ \textstyle\sum_{v'c'} K^{BA}_{vc,v'c'}(\Omega_S) A^S_{v'c'} + (E_c - E_v) B^S_{vc} \\ + \textstyle\sum_{v'c'} K^{BB}_{vc,v'c'}(\Omega_S) B^S_{v'c'} = -\Omega_S B^S_{vc}\end{aligned} \tag{2.109}$$

where the energies of the quasiparticles are E_c and E_v. The electron-hole interaction kernel's symbol is K. In the above equation, A^S_{vc} corresponds to the coupling coefficients.

The electron-hole interaction matrix components are defined as:

$$\begin{aligned}K^{AA}_{vc,v'c'}(\Omega_S) =& i \int d(3456) \psi_v(\mathbf{x}_4) \psi^*_c(\mathbf{x}_3) K(35,46;\Omega_S) \\ & \times \psi^*_{v'}(\mathbf{x}_5) \psi_{c'}(\mathbf{x}_6), \\ K^{AB}_{vc,v'c'}(\Omega_S) =& i \int d(3456) \psi_v(\mathbf{x}_4) \psi^*_c(\mathbf{x}_3) K(35,46;\Omega_S) \\ & \times \psi^*_{v'}(\mathbf{x}_6) \psi_{c'}(\mathbf{x}_5),\end{aligned} \tag{2.110}$$

Both K^{BB} and K^{BA} also exhibit similar expressions.

The diagonal terms in a matrix are the energy difference ($E_c - E_v$) and the components of the interaction matrix (K^{AA} and K^{BB}). The terms K^{AB} and K^{BA} are off-diagonal. Off-diagonal terms are typically found to be quite tiny. Therefore, in Eq. 2.109 we set $K^{AB} = K^{BA} = 0$. As a result, Eq. 2.109 decouples into two equations, A^S_{vc} and B^S_{vc}, leading to identical excitations (except change in negative sign). The final eigenvalue equation is given by:

$$(E_c - E_v) A^S_{vc} + \sum_{v'c'} K^{AA}_{vc,v'c'}(\Omega_S) A^S_{v'c'} = \Omega_S A^S_{vc} \tag{2.111}$$

This electron-hole interaction kernel term K will be regarded as an approximate independent particle if it is ignored. The associated electron-hole term is defined as:

$$|N,S\rangle = \sum_v^{\text{hole}} \sum_c^{\text{elec}} A^S_{vc} \hat{a}^\dagger_v \hat{b}^\dagger_c |N,0\rangle =: \sum_v^{\text{hole}} \sum_c^{\text{elec}} A^S_{vc} |vc\rangle, \tag{2.112}$$

When we shine light on the ground state $|N,0\rangle$, a hole and electron are created in the system, which are denoted by $\hat{b}^\dagger_c$ and $\hat{a}^\dagger_v$, respectively. Tamm-Dancoff approximation is the expansion of Eq. 2.112. Finding the electron-hole interaction kernel K is the next job. To achieve this, we must perform a functional derivative with respect to G.

$$K(35;46) = \frac{\delta\left[V_{\text{Coul}}(3)\delta(3,4) + \Sigma(3,4)\right]}{\delta G_1(6,5)} \tag{2.113}$$

Further, we approximate the self-energy operator Σ using the GW method. Here, we have disregarded W's derivative relative to G_1.

$$\begin{aligned} K(35;46) = & -i\delta(3,4)\delta\left(5^{-},6\right)v(3,6) \\ & +i\delta(3,6)\delta(4,5)W\left(3^{+},4\right) \\ =: & \, K^{x}(35;46)+K^{d}(35;46) \end{aligned} \tag{2.114}$$

According to Figure 2.13, K^x is the exchange interaction term derived from the Coulomb potential, and K^d is the direct interaction term derived from filtered exchange self-energy. The features of the excitation spectrum, such as (i) the splitting between spin-singlet and spin-triplet excitations and (ii) the longitudinal-transverse splitting of the s excitons are mostly controlled by the exchange interaction term (K^x). The attractiveness of the electron-hole interaction and the production of excitons are both controlled by the direct interaction term (K^d). The bare Coulomb interaction v and the screened Coulomb interaction W, respectively, are involved in K^x and K^d.

The electron-hole interaction kernel K's matrix elements are given by:

$$\begin{aligned} & \left\langle vc\left|K^{AA,d}\left(\Omega_S\right)\right|v'c'\right\rangle \\ & \quad = \textstyle\int d\mathbf{x}d\mathbf{x}'\psi_c^*(\mathbf{x})\psi_{c'}(\mathbf{x})\psi_v\left(\mathbf{x}'\right)\psi_{v'}^*\left(\mathbf{x}'\right) \\ & \times \tfrac{i}{2\pi}\textstyle\int d\omega e^{-i\omega 0^+}W\left(\mathbf{r},\mathbf{r}',\omega\right) \\ & \times\left[\tfrac{1}{\Omega_S-\omega-\left(E_{c'}^{\mathrm{QP}}-E_v^{\mathrm{QP}}\right)+i0^+}\right. \\ & \left.+\tfrac{1}{\Omega_S+\omega-\left(E_c^{\mathrm{QP}}-E_v^{\mathrm{QP}}\right)+i0^+}\right], \end{aligned} \tag{2.115}$$

and

$$\begin{aligned} \left\langle vc\left|K^{AA,x}\right|v'c'\right\rangle = & \int d\mathbf{x}d\mathbf{x}'\psi_c^*(\mathbf{x})\psi_v(\mathbf{x})v\left(\mathbf{r},\mathbf{r}'\right) \\ & \times\psi_{c'}\left(\mathbf{x}'\right)\psi_{v'}^*\left(\mathbf{x}'\right) \end{aligned} \tag{2.116}$$

Then, in the plasmon-pole model, expand the Coulomb screened interaction W:

$$\begin{aligned} W\left(\mathbf{r},\mathbf{r}',\omega\right) = & \sum_l W_l\left(\mathbf{r},\mathbf{r}'\right)\frac{\omega_l}{2} \\ & \times\left(\frac{1}{\omega-\omega_l+i0^+}-\frac{1}{\omega+\omega_l-i0^+}\right), \end{aligned} \tag{2.117}$$

where $W_l\left(\mathbf{r},\mathbf{r}\prime\right)$ and ω_l correspond to the spatial component of the plasmon mode l and the plasmon frequency, respectively. After that, we have integrated the frequencies.

$$\begin{aligned} \left\langle vc\left|K^{AA,d}\left(\Omega_S\right)\right|v'c'\right\rangle = & -\sum_l\int d\mathbf{x}d\mathbf{x}'\psi_c^*(\mathbf{x})\psi_{c'}(\mathbf{x})\psi_v\left(\mathbf{x}'\right)\psi_{v'}^*\left(\mathbf{x}'\right)W_l\left(\mathbf{r},\mathbf{r}'\right) \\ & \times\frac{\omega_l}{2}\left[\frac{1}{\omega_l-\left(\Omega_S-\left(E_{c'}^{\mathrm{QP}}-E_v^{\mathrm{QP}}\right)\right)}+\frac{1}{\omega_l-\left(\Omega_S-\left(E_c^{\mathrm{QP}}-E_v^{\mathrm{QP}}\right)\right)}\right] \end{aligned} \tag{2.118}$$

The excitation energies result from transitions from the valence band to the conduction band. Since excitation energies Ω_S, which are mostly applicable to semiconductors, are near to the transition energies $\left(E_c^{\mathrm{QP}}-E_v^{\mathrm{QP}}\right)$, this means that they are close to them as well. Because of this, the term $\Omega_S-\left(E_c^{\mathrm{QP}}-E_v^{\mathrm{QP}}\right)$ is significantly less than the ω_l. The Eq. 2.118 can be written as:

$$\begin{aligned}
&\left\langle vc\left|K^{AA,d}\right|v'c'\right\rangle \\
&\quad=-\int d\mathbf{x}d\mathbf{x}'\psi_c^*(\mathbf{x})\psi_{c'}(\mathbf{x})\psi_v\left(\mathbf{x}'\right) \\
&\quad\times\psi_{v'}^*\left(\mathbf{x}'\right)W\left(\mathbf{r},\mathbf{r}',\omega=0\right)
\end{aligned} \tag{2.119}$$

Only the static attributes of W are included in Eq. 2.119, while its dynamic aspects are ignored. Next, we study the case when the transition energies $\left(E_c^{\mathrm{QP}}-E_v^{\mathrm{QP}}\right)$ and excitation energies Ω_S are substantially different. Specifically, with regard to atoms and molecules, this is possible. In that situation, Eq. 2.119 might not hold, forcing us to apply Eq. 2.118. The Ω_S component in this equation necessitates careful convergence of both the electron-hole interaction term and the self-consistent BSE. We employ an iterative process for this. First, we ignore the dynamics of W and just consider static screening (K^d is determined using Eq. 2.119). The excited state $|S\rangle$ and an initial estimate of the excitation energy (let's say Ω_S^0) are then determined by solving the BSE. Then, we recalculate K^d and enter Ω_S^0 in the equation reference Eq. 2.118. To further increase the value of Ω_S, we calculate the difference between the updated K^d and the original K^d, which is defined as a first order perturbation. In order to reach the converged value of Ω_S, these steps should be repeated. Put the value of K in Eq. 2.111, then build a Hamiltonian. The Hamiltonian is then diagonalized. Correlated electron-hole states $|S\rangle$ will result from it.

We have used Fermi's golden rule to determine the optical spectra in the next section.

2.15.1 Optical response using BSE

Fermi's Golden rule can be used to identify optical transitions. Let's assume that there is no contact between the electron and the hole and that the independent electron and the independent hole decide the vertical transitions. Let's imagine that an operator, such as a velocity or momentum operator, is used to transfer electrons from their beginning state to their end state. We have estimated the imaginary portion of the macroscopic transverse dielectric function for the optical response function:

$$\epsilon_2^{(0)}(\omega)=\frac{16\pi e^2}{\omega^2}\sum_{v,c}|\vec{\lambda}\cdot\langle v|\vec{v}|c\rangle|^2\delta\left(\omega-\left(E_c-E_v\right)\right), \tag{2.120}$$

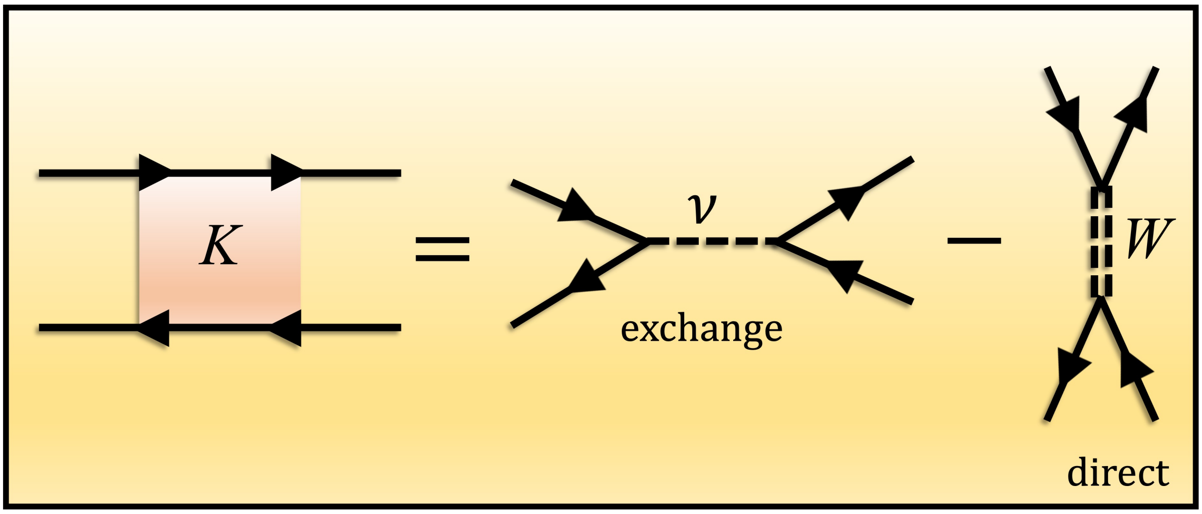

Figure 2.13: Schematic diagram of many body interaction (exchange and the direct interaction)term.

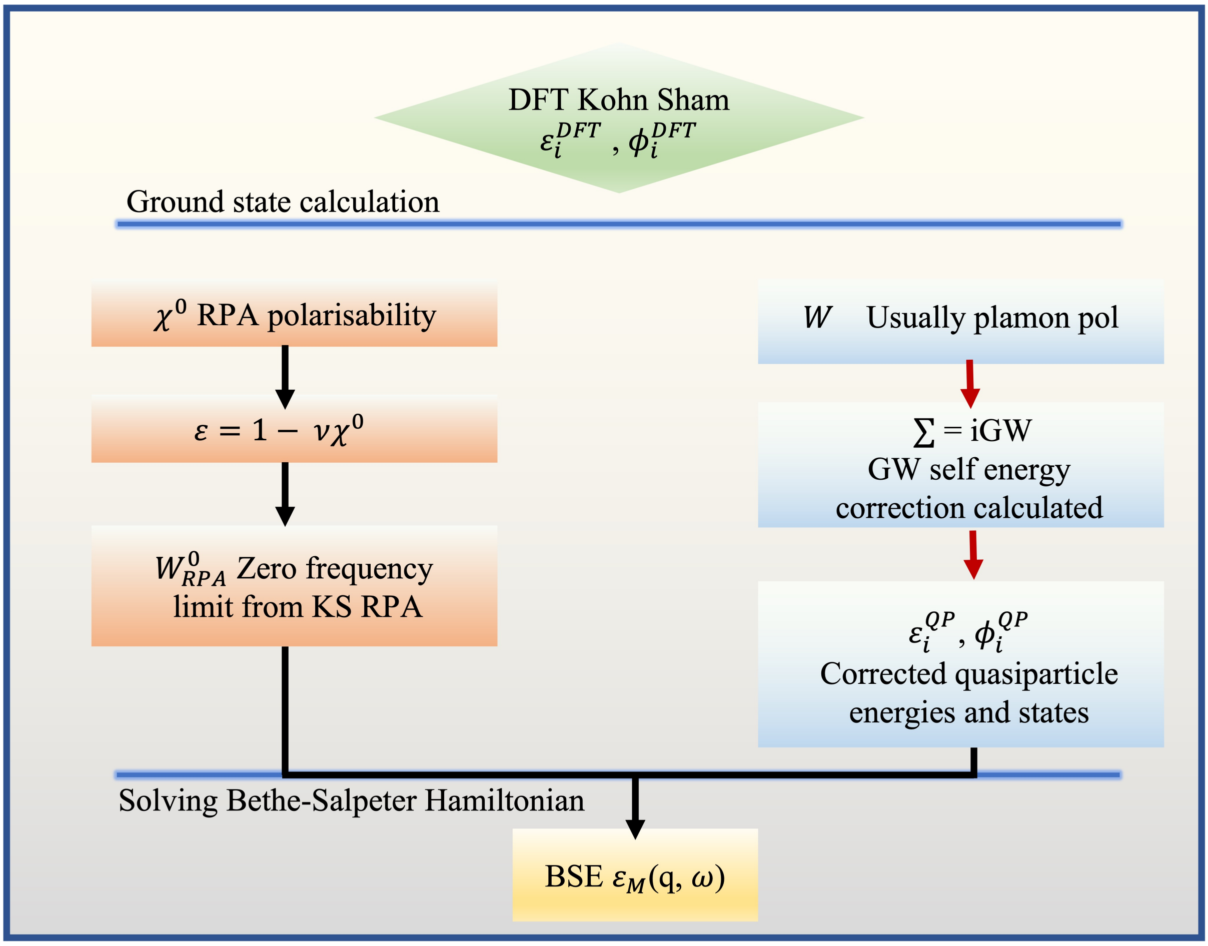

Figure 2.14: Flow chart for the BSE calculations.

where $\lambda = \frac{\vec{A}}{|\vec{A}|}$ corresponds to the light's polarisation vector and $\vec{v}$ corresponds to the single particle velocity operator, $\delta\left(\omega - \left(E_c - E_v\right)\right)$ corresponds to the term for energy conservation, c and v denote the conduction and valence states.

Since electrons and holes will interact in reality, the imaginary portion of the macroscopic transverse dielectric function is as follows:

$$\epsilon_2(\omega) = \frac{16\pi e^2}{\omega^2} \sum_S |\vec{\lambda} \cdot \langle 0|\vec{v}|S\rangle|^2 \delta\left(\omega - \Omega_S\right), \tag{2.121}$$

The associated electron-hole term is $|S\rangle$. The optical transition matrix is $\langle 0|\vec{v}|S\rangle$ This formula yields the optical transition matrix:

$$\langle 0|\vec{v}|S\rangle = \sum_v^{\text{hole}} \sum_c^{\text{elec}} A_{vc}^S \langle v|\vec{v}|c\rangle, \tag{2.122}$$

While considering pseudopotentials, one should exercise extreme caution when calculating the transition matrix elements $\langle v|\vec{v}|c\rangle$. The velocity operator ($\vec{v} = i[H, \vec{r}]$) is also known as the current operator. If and only if the potential and position operators commute, $[V(\vec{r}), \vec{r}]$=0, the velocity operator for local pseudopotentials can be substituted by the momentum operator. On the other hand, we must consider the commutator term $[V(\vec{r}), \vec{r}]$ for non-local pseudopotentials. Consequently, in addition to the momentum operator, there is another commutator term.

$$\langle v|\vec{v}|c\rangle = \langle v\left|\vec{p} + i\left[V_{\text{ps}}, \vec{r}\right]\right|c\rangle \tag{2.123}$$

2.15.2 Challenges while performing BSE calculations

Let's use the Hamiltonian's solution in a plane wave basis set as an example to better grasp the difficulties. Valence and conduction bands at a certain k-point make up each basis. Let's look at a Silicon example (Si). 4 valence bands make up Si. Suppose it contains four conduction bands. Create a 4×4 matrix with k-points in it. Let's assume that 1000 k-points, or 10×10×10, are needed for the optical spectra to converge. This demonstrates that we have a matrix that is 4×4×1000, or 6000×16000. It implies that we must build a very large matrix and further diagonalize it. This matrix ought to be non-Hermitian in theory. Because each exciton exhibits certain lifetime. From the imaginary portion of the Green's function, lifetime can be calculated. Hence, if we claim that a matrix is Hermitian, it should not be connected to any hypothetical component. As a result, it implies that the matrix is not Hermitian. It should be noted that computing the non-Hermitian matrix is in fact an extremely difficult process because solving the Hermitian matrix is itself a difficult task. The non-Hermitian matrix is then made into a

Hermitian one using the Tamm-Dancoff [63] and static screening approximations, which are then solved to provide optical absorption.

It will be easier to comprehend the difficulty of solving BSE if we compare the DFT and the BSE computations. In reality, when we use DFT to calculate ground state energy, we are only concerned with the lowest eigenvalues; but, when we use BSE or excited state computations, we must take into account all of the eigenvalues. As a result, we must find solutions for all 16000 eigenvalues and 16000 eigenvectors for the Si example. Additionally, iterative techniques are no longer a practical choice for that (iterative methods are applicable for DFT, where we compute only a few eigenvalues). Consequently, it is difficult to fully diagonalize a matrix of this size. These techniques (GW and BSE) are therefore exceedingly costly to compute.

2.16 Exciton models and lifetimes

The electrostatic Coulomb force is used to attract bound electron-hole pairs, which are known as excitons. The two primary categories of excitons are Wannier-Mott excitons and Frenkel excitons. We provide some Frenkel exciton characteristics.

- These excitons are tightly bounded.
- Its radius is similar to the distance between atoms. As a result, it is localized to one atom or is strongly linked to certain atoms or molecules. Its probability of being discovered on the same atom is therefore quite high.
- It is often discovered in substances with high electron and hole effective mass values, low dielectric constants, and large bandgaps.
- The exciton binding energy of these excitons ranges from 0.1 eV to several eV.
- Alkali halide crystals are an example of an organic substance that contains these excitons (aromatic molecules) [64].

The characteristics of wannier excitons are then listed as follows:

- These excitons are weakly bounded or termed as free excitons.
- These excitons exhibit large radii.

- These excitons are loosely connected to certain atoms or molecules, thus they are free to travel anywhere in the crystal.
- They are often found in semiconductors which possess narrow bandgaps and high dielectric constants [64]. Wannier excitons are important since we focused on broad bandgap semiconductors in this thesis.

2.17 Wannier exciton

By assuming the most basic system, the hydrogenic system, we may create a Hamiltonian for a bound electron-hole pair using Bohr's model. The formula for the effective Hamiltonian is:

$$H_{exc} = E_g - \frac{\hbar^2}{2m_c}\nabla_e^2 - \frac{\hbar^2}{2m_v}\nabla_h^2 - \frac{e^2}{4\pi\epsilon_{r(0)}\left|\mathbf{r}_e - \mathbf{r}_h\right|} \tag{2.124}$$

The symbols m_c and m_v, respectively, stand for the effective masses of an electron and a hole, respectively. An electron's position vector is $\mathbf{r}_e$, whereas a hole's location vector is $\mathbf{r}_h$. E_g is a symbol for the semiconductor's direct bandgap. Excitation is travelling in the medium $\epsilon_{r(0)}$. We construct a Hamiltonian for the relative motion of electrons and holes using knowledge of atomic physics.

$$R = \frac{m_e\mathbf{r}_e + m_h\mathbf{r}_h}{m_e + m_h}, \quad \mu = \frac{m_e m_h}{m_e + m_h}, \mathbf{r} = \mathbf{r}_e - \mathbf{r}_h \tag{2.125}$$

$$H_{exc} = E_g - \frac{\hbar^2}{2\mu}\nabla_{\mathbf{r}}^2 - \frac{\hbar^2}{2\left(m_e + m_h\right)}\nabla_R^2 - \frac{e^2}{4\pi\epsilon_{r0}\mathbf{r}} \tag{2.126}$$

The wavefunction explains how an electron and a hole move in relation to one another.

$$\psi\left(\mathbf{r}_e, \mathbf{r}_h\right) = e^{-\mathbf{k}\cdot\mathbf{R}}\phi_n(\mathbf{r}) \tag{2.127}$$

where **k** is a wavevector that symbolizes the propagation of an electron and hole pair. Here, $\phi_n(\mathbf{r})$ gives the information about the relative motion of hole and electron and depends on **r**. The form of the Schrödinger equation is identical to that of the Hydrogen atom.

$$\left(-\frac{\hbar^2}{2\mu}\nabla_{\mathbf{r}}^2 - \frac{e^2}{4\pi\epsilon_{\mathbf{r}0}\mathbf{r}}\right)\phi_n(\mathbf{r}) = E_n\phi_n(\mathbf{r}) \tag{2.128}$$

The wavefunction [65] of exciton is defined as follows:

$$\psi_{\mathbf{kr}}(\mathbf{R}, \mathbf{r}) = e^{\mathbf{k}\cdot\mathbf{r}}\phi_n(\mathbf{r})\phi_c\left(\mathbf{r}_e\right)\phi_v\left(\mathbf{r}_h\right) \tag{2.129}$$

where $\phi_c(\mathbf{r}_e)$ ($\phi_v(\mathbf{r}_h)$) denotes the Bloch function for conduction band electron (valence band hole). n represents the principle quantum number. The eigenvalues of Hamiltonian are given by:

$$E_{\mathrm{k}n} = E_B(n) + \frac{\mathbf{k}^2}{2(m_e + m_h)} \tag{2.130}$$

The energy eigenvalues of a bound electron and hole pair are denoted as $E_B(n)$.

$$E_B(n) = -\frac{E_B}{n^2} \tag{2.131}$$

In terms of Rydberg energy, E_B is represented as follows:

$$E_B = \frac{\mu}{m_0 \epsilon_r(0)^2} E_{Ry} \tag{2.132}$$

E_{Ry} corresponds to the hydrogen atom's Rydberg energy [66, 64].

Similar to the hydrogen radius, the exciton radius is determined by:

$$r_{exc} = \frac{m_0}{\mu} \epsilon_r(0) n^2 r_{Ry} \tag{2.133}$$

where r_{Ry} is the hydrogen atom's Bohr radius and r_{exc} represents the exciton radius.

2.18 Optical transition

2.18.1 Fermi's golden rule

The electronic or atomic transition rates that take place between the beginning and final states are defined by Fermi's golden rule, a quantum mechanically based formalism. This rule was initially discovered by Dirac [67] , not Fermi. Fermi's golden rule is a well-known name for it. Nevertheless, this is due to Fermi's application of this rule in his well-known hypothesis, beta decay, which he considered to be a golden rule [68]. When the starting and end states of an electronic or optical transition are represented by wavefunctions, Fermi's golden rule is applicable. First order perturbation theory is employed to calculate the transition rate. It may be calculated using the elements of the transition matrix and is defined as the probability of transition per unit time. The Fermi principle is given by:

$$\gamma_i^f = \frac{2\pi}{\hbar} \left|\langle i \left| H' \right| f \rangle\right|^2 \delta\left(E_f - E_i - \hbar\omega\right) \tag{2.134}$$

where $|f\rangle$ and $\langle i|$ denotes the final and the initial states, respectively. H' represents the perturbative Hamiltonian. The decay probability, which provides information of the inverse of lifetime, is also known as Fermi's golden rule.

Let's calculate the absorption process' transition rate. An electron moves from its valence band to its conduction band as a result of photon absorption. Let's construct a Hamiltonian to describe how the electron interacts with the electromagnetic field. Two variables (i) the scalar potential (ϕ) and (ii) the vector potential ($\mathbf{A}$) describe the electromagnetic field. $\mathbf{E}$ and $\mathbf{B}$ are calculated using ϕ and $\mathbf{A}$ as follows:

$$\mathbf{E} = -\nabla\phi - \frac{1}{c}\frac{\partial \mathbf{A}}{\partial t}, \quad \mathbf{B} = \nabla \times \mathbf{A} \tag{2.135}$$

The following equation gives the Hamiltonian for a particle with mass m and charge e in an electromagnetic field:

$$H = \frac{1}{2m_c}\left(\mathbf{p} - \frac{e}{c}\mathbf{A}\right)^2 + e(\phi + V(r)) \tag{2.136}$$

Here, $V(r)$ denotes the periodic potential in absence of electromagnetic field.

$$H = \frac{1}{2m}p^2 + \frac{e}{2m}\left(-(\mathbf{A}\cdot\mathbf{p} + \mathbf{p}\cdot\mathbf{A}) + \frac{e}{c}\mathbf{A}^2\right)\right) + e(\phi + V(r)) \tag{2.137}$$

The quadratic term $\mathbf{A}^2$ is disregarded due to its extreamly small value. In order to make calculations simpler, we are free to select the gauze. For the scalar potential, $\phi = 0$ is the simplest gauze. Let's assume the Coulomb gauze [69] $\Delta \cdot \mathbf{A} = 0$, $\mathbf{A}\cdot\mathbf{p} = \mathbf{p}\cdot\mathbf{A}$ [69] is satisfied, , therefore $\Delta \cdot \mathbf{A} = 0$, $\mathbf{A}\cdot\mathbf{p} = \mathbf{p}\cdot\mathbf{A}$

Take a plane wave as an example of an electromagnetic vector potential ($\mathbf{A}$).

$$\mathbf{A} = \mathbf{A}_0\hat{\mathbf{e}}(\exp[i(\mathbf{k}\cdot\mathbf{r} - \omega t)] + \exp[-i(\mathbf{k}\cdot\mathbf{r} - \omega t)]) \tag{2.138}$$

where $\hat{\mathbf{e}}$ represents unitvector pointing in the plane wave's direction.

$$H = H_0 + H', \quad H_0 = \frac{p^2}{2m} + eV \tag{2.139}$$

The Hamiltonian of perturbation H'

$$H' = -\frac{e}{mc}\mathbf{A}\cdot\mathbf{p} \tag{2.140}$$

When Eq. 2.140 and Eq. 2.138 are substituted into Eq. 2.134, the transition rate for the absorption process is obtained as follows:

$$\gamma_i^f = \frac{2\pi}{\hbar}\frac{e^2}{m^2c^2}A_0^2\sum_{\mathbf{k}}\left|\left\langle v\mathbf{k}\left|e^{(i\mathbf{k}\cdot\mathbf{r})}\hat{\mathbf{e}}\cdot\mathbf{p}\right|c\mathbf{k}\right\rangle\right|^2\delta\left(E_f - E_i - \hbar\omega\right) \tag{2.141}$$

The emission process is described similarly by:

$$\gamma_i^f = \frac{2\pi}{\hbar}\frac{e^2}{m^2c^2}A_0^2\sum_{\mathbf{k}}\left|\left\langle v\mathbf{k}\left|e^{(-i\mathbf{k}\cdot\mathbf{r})}\hat{\mathbf{e}}\cdot\mathbf{p}\right|c\mathbf{k}\right\rangle\right|^2\delta\left(E_f - E_i - \hbar\omega\right) \tag{2.142}$$

E_f and E_i correspond to the eigenstate $|ck\rangle$ and $|vk\rangle$, respectively.

Convert the expression $e^{(-i\mathbf{k}\cdot\mathbf{r})}$ into a Taylor series.

$$e^{-i\mathbf{k}\cdot\mathbf{r}} \approx 1 - i\mathbf{k}\cdot\mathbf{r} + \cdots \tag{2.143}$$

where, $\mathbf{k} = \frac{2\pi}{\lambda}$. Assume that the wavelength of electromagnetic radiation is substantially greater than the size of an atom or a molecule. As a result, in Eq 2.143, $\mathbf{k}$ and $\mathbf{k}^2$ term are ignored. Consequently, $e^{-i\mathbf{k}\cdot\mathbf{r}} \approx 1$. This is termed as electric dipole approximation. Dipole transition matrix element in Eq. 2.141 and 2.142 is now:

$$\left\langle v\mathbf{k} \left| e^{(-i\mathbf{k}\cdot\mathbf{r})}\hat{\mathbf{e}}\cdot\mathbf{p} \right| c\mathbf{k} \right\rangle \approx \hat{\mathbf{e}}\cdot\langle v\mathbf{k}|\mathbf{p}|c\mathbf{k}\rangle \tag{2.144}$$

The following is the relationship between the matrix elements of a momentum operator and a position operator:

$$\langle v\mathbf{k}|\mathbf{p}|c\mathbf{k}\rangle = \frac{im}{\hbar}\left(E_i - E_f\right)\langle v\mathbf{k}|\mathbf{r}|c\mathbf{k}\rangle \tag{2.145}$$

The dipole transition matrix may be expressed as follows using the Eq. 2.145 and Eq. 2.144:

$$|\langle v\mathbf{k}|\mathbf{p}|c\mathbf{k}\rangle|^2 = m^2\omega^2|\langle v\mathbf{k}|\mathbf{r}|c\mathbf{k}\rangle|^2 \tag{2.146}$$

In the case when Eq. 2.146 is substituted for Eq. 2.142, the transition rate is given by:

$$\gamma_i^f = \frac{2\pi}{\hbar}\frac{e^2\omega^2}{c^2}A_0^2\sum_{\mathbf{k}}|\langle v\mathbf{k}|\hat{\mathbf{e}}\cdot\mathbf{r}|c\mathbf{k}\rangle|^2\delta\left(E_f - E_i - \hbar\omega\right) \tag{2.147}$$

The aforementioned equation demonstrates how the dipole matrix members directly relate to transition rate.

$$\gamma_i^f \propto \sum_{\mathbf{k}}|\langle v\mathbf{k}|\hat{\mathbf{e}}\cdot\mathbf{r}|c\mathbf{k}\rangle|^2 \tag{2.148}$$

The excitonic impact will then be included into the transition dipole matrix components. We have combined Fermi's golden rule with the Wannier approach for this purpose.

2.19 Wannier approach

2.19.1 k.p perturbation theory

We calculate the transition dipole matrix element and numerous excitonic characteristics using this method. We have employed the perturbation theory of **k·p** for this purpose. It determines the Bloch state's wavefunction and energy bands. Unperturbed Hamiltonian H_0 and perturbed Hamiltonian H' are added to form the total Hamiltonian.

$$H_{\mathbf{k}.\mathbf{p}} = H_0 + H' \tag{2.149}$$

It is possible to write the eigenvalue equation for $H_{\mathbf{k}.\mathbf{p}}$ as follows:

$$H_{\mathbf{k}.\mathbf{p}} u_{n,\mathbf{k}} = E_{n,\mathbf{k}} u_{n,\mathbf{k}} \tag{2.150}$$

The mathematical expression of $H_{\mathbf{k}.\mathbf{p}}$ is given by:

$$H_{\mathrm{k,p}} = \frac{\mathrm{p}^2}{2m} + V + \frac{\hbar}{m}\mathbf{k}\cdot\mathbf{p} + \frac{\hbar^2\mathbf{k}^2}{2m} \tag{2.151}$$

The system's potential energy is V. The unperturbed and perturbed Hamiltonians [70] are provided by comparing Eq. 2.151 and 2.149.

$$H_0 = \frac{\mathbf{p}^2}{2m} + V, \quad H' = \frac{\hbar}{m}\mathbf{k}\cdot\mathbf{p} + \frac{\hbar^2\mathbf{k}^2}{2m} \tag{2.152}$$

where $\mathbf{k}\cdot\mathbf{p}$ is represented as follows:

$$\mathbf{k}\cdot\mathbf{p} = \left(-i\hbar\frac{\partial}{\partial x}\right)k_x + \left(-i\hbar\frac{\partial}{\partial y}\right)k_y + \left(-i\hbar\frac{\partial}{\partial z}\right)k_z \tag{2.153}$$

The solution to Eq. 2.149 is obtained by using the second order of the perturbation [70] $\mathbf{k}\cdot\mathbf{p}$:

$$u_{n,\mathbf{k}} = u_{n,0} + \frac{\hbar}{m}\sum_{n'\neq n}\frac{\langle u_{n,0}|\mathbf{k}\cdot\mathbf{p}|u_{n',0}\rangle}{E_{n,0}-E_{n',0}}u_{n',0} \tag{2.154}$$

$$E_{n,\mathbf{k}} = E_{n,0} + \frac{\hbar^2\mathbf{k}^2}{2m} + \frac{\hbar^2}{m^2}\sum_{n'\neq n}\frac{|\langle u_{n,0}|\mathbf{k}\cdot\mathbf{p}|u_{n',0}\rangle|^2}{E_{n,0}-E_{n',0}} \tag{2.155}$$

The matrix element can be stated simply as:

$$\langle u_{n,0}|\mathbf{k}\cdot\mathbf{p}|u_{n',0}\rangle = \langle u_{n,0}|\mathbf{p}|u_{n',0}\rangle\cdot\mathbf{k} \tag{2.156}$$

Now substitute Eq. 2.156 into Eq. 2.155

$$E_{n,\mathbf{k}} = E_{n,0} + \frac{\hbar^2\mathbf{k}^2}{2m} + \frac{\hbar^2}{m^2}\sum_{ij}\sum_{n'\neq n}\frac{|\langle u_{n,0}|\mathbf{p}|u_{n',0}\rangle|^2 k_i k_j}{E_{n,0}-E_{n',0}} \tag{2.157}$$

The formula for effective mass is obtained from the ref. [70]:

$$E_n(\mathbf{k}) = E\left(\mathbf{k}_0\right) + \frac{\hbar^2}{2m}\sum_{ij}\left(\frac{m}{m^*}\right)_{ij}\mathbf{k}_i\mathbf{k}_j \tag{2.158}$$

Comparing Eq. 2.158 with Eq. 2.157:

$$\left(\frac{m}{m^*}\right)_{ij} = \delta_{ij} + \frac{2}{m}\sum_{n\neq n'}\frac{|\langle u_{u,0}|\mathbf{p}|u_{n',0}\rangle|^2}{E_{n,0}-E_{n',0}} \tag{2.159}$$

We may use Eq. 2.159 to get the optical transition matrix given the effective mass and bandgap.

2.20 Excitonic parameters

Let's create a momentum matrix element $\mathbf{p}$, where the change from the $|0\rangle$ ground state to the n exciton state may be expressed as follows[65]:

$$\langle n|\mathbf{p}|0\rangle = \sum_{\mathbf{k}} \langle n \mid \mathbf{k}\rangle \langle c\mathbf{k}|\mathbf{p}|\mathbf{k}v\rangle \tag{2.160}$$

The momentum matrix element's transition probability is inversely proportional to [65]:

$$|\langle n|\mathbf{p}|0\rangle|^2 \propto |\langle c|\mathbf{p}|v\rangle|^2 \left(\sum_{\mathbf{k}} \langle n \mid \mathbf{k}\rangle\right) \left(\sum_{\mathbf{k}'} \langle \mathbf{k}' \mid n\rangle\right) \tag{2.161}$$

The wavefunction of exciton is defined as follows [65]:

$$\phi_n(\mathbf{r}) = \sum_{\mathbf{k}} e^{i\mathbf{k}\cdot\mathbf{r}} \langle \mathbf{k} \mid n\rangle \tag{2.162}$$

Photons will be produced when an electron and a hole annihilate. Only when the electron and hole are at the same location, $\mathbf{r}_e = \mathbf{r}_h$, is this feasible. As a result, the exciton wavefunction is given by when the relative position is $\mathbf{r} = 0$ [65].

$$\phi_n(0) = \sum_{\mathbf{k}} \langle \mathbf{k} \mid n\rangle \tag{2.163}$$

Replace Eq. 2.163 with Eq. 2.161. The momentum matrix element's transition probability has the following form:

$$|\langle n|\mathbf{p}|0\rangle|^2 \propto |\langle c|\mathbf{p}|v\rangle|^2 \, |\phi_n(0)|^2 \tag{2.164}$$

The probability of an electron hole pair at zero separation is inversely proportional to the exciton radius and directly dependent on the derivative of the eigenvalues of a limited hydrogenic system with respect to the principal quantum number[64].

$$|\phi_n(0)|^2 = \frac{1}{2\pi \left(\mathbf{r}_{exc}\right)^3 E_B} \frac{dE_B(n)}{dn} \tag{2.165}$$

Eq. 2.131 and Eq. 2.132 are used to calculate the probability of the exciton wavefunction, which is:

$$|\phi_n(0)|^2 = \frac{1}{\pi \left(\mathbf{r}_{exc}\right)^3 n^3} \tag{2.166}$$

2.21 Exciton lifetime

Using Eq. 2.148, $\gamma_i^f \propto \sum_{\mathbf{k}} |\langle v\mathbf{k}|\hat{\mathbf{e}} \cdot \mathbf{r}|c\mathbf{k}\rangle|^2$

Let's concentrate on analysing the expression $|\langle v\mathbf{k}|\hat{\mathbf{e}} \cdot \mathbf{r}|c\mathbf{k}\rangle|^2$. Beginning with the relationship between the position operator and transition dipole matrix of the momentum:

$$|\langle v\mathbf{k}|\hat{\mathbf{e}}\cdot\mathbf{r}|c\mathbf{k}\rangle|^2 = \frac{1}{m_0^2\omega^2}|\langle v\mathbf{k}|\hat{\mathbf{e}}\cdot\mathbf{p}|c\mathbf{k}\rangle|^2 \tag{2.167}$$

The following expression is derived from the $\mathbf{k}\cdot\mathbf{p}$ method: $\langle v\mathbf{k}|\hat{\mathbf{e}}\cdot\mathbf{p}|c\mathbf{k}\rangle|^2$

$$\left[\left(\frac{m_0}{m^*}\right)_{ij} - \delta_{ij}\right]\frac{m_0 E_g}{2} = \sum_{\mathbf{k}}|\langle v\mathbf{k}|\hat{\mathbf{e}}\cdot\mathbf{p}|c\mathbf{k}\rangle|^2 \tag{2.168}$$

The transition dipole matrix elements for the exciton transitions are obtained using Fermi's golden rule as follows:

$$\sum_{\mathbf{k}}|\langle v\mathbf{k}|\hat{\mathbf{e}}\cdot\mathbf{r}|c\mathbf{k}\rangle|^2 \approx V_{exc}\cdot|\phi_n(0)|^2\,|\langle v\mathbf{k}_0|\hat{\mathbf{e}}\cdot\mathbf{r}|c\mathbf{k}_0\rangle|^2 \tag{2.169}$$

if V_{exc} is a volume, then $V_{exc} = \frac{4\pi}{3}\left(r_{exc}\right)^3$. Substituting Eq. 2.169 into Eq. 2.148:

$$\gamma_i^f \propto V_{exc}\,|\phi_n(0)|^2\,|\langle v\mathbf{k}_0|\hat{\mathbf{e}}\cdot\mathbf{r}|c\mathbf{k}_0\rangle|^2 \tag{2.170}$$

This equation demonstrates that the transition rate and the components of the transition dipole matrix are exactly related.

This equation shows that transition rate is directly proportional to the transition dipole matrix elements. The exciton lifespan will be determined by the inverse of the transition rate:

$$\tau_{exc} = \frac{1}{\gamma_i^f} \tag{2.171}$$

2.22 Geometry optimization

From a random starting geometry where all the atoms are placed in the ground state, geometry optimization is used to find the equilibrium configuration of a system. The first stage in material modelling is to find the lowest energy structure. Until the total energy is reduced, the atoms inside the unit cell or supercell move in accordance with the Hellmann–Feynman force [71]. When the force acting on each atom is equal to zero or less than a specified threshold value, the local energy minimum is reached. The following statement describes how the Hellmann-Feynman force acts on the I^{th} atom:

$$F_I = -\frac{\partial E}{\partial \mathbf{R}_I} \tag{2.172}$$

where E represents the system's overall energy. The location of the I^{th} atom is indicated by the symbol $\mathbf{R}_I$.

$$
\begin{aligned}
F_I &= -\frac{\partial}{\partial \mathbf{R}_I}\langle\Psi|H|\Psi\rangle \\
&= -\langle\Psi|\frac{\partial H}{\partial \mathbf{R}_I}|\Psi\rangle - \langle\frac{\partial \Psi}{\partial \mathbf{R}_I}|H|\Psi\rangle - \langle\Psi|H|\frac{\partial \Psi}{\partial \mathbf{R}_I}\rangle
\end{aligned}
\tag{2.173}
$$

Ψ is an eigenfunction of H in this instance.

$$
\begin{aligned}
F_I &= -\langle\Psi|\frac{\partial H}{\partial \mathbf{R}_I}|\Psi\rangle - E\langle\frac{\partial \Psi}{\partial \mathbf{R}_I}|\Psi\rangle - E\langle\Psi|\frac{\partial \Psi}{\partial \mathbf{R}_I}\rangle \\
&= -\langle\Psi|\frac{\partial H}{\partial \mathbf{R}_I}|\Psi\rangle - E\frac{\partial}{\partial \mathbf{R}_I}\langle\Psi|\Psi\rangle
\end{aligned}
\tag{2.174}
$$

Since the final term in the aforementioned calculation vanishes due to the normalisation of Ψ ($\langle\Psi|\Psi\rangle = 1$), the force acting on the I^{th} atom may be written as follows:

$$F_I = -\langle\Psi|\frac{\partial H}{\partial \mathbf{R}_I}|\Psi\rangle \tag{2.175}$$

The utilization of the aforementioned procedure is affected by two key considerations. The inaccuracies resulting from non-self-consistency are one, and the explicit dependency of the basis functions on the location of the ions is another. The Pulay troops are born from the latter. To stop the computations from making more mistakes, these problems must be resolved. For the detailed discussion refer to the Ref. [30].

2.23 Molecular dynamics

A computer approach called molecular dynamics (MD) is used to examine how a molecular system evolves over time. MD offers techniques for analyzing atom and molecule mobility under the influence of environmental factors including temperature and pressure [72]. The structure and behavior of many complex systems are studied using MD techniques. Newtonian mechanics is the foundation of every MD simulation. The dynamics of a system are clarified by using MD simulations to solve Newton's equations of motion.

$$F_I = m_I a_I = m_I \frac{d^2 R_I}{dt^2} \tag{2.176}$$

The second law of motion of Newton is shown in the equation above. In this case, F_I stands for the instantaneous force exerted on a particle with mass m and a current location R. Another way to describe the force is as a gradient of potential energy:

$$F_I = \nabla_I U(R_1, R_2, ...R_N) = \frac{\partial U(R_1 R_2, ...R_N)}{\partial R_I} \tag{2.177}$$

U is the system's potential energy. Eq. 2.176 and Eq. 2.177 together give us:

$$\frac{\partial U(R_1 R_2, ...R_N)}{\partial R_I} = m_I a_I \tag{2.178}$$

Standard numerical integration techniques are used to determine the particle's location and velocity.

$$\upsilon_I(t) = \frac{1}{m_I} \int \frac{\partial U(R_1, R_2, ...R_N)}{\partial R_I} dt + \upsilon_0 \tag{2.179}$$

$$R_I(t) = \int \upsilon_i(t) dt + R_0 \tag{2.180}$$

The starting velocities and positions of the particle are shown here by υ_0 and R_0, respectively. The gradient of the interatomic potential may readily be used to estimate the track of particles at each time step if the system's starting state is known. Usually, the molecular structure is used to determine the starting locations of the particles. While the distribution of velocities is often derived from the distribution functions, such as the Gaussian or Boltzmann distribution functions, that define the velocity of a certain particle at a given temperature. Calculating other transport parameters of the material, such as ion diffusion and system equilibrium, makes use of the particle trajectories at each time step that was thusly collected.

Interatomic potentials: All interactions between the system's particles are governed by the potential energy function $U(R_1, R_2, ...R_N)$. AIMD simulation must have interatomic potentials in order to run. An equation set defining the interatomic potentials makes up a force field. Different empirical and semiempirical force fields, such as CHARMM, Lennard-Jones, Morse, and Born-Mayer, define the interatomic potentials in classical MD. To match the experimental data for a particular system, a set of parameters governing these force fields must be tuned. Accuracy, calculation time, and transferability are only a few of the numerous variables that influence the selection of an appropriate force field. However, the force fields that are now in use may not accurately represent the new complicated systems. The force fields do not exist in a single form. A formulation of potentials that is effective for one system could not produce the intended effects for another system.

2.23.1 *Ab Initio* Molecular Dynamics

Such force fields are unnecessary in simulations of *Ab Initio* molecular dynamics. The electronic structure computations are used to determine the interatomic potentials "on the fly". Newton's equations of motion regulate the motion of particles in this situation in a classical

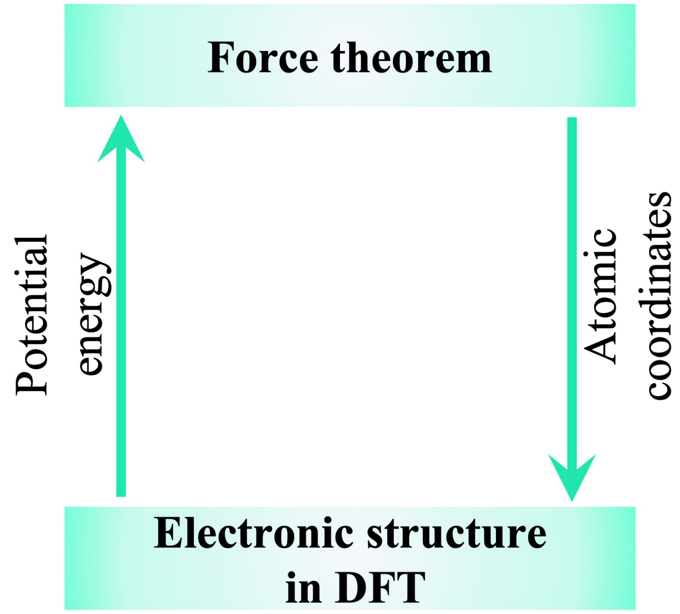

Figure 2.15: Work flow diagram for *ab-initio* molecular dynamics (AIMD).

manner while quantum mechanics is used to determine the interatomic potentials. Consequently, AIMD is one parameter-free method that makes it easier to examine materials for which the formulation of the parameters is not simple. This approach has completely changed theoretical research on novel complex solids. The motion of nuclei and electrons is handled independently in AIMD using the well-known Born Oppenheimer or adiabatic approximation. The nuclei being much heavier than the electrons, are considered classical masses. At each time-step, the nuclei move, whereas the electrons are assumed to be in their stationary ground states. The instantaneous forces on the nuclei are obtained from the Hellmann-Feynman theorem, also called the "force theorem" [73].

$$F_I = -\frac{\partial E}{\partial R_I} \tag{2.181}$$

In this case, F_I stands for the force that a nucleus at point R_I would experience. E represents the system's energy, which is represented by the hamiltonian expectation value.

$$E = \langle \Psi | \hat{H} | \Psi \rangle \tag{2.182}$$

Therefore,

$$F_I = -\left(\langle \frac{d\Psi}{dR_I} | \hat{H} | \Psi \rangle + \langle \Psi | \frac{d\hat{H}}{dR_I} | \Psi \rangle + \langle \Psi | \hat{H} | \frac{d\Psi}{dR_I} \rangle \right) \tag{2.183}$$

The assumption that the electrons are in their ground state is known as the adiabatic approximation. As a result, the electronic wavefunction's differential with regard to the nuclear position is zero. Using Eq. 2.181 and Eq. 2.183, above equation reduced to:

$$F_I = -\langle\Psi|\frac{d\hat{V}_{ext}}{dR_I}|\Psi\rangle - \langle\Psi|\frac{dE_{II}}{dR_I}|\Psi\rangle \tag{2.184}$$

$$F_I = -\int d^3rn(r)\frac{d\hat{V}_{ext}}{dR_I} - \frac{dE_{II}}{dR_I} \tag{2.185}$$

The force theorem is expressed in the aforementioned equation. As a result, neither the kinetic energy nor the exchange correlation functional affect the instantaneous force exerted on the nuclei. It is explicitly determined using the electron ground state density. However, this formulation necessitates that the nuclei move while the electrons stay in their ground state. The nuclei are advanced to the following time step (t → t + Δ t), where the new coordinates for the phase space are determined classically, and the force is calculated at each time step from the aforementioned relation.

2.23.2 Integration algorithms

By integrating the equations of motion with the use of conventional numerical integration techniques, the locations and momenta of the nuclei at time step t + Δ t are determined. These include the velocity-verlet algorithm, the verlet algorithm, and numerous numerical integration techniques like the leapfrog algorithm. The most used technique is the velocity-verlet algorithm. The extension of position and velocity into a series is known as the velocity-verlet technique. The following is how the location and velocity formula is expressed:

$$R\left(t+\Delta\right) = R\left(\left(t\right)\right) + \Delta t v\left(t\right) + \frac{1}{2}\left(\Delta t\right)^2 a\left(t\right) \tag{2.186}$$

$$v\left(t+\Delta\right) = v\left(\left(t\right)\right) + \frac{1}{2}\Delta t\left[a\left(t\right) + a\left(t+\Delta t\right)\right] \tag{2.187}$$

2.23.3 Ensembles

A group of several samples of the same system that are identical in terms of their macroscopic characteristics but may differ in their microscopic states is known as an ensemble. Using ensemble average, it is possible to determine the average of a certain observable as shown below:

$$\langle A\rangle_{enemble} = \int\int \rho\left(r^N, p^N\right) A\left(r^N, p^N\right) dr^N dp^N \tag{2.188}$$

where A denotes the observable and r, p stand for the system's position and momentum, respectively. The probability density, which may be determined using the partition function approach as described below, is represented as $\rho(r^N; p^N)$:

$$\rho\left(r^N, p^N\right) = \frac{exp\left[-H(r^N, p^N)/k_\mathrm{B}T\right]}{\int\int dr^N dp^N exp\left[-H(r^N, p^N)/k_\mathrm{B}T\right]} \tag{2.189}$$

The partition function is represented by the denominator in the equation above. As a result, in order to calculate the ensemble average of a quantity, all system states must be considered.

Ergodic hypothsis

According to the ergodic theory, "a system will pass through all potential states if it is allowed to evolve for a sufficiently enough period". In other words, computing the average over a big ensemble and over a long time is similar. The hypothesis can be described using the following expression:

$$\langle A\rangle_{ensemble} = \langle A\rangle_{time} \tag{2.190}$$

The time average is expressed as follows:

$$\langle A\rangle_{time} = \lim_{\tau\to\infty} \frac{1}{\tau}\int_{t=0}^{\tau} A\left(r^N(t), p^N(t)\right) dt \tag{2.191}$$

The ergodic hypothesis serves as the foundation for the MD simulations. The time restriction must be unlimited in order to comply with the axiom above. Practical simulations, however, are fixed in time. It is therefore typically recommended to sample the phase space as widely as feasible. Microcanonical, canonical, and grand canonical ensembles are various ensemble settings under which MD simulations can be run.

Microcanonical (NVE) ensemble

MD is performed in a microcanonical ensemble where the total number of particles (N), lattice volume (V), and system energy (E) are kept constant throughout the simulation. Here, system remains completely isolated, no heat or matter exchange takes place between the system and the environment.

Canonical (NVT) ensemble

The canonical ensemble has constant thermodynamic parameters for the total number of particles (N), cell volume (V), and temperature (T). Here, a never-ending supply of heat is maintained for the system. Particle exchange is severely constrained, though. Thermostats are used to control the temperature in isothermal MD simulations. Different thermostats use different algorithms to trade energy with the system and maintain a constant temperature. "Velocity scaling", "Langevin's thermostat","Anderson's thermostat", "Berendsen's thermostats", and

"Nose-Hoover thermostats" are a few examples of thermostat algorithms.

Velocity rescaling method: Isokinetic thermostat

A random collection of particle initial velocities is used as the starting point for the velocity-rescaling process. The following equation is then used to scale the values of the velocities that were randomly chosen to the suitable results for the intended temperature:

$$\frac{3}{2}k_{\mathrm{B}}T = \frac{1}{2}M\upsilon^2 \tag{2.192}$$

Where M denotes the particle's mass, k_{B} and T are Boltzmann constat and the preferred temperature, respectively. υ is the speed of the particle.

After a specific number of time steps, the velocities of all the particles are rescaled by multiplying with a factor of $\sqrt{T/T(t)}$, where the current temperature is denoted by $T(t)$. The number of time steps after which the velocities are rescaled determines how far the velocity-rescaling technique may diverge from the classical ensemble conditions.

Velocity rescaling method: Berendsen thermostat

In Berendsen thermostat approach, the temperature is altered by coupling the system with a heat bath maintained at temperature T_0 [74]. The velocities are rescaled by multiplying them with a factor given below:

$$\lambda = \sqrt{1 + \frac{\Delta t}{\tau}\left(\frac{T(t)}{T_0} - 1\right)} \tag{2.193}$$

The instantaneous temperature is $T(t)$, and is the time-step of the MD simulation. τ indicates the coupling constant that controls how well the system and the heat bath are coupled.

Stochastic collision method: Anderson's thermostat

By connecting the system to a heat bath, Anderson's thermostat keeps the temperature at the correct level [75]. Stochastic collisions that take place on the randomly selected particles after a few time steps aid in coupling. One particle experiences a change in momentum with every stochastic contact. The system develops in between the two subsequent collisions in accordance with the customary equations of motion. The probability of a collision occurring between the times t and $t+$ is given by the Poisson's distribution:

$$P(t,\nu) = \nu exp[-\nu t] \tag{2.194}$$

The coupling between the system and the heat bath is determined by the frequency of collisions, which is represented by ν. One particle is affected by each collision at a time, and the Boltzmann distribution is used to calculate this particle's new momentum value. At the point of impact, the particle's change in momentum is added to the equations of motion; at all other moments, the equations of motion are solved normally for all the particles.

Extended system method: Nose-Hoover thermostat

The system is connected to a heat bath where an additional degree of freedom corresponding to the heat bath is added to the real equations of motion in the extended system technique to preserve the canonical ensemble in an MD simulation [76, 77]. It is believed that the additional degree of freedom, S, has a mass called "Q". The variables are scaled in accordance with the following relations in the expanded phase space:

$d\tilde{t} = dt/S$;

$\tilde{q} = q$;

$\tilde{p} = p/S$;

$\dot{\tilde{q}} = S\dot{q}$;

$\dot{\tilde{p}} = \dot{p}$

The coordinates of phase space in the actual system are represented here by q and p. The extended system coordinates are indicated by the symbols $\tilde{q}$ and $\tilde{p}$. The expression for the Lagrangian in the extended system is as follows:

$$L_{ext} = \sum_{I}^{N} \frac{1}{2} M_I \tilde{\dot{q}}_I^2 - U(\tilde{q}) + \frac{1}{2} Q \dot{S}^2 - g k_{textrmB} T \ln S \tag{2.195}$$

which results:

$$L_{ext} = \sum_{I}^{N} \frac{1}{2} M_I S^2 \dot{q}_I^2 - U(q) \frac{1}{2} Q \dot{S}^2 - g k_{textrmB} T \ln S \tag{2.196}$$

The first component in this equation is the kinetic energy of the particles, the second term is the potential energy, and the third and fourth terms, respectively, are the kinetic energy and potential energy of the extra entity S. The g, is one more than the typical degree of freedom for the actual system. The extended system behaves in a canonical manner attributed to the logarithmic term in the potential energy.

The extended system's hamiltonian is expressed as follows:

$$H_{ext} = \sum_{I}^{N} \frac{p_I^2}{2 M_I S^2} + U(q) + \frac{p_S^2}{2Q} + g k_{\mathrm{B}} T \mathrm{In} S \tag{2.197}$$

where, p_S denotes the momentum related to S.

The system develops according to the following equations of motion:

$$\frac{dq_I}{dt} = \frac{\partial H_{ext}}{\partial p_I} \tag{2.198}$$

$$\frac{dp_I}{dt} = -\frac{\partial H_{ext}}{\partial q_I} \tag{2.199}$$

$$\frac{dS}{dt} = \frac{\partial H_{ext}}{\partial p_S} \tag{2.200}$$

$$\frac{dp_S}{dt} = -\frac{\partial H_{ext}}{\partial S} \tag{2.201}$$

Grandcanonical (μ,V,T) ensemble

Grandcanonical ensemble refers to a system with constant chemical potential (μ), cell volume (V), and temperature (T). The system is connected to an internal heat source in this instance, allowing for the flow of both heat and matter.

CHAPTER 3

Role of defects in modulating the ionic-diffusivity in solid state electrolytes for battery materials

3.1 Introduction

Advanced energy materials have become a burgeoning field of research to meet the growing energy demand of 21^{st} century [78, 79]. Therefore, for the sustainable development of human society, cheap, clean, compact and renewable sources of energy are required [80, 81, 82]. The large scale use of renewable energy resources is attributable to the importance of energy conversion and storage. Rapidly increasing energy demands worldwide arouse intensive efforts to explore novel energy storage technologies to meet the developing social needs. Insight into this, Li-ion batteries have powered the revolution in moveable electronic devices and led to their adoption in modern technologies due to high energy density and long cycle life [83, 84, 85, 86, 87]. Unfortunately, serious safety concerns still exist due to their use of flammable organic solvent electrolytes [88]. Moreover, currently the conventional lithium intercalation-based battery almost reaches its limit and there seems to be no further room for improvement [89, 90, 91]. Solid-state battery (SSB) technology is expected to be an alternative to Li-ion batteries [92, 93, 94, 95, 96]. The former is believed to be safer, capable of delivering higher energy density, faster recharging, higher voltage capability and longer cycle life. Nevertheless, despite significant experimental research initiatives taken by leading commercial companies, presently they are expensive and obscure [97, 98, 99, 100, 101]. However, SSBs with inorganic solid-state electrolytes have the potential to drastically improve safety and performance of progressive battery technology alongside of simple fabrication [102, 103, 104, 105, 106, 107, 108, 109, 110].

Various structural families for e.g., LISICON [111, 112], garnet [113, 114], NASICON [115, 116, 117, 118, 119], perovskite-type [120] and thio-LISICON are explored to acknowledge prospective ion-conducting solid-state electrolytes. Among these structural families, sulfide-based compositions $\mathrm{Li_{10}GeP_2S_{12}}$ [121, 122], $\mathrm{Li_7P_3S_{11}}$ [123, 124] and $\mathrm{Li_{3.25}Ge_{0.25}P_{0.75}S_4}$ [125, 126, 127, 128, 129] have been already widely reported in the literature owing to the high ionic conductivities. However, they operate in restricted voltage windows, chemically unstable, and possess hydroscopic nature [130, 131]. Though oxide-based electrolytes do not exhibit high ionic conductivity like sulfide-based, they are chemically stable and straightforward to manufacture. The $\mathrm{Li_4SiO_4}$ manifests a LISICON-type structure, that has been widely studied and identified as potential solid electrolyte [132, 133]. It has been considered that ionic conductivity can be enhanced by few orders of magnitude for compositions $\mathrm{Li}_{4-x}\mathrm{Si}_{1-x}\mathrm{P}_x\mathrm{O}_4$ as compared to the pristine $\mathrm{Li_4SiO_4}$ [134, 135, 136, 137, 138]. It has been also mentioned that Li-ion vacancy and doping facilitate high ionic conductivity in such materials [136, 139]. However, any theoretical reports at the level of atomic-scale understanding, for the local structural and thermodynamic stability of some of the point defects in pristine $\mathrm{Li_4SiO_4}$, are hitherto unknown. It is, therefore, important to provide theoretical guidance to experiment and technology for this immensely promising sustainable energy material.

In this article, we have studied ionic diffusion and it's correlation with dopants/defects in a promising SSB material viz. LISICON [136, 137]. As a first step, using density functional theory (DFT) [140], we compute the formation energies of different defects in LISICON to determine the thermodynamically stable configurations. Our results reveal that the defects which maintain the charge neutrality are the most stable ones. Following this, we have performed *ab initio* molecular dynamics (AIMD) simulation on (meta)stable (un)doped systems to study the diffusion and ionic conductivity of Li-ions. On analyzing our AIMD simulation results, to get the insights on synergistic effect of point defects, we have compared the amplitude of vibration, tracer diffusivity, ionic conductivity, jump rate, charge density and activation barrier for both pristine as well as defected systems. Strikingly, we find that the jumps between different planes are not similar, leading to anisotropy in ionic conductivity in LISICON. The interplanar jumps are minimum in bc planes that limits its ionic conductivity in that direction. We also report that the limited jump rate can be enhanced at room temperature explicitly by point defects, viz. Li-vacancy and substitution at Si-sites with different elements e.g. P, Ge, Al.

3.2 Methodology

We have performed the DFT calculations with PAW pseudopotential method [10, 11, 141] as implemented in Vienna *ab initio* simulation package (VASP) [142, 143]. The elemental constituents viz. Li, O, Si, P, Al and Ge pseudopotentials contain one, six, four, five, three and four valence electrons, respectively. Li_4SiO_4 is a monoclinic structure having space group $P2_1$/m. It comprises of 126 atoms (14 formula unit) in the unit cell i.e., $Li_{56}Si_{14}O_{56}$. The lattice parameters (a = 11.546 Å, b = 6.090 Å, c = 16.80 Å and β = 99.5^0) are taken from existing experimental results [144]. The generalized gradient approximation (GGA) has been performed with the Perdew-Burke-Ernzerhof (PBE) [145] exchange-correlation (ϵ_{xc}) functional. We have cross-checked and validated our results with advanced hybrid functional HSE06 [146], wherever is applicable. In all the calculations, electronic self-consistency has been attained with energy tolerance of 10^{-5} eV. For high precision calculations, we have used cutoff energy of 600 eV for plane-wave basis set. For obtaining the optimized ground state structure, Hellman-Feynman forces have been converged with limit of 0.005 eV/Å by conjugate gradient (CG) minimization [147]. The k-point mesh has been generated by the Monkhorst-Pack [41] method. Here, all the structures are fully relaxed with k-mesh $2\times2\times2$, whereas for single-point energy calculation we have done all the calculations with k-mesh $5\times5\times5$. For AIMD calculations, we have used the NVT ensemble, and the Nose-Hoover thermostat is used for our calculations [148]. We have performed the simulation with a unit cell containing 126 atoms, where the number of particles and volume are kept fixed with periodic boundary conditions imposed along three directions. For all AIMD simulations, time step of 2 fs has been used. To ensure that the system converges to thermal equilibrium states, a maximum time duration of 30 ps for each run has been performed. Note that due absence of suitable classical force field (especially to address PO_4 system well), it's not possible to perform very long MD simulation of the order of nanoseconds to estimate properties accurately at the classical forcefield level. This is one of the main reasons of doing everything at the level of AIMD approach under the framework of DFT. However, within DFT, it is rather challenging to converge 30 ps long AIMD simulation run for a supercell size of 100+ atoms. Therefore, we have carefully validated that 30 ps may be good enough to yield statistically meaningful numbers. Here, in Figure 3.1(a), we have plotted the Gaussian curve fit of the average temperature of Li_4SiO_4 during the AIMD run. Here, three curves correspond to three AIMD runs for which total time periods are 30 ps, 40 ps, and 50 ps, respectively at 300 K for Li_4SiO_4. To avoid the temperature fluctuations which occur in the initial time steps of the AIMD run in all the three cases, we have ignored the data of temperature corresponding to the initial time steps i.e., up to 15 ps. From this Figure, we can find that the attained average temperature is also well converged in all these three AIMD runs viz. 30 ps, 40 ps and 50 ps. we have also computed the jump rate with AIMD simulations of 30 ps, 40 ps and 50 ps. We find that jump rates (for pristine system) are 0.31×10^{13} Hz [30 ps], 0.31×10^{13} Hz [40 ps], and 0.32×10^{13} Hz [50 ps], respectively. Since with 40 and 50 ps AIMD runs, we get well converged numbers (as comparable with 30 ps AIMD run) and in addition to this, the trend is very well in agreement with experiments, we believe this is sufficient to assume that within *ab initio* MD, 30 ps is sufficiently long. From AIMD simulation, we have determined the positions of all the atoms at each time step. Following this, the absolute displacement at each time step is determined.

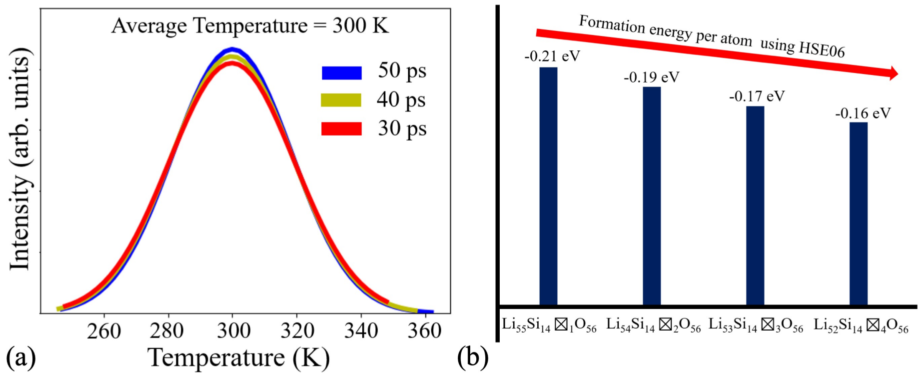

Figure 3.1: (a) Gaussian curve fit of the average temperature of Li_4SiO_4 during AIMD run of time period 30 ps, 40 ps and 50 ps, respectively at 300 K. (b) Formation energy per atom (E_f), with increase in Li-☒ in $Li_{56}Si_{14}O_{56}$, using HSE06 functional.

3.3 Results and Discussions

3.3.1 Formation energy of defects

As a first step, formation energy (E_f) of different defects (i.e., P-substitution and Si-☒/Li-☒ in 126-atom unit cell) in Li_4SiO_4 is calculated from the total energies of their precursor materials viz. Li_2O, SiO_2, P_2O_5 and O_2 using following expressions [149, 150]:

$$\begin{aligned}\mathrm{E}_f(\mathrm{Li}_{56-x-y}\mathrm{Si}_{14}\mathrm{P}_y \boxtimes_x \mathrm{O}_{56}) &= \mathrm{E}(\mathrm{Li}_{56-x-y}\mathrm{Si}_{14} \boxtimes_x \mathrm{P}_y\mathrm{O}_{56}) - 14\mathrm{E}(\mathrm{SiO}_2)\\ &-\frac{y}{2}\mathrm{E}(\mathrm{P}_2\mathrm{O}_5) + \left(y - \frac{x}{4}\right)\mathrm{E}(\mathrm{O}_2) - \left(28 - \frac{x+y}{2}\right)\mathrm{E}(\mathrm{Li}_2\mathrm{O}),\end{aligned} \tag{3.1}$$

$$\begin{aligned}\mathrm{E}_f(\mathrm{Li}_{56}\mathrm{Si}_{14-x-y}\mathrm{P}_y \boxtimes_x \mathrm{O}_{56}) &= \mathrm{E}(\mathrm{Li}_{56}\mathrm{Si}_{14-x-y}\mathrm{P}_y \boxtimes_x \mathrm{O}_{56}) - 28\mathrm{E}\,(\mathrm{Li}_2\mathrm{O})\\ &-\frac{y}{2}\mathrm{E}(\mathrm{P}_2\mathrm{O}_5) + \left(\frac{y-4x}{4}\right)\mathrm{E}(\mathrm{O}_2) - (14 - x - y)\mathrm{E}(\mathrm{SiO}_2),\end{aligned} \tag{3.2}$$

$$\begin{aligned}\mathrm{E}_f(\mathrm{Li}_{56-x}\mathrm{Si}_{14-y-k}\mathrm{P}_y \boxtimes_x \boxtimes_k\mathrm{O}_{56}) &= \mathrm{E}(\mathrm{Li}_{56-x}\mathrm{Si}_{14-y-k}\mathrm{P}_y \boxtimes_x \boxtimes_k\mathrm{O}_{56}) - \left(28 - \frac{x}{2}\right)\mathrm{E}(\mathrm{Li}_2\mathrm{O})\\ &+\left(\frac{y-x}{4} - k\right)\mathrm{E}(\mathrm{O}_2) - (14 - y - k)\mathrm{E}(\mathrm{SiO}_2) - \frac{y}{2}\mathrm{E}(\mathrm{P}_2\mathrm{O}_5).\end{aligned} \tag{3.3}$$

The coefficient of each term on the right hand side of above equations is chosen so that they stoichiometrically balance the number of Li, P, Si and O atoms in $\mathrm{Li}_{56-y-x}\mathrm{P}_y\mathrm{Si}_{14} \boxtimes_x \mathrm{O}_{56}$, $\mathrm{Li}_{56}\mathrm{Si}_{14-y-x}\mathrm{P}_y \boxtimes_x \mathrm{O}_{56}$ and $\mathrm{Li}_{56-x}\mathrm{Si}_{14-y-k}\mathrm{P}_y \boxtimes_x \boxtimes_k\mathrm{O}_{56}$. Here, E donotes the total energy of corresponding compounds.

In Figure 3.2(a), 3.2(b) and 3.2(c), we have plotted the formation energy per atom (E_f) for all possible values of x, y and k. In Figure 3.2(d), we have shown substitution of P at Si site in pristine system. Firstly, to determine the stable configurations as a function of P-substitution in the Li/Si framework, we have adopted an iterative strategy: starting with the pristine $\mathrm{Li}_{56}\mathrm{Si}_{14}\mathrm{O}_{56}$, we have identified the most favorable sites for the P-substitution/Li-⊠ by scanning over all possible framework positions. For the subsequent P-substitution/Li-⊠, we have retained the previous composition and scanned over the rest of the available framework sites. Then, the E_f of the phases (P-substitution and Li-⊠) are calculated using Equation 3.1. From Figure 3.2(a), we have observed that substitution of P at the Li position is less favorable in comparison to Li-⊠. We have also calculated the formation energy per atom for Li-⊠ using HSE06 [151] ϵ_{xc} functional (see Figure 3.1(b)). Here, we have found that stability decreases with increase in Li-⊠, thus similar to the case obtained using PBE ϵ_{xc} functional as shown in Figure 3.2(a). Therefore, one must needs to opt for limited Li-⊠ in order to retaining its stability.

Similarly, we have calculated the E_f for Si-⊠ along with P-substitution as in the aforementioned case using Equation 3.2. From Figure 3.2(b), we have seen that configurations with

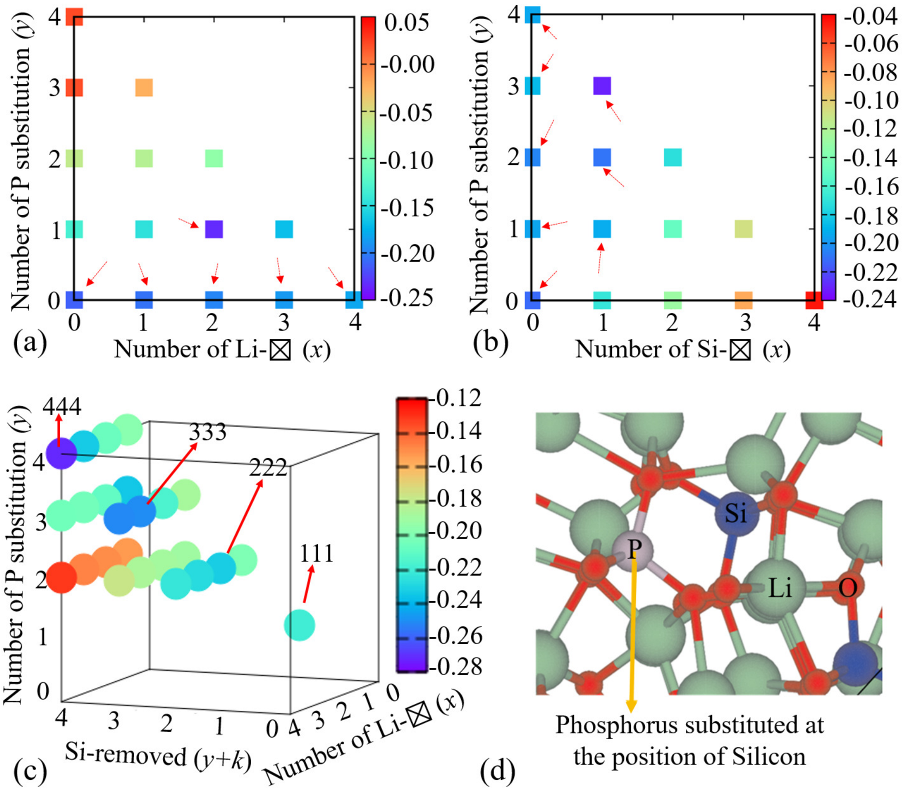

Figure 3.2: Formation energy per atom (E_f) of different structures are represented as a function of (a) P-substitution at Li and Li-⊠ (for $Li_{56-y-x}P_ySi_{14}\boxtimes_x O_{56}$), (b) P-substitution at Si and Si-⊠ (for $Li_{56}Si_{14-y-x}P_y \boxtimes_x O_{56}$) and (c) P-substitution at Si, along with Si-vacancy and Li-⊠ (for $Li_{56-x}Si_{14-y-k}P_y \boxtimes_x \boxtimes_k O_{56}$). The color bar represents E_f in eV. A guide to eye for the configuration with minimum E_f is marked with red arrows. (d) Optimized structure of the system with P-substitution at Si-site.

P-substitution are more stable in comparison to Si-⊠ for our system. However, few configurations containing P-substitution and a single Si-⊠ are also stable. Subsequently, with the identified best compositions in $Li_{56}Si_{14-x-y}P_y \boxtimes_x O_{56}$, we have stepwise removed the Li atoms by scanning over all the framework sites. For creating further Li-⊠, we have retained the vacancy at the already identified position and scanned over the rest of the available framework sites. From Figure 3.2(c), we have concluded that $Li_{56-x}Si_{14-y}P_y \boxtimes_x O_{56}$ (x=y) configurations always have lower E_f and thus, are thermodynamically stable. We have also checked the stability of substitution of Al and Ge at Si sites using aforementioned technique. We find, $Li_{56}Si_{14-x}Ge_xO_{56}$ is stable but $Li_{56}Si_{14-x}Al_xO_{56}$ is not after few Al substitution. But this gets stabilized once Al is substituted simultaneously with P forming $Li_{56}Si_{14-2x}Al_xP_xO_{56}$.

3.3.2 Change in amplitude of vibration with temperature and doping

Next we have carried out AIMD simulation, which provides the position of all the atoms at each time-step that could be used to acquire absolute displacement per time-step. During simulation, we have fixed the parameters: (i) time-step is 2 fs and (ii) ionic iterations are 15000, so that the total time of simulation is 30 ps. The atomic vibration is the vibration of atoms about their mean position. Here, vibration is obtained from the amendment in absolute displacement that can be negative or positive. The amplitude of vibration [152] is outlined as:

$$\mathrm{A} = \mathrm{r_i(t)} - \mathrm{r_i(t-1)}. \tag{3.4}$$

where A corresponds to the amplitude of vibration. $\mathrm{r_i(t)}$ and $\mathrm{r_i(t-1)}$ correspond to the coordinates of atom i at time t and $\mathrm{t}-1$, respectively. Here, we have chosen some identified thermodynamically stable compositions viz. $\mathrm{Li}_{56-x}\mathrm{Si}_{14-y}\mathrm{P}_y \boxtimes_x \mathrm{O}_{56}$, where x and y∈[0,4], for AIMD simulation at different temperatures. In Figure 3.3(a), 3.3(b) and 3.3(c), we have plotted the histogram profile (all the mid points are connected and fitted via gaussian curve fitting) of amplitude of vibration of Li-ions for different configurations ((a) x=0, y=0; (b) x=2, y=2; (c) x=4, y=4) at different temperatures viz. 300 K, 600 K and 900 K. In Figure 3.3(d), we have shown how amplitude of vibration is changing with creation of point defects in the system at a particular temperature (300 K).

In Figure 3.3, full width at half maximum (FWHM) corresponds to standard deviation (SD) of amplitude of vibration of Li-ions. We have observed the broadening in gaussian curves or amplification of SD with increase in temperature for pristine as well as for defected systems (see Figure 3.3(a-c)). Also, we have noticed that amplification of SD is more pronounced for the pristine system as compared to defected system. Moreover, at a particular temperature, there is an amplification in amplitude of vibration or SD on creation of defects (see Figure 3.3(d)). After monitoring Figure 3.3, we have concluded that amplitude of vibrations, which are close to zero are highly intense, whereas broadening occurs due to a very small proportion of vibrations with amplitude greater than 0.5 Å. However, these vibrations result into ionic jumps between different symmetric crystallographic sites, which are described in the following section (Estimation of jump rate).

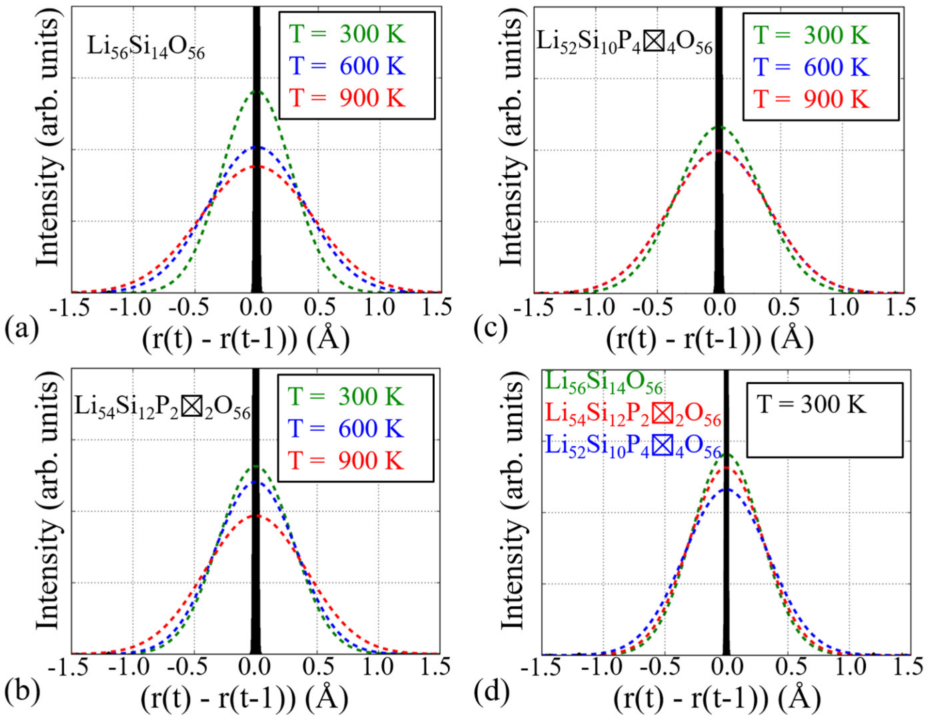

Figure 3.3: Histogram showing the amplitude of vibration of Li-ions at 300 K, 600 K and 900 K in $Li_{56-x}Si_{14-y}P_y \boxtimes_x O_{56}$ for (a) $x = 0$ and $y = 0$, (b) $x = 2$ and $y = 2$ and (c) $x = 4$ and $y = 4$. (d) Histogram of amplitude of vibration of Li-ions in $Li_{56-x}Si_{14-y}P_y \boxtimes_x O_{56}$ at 300 K, where values of x and y are (0, 2, and 4). The colored dotted lines correspond to gaussian curve fitting.

3.3.3 Tracer diffusivity and ionic conductivity

Mean squared displacement has been used to determine the tracer diffusivity (D) [153, 154, 155, 156]. Tracer diffusivity is calculated as follows:

$$D = \frac{1}{2dNt}\sum_{i=1}^{N}([r_i(t+t_0)] - [r_i(t_0)])^2, \tag{3.5}$$

where d=3, which corresponds to dimension for diffusion of atoms in the system. Here, we have ignored the D_{offset} [155]. N corresponds to the total number of diffusing atoms and t corresponds to the total time of AIMD simulation. In Equation 3.5, $r_i(t_0)$ is the position of ith diffusing atom at time t_0 and $r_i(t+t_0)$ is the position after time t. In Figure 3.4(a), we have plotted tracer diffusivity of Li-ions at different temperatures.

We have discerned the beneficial effects that have been reflected in tracer diffusivity of Li-ions in three-dimensional diffusion with change in temperature and creation of point defects.

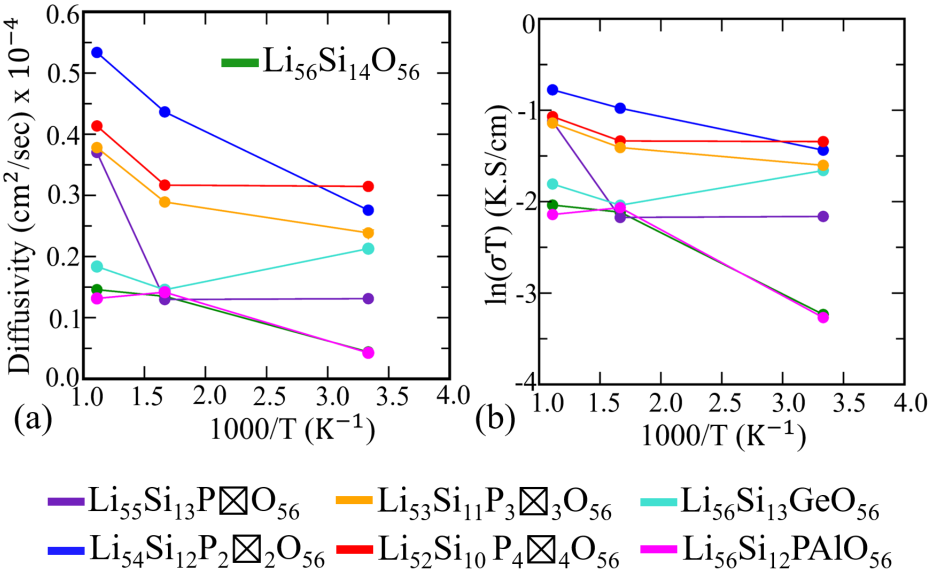

Figure 3.4: Histogram showing the amplitude of vibration of Li-ions at 300 K, 600 K and 900 K in $\mathrm{Li}_{56-x}\mathrm{Si}_{14-y}\mathrm{P}_y \boxtimes_x \mathrm{O}_{56}$ for (a) $x = 0$ and $y = 0$, (b) $x = 2$ and $y = 2$ and (c) $x = 4$ and $y = 4$. (d) Histogram of amplitude of vibration of Li-ions in $\mathrm{Li}_{56-x}\mathrm{Si}_{14-y}\mathrm{P}_y \boxtimes_x \mathrm{O}_{56}$ at 300 K, where values of x and y are (0, 2, and 4). The colored dotted lines correspond to gaussian curve fitting.

Mostly, the diffusivity is increased with increase in temperature. The increment in tracer diffusivity for the defected configuration $\mathrm{Li}_{52}\mathrm{Si}_{10}\mathrm{P}_4 \boxtimes_4 \mathrm{O}_{56}$ is $\sim$ ten times than pristine at ambient temperature. It should be mentioned here that until now, we have not found any prior experimental studies, where a similar percentage of doping or point defects in the host is available. There are few reports where people have done heavy doping [136, 139] [i.e. kind of alloying] and have shown increment in ionic conductivity in a similar system (with doping). Yet the reason behind such behavior of material with doping was not clear. Because of this, to have a better insight, we have tried to report the fundamental role of doping and point defects in this system. Note that on purpose, we have restricted ourselves to smaller doping concentration to better understand the reason behind this change in ionic conductivity atomistically. Modelling heavy doping/alloying leads to additional constraints of defect-defect interactions in a supercell and disentangling such interaction is sometimes quite important but challenging to understand the interaction of doping atomistically. However, the qualitative trend of our results for different configurations viz. $\mathrm{Li}_{56-x}\mathrm{Si}_{14-y}\mathrm{P}_y \boxtimes_x \mathrm{O}_{56}$ for different values of x and y are well in agreement to other experimental studies [136, 139].

From AIMD simulation, we can also predict the ionic conductivities of different ions in the systems under consideration. Using Nernst-Einstein relation, conductivity(σ) is expressed as follows:

$$\sigma = \frac{\mathrm{Ne}^2\mathrm{z}^2}{\mathrm{V}k_\mathrm{B}\mathrm{T}}\mathrm{D}. \tag{3.6}$$

Here, we have assumed Heaven ratio [155, 156] is equal to one and N corresponds to number of diffusing atoms. V is the volume of the system. e corresponds to the elementary charge, z is the ionic charge of diffusing atoms under consideration. T is the temperature in kelvin and k_B is the Boltzmann's constant. In Figure 3.4(b), AIMD simulated ionic conductivity of thermodynamically stable configurations viz. $\mathrm{Li}_{56-x}\mathrm{Si}_{14-y}\mathrm{P}_y\boxtimes_x\mathrm{O}_{56}$, $\mathrm{Li}_{56}\mathrm{Si}_{12}\mathrm{PAlO}_{56}$ and $\mathrm{Li}_{56}\mathrm{Si}_{13}\mathrm{GeO}_{56}$ have been plotted in form of ln(σT) as a function of 1000/T. From Figure 3.4(b), we can clearly see that each composition shows non-Arrhenius relationship. The non-Arrhenius behavior of ionic conductivity for Li-ion conductors has been already mentioned in literature [157]. The ionic conductivity is enhanced in defected systems. We have obtained that the ionic conductivity of configurations $\mathrm{Li}_{56-x}\mathrm{Si}_{14-y}\mathrm{P}_y \boxtimes_x \mathrm{O}_{56}$ increases with increasing x and y, where x and $y\in$[0,4] at 300 K. However, on increasing the temperature, the ionic conductivity is decreased due to increase in lattice vibrations that hinder the path of Li-ions. Our calculated values of conductivities given in Table S1 in SI). Note that despite absolute values are different in experiments due to the reason of heavy doping condition as employed in the experiments, qualitative trend of ionic conductivity for different configurations ($\mathrm{Li}_{56-x}\mathrm{Si}_{14-y}\mathrm{P}_y \boxtimes_x \mathrm{O}_{56}$) is quite appreciable and close to the experimental work [158].

3.3.4 Estimation of jump rate

Using AIMD simulation we can detect the transitions occurring between different symmetric crystallographic sites. The transition between two sites that are far apart (more than 1 Å) has been considered as a jump. Mean jump rate (Γ_i) can be provided by counting the number of jumps (J_i) occurring between different types of sites.

$$\Gamma_\mathrm{i} = \frac{\mathrm{J}_\mathrm{i}}{\mathrm{Nt}}, \tag{3.7}$$

where subscript i corresponds to a type of jump, N is the number of diffusing atoms, and t corresponds to the total simulation time of AIMD run.

We have focussed on interplanar jumps occurring in pristine/defected system. Note that these interplanar jumps are different in different planes. In Figure 3.5, we have plotted interplanar jump rate as a function of temperature.

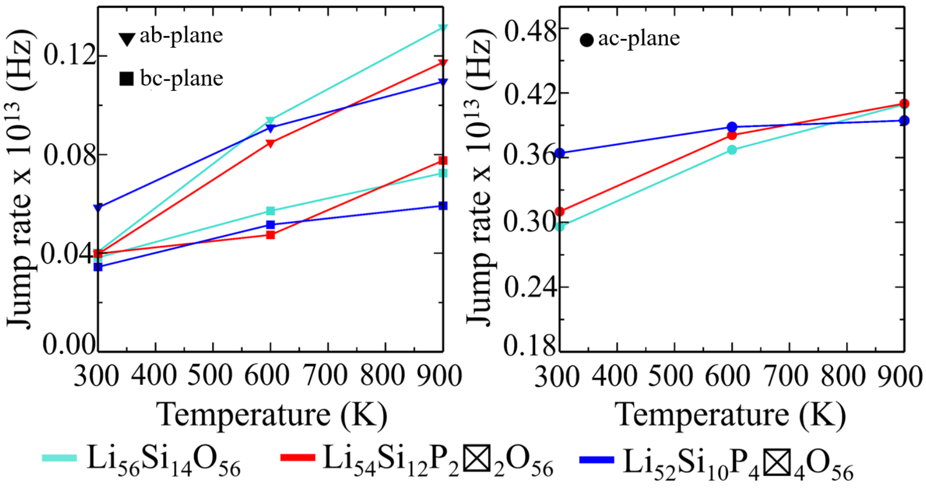

Figure 3.5: Jump rates of pristine and defected systems at different temperatures for different planes.

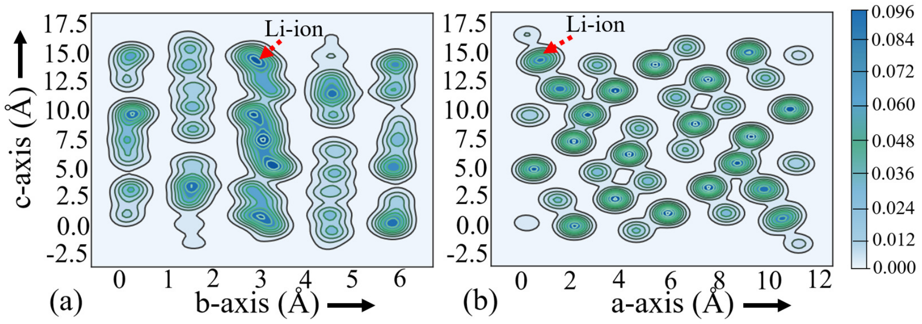

Figure 3.6: Contour density plots of Li-ion diffusion for Li_4SiO_4 in (a) bc-plane (b) ac-plane, at 600 K.

Note that in Figure 3.5, X, Y and Z-axis correspond to lattice vector a, b and c, respectively of unit cell of pristine system. Hence, jumps occurring along X, Y and Z-axis correspond to interplanar jumps in bc, ac and ab planes, respectively. For pristine system, interplanar jump rates are maximum in ac plane (see Figure 3.5), whereas these are surprisingly quite low in bc and ab planes. This anisotropy in jump rate affects the ionic conductivity. To have a better visualization of interplanar jumps due to Li-ion diffusion, we have shown the position of Li-ions during the whole AIMD simulation for Li_4SiO_4 using a contour density plot (see Figure 3.6). In Figure 3.6(a) and (b), we have shown 2D view of Li-ion contour density in bc and ac-plane, respectively. Here, in the contour, blue color corresponds to the maximum density of Li-ion. From Figure 3.6(a), we see that in bc plane the density of Li-ions are restricted in five distinct regions. This behaviour clearly restricts the movements of Li-ions along b-axis. However, in ac plane we have no such restriction for possible interplanar jumps [see Figure 3.6(b)], which helps the faster movement of Li-ions in any direction. This clearly explains the anisotropic nature of the material (in line to our observation as in Figure 3.5).

To validate the anisotropy, the frequency dependent complex dielectric function, $\varepsilon(\omega) = \text{Re}(\varepsilon) + \text{Im}(\varepsilon)$ which constitutes a linear response of the system to the external magnetic field is calculated for pristine system [159]. Kramer-Kroning transformation is used to obtain real part. Imaginary part of dielectric function is attained by calculating the interband matrix elements of the momentum operators. From the real and imaginary part of frequency dependent dielectric function, we have reconfirmed an anisotropy in this system as evident from our AIMD simulation results. The limited jump rates in bc and ab planes may be responsible for low ionic conductivity for the pristine system. However, jump rates are increased with point defects. From Figure 3.5, we can perceive how the jump rates are varying with temperature. We have estimated that alike to amplitude of vibration, jump rate is increased with increase in temperature, but the effect of temperature is less pronounced for defected systems. As we increase the temperature, the system becomes softer and more amorphous in nature. As a matter of fact, at high temperature, the minimum energy (i.e., the activation energy) for Li-ion to jump from one site to another is compensated by some extra thermal energy. This thermal energy results in kinetic energy of Li-ions. Now, the number of Li-ions is more in pristine system, which results in more number of jumps at high temperature as compared to a defected system (see Figure 3.5). However in the defected system, due to presence of Li-vacancies, there are less number of jumps that take place as compared to pristine. Notably, the main motivation of this work is to have enhanced ionic conductivity not at high temperature but at room temperature. It is clearly seen from Figure 3.5 that the jumps, which are occurring along Y-axis (b-lattice vector or in ac plane) are maximum, and minimum along X-axis (a-lattice vector or in bc plane). On applying field (electric field), these jumps can be forced in one direction and restricted in other direction. This anisotropic nature of ionic conductivity is to be kept in mind during application of this material in solid state batteries as an electrolyte.

3.3.5 Polarization and lattice softening

Next, we have tried to understand the underlying reason for the increment in the vibration/jumps, diffusivity and the ionic conductivity with defects at a particular temperature. For that we have compared the charge density plots of pristine and defected system as shown in Figure 3.7(a) and 3.7(b). Herein, we have plotted the surface charge density of 001 plane for pristine unit cell and defected system, respectively. In Figure 3.7(a), all labeled O-atoms are covalently bonded to only Si-atoms, whereas in Figure 3.7(b), a few O-atoms are covalently bonded to P-atoms. Both Si, P are lying just above the given plane. In defected system, we have doped P at Si-sites. On substitution with P, this results in formation of anionic group $[PO_4]^{-3}$ instead of $[SiO_4]^{-4}$. Here, Si and P both are sp^3 hybridized. However, note that P has one extra electron than Si. Therefore on substitution of P at Si site, this additional electron is being shared amongst the

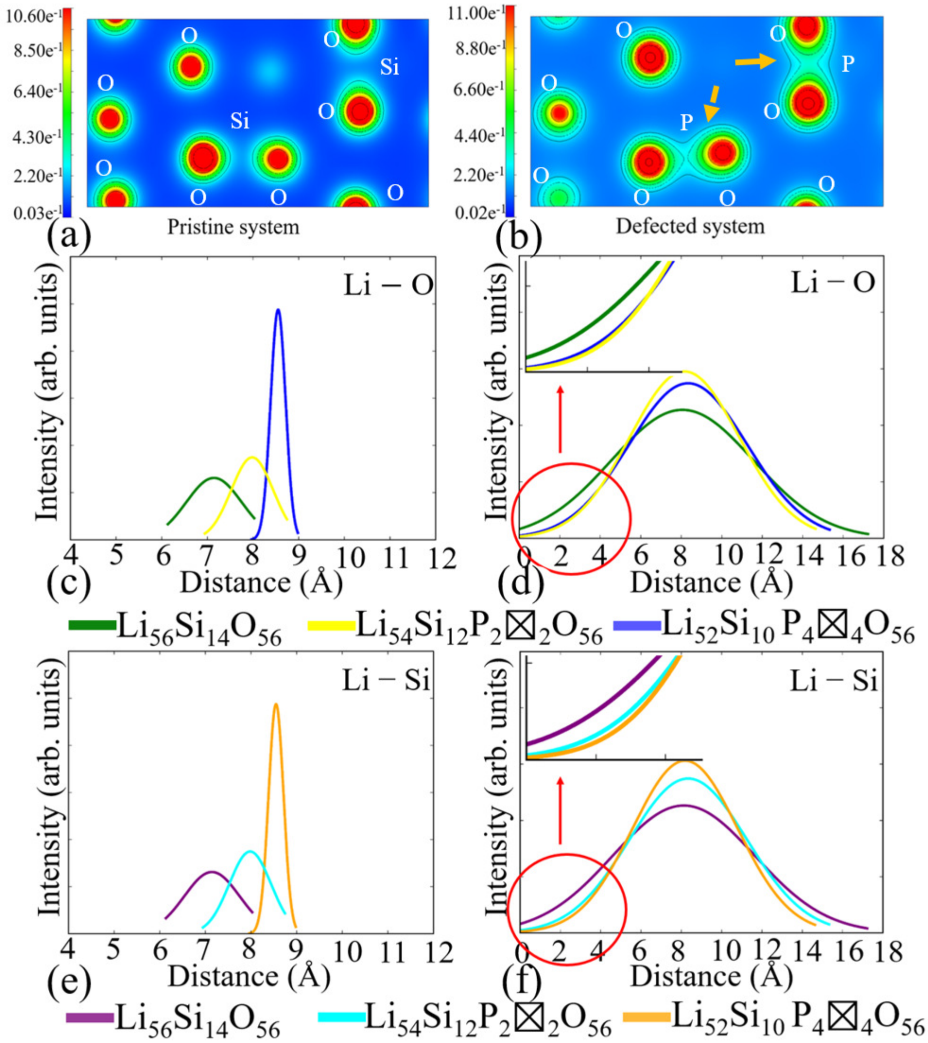

Figure 3.7: Charge density plot for plane with miller indices (001) at a distance 11 Å from origin for (a) $Li_{56}Si_{14}O_{56}$, (b) $Li_{54}Si_{12}P_2 \boxtimes_2 O_{56}$ at 600 K. Note that Si and P labeled atoms in (a) and (b) are lying slightly above the given plane. During whole AIMD simulation at 600 K, radial distribution of (c) single Li w.r.t. all O (d) all Li w.r.t. all O, (e) single Li w.r.t. all Si (f) all Li w.r.t. all Si. Here different color corresponds to three different configurations in $Li_{56-x}Si_{14-y}P_y \boxtimes_x O_{56}$.

unsaturated O-atoms resulting a stronger O-O bonds. Consequently, a change in charge density is observed. It is clearly seen that system with point defect is more polarized (see Figure 3.7(b)). As a consequence of this, the Li-O interaction gets weakened. Thus movement of Li inside the lattice becomes easier on P substitution. As a direct consequence, this helps in Li-ions diffusions with enhanced jump rates. Lattice polarizability is caused due to the doping with larger ions or ions with different valency. Further, to investigate the effect of doping on the bond strength of Li with O/Si, we have plotted the radial distribution of Li with O/Si as shown in Figure 3.7(c-f). In Figure 3.7(c) and 3.7(e), we have plotted the gaussians fit of radial distribution of a common Li-atom w.r.t. all the O-atoms and Si-atoms, respectively at each time-step of AIMD. And in Figure 3.7(d) and 3.7(f) the same is done but with all the Li-atoms w.r.t. all the O-atoms and Si-atoms, respectively at each time-step of the AIMD run. From Figure 3.7(c) and 3.7(e), we can clearly see the shift of gaussian curve towards higher radial distance for defected systems. This reveals the softening of bonds on creation of the defects. Note that, from Figure 3.7(d) and 3.7(f), there is decrease in the intensity of nearest neighbour with defects as shown in the inset (encircled region). It also admits the average increase in radial distance and hence, bond softening on doing doping. Therefore, figure 3.7(c-f), we can see that intensity of the first nearest neighbour of the radial length decreases as we increase the concentration of defects in system. The first nearest neighbour is shifted towards right (i.e. nearest neighbour radial distance is increased) on doping. This is due to the increase in bond strength, i.e., the lattice becomes soft. This decrement in bond strength is attributed to the polarization occurring in the system. When system becomes soft, its activation barrier decreases and jumps among symmetric crystallographic sites increase. Consequently, ionic conductivity also increases with point defects. This is also clear from conductivity plot (see Figure 3.4(b)). Hence, we can clearly see the influence of lattice polarizability on the ionic conductivity, which is well in agreement with previous experimental study [160]. Finally to prove lattice softening with defects, we have varied the volume of unit cell of pristine and defected systems respectively, and the corresponding ground state energies are noted. Such variations in energy of unit cell w.r.t variation of lattice constant (volume) is been plotted in Figure 3.8 for $Li_{56}Si_{14}O_{56}$ and $Li_{54}Si_{12}P_2 \boxtimes_2 O_{56}$ to establish how the system becomes soft with doping. We have observed that curvature (of energy vs lattice vector) is large in defected system. However, due to the small concentration of P, the spread is also very small. Therefore, to have a clear picture, we have shown schematic view of our results in Figure 3.8 (lower panel) and the real simulated

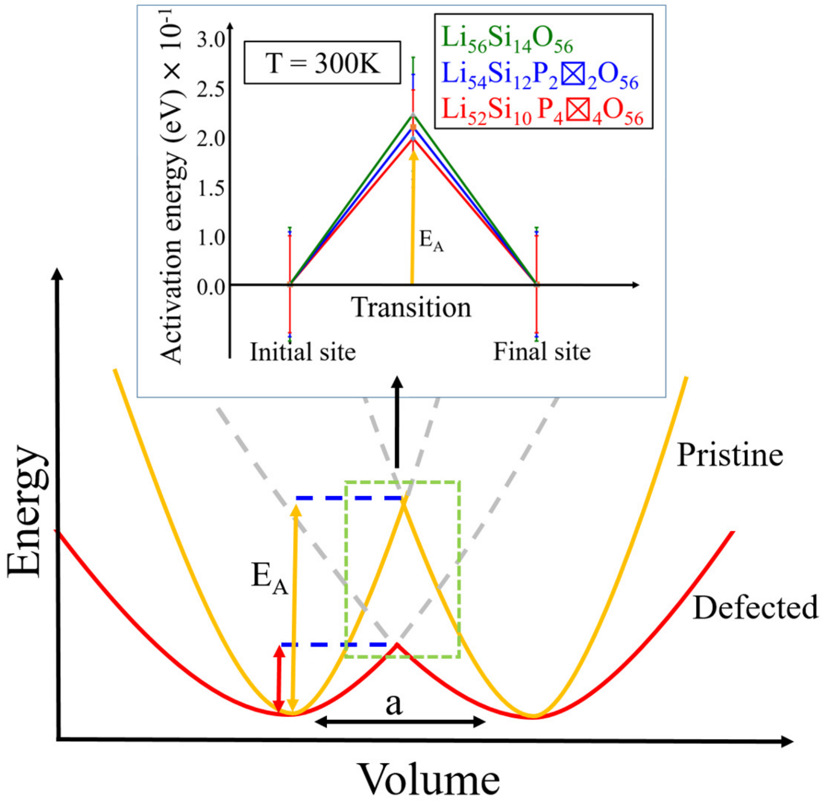

Figure 3.8: Schematic diagram of the effect of lattice softening on activation barrier (lower panel) and simulated one (upper panel). With increasing lattice softness, i.e., with decreasing bond strength, the activation barrier gets reduced for the defected systems.

one in the upper panel. From this schematic plot, one can understand the strategy of computing the activation barrier from two such curves one for pristine and the other for defected one. We can clearly see that system becomes softer after creating point defects and activation barrier decreases. The panel above shows the activation barrier for transition of Li-ion from one site to another. To obtain these activation barriers, first we have calculated average attempt frequency for $Li_{56}Si_{14}O_{56}$, which comes out to be 2.5×10^{12} Hz, whereas "standard value" for such systems is 1×10^{13} Hz. We have found that the activation barrier at 300 K is 0.19 eV, 0.21 eV and 0.23 eV for $Li_{52}Si_{10}P_4 \boxtimes_4 O_{56}$, $Li_{54}Si_{12}P_2 \boxtimes_2 O_{56}$ and $Li_{56}Si_{14}O_{56}$, respectively[1]. These values

---

[1] Note that it may appear to be feasible to compute the the activation barrier via Nudged Elastic Band (NEB) method as well. But in this supercell we have total 56 Li atoms. Therefore, one Li atom has, in principle, plenty of possible sites around to jump giving rise to different values of activation barrier (at different sites). They are assumed to be of similar order of magnitude but still different in numbers and depends on the site of concern. Thus, to get a meaningful average value, one needs to account all possible jumps (via NEB) to all possible sites. Therefore, to avoid those many large NEB jobs, we have computed the activation barrier using AIMD and this is indeed in good agreement with the experimental observation.

are in good agreement with the experiments [136]. This further confirms that doping reduces the activation barrier and consequently the Li ion transport is enhanced. The latter helps in achieving higher conductivity for having application in solid state battery electrolytes.

3.4 Conclusion

In summary, we have used DFT calculations to investigate the thermodynamic stability of point defects in LISICON. We have concluded that $\mathrm{Li}_{56-x}\mathrm{Si}_{14-y}\mathrm{P}_y\boxtimes_x\mathrm{O}_{56}$ (x=y), where x and $y\in[0,4]$ are thermodynamically most stable configurations. The AIMD calculations are performed to get the insights of enhanced ionic conductivity. The diffusion of Li-ions increases with the temperature for pristine as well as for the doped system. We have also shown that on creating point defects (Li-$\boxtimes$, P, Al and Ge substitutional impurities) at a given temperature, the Li-ion diffusion is increased in our system. The jumps (vibrations) of Li-ions are in the order of plane ac $>$ ab $>$ bc, which indicates the anisotropy in our system. Further, the impurities polarize the system, which leads to bond softening and thus, hopping of Li-ions becomes easier due to reduction in activation barrier. Our results reveal that ionic conductivity of LISICON is enhanced on creating various point defects. Specifically, substitution of P at Si with Li-$\boxtimes$ are the most potential candidates to enhance the ionic conductivity.

CHAPTER 4

Bandgap engineering by doing sublattice mixing in double perovskites

4.1 Introduction

Inorganic-organic (IO) hybrid halide perovskites (AM(II)X_3, A = methylammonium (MA^+), formamidinium (FA^+); M(II) = Pb^{2+}; X = Cl^-, Br^-, I^-) have brought a huge revolution in the field of photovoltaics [161, 162, 163, 164, 165]. These alluring materials exhibit high absorption coefficient, long carrier diffusion length, high carrier mobility, low trap density, low manufacturing cost and high defect tolerance [166, 167, 168, 169, 170]. Starting from 3.8%, their power conversion efficiency (PCE) has risen to 22.7% [166, 171, 172] in just a decade. Despite these attainments, the intrinsic instability owing to monovalent organic cation [173] and toxicity of Pb [174] hinder their large scale commercialization. To address these problems, extensive efforts have been paid to find stable and green alternatives for optoelectronic applications. In the recent years, despite large success of IO hybrid perovskites, researchers are getting back to inorganic perovskites as the former suffers from intrinsic stability. It has been reported that the problem of intrinsic instability can be overcome by replacing organic cation with inorganic cation i.e., Cs^+. This not only upgrades the thermal stability but also exceeds device's life span [175, 176]. However, in $CsPbX_3$, toxic nature of Pb is still a big issue and replacement of Pb with some non-toxic element provides a permanent solution. Also, complete replacement of Pb with elements belonging to the same group like Sn and Ge is not suitable due to their tendency of oxidization from +2 state to +4 state [177, 178]. Considering any other divalent cation in place of Pb results in poor optoelectronic properties owing to their large band gap [179, 180]. Alternatively, without varying the total number of valence electrons, two Pb^{2+} cations can be transmuted by one monovalent (M(I)) and one trivalent (M(III)) cation. It leads to a new configuration i.e., $Cs_2M(I)M(III)X_6$ [181, 182, 183], which procures a double perovskite structure. Following this kind of design strategy, a few experimentally reported double perovskites are Cs_2AgBiX_6 [X=Cl, Br, I] [184, 185, 186], Cs_2AgSbX_6 [187, 188], Cs_2AgInX_6 [189, 190] and $Cs_2InM(III)X_6$ [M(III)=Sb, Bi] [191]. However, none of them are ideal for solar cell applications due to the imperfections associated with them. In case of $Cs_2AgM(III)X_6$ [M(III)=Sb,Bi], the large indirect band gap results in poor solar absorption. On the other hand, parity forbidden transition and inevitable conversion of In^{1+} to In^{3+} in Cs_2AgInX_6 [189] and $Cs_2InM(III)X_6$ [M(III)=Sb,Bi] [192], respectively, lead to degradation of photovoltaic performance.

In this article, we present an intensive theoretical study on band gap modification of Cs_2Ag $BiCl_6$ by means of sublattice mixing. The sublattice mixing is done by substituting M(I) at Ag-sites, M(II) at Ag- and Bi-sites simultaneously, and M(III) at Bi-sites in various concentrations for enhancing the optical properties of $Cs_2AgBiCl_6$. A high-throughput screening is performed by carrying out the hierarchical computations employing state-of-the-art first-principles based methodologies under the framework of density functional theory (DFT). We start doing a lot of pre-screening of a large number of configurations with DFT using generalized gradient approximation based exchange-correlation (ϵ_{xc}) functional (PBE [145]) and following that the promising candidate structures are further analyzed using hybrid DFT with HSE06 [193]. The latter ϵ_{xc} functional helps for more accurate understanding of the excited state properties [194]. Note that in all the above calculations (viz. PBE or HSE06), the effect of spin-orbit coupling (SOC) is always taken into consideration. This is a crucial step to determine the accurate band gap and band-edge positions of these systems due to presence of heavy metal atoms. We have started with 64 sets of different combinations of metals M(I), M(II), and M(III), respectively. Firstly, the structural stability is predicted using the Goldschmidt's tolerance factor and octahedral factor. It is worth noting that structural stability alone is not sufficient for the formation of perovskites. Hence, to validate the material's thermodynamic stability, the enthalpy of decomposition per atom (ΔH_D) is calculated. Then, from ΔH_D and band gap range (which expands the spectral response in visible region), the promising stable double perovskite configurations are identified. Following identification of such potential candidate structures, detailed electronic structure is carried out alongside of computing optical properties. The real and imaginary parts of the dielectric function are analyzed to understand the effect of sublattice mixing in $Cs_2AgBiCl_6$ for modification of band gap. Subsequently, we determine spectroscopic limited maximum efficiency (SLME) of all the stable configurations that possess direct band gap, to determine efficient solar cell absorber.

4.2 Methodology

First-principles calculations have been performed using DFT with PAW pseudopotential method [10, 11, 45, 195] as implemented in Vienna *ab initio* simulation package (VASP) [196]. $Cs_2AgBiCl_6$ is a cubic structure having space group *Fm*$\overline{3}$*m* [255] [197]. It comprises of 40 atoms (with 4 formula units) in the unit cell i.e., $Cs_8Ag_4Bi_4Cl_{24}$ and single defect state remains fully localized with periodic boundary conditions. We have used exchange-correlation (ϵ_{xc}) functionals viz. GGA (PBE [145]) and hybrid functional HSE06 [193] with and without SOC for the calculations. The total energy tolerance is set to 0.001 meV. The Hellmann-Feynman forces [147] have been converged upto 0.001 eV/Å by conjugate gradient (CG) minimization to obtain optimized ground state structures. The k-mesh has been generated by the Monkhorst-Pack [41] method. All the structures are fully relaxed with k-mesh $2\times2\times2$. For single-point energy calculation, k-mesh is converged and kept fixed at $5\times5\times5$. Also, to compute dielectric properties k-mesh is converged to $5\times5\times5$ (see Figure 4.1(a-b)). The plane wave energy cut-off is set to 600 eV in our calculations.

4.3 Results and Discussions

4.3.1 Validation of exchange-correlation (ϵ_{xc}) functional for $Cs_2AgBiCl_6$

Initially, the benchmarking of ϵ_{xc} functional has been performed by calculating the band gap of pristine system viz. $Cs_2AgBiCl_6$. The band gap of $Cs_2AgBiCl_6$ with PBE ϵ_{xc} functional is 2.06 eV, which is not in agreement with the experimental value of 2.77 eV [197]. As this system contains heavy metal atom (viz. Bi), the inclusion of SOC becomes important [168]. However, incorporation of SOC with PBE underestimates the band gap (1.68 eV) further due to splitting of the conduction band minimum (CBm). The latter gets shifted to lower energy toward Fermi level, whereas the valence band maximum (VBM) remains unaffected (see Figure 4.1(e)). On the other hand, to include the self-interaction error of a many-electron system in the expression of ϵ_{xc} functional, advanced hybrid ϵ_{xc} functional viz. HSE06 becomes essential [168, 198]. It gives a band gap of 3.15 eV (without SOC, HSE06 only) and 2.60 eV (with SOC, HSE06+SOC), respectively with default (0.25) Hartree-Fock exchange fraction (α) (see Fig-

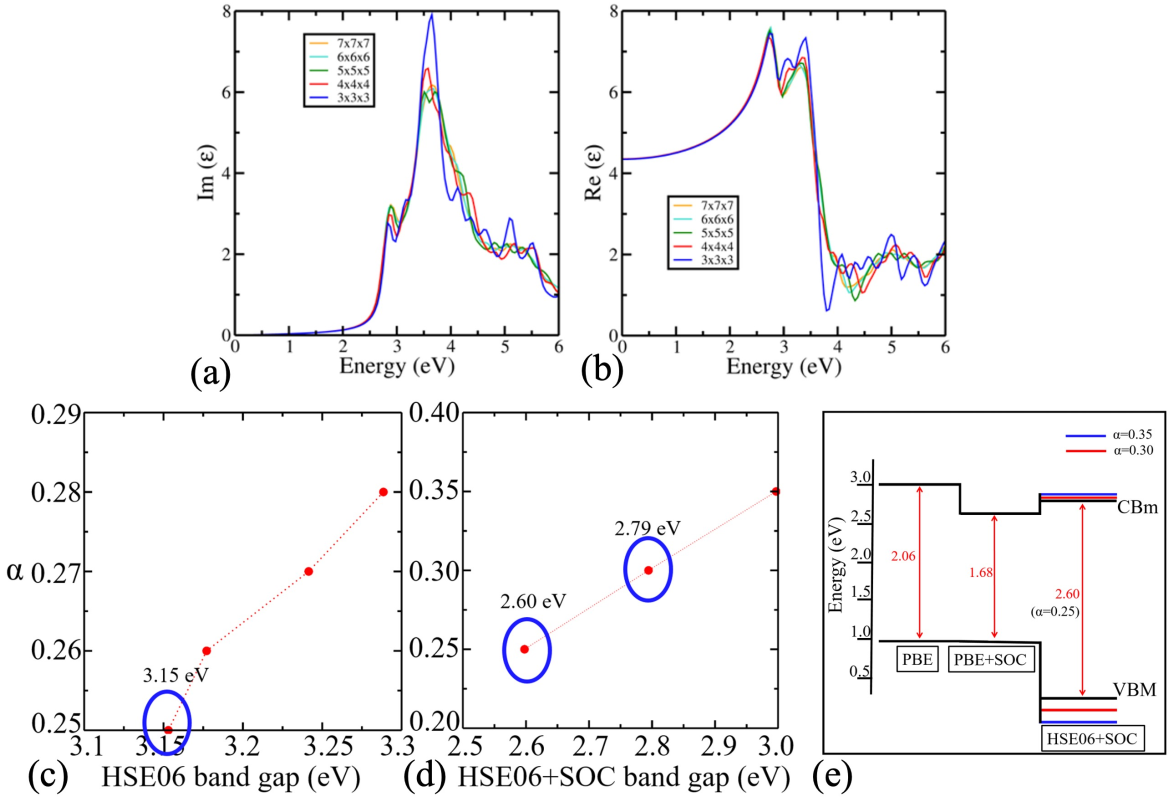

Figure 4.1: Convergence of *k*-mesh for (a) imaginary and (b) real part of dielectric function using PBE ϵ_{xc} functional. Band gap of $Cs_2AgBiCl_6$, using (c) HSE06 and (d) HSE06+SOC ϵ_{xc} functionals with different values of Hartree-Fock exchange fraction (α). (e) Band edge alignment of VBM and CBm with PBE, PBE+SOC and HSE06+SOC.

ure 4.1(c-e)). On increasing α to 0.30 and 0.35, we have obtained band gaps of 2.79 and 2.99 eV, respectively using HSE06+SOC (see Figure 4.1(c-e)). Note that using HSE06+SOC w.r.t the experimental value, though the band gap with α = 0.30 is more accurate than that of default value (i.e. α = 0.25), we still have proceeded with default one for further calculations. This is due to the fact that on alloying with various metals, the value of α can vary from one system to other, and determining the same without experimental results is next to impossible for new configurations. Therefore, we expect, atleast the default α should give a correct trend qualitatively even if the actual numbers may differ marginally as in the case of pristine $Cs_2AgBiCl_6$.

4.3.2 Screening of conformers based on band gap values and stability against decomposition

We have exercised a well-defined iterative strategy [199, 200, 201] to configure different alloyed double perovskites. The conventional cubic unit cell of $Cs_2AgBiCl_6$ consists of 40 atoms

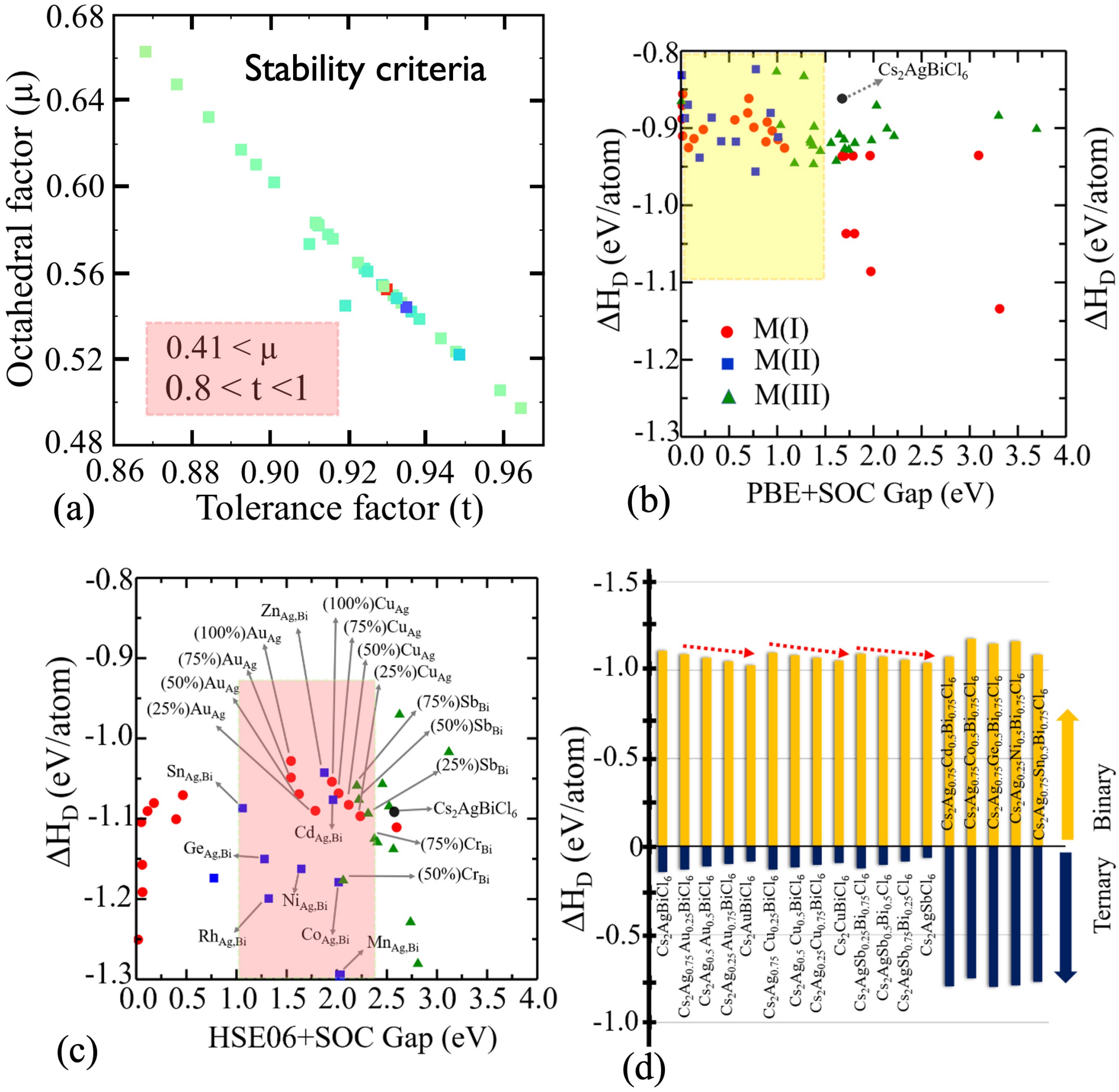

Figure 4.2: (a) Variation of tolerance and octahedral factor for different conformers. Band gap vs ΔH_D using (b) PBE+SOC (Here, the highlighted region shows the promising configurations that lie within the band gap of 0.0 to 1.5 eV) and (c) HSE06+SOC ϵ_{xc} functionals (highlighted region shows the promising configurations that lie within the band gap of 1.0 to 2.3 eV). (Here, red, blue and green color circular dots correspond to M(I) (e.g., substitution of 25% Au at Ag-site ((25%)Au_{Ag})), M(II) (e.g., substitution of Sn at Ag- and Bi-site simultaneously ($Sn_{Ag,Bi}$)) and M(III) (e.g., substitution of 25% Sb at Bi-site ((25%)Sb_{Bi})), respectively) (d) Enthalpy of decomposition for decomposition of pristine and alloyed double perovskites into binary/ternary compounds, using HSE06+SOC ϵ_{xc} functional.

(viz. 8 Cs^{+1}, 4 Ag^{+1}, 4 Bi^{+3} and 24 Cl^{-1}). In order to configure alloyed double perovskites, we have done substitution at Ag- and Bi-sites. Here, Ag, Bi, Cs and Cl occupy 4a (0.5, 0.5, 0.5), 4b (0, 0, 0), 8c (0.25, 0.25, 0.25) and 24e (0.2513(9), 0, 0) Wyckoff sites, respectively. As an initial step, we have checked that all the four sites of Ag and Bi are energetically equivalent. Then for obtaining 25%, 50%, 75% and 100% M(I) substituted configurations, respectively, we have replaced Ag atoms with M(I) one by one in following order i.e., (0.5,0,0), (0,5,0.5,0.5), (0,0.5,0), and (0,0,0.5). Likewise, for 25%, 50%, 75% and 100% M(III) substituted configurations, we have replaced Bi atoms with M(III) one by one in this [(0,0.5,0.5), (0,0,0), (0.5,0,0.5), (0.5,0.5,0)] order. Note that we have checked all possible positions to obtain energetically lowest configuration with 25%/50%/75% substitution of M(I) ion at Ag-site or M(III) ion at Bi-site. However, in our case, after doing 25%/50%/75% substitution, all other sites are found energetically equivalent. For M(II) substitution, there are two possible ways of substitution. We have chosen one of them i.e., we have substituted M(II) at Ag(0.5,0.5,0.5) and Bi(0,0,0) sites. Practicing preceding strategy, we have started with 64 configurations of double perovskites obtained on mixing the Ag-Cl and Bi-Cl sublattices with M(I) (viz. Au, Cu, In, K, Na, and Ti), M(II) (viz. Cd, Co, Cu, Ge, Mn, Mo, Ni, Sn, V, Zn, and Rh), and M(III) (viz. Cr, Ga, In, Tl, Sb, and Y). Here, we have varied the concentration of the alloying atom viz. 25%, 50%, 75% and 100%. Two fundamental factors need to be satisfied for the stability of double perovskites to exist in high symmetry cubic structure, viz. Goldschmidt's tolerance factor (t) [202] and octahedral factor (μ) [203]. For structural stability, t should lie between 0.8 and 1.0, and μ should be greater than 0.41 [204]. To calculate these two fundamental factors for various double perovskite configurations, we have employed a strategy [205]. All the selected double perovskite configurations satisfy these stability criteria (see Figure 4.2(a)). After structural stability, we have also determined the thermodynamic stability by calculating ΔH_D for decomposition of different conformers (obtained after alloying with M(I), M(II), and M(III)) into binary compounds, using following equations:

$$\begin{aligned}\Delta \mathrm{H_D}(\mathrm{M(I)}) = {} & \mathrm{E}\left(\mathrm{Cs_8Ag}_{4-x}\mathrm{M(I)}_x\mathrm{Bi_4Cl_{24}}\right) - (4-x)\,\mathrm{E}\,(\mathrm{AgCl}) - 8\mathrm{E}\,(\mathrm{CsCl}) \\ & - 4\mathrm{E}\,(\mathrm{BiCl_3}) - x\mathrm{E}\,(\mathrm{M(I)Cl})\end{aligned} \tag{4.1}$$

$$\begin{aligned}\Delta \mathrm{H_D}(\mathrm{M(II)}) = {} & \mathrm{E}\,(\mathrm{Cs_8Ag_3M(II)_2Bi_3Cl_{24}}) - 3\mathrm{E}\,(\mathrm{AgCl}) - 8\mathrm{E}\,(\mathrm{CsCl}) \\ & - 3\mathrm{E}\,(\mathrm{BiCl_3}) - 2\mathrm{E}\,(\mathrm{M(II)Cl_2})\end{aligned} \tag{4.2}$$

$$\begin{aligned}\Delta \mathrm{H_D}(\mathrm{M(III)}) = {} & \mathrm{E}\,(\mathrm{Cs_8Ag_4M(III)}_x\mathrm{Bi}_{4-x}\mathrm{Cl_{24}}) - 4\mathrm{E}\,(\mathrm{AgCl}) - 8\mathrm{E}\,(\mathrm{CsCl}) \\ & - (4-x)\,\mathrm{E}\,(\mathrm{BiCl_3}) - x\mathrm{E}\,(\mathrm{M(III)Cl_3})\end{aligned} \tag{4.3}$$

In Equation 4.1 and 4.3, x can have value 1, 2, 3 or 4. Based on the band gap and $\Delta \mathrm{H_D}$ (calculated using PBE+SOC), a pre-screening process has been employed to find the suitable configurations. In Figure 4.2(b), the promising configurations lie within the shaded region for which band gap is varying from 0.0 to 1.5 eV. For all the prescreened configurations of double perovskite, $\Delta \mathrm{H_D}$ is negative, indicating that all the considered systems are stable and these will not decompose into respective binary components. Subsequently, we have calculated $\Delta \mathrm{H_D}$ and band gap using HSE06+SOC ϵ_{xc} functional for aforementioned selected configurations (see Figure 4.2(c)). In Figure 4.2(c), restoring Shockley-Queisser (SQ) criterion [206], we have identified 19 double perovskite configurations for which band gap lies within 1.0 to 2.3 eV, which is relevant for solar cell and other optoelectronic devices. As the path of decomposition into binary compounds is not sufficient in discussing alloy's stability, we have also computed enthalpy of decomposition ($\Delta \mathrm{H_D}$) of these double perovskites into respective ternary compounds. Note that the latter is generally the most prominent decomposition pathway for this class of systems. $\Delta \mathrm{H_D}$ for ternary decomposition is also found to be negative in our case. However, from Figure 4.2(d), we have observed that $\Delta \mathrm{H_D}$ for double perovskites into ternary decomposition is less negative than their corresponding binary decomposition [1]. Hence, ternary decomposition is more probable in these compounds than binary decomposition. From Figure 4.2(d), on comparing $\Delta \mathrm{H_D}$ for decomposition into ternary compounds, we can conclude that ternary decomposition is less probable for M(II) substituted configurations than that of M(I) and M(III) substituted configurations at Ag- and Bi-sites that can be attributed to large negative value of $\Delta \mathrm{H_D}$. Moreover, it has been pinpointed that $\Delta \mathrm{H_D}$ becomes less negative on increasing the percentage of M(I) and M(III) at Ag and Bi, respectively for M(I) and M(III) substituted configurations. Hence, stability decreases from 25% to 100% M(I) and M(III) substitution at Ag- and Bi-sites, respectively (see Figure 4.2(d)).

---

[1] Note that, we have chosen mostly those M(I) and M(III) elements, which have been experimentally/theoretically reported as $\mathrm{Cs_2M(I)M(III)X_6}$ double perovskites. Here, we have studied their partial substitution in addition to 100% substitution. Hence, for M(I) and M(III) partial substitution, there is more probability that $\Delta \mathrm{H_D}$ will be negative. For instance, $\mathrm{Cs_2NaBiCl_6}$ has been synthesized experimentally. So there are high chances that partial substitution of Na at Ag-sites will also form a stable configuration. In our previous theoretical and experimental combined study, we have reported the partial substitution of Na in $\mathrm{Cs_2AgBiCl_6}$ [186]

4.3.3 Inconsistency in the band gap with different percentage of substitution

Note that on increasing the concentration of the external element, if the band gap is increased (or decreased), it increases (or decreases) consistently on further increasing the concentration. However, in some cases, we have noticed an irregular change in band gap on varying the concentration of the alloying atoms. For instance, on increasing the percentage of Sb at Bi-sites, band gap decreases up to 75% substitution, and thereafter, an increment in band gap has been observed on 100% substitution. Similar kind of change in band gap has also been observed on complete substitution of other elements at Ag or Bi-site. To understand this change in the band gap on 100% substitution of Sb, we have plotted the band structures of Sb-alloyed system with different concentrations of Sb (see Figure 4.3). We can clearly see that on 100% substitution of

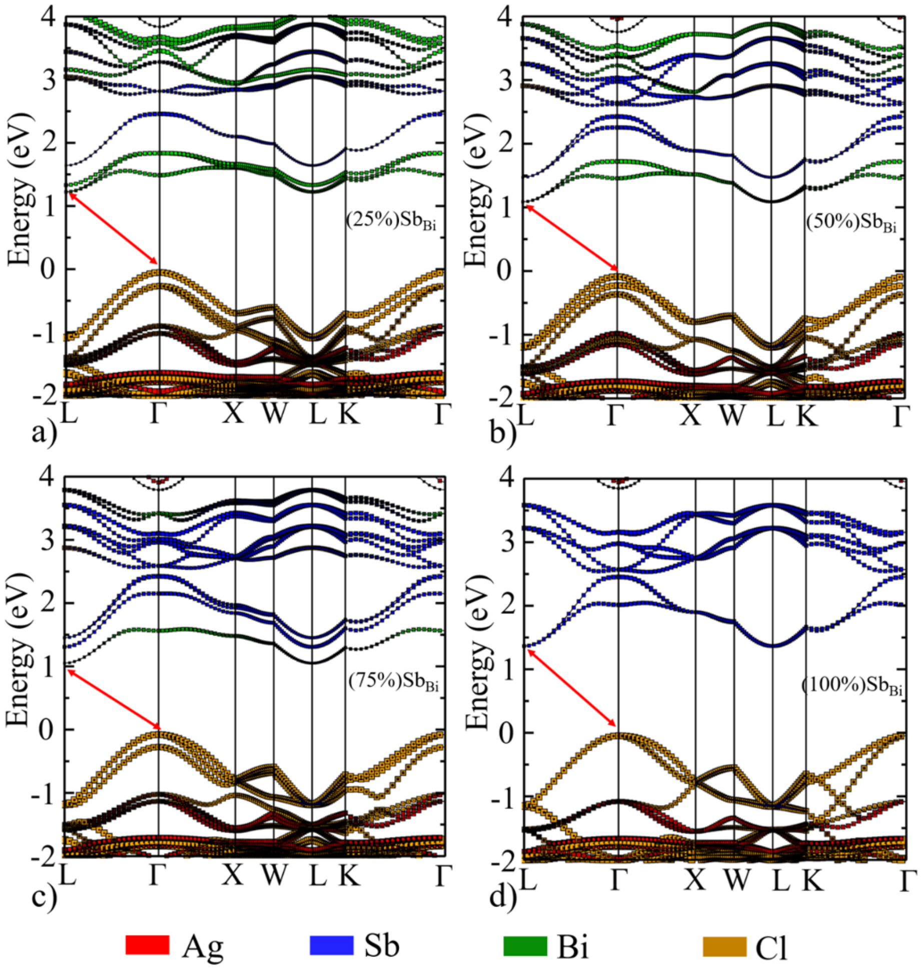

Figure 4.3: Band structure of (a) $Cs_8Ag_4Sb_1Bi_3Cl_{24}$, (b) $Cs_8Ag_4Sb_2Bi_2Cl_{24}$, (c) $Cs_8Ag_4Sb_3Bi_1Cl_{24}$ and (d) $Cs_8Ag_4Sb_4Cl_{24}$ using PBE+SOC ϵ_{xc} functional.

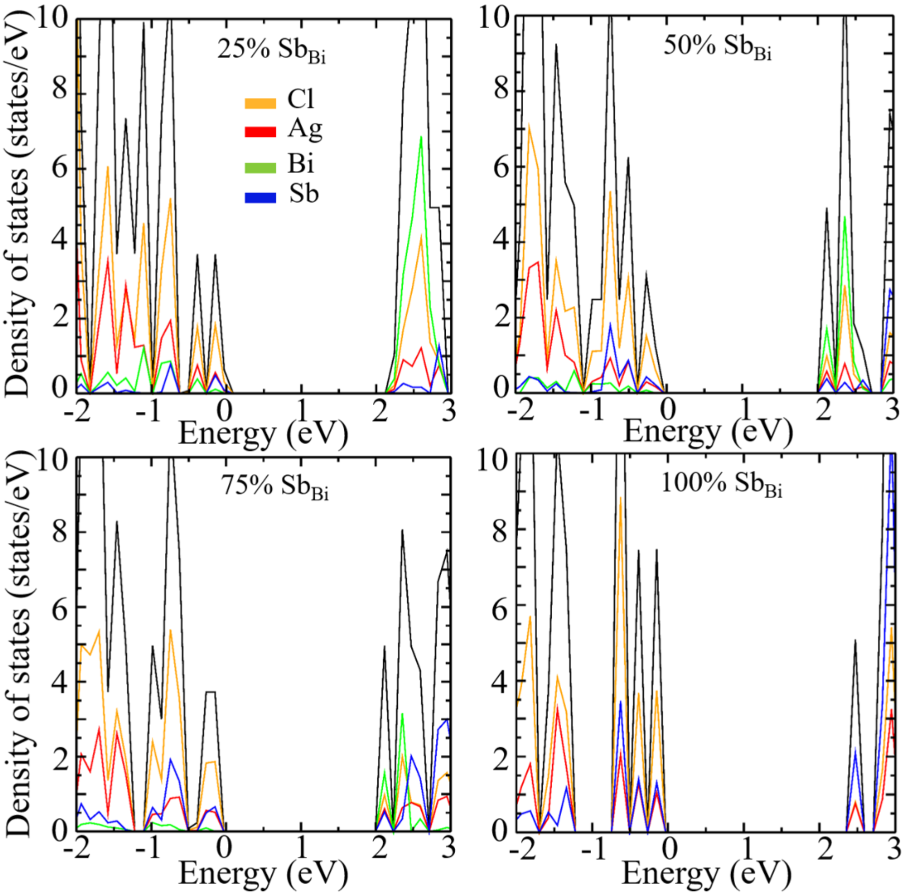

Figure 4.4: Partial density of states (pDOS) for Sb substitution at Bi-sites of $Cs_2AgBiCl_6$, using HSE06+SOC ϵ_{xc} functional. Different color corresponds to different atoms in the system.

Sb at Bi-sites, the lowest energy level (where Bi is the dominating contributor) in the conduction band (that is present in Figure 4.3(a-c)) disappears. Consequently, there is an increment in the band gap (see Figure 4.3(d)). In addition, to have a clear picture, we have plotted partial density of dos (pDOS) for Sb substituted configurations at Bi-sites, using HSE06+SOC (see Figure 4.4). Note that in Figure 4.4, the VBM is set to the zero of energy. However, on Sb substitution both VBM and CBm shift can be inspected clearly from the band edge positions given in Table 4.1. When we substitute one Sb at one of the Bi-sites, the energy difference between Sb-5s and Cl-3p orbitals is less than that of Bi-6s and Cl-3p orbitals. As a result, Sb-5s/Cl-3p antibonding orbital lies above Bi-6s/Cl-3p antibonding orbital and VBM is shifted to higher energy. On the other side, Sb-5p splits into Sb-5p$_{\frac{1}{2}}$ and Sb-5p$_{\frac{3}{2}}$. It should be noted that in case of Sb, splitting of Sb-5p is very small in comparison of Bi-6p splitting into Bi-6p$_{\frac{1}{2}}$ and Bi-6p$_{\frac{3}{2}}$. Bi-6p$_{\frac{1}{2}}$ is of lower energy than Sb-5p. Hence, Bi-6p/Cl-3p antibonding orbital contributes maximum in CBm. When we substitute one Bi with Sb, the lowest conduction band

Table 4.1: Band edge alignment of pristine and alloyed configurations, using HSE06+SOC ϵ_{xc} functional

Conformers	VBM (eV)	CBm (eV)
$Cs_8Ag_4Bi_4Cl_{24}$	0.228	2.826
$Cs_8Ag_4Sb_1Bi_3Cl_{24}$	0.582	2.900
$Cs_8Ag_4Sb_2Bi_2Cl_{24}$	0.714	2.935
$Cs_8Ag_4Sb_3Bi_1Cl_{24}$	0.764	2.964
$Cs_8Ag_4Sb_4Cl_{24}$	0.811	3.382
$Cs_8Ag_3Au_1Bi_4Cl_{24}$	0.678	2.464
$Cs_8Ag_2Au_2Bi_4Cl_{24}$	0.847	2.464
$Cs_8Ag_1Au_3Bi_4Cl_{24}$	0.922	2.466
$Cs_8Au_4Bi_4Cl_{24}$	0.923	2.467

width gets decreased, and CBm is shifted to higher energy level (see Table 4.1). Although both VBM and CBm get shifted to higher energy levels, the shift in VBM is more, which results in a decrease in the band gap. This is why, when we substitute two or three Sb at Bi-sites the overall band gap is decreased (see Figure 4.4 and Table 4.1). However, when we do 100% substitution of Sb at Bi-sites, the spin-orbit coupling (SOC) effect gets diminished, which was there before due to presence of Bi. Therefore, CBm is now shifted more to much higher energy level, where maximum contribution is from Sb-5p and Ag-5s orbitals (see Figure 4.4. We have also plotted electron localized function (ELF) for pristine and Sb substitution (see Figure 4.5). From Figure 4.5, we can see that on complete substitution of Sb, electron density (note the red color that corresponds to more electron density) around Cl and Sb atoms is increased. From our results, mainly Bi element is responsible for SOC effect in $Cs_2AgBiCl_6$. As it has been mentioned by Savory et al. [207] that fundamental mismatch of Ag-d and Bi-s orbitals results in large and indirect band gap. When we do substitution at Ag- or Bi-sites this mismatch decreases as in case of Au/Sb substitution at Ag/Bi-sites. From Figure 4.6, Ag-4d/Cl-3p antibonding orbital is contributing more than Bi-6s/Cl-3p antibonding orbital in VBM. From Figure 4.6, we can see that for $Cs_2AgBiCl_6$ VBM is dominated by Ag-4d and Cl-3p, whereas Bi-6s is contribution is less. Ag-5s/Cl-3p and Bi-6p/Cl-3p antibonding orbital character can be seen in CBm. Moreover, Bi-6p/Cl-3p antibonding orbital is of lower energy (hence more dominating in CBm) than Ag-4d/Cl-3p antibonding orbital. On 25% substitution of Au at Ag, it shifts the CBm to lower

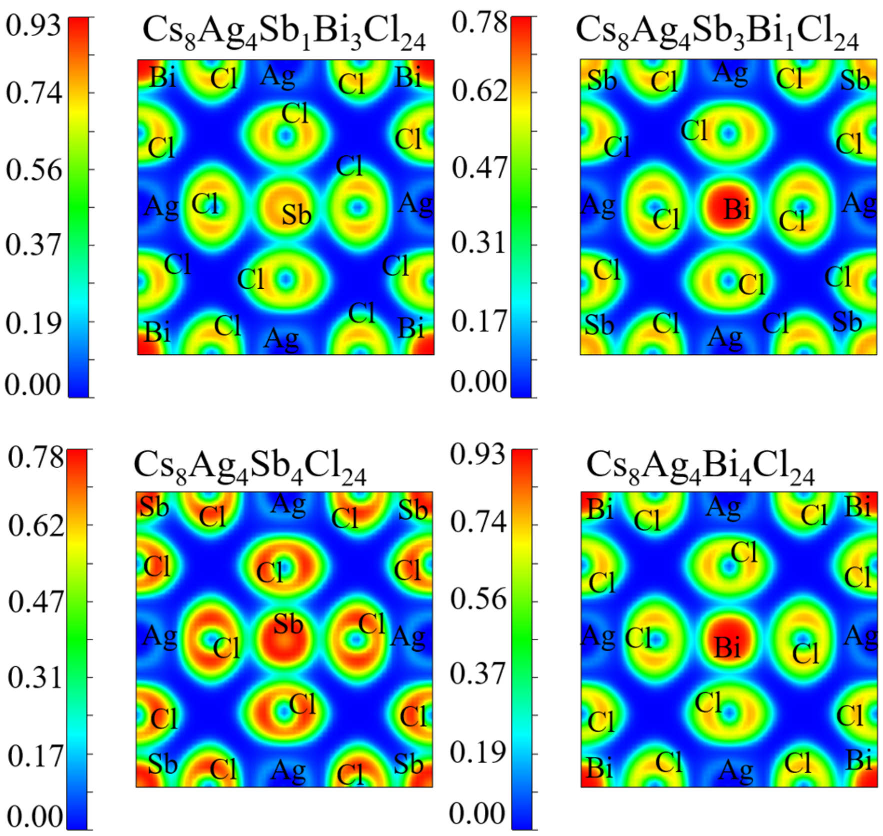

Figure 4.5: Electron localized function (ELF) for $Cs_2AgBiCl_6$ and Sb substituted configurations.

level owing to lower energy of Au-6s/Cl-3p antibonding orbital (see Table 4.1). VBM gets shifted upward due to occurrence of Au-5d/Cl-3p antibonding orbital that lies above Ag-4d/Cl-3p orbital (see Figure 4.6 and Table 4.1). However, on further substitution of Au at Ag-sites. There is no further shift in CBm, only VBM shifts to a more higher level on increasing Au owing to the increase in the width of valence band. On 100% Au substitution, there negligible change in band gap.

We have also observed a sudden increment in the band gap on doing 100% substitution of Na/K at Ag sites. For 25% to 75% substitution of Na/K at Ag reduces the valence band (i.e., due to the combination of Ag-4d and Cl-3p orbitals) width decreases. It is so because Ag-4d/Cl-3p antibonding orbital contributes maximum in VBM. However, on 100% Na/K substitution at Ag-sites totally eliminates this valence band and s-orbital of K/Na does not contribute in VBM. Besides, Cl gets more attracted towards Na/K that can be attributed to their more electropositive character. As a consequence, sudden increase in the band gap can be seen on 100% Na/K substitution at Ag-sites (see section A.1 and A.2 in Appendix). Note, in present work we have pointed few cases. Overall, we can conclude that partial substitution or mixed cations studies could be interesting in these double perovskites apart from complete substitution.

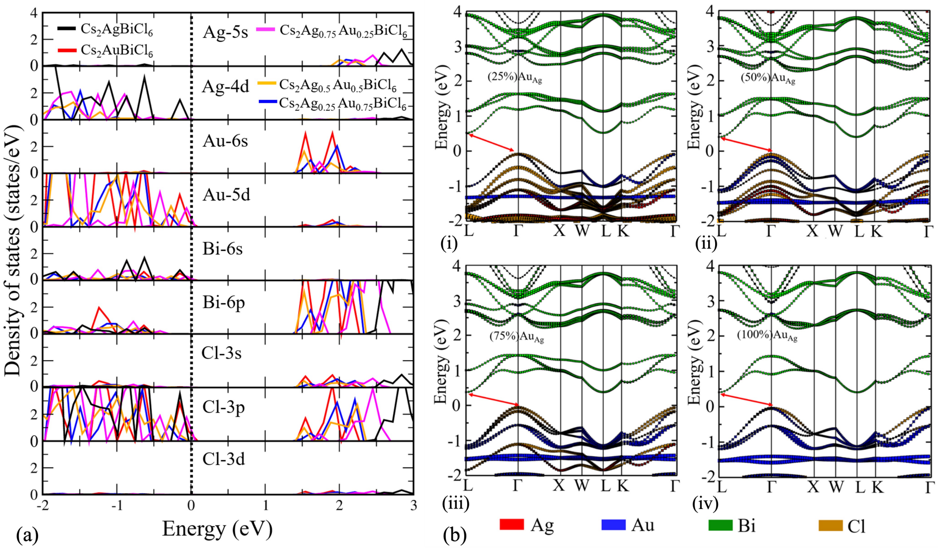

Figure 4.6: (a) Partial density of states (pDOS) of pristine and alloyed $Cs_2AgBiCl_6$ calculated using HSE06+SOC ϵ_{xc} functional. (b) Band structure of (i) $Cs_8Ag_3Au_1Bi_4Cl_{24}$, (ii) $Cs_8Ag_2Au_2Bi_4Cl_{24}$, (iii) $Cs_8Ag_1Au_3Bi_4Cl_{24}$ and (iv) $Cs_8Au_4Bi_4Cl_{24}$, using PBE+SOC ϵ_{xc} functional.

4.3.4 Optical properties of potential conformers

Next, we have determined the optical properties of the 19 potential candidate structures (viz. $Cs_8Ag_{4-x}M(I)_xBi_4Cl_{24}$ (M(I) = Au and Cu); $x \in [1, 4]$), $Cs_8Ag_3M(II)_2Bi_3Cl_{24}$ (M(II = Sn, Ge, Rh, Ni, Co, Cd, Mn and Zn), and $Cs_8Ag_4Sb_xBi_{4-x}Cl_{24}$ ($x \epsilon [1, 3]$), which possess band gap in an appropriate range for solar cell and other optoelectronic applications.[2] To determine optical properties, frequency dependent complex dielectric function, $\varepsilon(\omega)$ = Re(ε) + Im(ε) has been calculated using HSE06+SOC ϵ_{xc} functional as shown in Figure 4.7. Therefore, using Re(ε) and Im(ε) of dielectric function, various optical properties, e.g., refractive index (η), extinction coefficient (κ), and absorption coefficient (α) can be computed using following expressions:

$$\eta = \frac{1}{\sqrt{2}}\left[\sqrt{\mathrm{Re}(\varepsilon)^2 + \mathrm{Im}(\varepsilon)^2} + \mathrm{Re}(\varepsilon)\right]^{\frac{1}{2}} \tag{4.4}$$

---

[2] It may happen that at higher temperatures, different configurations can undergo phase transition, however, no drastic change in the band gap has been observed as we go from cubic to tetragonal or orthorhombic phases [208]. Hence, we conclude that even if the phase deviates from cubic symmetry, it will not affect the optical properties at large scale. The qualitative trend of optical properties will remain same.

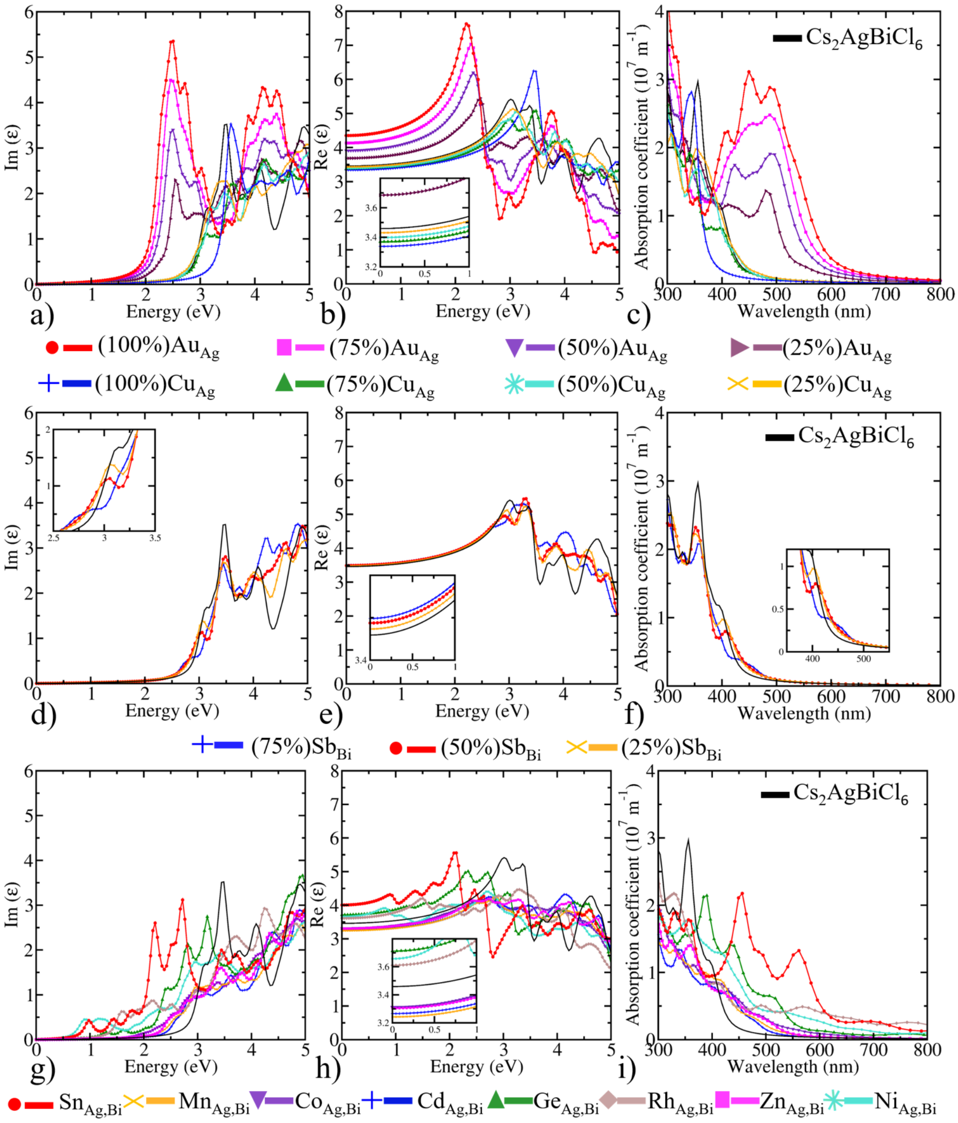

Figure 4.7: Variation of imaginary part of dielectric constant (Im(ε)) of $Cs_2AgBiCl_6$ sublattice mixed with (a) monovalent (M(I)), (d) divalent (M(II)) and (g) trivalent (M(III)) cations, respectively. Variation of real part of dielectric constant (Re(ε)) of $Cs_2AgBiCl_6$ sublattice mixed with (b) monovalent (M(I)), (e) divalent (M(II)) and (h) trivalent (M(III)) cations, respectively. Absorption coefficient of $Cs_2AgBiCl_6$ sublattice mixed with (c) monovalent (M(I)), (f) divalent (M(II)) and (i) trivalent (M(III)) cations, respectively. Note that all calculations have been done using HSE06+SOC ϵ_{xc} functional.

$$\kappa = \frac{1}{\sqrt{2}}\left[\sqrt{\text{Re}(\varepsilon)^2 + \text{Im}(\varepsilon)^2} - \text{Re}(\varepsilon)\right]^{\frac{1}{2}} \tag{4.5}$$

$$\alpha = \frac{2\omega\kappa}{c} \tag{4.6}$$

Here, in Equation 4.6, ω and c correspond to angular frequency and speed of light, respectively. In Figure 4.7(a), peaks of conformers are red shifted w.r.t. $Cs_2AgBiCl_6$. Here, red shift is attributed to the reduction of the band gap. There is more red shift on increasing the concentration of Au in comparison to Cu. On the other hand, the real part of the dielectric constant ($\omega = 0$) increases, with increase in the concentration of Au and decreases, with increase in the concentration of Cu (see Figure 4.7(b)). For high degree of charge screening, which can prohibit radiative electron-hole recombination, a large value of Re(ω) at $\omega = 0$ is indispensable [159]. Hence, the solar cell absorber, which exhibits large Re(ω) at $\omega = 0$ is more efficient. In view of this, Au substitution is more beneficial than Cu for replacing Ag-sites.

In Figure 4.7(c), we can clearly see that peaks corresponding to Au substitution are red shifted w.r.t. $Cs_2AgBiCl_6$ and show good optical absorption within visible region. Hence, we have discerned that in case of alloying with M(I), substitution of Au at Ag-sites acts as a promising candidate rather than Cu. Likewise, in case of alloying with M(III), substitution with Sb at Bi-sites acts as a promising candidate. From Figure 4.7(d), the red shift w.r.t. pristine (see inset to have a clear view) conveys that band gap decreases on increasing the concentration of Sb. However, for 100% Sb_{Bi}, band gap increases, which can be seen from band structure (see Figure 4.3(d)). From Figure 4.7(e) and 4.7(f), we can see that optical properties are enhanced on increasing the concentration of Sb (upto 75%) w.r.t. pristine. Similarly, in case of alloying with M(II), from Figure 4.7(g) and 4.7(i), there is a red shift of absorption peak w.r.t. $Cs_2AgBiCl_6$. Moreover, static value of Re(ω) at $\omega = 0$ for $Sn_{Ag,Bi}$, $Rh_{Ag,Bi}$, $Ni_{Ag,Bi}$ and $Ge_{Ag,Bi}$ is larger than pristine system; but for other alloyed systems (viz. $Zn_{Ag,Bi}$, $Co_{Ag,Bi}$, and $Mn_{Ag,Bi}$), it is lower than pristine system (see Figure 4.7(h)). Out of all the M(II) selected candidates, these four (viz. Sn, Rh, Ni and Ge) are the best aspirants. Although, only $Sn_{Ag,Bi}$ and $Ge_{Ag,Bi}$ show direct band gap, the other two are to be more suitable for optoelectronic devices excluding solar cell. On the other hand, since Sn is cheaper than Ge, it serves as better candidate for alloying. It has been reported that complete substitution of Sn degrades the properties of the system [177, 178]. Therefore, in order to overcome this problem, we have done partial substitution of Sn. Also, from Figure 4.7, we can compare the scales (viz. values of dielectric constants and peaks of absorption coefficient in visible region) and infer that alloying with M(II) is a better choice to enhance the optical properties.

On comparing all the above results in Figure 4.2 and 4.7, we have revealed that partial Sn substitution acts as a promising candidate to enhance the optical properties of $Cs_2AgBiCl_6$ without degrading the stability. In addition, it also exhibits direct band gap property. Thus $Sn_{Ag,Bi}$ acts as a rational candidate for solar cell application.

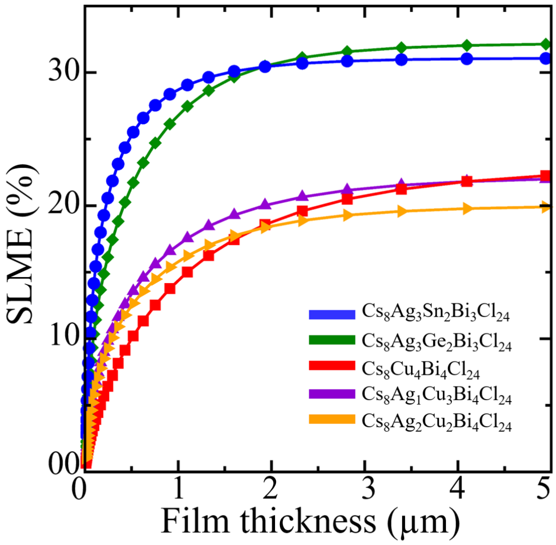

Figure 4.8: Variation of SLME w.r.t. the thickness of solar cell absorber.

4.3.5 Spectroscopic limited maximum efficiency (SLME)

Lastly, to design highly efficient solar cell absorber, spectroscopic limited maximum efficiency (SLME) [204, 210] has been calculated. Solar cell power conversion efficiency η is defined as follows:

$$\eta = \frac{P_m}{P_{in}} \tag{4.7}$$

where, P_{in} corresponds to the total incident solar power density from sun. P_m is the maximum output power density which can be obtained by maximizing the product of current density (J) and voltage (V). J and V are related as follows:

$$\mathrm{J} = \mathrm{J}_{sc} - \mathrm{J}_0(1 - e^{\frac{\mathrm{eV}}{k_\mathrm{B}\mathrm{T}}}) \tag{4.8}$$

In above equation, J_{sc} is the short-circuit current, J_0 is the reverse saturation current, e is the elementary charge, V is the voltage, k_B is the boltzmann constant and T is the temperature. J_{sc} can be calculated as:

$$\mathrm{J}_{sc} = \mathrm{e}\int_0^\infty \mathrm{a(E)I_{sun}(E)dE} \tag{4.9}$$

where, a(E) is the photon absorptivity, I_sun is the photon flux coming from sun to solar cell, E corresponds to the energy. The reverse saturation current is given by the expression:

$$\mathrm{J}_0 = \mathrm{J}_0^{nr} + \mathrm{J}_0^{r} = \frac{\mathrm{J}_0^{r}}{f_r} \tag{4.10}$$

Here, J_0^{nr} and J_0^{r} correspond to the non-radiative and radiative electron-hole recombination current density, respectively. f_r corresponds to the fraction of radiative recombination current

Table 4.2: Comparison of SLME of double perovskites with hybrid perovskite at 5 μm absorber layer thickness.

Conformers	SLME (%)
$Cs_8Ag_3Ge_2Bi_3Cl_{24}$	32.08
$Cs_8Ag_3Sn_2Bi_3Cl_{24}$	30.91
$Cs_8Cu_4Bi_4Cl_{24}$	22.24
$Cs_8Ag_1Cu_3Bi_4Cl_{24}$	21.85
$Cs_8Ag_2Cu_2Bi_4Cl_{24}$	19.80
$MA_8Pb_8I_{24}$	31.02 [168]
$MA_8Pb_7Sn_1I_{24}$	33.02 [168]
$FA_8Pb_4Sn_4Br_{24}$	26.74 [209]

($f_r = e^{\frac{-\Delta}{k_B T}}$, where $\Delta = E_g^d - E_g^{id}$. E_g^d and E_g^{id} correspond to the direct and indirect band gap, respectively). Using principle of detailed balance, in dark rate of emission and absorption of photons must be equal under equilibrium. Hence, J_0^r can be can be calculated as follows:

$$J_0^r = e\pi \int_0^\infty a(E) I_{bb}(E, T) dE \tag{4.11}$$

In above equation, I_{bb} corresponds to the black-body spectrum at temperature T. Finally, we can conclude that η can be computed once we have a(E) and f_r. In SLME calculation, a(E) = 1-$e^{-2\alpha(E)L}$, where α(E) is the absorption coefficient that can be calculated from first principles calculations and L is film thickness. Note that we have calculated the SLME as a function of thickness of the absorber layer (see Figure 4.8) only for those alloyed systems, which possess direct band gap. In Table 4.2, we have shown SLME of few double perovskites at 5 μm thickness and compared our results with other efficient hybrid perovskites that are reported recently. From Table 4.2, SLME of $Cs_8Ag_3Ge_2Bi_3Cl_{24}$ and $Cs_8Ag_3Sn_2Bi_3Cl_{24}$ are 32.08% and 30.91%, respectively. These numbers are very much encouraging from application perspective in solar cells. In addition, they are more stable, while in contact with air and moisture as compared to IO hybrid perovskites [197, 211].

4.4 Conclusion

In summary, we have presented a thorough study of alloying double perovskite $Cs_2AgBiCl_6$ with M(I), M(II) and M(III) cations. The role of SOC is important to accurately predict the band gap and band-edge positions in such systems. All the mixed sublattices are structurally stable as indicated by the Goldschmidt's tolerance factor and octahedral factor. The enthalpies of decomposition are negative, indicating the thermodynamic stability of alloyed systems. We have revealed that for substitution at Bi-sites, on increasing the concentration of Sb, band gap decreases up to 75% Sb_{Bi} substitution. However, there is a sudden increase in band gap for 100% Sb_{Bi} due to complete removal of Bi. A sudden increase in band gap has been observed on complete substitution of alkali metal (Na/K) at Ag-sites. We have also identified that partial Au substitution (i.e., 25% to 75%) can enhance the optical properties effectively due to a reduction in band gap. Also, we have observed stability decreases on increasing the substitution at Ag or Bi-sites. Hence, we have concluded that partial substitution of Au and Sb at Ag- and Bi-sites, respectively, will be cost-effective, more stable and efficient to enhance the optical properties. Out of alloying with M(I), M(II) and M(III), M(II) ($Sn_{Ag,Bi}$, $Rh_{Ag,Bi}$, $Ni_{Ag,Bi}$ and $Ge_{Ag,Bi}$) substitutions come out to be superior for optical properties. However, only in case of $Sn_{Ag,Bi}$ and $Ge_{Ag,Bi}$, direct band gaps are noticed. SLME of $Cs_8Ag_3Ge_2Bi_3Cl_{24}$ and $Cs_8Ag_3Sn_2Bi_3Cl_{24}$ are 32.08% and 30.91%, respectively, which definitely suggest huge promise towards prospective solar cell absorbers.

CHAPTER 5

Exploring the effects of the defects in layered hybrid perovskite

5.1 Introduction

In the past few years, 3D inorganic-organic hybrid perovskites (IOHPs) have brought revolution in the field of optoelectronics owing to their exotic optoelectronic properties. These materials exhibit high absorption coefficient, tunable bandgap, high carrier mobility and large carrier diffusion length [212, 213, 214, 215, 216, 217, 218, 219, 220, 221, 222]. Despite the huge success, poor stability (i.e. the solar cell loses efficiency during operation) and lead-toxicity have hindered their large scale commercialization [223, 224]. Thus, a sustainable future calls for the development of an efficient, cost-effective, non/less-toxic, eco-friendly and environmentally stable solar material to meet the necessity of potential energy at large scale.

In this quest, researchers are looking into 2D layered perovskites [166, 171, 172, 225, 83, 84]. A perfect 2D layered perovskite has the general formula $(\mathrm{R\text{-}NH_3})_2\mathrm{BX_4}$, where R is the organic moiety, which can be derived from basic $\mathrm{ABX_3}$ type perovskite structure [226]. Note that in 3D perovskite, the A-site cation sits in voids of the 3D network. However, the latter has limited allowed space for A-site cations (see Figure 5.1(a)). In 1926, Goldschmidt derived a tolerance factor (t) formula (Equation 5.1)[227] that determines this allowed space i.e., maximum allowed ionic radius for A-site cation. For a perfect cubic perovskite structure $\mathrm{ABX_3}$,

$$r_{\mathrm{A}} + r_{\mathrm{X}} = t\sqrt{2}(r_{\mathrm{B}} + r_{\mathrm{X}}) \tag{5.1}$$

where, r_{A}, r_{B}, and r_{X} are the effective ionic radii of A-site, B-site and X-site ions, respectively. The Goldschmidt tolerance factor must be in the range $0.8 \leq t \leq 1.0$ for a cubic perovskite structure.[228, 229]. If B-site cation is a metal ion Pb^{2+} with r_{Pb} = 1.03 Å, and X-site anion is a

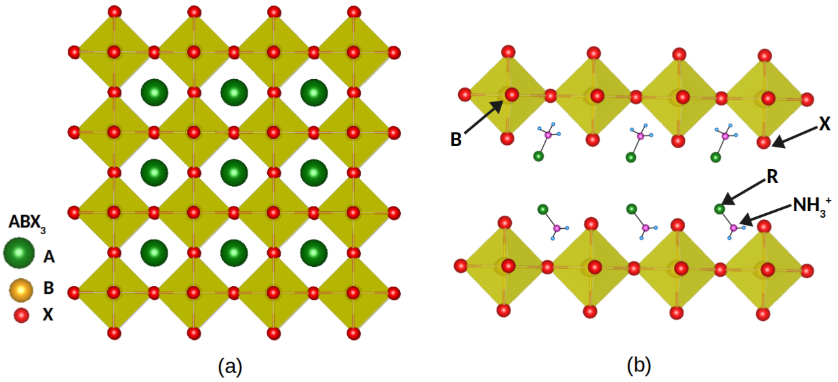

Figure 5.1: (a) A 3D cubic perovskite structure with chemical formula ABX_3, where A, B and X are organic cation, divalent metal cation and monovalent halide anion, respectively. (b) Schematic drawing of 2D layered structure of the $(R\text{-}NH_3)_2BX_4$ hybrids.

halide ion I^- with $r_I = 2.20$ Å, then with maximum possible scenario i.e., $t = 1.0$, the geometric limit applied on A-site cation will be $r_A = 2.36$ Å. Hence, for $r_A > 2.36$ Å, the 3D network will be destroyed and could form 2D perovskite (see Figure 5.1(b)). Several studies have been done in 2D perovskite structures, which showed that the 2D perovskite has more structural and chemical flexibility in comparison to their 3D counterparts. Also, the long chain organic spacers which are hydrophobic in nature of 2D perovskite can enhance the poor stability of 3D IOHPs [230, 231, 232]. However, decreasing dimensionality of IOHPs from 3D to 2D structure causes an increase in bandgap and exciton binding energy. Due to the wide bandgap nature, 2D IOHPs show poor optical absorption in PV applications[233, 234, 235, 236, 237, 238, 239, 240, 231].

Therefore, there is justified interest to search for a stable and efficient 2D (layered) perovskite material with good optical absorption. Incidentally, we have studied and experimentally synthesized the primary cyclic ammonium-based ($C_nH_{2n-1}NH_3$; n = 3−6) inorganic-organic hybrid semiconductor series [241]. However, theoretically this system ($(C_nH_{2n-1}NH_3)_2PbI_4$; n=3-6) is rather unexplored and requires further attention to get more atomistic insights and electronic structures. Moreover, the wide bandgap nature and presence of toxicity due to lead (Pb) prohibit their applications. Therefore, in the present work, we study the role of Ge/Sn substitution and Pb-vacancy (Pb−⊠) to reduce concentration of Pb and enhance solar cell efficiency by the formation of mixed perovskite structures. To do that, we have first thoroughly benchmarked and validated the exchange and correlation (ϵ_{xc}) functionals in the framework of Density Functional Theory (DFT) so that the results are not any artefacts of the same. After that, we have investigated the thermodynamic stability [242] by calculating the formation energy, and structural stability [221, 243] with the help of Goldschmidt tolerance factor and octahedral factor. Thereafter, we have analyzed the electronic and optical properties of the stable configurations. Finally, we have computed exciton binding energy, strength of electron-phonon coupling and the spectroscopic limited maximum efficiency (SLME) to address their suitability and theoretical maximum efficiency as a potential solar cell materials.

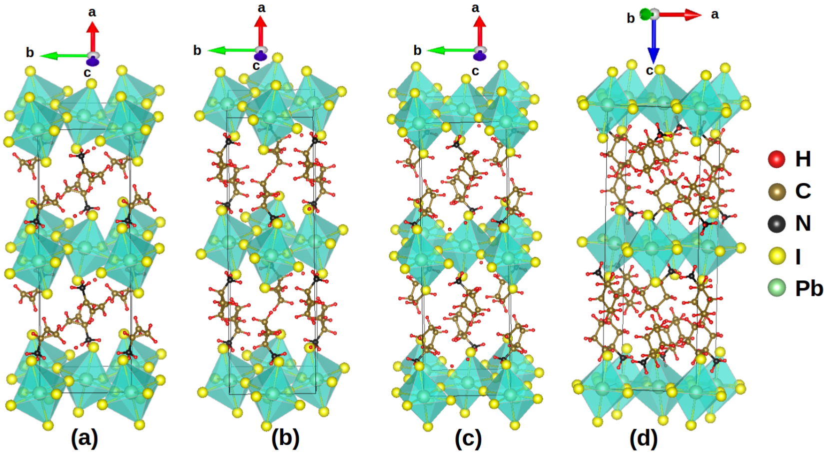

Figure 5.2: Crystal structures for compounds: (a) cyclopropyl ammonium tetraiodoplumbate (CPPI, n = 3), $(C_3H_5NH_3)_2PbI_4$, (b) cyclobutyl ammonium tetraiodoplumbate (CBPI, n = 4), $(C_4H_7NH_3)_2PbI_4$, (c) cyclopentyl ammonium tetraiodoplumbate (CPEPI, n = 5), $(C_5H_9NH_3)_2PbI_4$, and (d) cyclohexyl ammonium tetraiodoplumbate (CHXPI, n = 6), $(C_6H_{11}NH_3)_2PbI_4$.

5.2 Methodology

We have performed all the calculations using Vienna *Ab initio* Simulation Package (VASP)[244] and projector augmented-wave (PAW)[45] pseudopotentials within the framework of DFT.[10][11] We have optimized the crystal structures of all conformers using Perdew–Burke–Ernzerhof (PBE)[33] exchange-correlation (ϵ_{xc}) functional with a Γ-centered 2×2×2 k-point mesh, and set the criteria for convergence of total energy and forces (for optimization of atomic positions and lattice vectors) to 10^{-5} eV and 10^{-4} eV/Å, respectively. The energy cutoff was set to 600 eV. Later on, from convergence test, we have found that a Γ-centered 3×3×3 k-point mesh is sufficient for sampling the Brillouin zone (BZ), and so, the 3×3×3 k-point mesh has been used in our further calculations. We have used advanced hybrid ϵ_{xc} functional Heyd–Scuseria–Ernzerhof (HSE06)[193] to get more accuracy in our results because PBE functional commonly underestimates the bandgap of the materials. The spin orbit coupling (SOC) effect has been duly included in all the calculations.

5.3 Results and Discussions

The cyclic compounds cyclopropyl ammonium tetraiodoplumbate (CPPI), cyclobutyl ammonium tetraiodoplumbate (CBPI), cyclopentyl ammonium tetraiodoplumbate (CPEPI) and cyclohexyl ammonium tetraiodoplumbate (CHXPI) have well-defined 2D layers. There are changes in tilting of PbI_6 octahedra within layers and packing of ammonium cations between layers of these compounds, but the overall structure remains the same, i.e., 2D layered perovskite crystal structure (see Figure 5.2).[226] These cyclic inorganic-organic hybrid compounds have been synthesized experimentally, and show a decrement in electronic bandgap value from n = 3 to 6, an intense narrow exciton emission, and a strong room-temperature photoluminescence.[245, 241] However, these compounds have some drawbacks, such as wide bandgap and presence of toxic element Pb. Therefore, to overcome these issues, which are not good for solar cell, we have studied the effect of Ge/Sn substitution and/or Pb-☒ using hybrid DFT. All these mentioned layered structures will show quite similar optoelectronic properties due to their similarity in crystal structures. Therefore, in present work, we have chosen one of these compounds, viz. CPPI, as our prototypical model system, and the rest of our calculations are done by considering this system.

5.3.1 Benchmarking of DFT functionals

To ensure that our results are not merely the artefacts of DFT ϵ_{xc} functionals, we have benchmarked different ϵ_{xc} functionals by comparing the calculated bandgap (E_g^{cal}) and experimental bandgap (E_g^{exp}) of CPPI. The value of E_g^{exp} = 3.04 eV [245, 241]. Using PBE functional, we have found that the value of E_g^{cal} for CPPI is 2.39 eV (see Figure 5.3(a)), which shows that PBE functional underestimates the E_g^{exp} value. Since CPPI contains a heavy element Pb, we have included SOC effect with PBE functional, which results in the splitting of conduction band and the conduction band minimum (CBm) shifts to a lower value (see Figure 5.3(b)). As a result, E_g^{cal} comes out to be 1.70 eV using PBE+SOC. Thus, PBE functional can not reproduce the E_g^{exp} value. Therefore, we have also estimated the positions of valence band maximum (VBM) and conduction band minimum using more advanced ϵ_{xc} functionals (see Figure 5.4(a)). After that, we have checked bandgap using HSE06 functional, which corrects the electron self-interaction error. Although HSE06 functional with default α = 25% (fraction of Hartree-Fock exact exchange) is reproducing the experimental bandgap (E_g^{cal} = 3.03 eV, see Figure 5.3(c) 5.4(a) without including SOC, we need to include SOC effect due to the presence of heavy element Pb, as discussed earlier. Thereafter, we have obtained E_g^{cal} = 2.30 eV using HSE06+SOC with α = 25% (see Figure 5.4(a-b)), which is also not in good agreement with the E_g^{exp} value. Therefore, to reproduce the experimental bandgap by using HSE06+SOC, we have increased the amount of α, which further shifts the valence band maximum (VBM) with slight alteration of CBm.

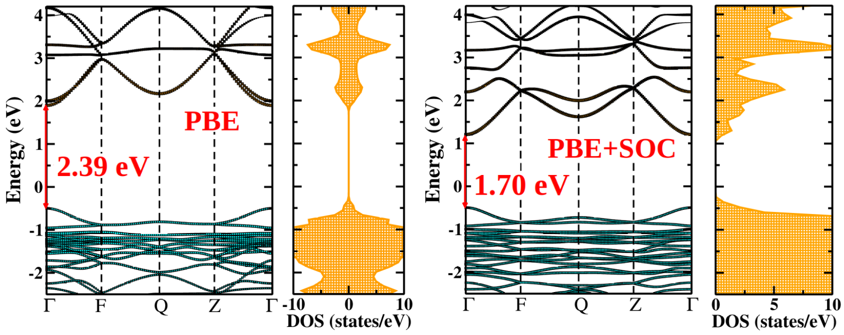

(a) Using PBE functional

(b) Using PBE+SOC functional

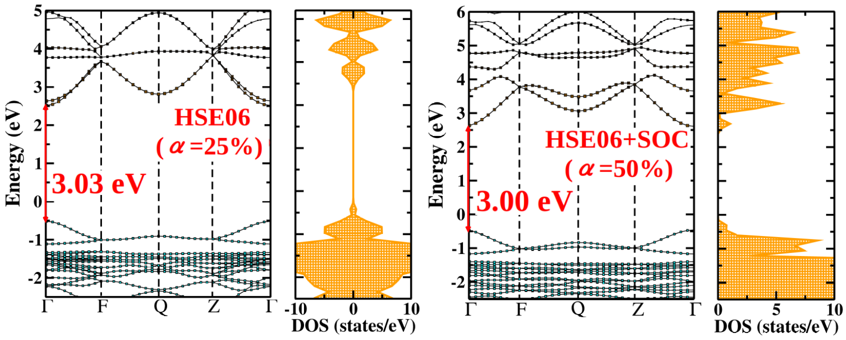

(c) Using HSE06 functional

(d) Using HSE06+SOC functional

Figure 5.3: Calculated band structures along with the density of states (DOS) of CPPI. The band paths are along the high symmetry *k*-points Γ (0, 0, 0), F (0, 0.5, 0), Q (0, 0.5, 0.5), and Z (0, 0, 0.5) of BZ.

Thus, we have reproduced the E_g^{exp} value using HSE06+SOC functional with increased amount of α = 50% (see Figure 5.3(d)). Figure 5.3 clearly depicts that band profile remains the same by both the functionals PBE and HSE06, the only difference is in the value of the direct bandgap at Γ point.

To validate the calculations done by HSE06+SOC with different amounts of α (see Figure 5.4(a)), we have calculated imaginary part of the dielectric function with four different values of α (i.e., α = 25%, 30%, 40%, and 50%) and found that the respective optical peaks are observed at 2.33, 2.45, 2.71 and 2.96 eV (see Figure 5.4(c)). The optical peak corresponding to α = 50% at 2.96 eV has a good agreement with E_g^{exp} value (see Figure 5.4(c)). We have checked for validation of different functionals of DFT for n=4, 5 and 6 in a similar way as in case n = 3. We have found that using HSE06+SOC functional with α = 50%, 55% and 55%, we can

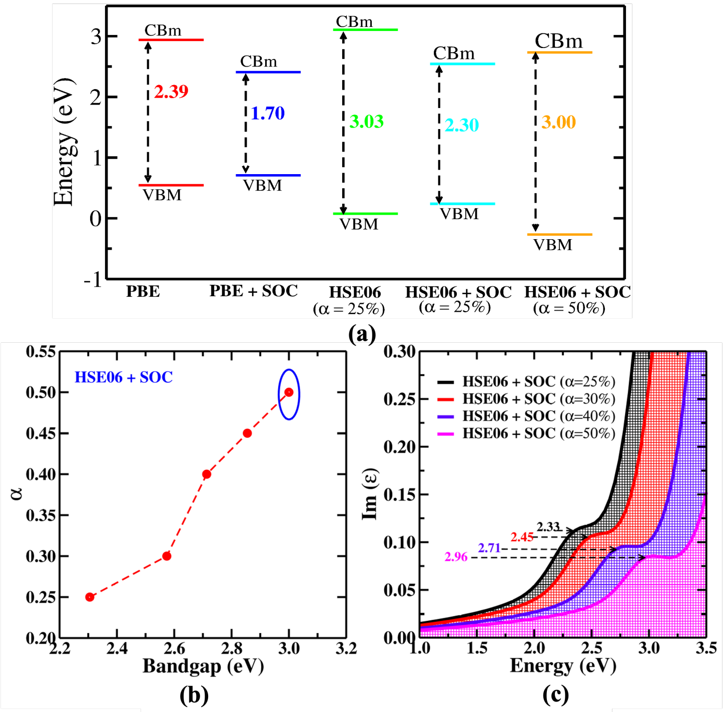

Figure 5.4: (a) Band edge alignment for for CPPI using PBE, PBE+SOC, HSE06 and HSE06+SOC functionals. (b) Variation in the bandgap of CPPI with α. The point inside blue ellipse represents the calculated bandgap, which is very close to the experimental bandgap. (c) Imaginary part of the dielectric function calculated using HSE06+SOC with different Hartree-Fock exact exchange (i.e., α = 0.25, 0.30, 0.40 and 0.50).

reproduce experimental bandgap [245, 241] for n=4, 5 and 6, respectively. Therefore, we have used HSE06 functional with SOC effect included in all our results.[1] In Figure 5.5(a) and 5.5(b), we have shown the pDOS for $(C_3H_5NH_3)_2PbI_4$ with and without organic moiety (i.e. only the inorganic cage). The CBm is contributed by Pb p-orbitals, whereas VBM is contributed by I

---

[1] Notably, in the present work, the main motive of our work is to understand the effect of Sn/Ge substitution at P-sites and Pb-☒ in pristine $(C_3H_5NH_3)_2PbI_4$. That results into new a composite system viz. $(C_3H_5NH_3)_2Pb_{1-x-y}Sn_{x+y}I_4$, where the SOC effect changes as a function of the amount of Pb. Thus it is not necessary that if in the pristine 50% exact exchange gives the correct bandgap and energetics, for the same exact exchange a composite system with x substituted Sn/Ge atoms and y Pb-☒ will also reproduce the accurate energetics. In absence of any experimental inputs it is not possible to determine it accurately for the composite system. In view of this, rest of calculations have been performed with default α = 25% as in HSE06 with SOC. For sure over/underestimation of combined effect of the electron's self-interaction error and SOC may lead to some unprecedented error in the energetics. However, to compute the formation energies of pristine and mixed conformers, we take the difference of total energies. Thus in taking the differences of the total energies, we assume the elimination of error (if any) in the energetics is intrinsically incorporated. Hence, it is justified to use default value of α to perform rest of calculations for pristine and mixed conformers.

p-orbitals and Pb s-orbitals (see Figure 5.5(a) and 5.5(b)). Here, it should be noted that these organic moieties do not contribute to the VBM and CBm. Moreover, the overall pDOS and bandgap remain same with and without organic moiety (see Figure 5.5(a) and 5.5(b)). The only change is in the fermi level position, which is shifted to zero in both the cases. Here, we have observed that electronic structure for n=3 to 6 remains the same except slight decrease in the bandgap as we go from n=3 to n=6 (see Figure 5.6). This is due to the shift in the CBm with change in the size of the organic-moiety. For more details see section II in SI. Moreover, their optical properties are also quite similar (see Figure 5.7). As electronic configurations of all these systems are quite similar and organic moieties only bring the change in the structure (i.e., octahedral tilting with increase in the size of organic moiety) which results in the shift in CBm. So it is justified to assume that if we do substitution at Pb-sites or Pb-☒ we will get similar change in optical response for n=3 to 6. Hence, we have shown effect of substitution or Pb-☒ only considering n=3 as a prototypical system. As we go from n=3 to n=6, the system becomes larger and larger. Hence, converging HSE06+SOC for such large systems and their mixed conformers is quite challenging as well as computationally expensive. Hence, we have tried substitution or Pb-☒ effect only in one system that is the smallest one amongst all these systems. Note that we have chosen the alternatives Ge, Sn and/or Pb-☒ to remove/reduce the amount of toxic Pb from CPPI (beacuse Ge, Sn and Pb belong to the same group in the periodic table and have similar valence electronic configurations). For substitution of Ge/Sn to replace Pb, we have used a 58 atoms supercell, i.e., $(C_3H_5NH_3)_4Pb_2I_8$, where the Pb-defect is localized.

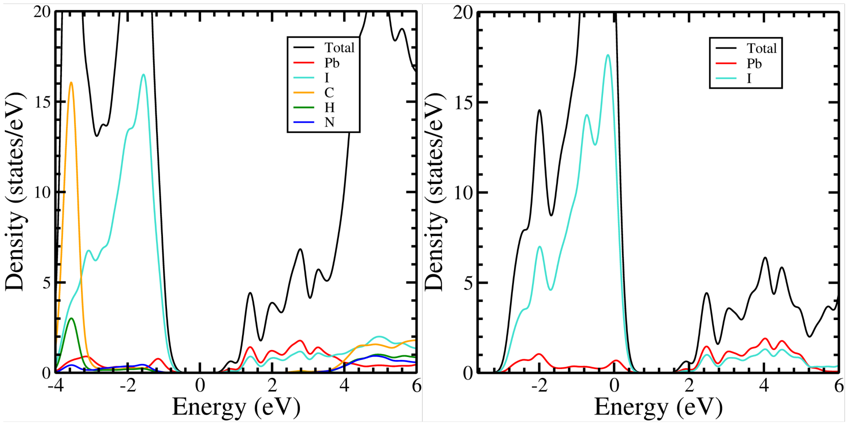

(a) (b)

Figure 5.5: (a) Partial density of states of $(C_3H_5NH_3)_2PbI_4$; (b) Partial density of states of inorganic cage of $(C_3H_5NH_3)_2PbI_4$.

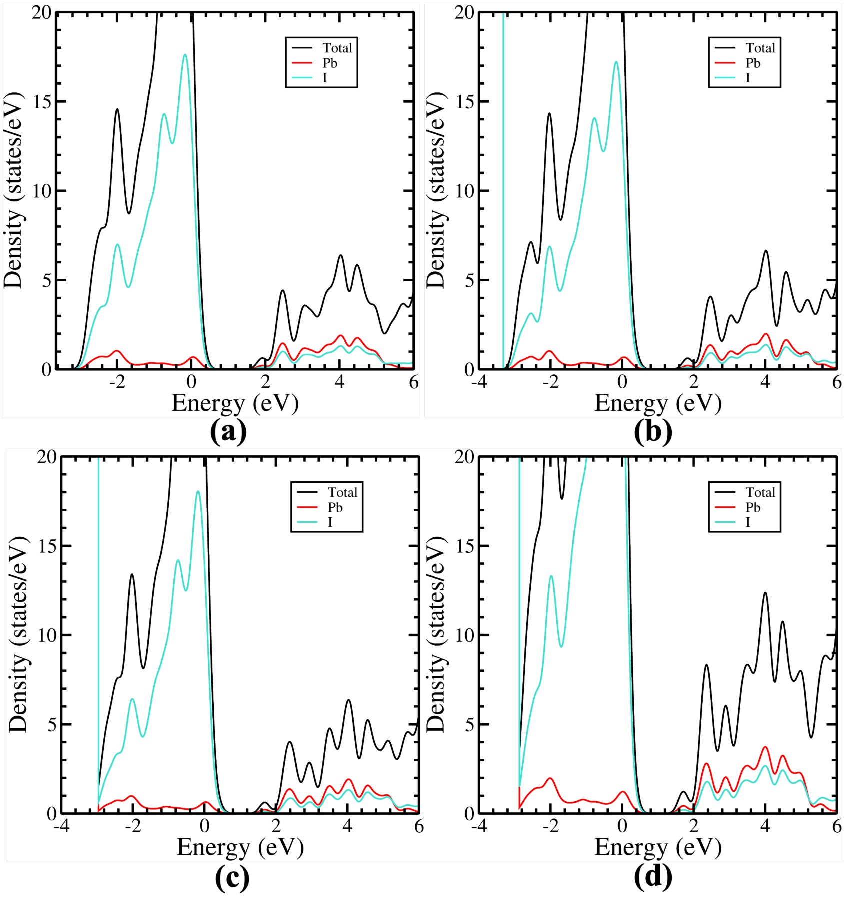

Figure 5.6: Partial density of states of inorganic cage of (a) $(C_3H_5NH_3)_2PbI_4$; (b) $(C_4H_7NH_3)_2PbI_4$; (c) $(C_5H_9NH_3)_2PbI_4$; (d) $(C_6H_{11}NH_3)_2PbI_4$. Notably, since VBM and CBm are contributed by In and Pb orbitals (organic moieties mainly contribute in the deep of the conduction and valence band). Hence, only inorganic cage has been taken into account.

5.3.2 Thermodynamic Stability

Note that the amount of substitution of Ge, Sn and Pb-$\boxtimes$ will affect the SOC role in mixed perovskites, $(C_3H_5NH_3)_2Pb_{1-x-y}Sn_x\boxtimes_yI_4$ and $(C_3H_5NH_3)_2Pb_{1-x-y}Ge_x\boxtimes_yI_4$ (x and y indicates the contents of Sn/Ge and Pb-$\boxtimes$, respectively), because SOC is mainly a function of extent of Pb in this system. Thus, although the correct positions of the VBM and CBm are obtained by using HSE06+SOC with α = 50% in the case of CPPI, it will not necessarily the same in the case of mixed perovskites. Hence, we have used the default value α = 25% for the energy calculations of mixed conformers. The bandgaps of different conformers with the default α are shown in the upper panel of Fig 5.8. Note that, this may lead to some error in the total energy expression due to under/overestimation of the combined effect of SOC and the electron's self-interaction error [220]. In order to eliminate this type of error, we took the difference of total energies for the calculation of the formation energy of different conformers with and without defects. In the case of Ge and Sn doping, the considered precursors are PbI_2, GeI_2, I_2, HI,

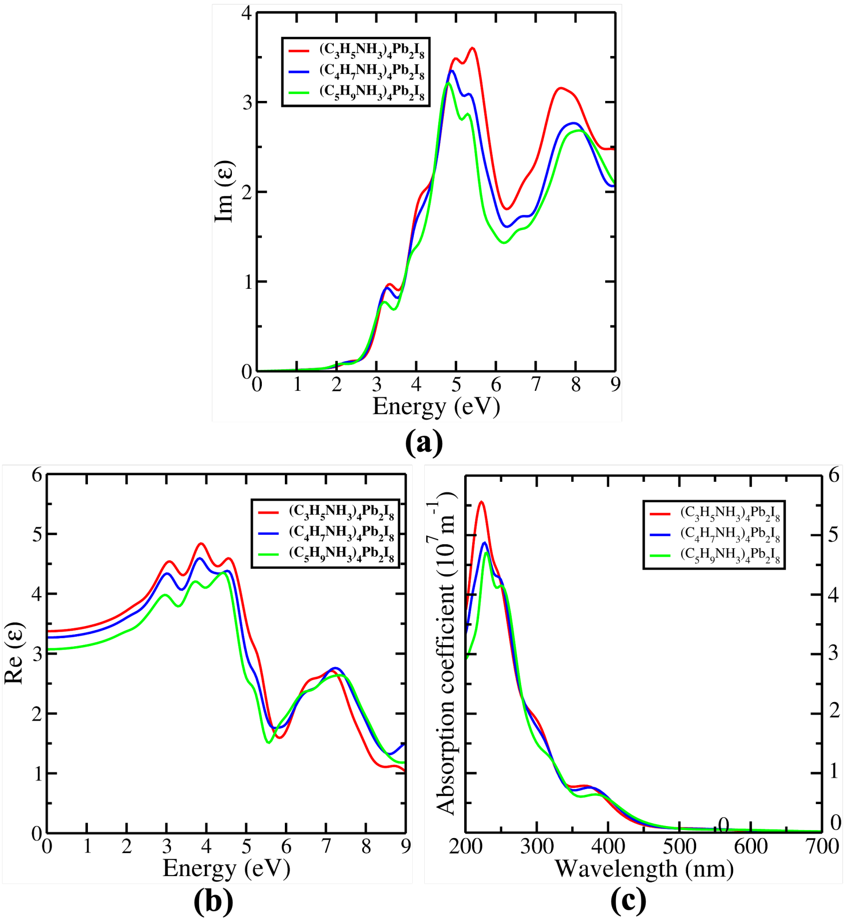

Figure 5.7: Variation of (a) imaginary (Im (ε)) and (b) real (Re (ε)) parts of dielectric function with energy; (c) variation of absorption coefficient with wavelength for ($(C_nH_{2n-1}NH_3)_2PbI_4$; n=3-5) using HSE06+SOC functional

$C_3H_5NH_3$ and SnI_2. We have calculated the formation energy as follows

$$\begin{aligned} E_{\mathrm{f}}(x,y) = {} & E(\mathrm{C_{12}H_{32}N_4Pb}_{2-x-y}\mathrm{Ge}_x \boxtimes_y \mathrm{I_8}) - (2-x-y)E(\mathrm{PbI_2}) \\ & -xE(\mathrm{GeI_2}) - yE(\mathrm{I_2}) - 4E(\mathrm{HI}) - 4E(\mathrm{C_3H_5NH_2}) \end{aligned} \tag{5.2}$$

where, $0 \leq x \leq 2$ and $0 \leq y \leq 2$ in the supercell of $(C_3H_5NH_3)_2PbI_4$ i.e., $(C_3H_5NH_3)_4Pb_2I_8$. In the case of Sn substitution, SnI_2 is used instead of GeI_2 in Equation 5.2.

First, we have determined the most favourable Pb site for Ge/Sn substitution alongside existence of Pb-⊠ via an iterative procedure [200, 220]. Here, it should be noted that both Pb sites are equivalent sites. Therefore, we can substitute alternative Ge/Sn at any Pb sites. We have found that the mixed conformer, which has complete Pb-⊠ with no Ge/Sn substitution is thermodynamically unstable with respect to the CPPI (see bottom panel of Figure 5.8)[2]. As the content of Sn substitution increases without Pb-☒, a gradual increase in thermodynamic stability is observed (see bottom panel of Figure 5.8). However, as the content of Ge substitution increases, it shows less thermodynamic stability with respect to CPPI (see bottom panel of Figure 5.8). Complete Sn substitution is thermodynamically the most stable one. Thus, Sn substitution is thermodynamically more preferable than Ge substitution. For the validation of our results, we have also calculated the formation energy along different possible paths. We have also performed ab initio Molecular Dynamics (AIMD) simulation to confirm the thermodynamic stability of Sn substituted conformers at higher temperature. We have also done *ab initio* Molecular Dynamics (AIMD) simulation for 4 picosecond for pristine and Sn substituted conformers. In Figure 5.9, we have plotted the radial distribution function (RDF) and compared the DFT structure (0K) with the one at 400K. From Figure 5.9, we can see from this RDF plot that there is no visible change in 1st, 2nd and so on nearest neighbors, which confirms the structural stability of $(C_3H_5NH_3)_2Pb_{1-x}Sn_xI_4$ on substitution with Sn in place of Pb.

5.3.3 Structural Stability

To investigate the structural stability of CPPI and all mixed conformers thoroughly, we have calculated Goldschmidt tolerance factor (t),[227] of all the therodynamically stable configurations. This Goldschmidt tolerance factor indicates the structural stability of the perovskite structure, as defined in Equation 5.1. We have found that all mixed conformers have $t > 1$, and form 2D perovskites.[226] However, the Goldschmidt tolerance factor alone is not sufficient to predict the stable perovskite structure. An additional criterion i.e., the octahedral factor (μ) is considered, which determines the stability of the BX_6 octahedra,[246] defined as

$$\mu = \frac{r_B}{r_X} \tag{5.3}$$

For stable BX_6 octahedra, the range of μ is $0.377 < \mu < 0.895$.[246] If the value of μ is beyond this range, then the perovskite structure will become unstable, even though the tolerance factor

---

[2] On doing 50% or 100% Pb-vacancy (Pb-☒) moderate structural changes are noted. Therefore, these systems may be treated as new materials. As our converged supercell consists of only two leads, we could do calculations only for 50% and 100% Pb-☒. For other percentage of Pb-☒ we need to make an even larger supercell of several hundreds of atoms, where doing calculations with HSE06+SOC becomes computationally extremely expensive. However, such calculations are not required since the systems having Pb-☒ are not usually stable. Hence, we have not considered such systems for electronic and optical calculations.

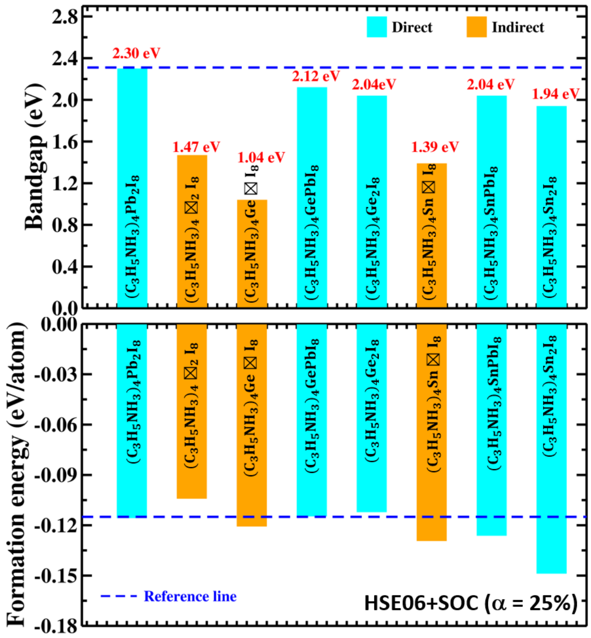

Figure 5.8: Formation energy (eV/atom) of different mixed conformers (the blue dotted line is the reference line corresponding to prototypical material (CPPI)), and their respective bandgap using HSE06+SOC with α = 25%.

is in some favorable range for the perovskite formation. The effective ionic radii of Pb^{2+}, Ge^{2+}, Sn^{2+}, and I^- are 1.03, 0.77, 0.97, and 2.20 Å, respectively.[247, 248] The octahedral factor for all mixed conformers are shown in Figure 5.10. We have found that all mixed conformers with Pb-⊠ and $(C_3H_5NH_3)_4Ge_2I_8$ have octahedral factor $\mu < 0.377$ and do not possess the octahedral stability (see Figure 5.10). Therefore, these are unstable perovskite structures, even though they have tolerance factor $t > 1.0$ and a favorable thermodynamic stability for 2D layered perovskite structures. The remaining mixed conformers, which are inside the blue box in Figure 5.10 have octahedral factor between the range $0.377 < \mu < 0.895$, and thus, these are structurally stable.

5.3.4 Electronic Properties

We have observed that the mixed conformers with Pb-⊠ have indirect bandgap (see upper panel of Figure 5.8) and thus, poor optical performance. Therefore, the mixed conformers containing Pb-⊠ are not suitable for solar cell applications. Hence, we have studied bandgap engineering by Ge and Sn substitutions only (i.e. without Pb-⊠) (see Table 5.1), where both VB and CB are shifted downward in the case of Sn substitution and upward in the case of Ge substitution (for more details see section VI in SI). We have plotted pDOS for stable mixed conformers to understand the high optical absorption of IOHPs. Figure 5.11(a) shows that Pb 6s and I 5p

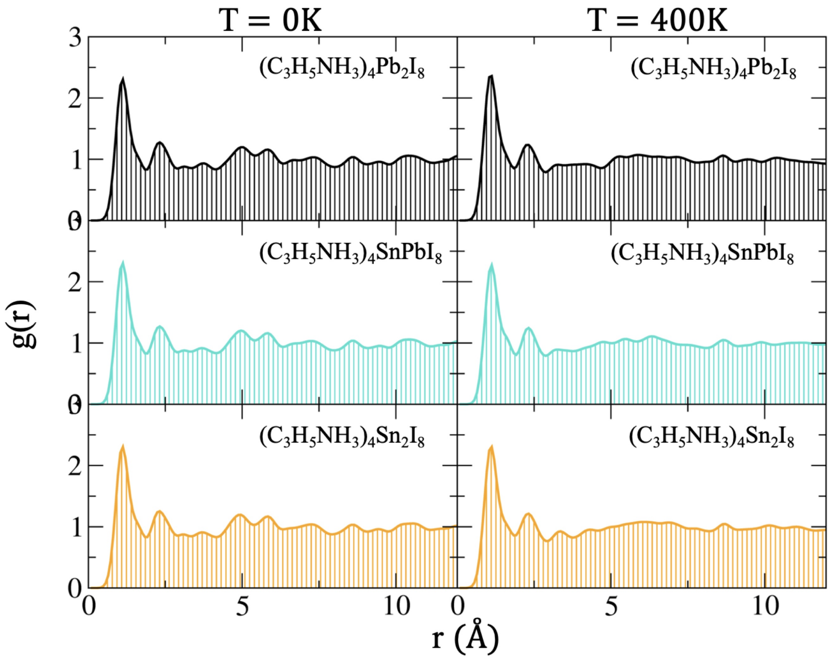

Figure 5.9: Radial distribution of stable phanses of $(C_3H_5NH_3)_2Pb_{1-x}Sn_xI_4$ at two different temperatures i.e., 0K and 400K.

orbitals are mainly contributing to the VBM, whereas the CBm is mainly composed of unoccupied Pb 6p, I 5s, and I 5p orbitals. A similar orbitals contribution has been observed in the case of $(C_3H_5NH_3)_4Sn_2I_8$, where Sn 5s and I 5s orbitals are mainly contributing to the VBM with a small contribution by Sn 5p orbitals, whereas the CBm is composed of unoccupied Sn 5p, I 5s, and I 5p orbitals (see Figue 5.11(c)). In the case of $(C_3H_5NH_3)_4SnPbI_8$, the VBM is primarily contributed by Sn 5s, Pb 6s, and I 5p orbitals with a small contribution by Pb 6p orbitals, whereas the CBm is mainly composed of unoccupied Sn 5p, Pb 6p, and I 5p orbitals with a small contribution by I 5s orbitals (see Figure 5.11(b)). Similarly, we can observe the behavior of orbitals contribution in the case of $(C_3H_5NH_3)_4GePbI_8$, as shown in Figure 5.11(d). Thus, a strong s–p and p–p coupling exist, that help in reducing the bandgap. Moreover, on increasing the Ge/Sn concentration, the bandgap is decreasing. Due to these direct p–p and s–p electronic transitions, strong absorption is expected in $(C_3H_5NH_3)_4GePbI_8$, $(C_3H_5NH_3)_4SnPbI_8$, and $(C_3H_5NH_3)_4Sn_2I_8$ materials [241]. Here, Sn, Ge and Pb show a similar contribution to the pDOS because of their similar valence electronic configurations. Thus, these electronic structure studies motivate us to explore the optical properties and theoretical maximum efficiency of the stable mixed conformers.

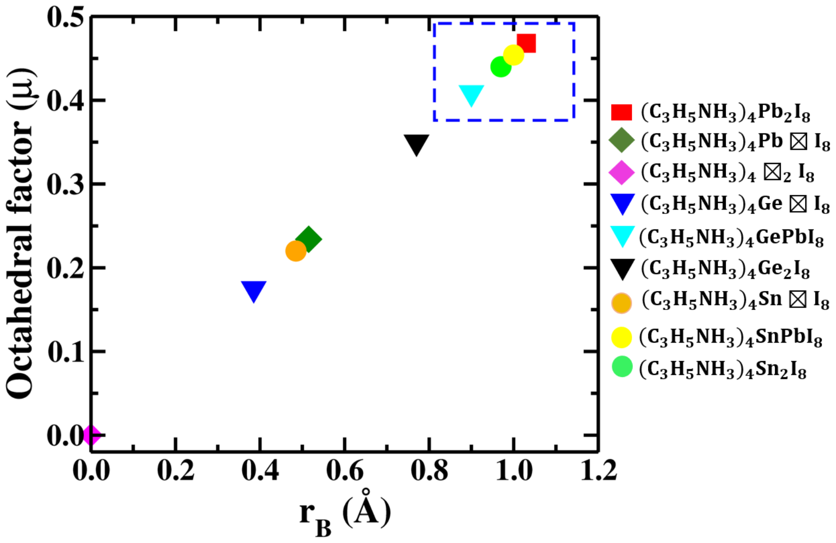

Figure 5.10: Calculated octahedral factor for different conformers.

Table 5.1: The bandgaps (E_g) calculated by HSE06+SOC with α = 25% of mixed conformers

Conformers	E_g (eV)	VB shift (eV)	CB shift (eV)
$(C_3H_5NH_3)_4Pb_2I_8$	2.30	0.000	0.000
$(C_3H_5NH_3)_4GePbI_8$	2.13	−0.051	−0.236
$(C_3H_5NH_3)_4Ge_2I_8$	2.04	−0.183	−0.447
$(C_3H_5NH_3)_4SnPbI_8$	2.04	+0.348	+0.091
$(C_3H_5NH_3)_4Sn_2I_8$	1.94	+0.583	+0.218

5.3.5 Optical properties

We can predict the suitability of the materials for optoelectronic applications by studying their optical properties such as dielectric function, extinction coefficient, refractive index and absorption coefficient. The linear optical properties are described by the frequency dependent complex dielectric function, $\varepsilon(\omega) = \mathrm{Im}(\varepsilon) + \mathrm{Re}(\varepsilon)$. Here, $\mathrm{Im}(\varepsilon)$ and $\mathrm{Re}(\varepsilon)$ are the imaginary and real part of the dielectric function, respectively. Using these, we have determined various optical properties, viz., refractive index (η), extinction coefficient (κ) and absorption coefficient (α). The respective formulae are [249, 243]

$$\eta = \frac{1}{\sqrt{2}}\left[\sqrt{\mathrm{Re}(\varepsilon)^2 + \mathrm{Im}(\varepsilon)^2} + \mathrm{Re}(\varepsilon)\right]^{\frac{1}{2}} \tag{5.4}$$

$$\kappa = \frac{1}{\sqrt{2}}\left[\sqrt{\mathrm{Re}(\varepsilon)^2 + \mathrm{Im}(\varepsilon)^2} - \mathrm{Re}(\varepsilon)\right]^{\frac{1}{2}} \tag{5.5}$$

$$\alpha = \frac{2\omega\kappa}{c} \tag{5.6}$$

where, ω is the frequency and c is the speed of light. The calculation of these optical properties is important for optoelectronic devices because these provide the response of the materials to incident electromagnetic radiations and demonstrate about the optimal solar energy conversion efficiency.

Since the optical calculation is hugely dependent on the bandgap, if we consider SOC effect with HSE06 ϵ_{xc} functional, then the optical properties get underestimated because HSE06+SOC with α = 25% hugely underestimates the CPPI bandgap (E_g^{cal} = 2.30 eV, see Figure 5.4(a)). To avoid this problem, we have calculated the optical properties by using both HSE06 and HSE06+SOC with α = 25% and compared the results. We have found that the lead-free mixed conformers follow the same trend using both HSE06 and HSE06+SOC. This is an expected result because those conformers do not contain the heavy element Pb, and thus, the inclusion/exclusion of SOC with HSE06 ϵ_{xc} functional has negligible effect on the results. The imaginary part of the dielectric function shows a red-shift towards the infrared region with increasing concentration of Sn/Ge (see Figure 5.12(a)). This is attributed to a decrement in the bandgap on increasing the amount of Sn/Ge. A large static value of the dielectric constant, i.e., Re(ϵ) (at ω = 0) is an essential requirement for an efficient solar absorber because it results in a high degree of charge screening, which can prohibit radiative electron-hole recombination and improves performance of the devices. From Figure 5.12(b), we have observed a rise in value of Re(ϵ) (at ω = 0) with increasing Sn/Ge concentration. Sn and Ge substituted conformers have higher optical absorption peak intensity and red-shifted peaks in comparison to pristine CPPI within the UV region (see Figure 5.15(a)).

5.3.6 Spectroscopic limited maximum efficiency (SLME)

To identify efficient materials with high power conversion efficiency (PCE) for PV applications, we have calculated SLME[215, 250, 251] of different stable mixed conformers. Another way to select the efficient materials for solar cell applications is the Shockley–Queisser (SQ) limit,[252] but SQ limit only considers the bandgap of materials and does not take care of material's properties such as absorber layer thickness and absorption coefficient. Therefore, to overcome these shortcomings of SQ limit, Yu and Zunger proposed the SLME approach, which considers the absorber layer thickness and absorption coefficient of the system. It also depends

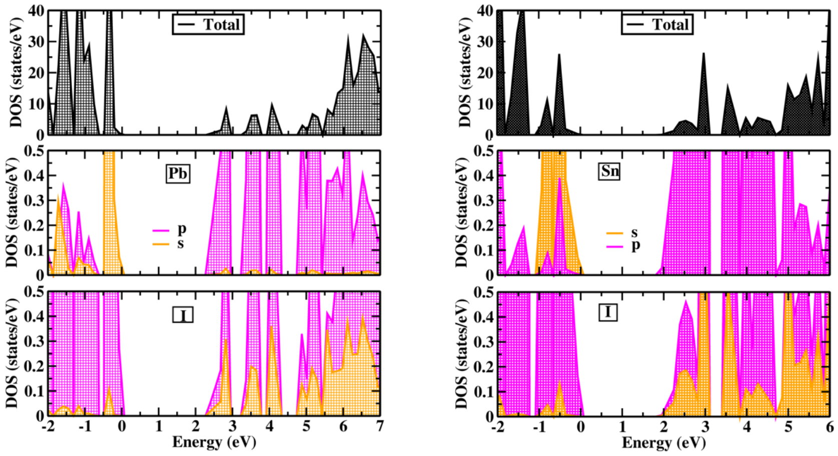

(a) For $(C_3H_5NH_3)_4Pb_2I_8$ **(c) For** $(C_3H_5NH_3)_4Sn_2I_8$

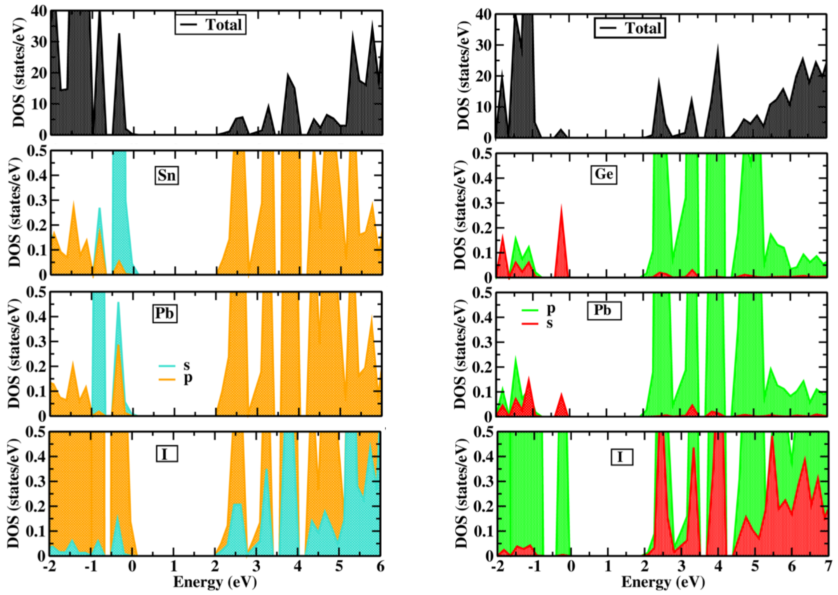

(b) For $(C_3H_5NH_3)_4SnPbI_8$ **(d) For** $(C_3H_5NH_3)_4GePbI_8$

Figure 5.11: Calculated total and partial density of states for (a) $(C_3H_5NH_3)_4Pb_2I_8$, (b) $(C_3H_5NH_3)_4SnPbI_8$, (c) $(C_3H_5NH_3)_4Sn_2I_8$, and (d) $(C_3H_5NH_3)_4GePbI_8$ using the HSE06+SOC with $\alpha = 25\%$. The VBM is set to 0 eV.

on nature of the bandgap (direct or indirect), and temperature. Thus, we have used this SLME metric and calculated the maximum theoretical efficiency for all the stable mixed perovskite structures using HSE06+SOC with $\alpha = 25\%$ (see Figure 5.13(b)). We have also tabulated the SLME values at 6 μm absorber thickness in Table 5.2. The temperature is set to 300 K. We have found that the conformer $(C_3H_5NH_3)_4Sn_2I_8$ has the maximum efficiency $\sim 24\%$, which is higher than that of CPPI PCE (see Table 5.2). Thus, we can conclude that complete removal of toxic element Pb with alternative Sn is possible with enhanced PCE. Therefore, we can recommend the substitution of Sn to replace toxic Pb completely, and to enhance the efficiency of solar cell based on 2D layered perovskites.

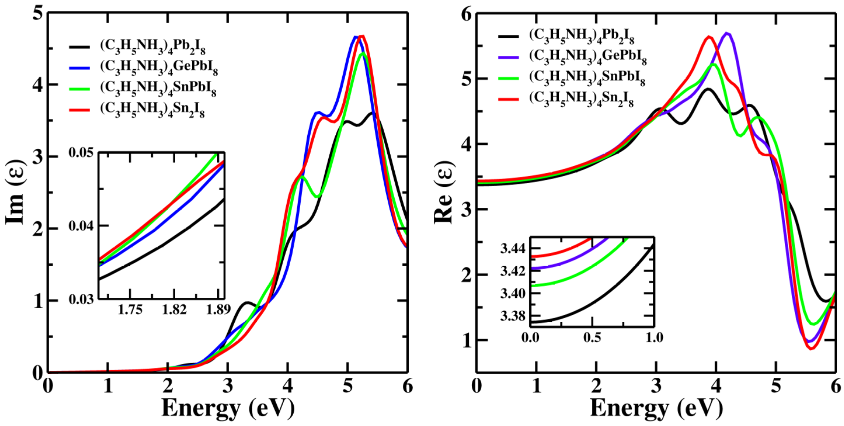

(a) (b)

Figure 5.12: (a) Calculated imaginary part of the dielectric function, Im(ε), and (b) calculated real part of the dielectric function, Re(ε) for different stable conformers using HSE06+SOC with α = 25%.

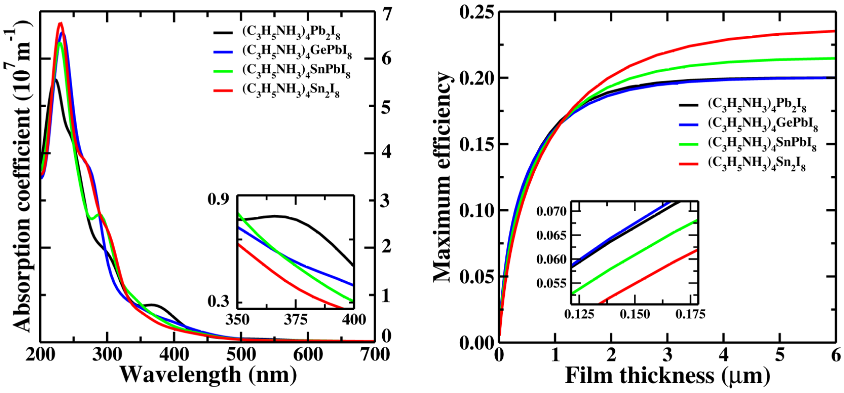

(a) (b)

Figure 5.13: (a) Calculated absorption coefficient, and (b) SLME vs film thickness, of different stable conformers using HSE06+SOC with α = 25%.

5.3.7 Wannier-Mott approach and exciton binding energy

For a screened interacting electron-hole (e-h) pair the exciton binding energy (E_B) can be calculated employing Wannier-Mott approach [253]. According to Wannier-Mott model E_B for a system is defined as follows:

$$E_B = \left(\frac{\mu}{\epsilon_{\text{eff}}^2}\right) R_\infty \qquad (5.7)$$

where, μ, ϵ_{eff}, and R_∞ are the reduced mass, effective dielectric constant and Rydberg constant, respectively. Note here that we have considered only electronic contribution to dielectric constant. Hence, for our case $\epsilon_{\text{eff}} = \varepsilon_\infty$, where ε_∞ corresponds to the electronic static dielectric constant. The effective mass of electrons and holes have been calculated using Wannier-Mott approach by plotting E-*k* dispersion curve (see Figure 5.10) for pristine $(C_3H_5NH_3)_4Pb_2I_8$ and different configurations obtained after doing substitution at Pb. The parabolic fitting of the dispersion curves have been done to compute the effective mass of the electrons and holes. The effective mass can be calculated using following equation:

$$\mathrm{m}^* = \frac{\hbar^2}{\frac{d^2\mathrm{E}(k)}{dk^2}} \tag{5.8}$$

where m* is the effective mass, E(k) is the energy, k is the wave vector, and $\hbar$ is the reduced Plank's constant. The calculated effective mass, reduced mass in terms of rest mass of electron (m_0) and exciton binding energy are tabulated in Table 5.3. From Table 5.3, we have observed that these compounds exhibit large exciton binding energy. On substituting Sn at Pb the exciton binding energy increases whereas it decreases when we substitute Ge at Pb. Large exciton binding energy shows that electron-hole pairs are strongly bouned in these materials than in conventional lead halide perovskites [220].[3]

Table 5.2: SLME of different stable conformers at 6 μm absorber layer thickness

Conformers	SLME (HSE06) (%)	SLME (HSE06+SOC) (%)
$(C_3H_5NH_3)_4Pb_2I_8$	4.26	20.02
$(C_3H_5NH_3)_4GePbI_8$	11.16	20.02
$(C_3H_5NH_3)_4SnPbI_8$	12.10	21.54
$(C_3H_5NH_3)_4Sn_2I_8$	23.85	23.78

5.3.8 Electron-phonon coupling strength

Electron-phonon coupling is an alluring paradox as it influences the physical/chemical properties of a material. In polar semiconductors (e.g., lead halide perovskites), the charge carriers interact with macroscopic electric field generated by longitudinal optical (LO) phonons,

---

[3] Note that here in order to predict the exciton binding energy (E_B), we have employed Wannier-Mott approach along with Fermi's golden rule. However, correct E_B can be obtained using BSE approach. Since our system consists of large number of atoms i.e. 58 atoms, it is computationally challenging to converge GW or BSE for large super cells with sufficiently large k-mesh and vacant orbitals. Moreover, Wannier-Mott is a well established approach to predict E_B in semiconductors. Hence, we can assume that provided numbers are sufficient enough to understand the trend of E_B in pristine and mixed conformers. Notably, here we have ignored the role of ionic contribution to dielectric constant as it is negligible for these systems.

known as the Fröhlich interaction. Hence, we have also studied electron-phonon coupling in our prototypical system ($(C_3H_5NH_3)_4Pb_2I_8$) using mesoscopic model, viz., Fröhlich's polaron model. Fröhlich coupling strength can be measured in terms of a dimensionless Fröhlich parameter [254] α that is given as:

$$\alpha = \frac{1}{4\pi\epsilon_0}\frac{1}{2}\left(\frac{1}{\epsilon_\infty} - \frac{1}{\epsilon_{\text{static}}}\right)\frac{\mathrm{e}^2}{\hbar\omega_{\text{LO}}}\left(\frac{2\mathrm{m}^*\omega_{\text{LO}}}{\hbar}\right)^{1/2} \tag{5.9}$$

where ϵ_∞ and ϵ_{static} correspond to the electronic and ionic static dielectric constants, respectively. m^* is the effective mass. ϵ_0 is the permittivity of free space. The characteristic frequency ω_{LO} can be calculated by taking the spectral average of all the possible infrared active optical phonon branches [255]. The calculated characteristic frequency and electron-phonon coupling constant for pristine ($(C_3H_5NH_3)_4Pb_2I_8$) are 3013.04 cm^{-1} and 0.67, respectively. Note that, the electron-phonon coupling constant is relatively smaller than that of hybrid halide perovskites [256]. Hence, electron-phonon coupling is expected to be smaller in Sn/Ge substituted configurations as well. From above results, we have observed that if we completely replace the Pb with Sn in hybrid layered perovskites the power conversion efficiency increases but decrease in the carrier mobility will degrade the practical performance. Hence, we have studied the lead free hybrid perovskites and studied the role of defects in such systems. Here, we have studied monoclinic 2D $(PEA)_4NaInCl_8$ and its Mn^{2+} doped configurations. First, to gain more insights at the atomistic level on how the dopant distribution affects the lattice, we have performed the DFT calculations to understand which dopant configuration leads to the lattice contraction or expansion. First lattice constants are obtained for pristine, Mn^{2+} substitutionally doped, and Mn^{2+} interstitially doped 2D $(PEA)_4NaInCl_8$ configurations. The optimized lattice constants of monoclinic 2D $(PEA)_4NaInCl_8$ and Mn^{2+} doped configurations are given in Table 5.4. Substitutional sites (In and Na) doping by Mn^{2+} results in overall lattice contraction (see Figure 5.14(a) and Table 5.15). On the other hand, for Mn^{2+} interstitially doped perovskite, the Mn^{2+} atom resides between two benzene rings, bounded with H and C atoms of two benzene rings close to the octahedra. Pushing them apart from each other, hence causing expansion in the lattice (see Figure 5.14(b) and Table 5.4). Optimized DFT model for pristine LDP, its band structure and partial density of states (pDOS) are shown in Figure 5.15.In undoped system, conduction band minima (CBM) is contributed by hybridized orbital of In 6s and Cl 3p orbitals. Here, 6s orbital of In is strongly hybridized with the 3p orbital of Cl, not with other orbitals. Hence, we observe a single band at CBM, whereas other dispersive conduction bands are slightly higher in energy. In valence band maxima (VBM), maximum contribution is

Table 5.3: Effective mass of hole m_h^*, electron m_e^*, reduced mass μ in terms of rest mass of electron m_0, static value of electronic dielectric constant (ε_∞), and exciton binding energy E_B (eV).

Conformers	m_h^*	m_e^*	μ	ε_∞	E_B (eV)
$(C_3H_5NH_3)_4Pb_2I_8$	-0.48	0.28	0.67	3.37	0.80
$(C_3H_5NH_3)_4GePbI_8$	-0.47	0.25	0.53	3.42	0.61
$(C_3H_5NH_3)_4Ge_2I_8$	-0.48	0.23	0.44	3.48	0.49
$(C_3H_5NH_3)_4SnPbI_8$	-0.40	0.26	0.74	3.41	0.87
$(C_3H_5NH_3)_4Sn_2I_8$	-0. 31	0.24	1.06	3.43	1.23

Table 5.4: Lattice parameters of pristine and Mn^{2+} doped configurations, with respective change in the lattice parameters with respect to pristine.

Configuration	a (Å)	b (Å)	c (Å)	Δ a%	Δ b%	Δ c%
$(PEA)_4NaInCl_8$	6.59	38.09	6.48	0	0	0
Substitutionally doped system	6.56	37.98	6.47	-0.46	-0.29	-0.15
Interstitially doped system	6.82	38.21	6.77	+3.49	+0.32	+4.48

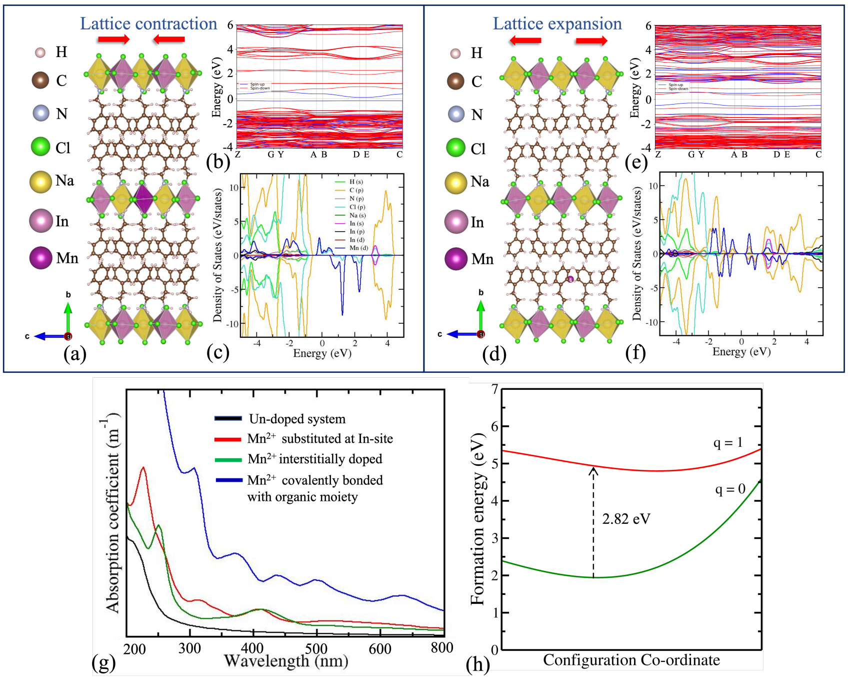

Figure 5.14: Single Mn^{+2} substitutionally doped at In-site of 2D RP $(PEA)_4NaInCl_8$ (a) optimized crystal structure of unit cell (b) band structure and (c) partial Density of States (pDOS). Single Mn^{+2} interstitially doped 2D RP $(PEA)_4NaInCl_8$ (d) optimized crystal structure of unit cell, (e) band structure and (f) pDOS. (g) Variation of absorption coefficient with the wavelength doped at In-site of 2D RP $(PEA)_4NaInCl_8$. (h) As a function of the displacement of atoms, the formation energies in two different charges states i.e., q=0 and q=1 are plotted.

from Cl 3p and C 2p orbitals. From the band structure, the VBM and CBM both lie at the Γ point with a band gap estimated to be 3.5 eV, which is not in agreement with the experimental value of 4.5 eV. Note that, we have done all DFT calculations with Perdew Burke–Ernzerhof (PBE) functional, which underestimates the band gap owing to self-interaction error of a many-electron system.

To overcome this problem advanced hybrid exchange–correlation (ϵ_{xc}) functional viz. HSE06 or GW becomes essential. As our unit cell consists of 188 atoms, doing HSE06 or GW is computationally very expensive and beyond our scope. However, the inferences derived from the present calculations should be qualitatively correct. The band structure and pDOS for substitutionally and interstitially doped configurations are shown in Figure 5.14(b,c) and Figure 5.14(e,f), respectively. In substitutionally doped system, VBM is contributed by C 2p and CBM is contributed by C 2p, In 5s, Cl 3p orbitals. A slight increase ($\sim$0.02 eV) in the band gap of dispersive bands is observed for the case of substitutionally doped system. Whereas, in interstitially doped system, VBM is contributed by C 2p and Mn 3d orbitals and CBM is

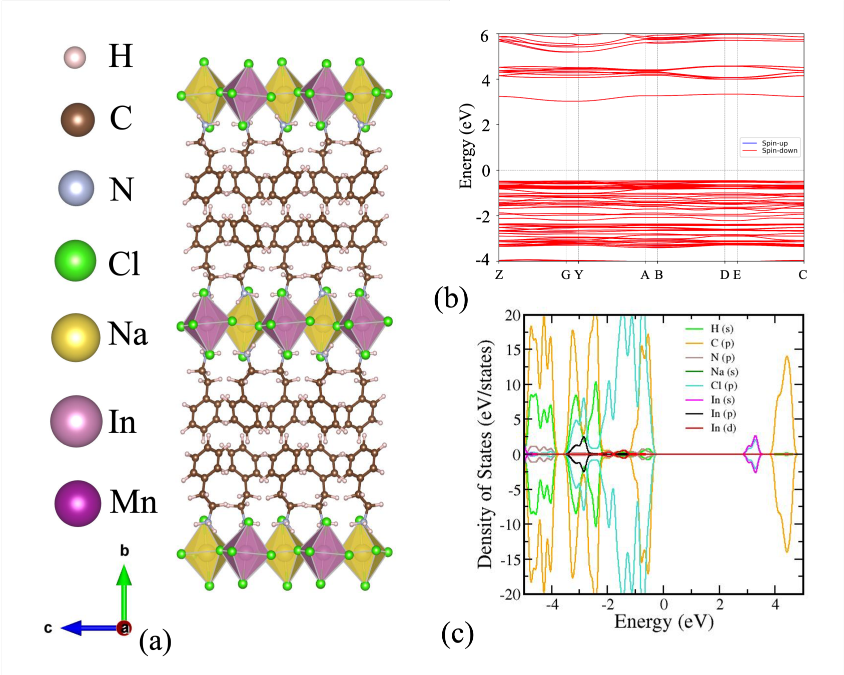

Figure 5.15: (a) Optimized crystal structure, (b) band structure, and (c) partial Density of States (pDOS) of 2D $(PEA)_4NaInCl_8$.

contributed by C 2p, In 5s, Cl 3p and Mn 3d orbitals. Mid-gap states are introduced by the impurity; doping Mn^{2+} either substitutionally or interstitially. For substitutionally doped system, there are two spin-up and two spin-down mid-gap bands. The lowest spin-up band lies 0.54 eV above the VBM. Two spin-down lies 0.81 eV below the CBM. As it is seen from the pDOS that these mid-gap bands are contributed by the Mn^{2+} 3d orbitals and bounded Cl 3p orbitals. Here, we expect Mn^{2+} d-d transition from spin-up bands above the VBM to spin-down bands below the CBM. In interstitially doped system, from band structure and pDOS, we observe three spin-up and three spin-down mid-gap bands. Where, two spin-up and one spin-down lie near the VBM. One spin-up and two spin-down bands lie near the CBM. Mn^{2+} d-d transitions from middle gap spin-up/spin-down bands near VBM to spin-down/spin-up bands near CBM in addition to band gap transition are expected.

Further, we have also plotted absorption spectrum using DFT approach by calculating dielectric coefficients for pristine and Mn^{2+} doped configurations. So that we can observe the red shifted absorption in case of Mn^{2+} doped configurations and absorption peak due to d-d transitions. Notably, as we have used PBE functional, we have manually shifted the energy by 12.04 eV so that the absorption peak of pristine coincides with that of experimental. From Figure 5.14(g), we can see that the absorption peak from the band gap transition is slightly red-shifted in the case of Mn^{2+} substitutionally doped and even more red-shifted in case of Mn^{2+}

interstitially doped. In the case of Mn^{2+} doped configuration, the absorption peak at 420 nm corresponds to the Mn^{2+} d-d transition, which is absent in the case of pristine LDPs.

Lastly, to capture the optical transition for the Mn^{2+} substituted at In-site, we have also plotted the configuration coordinate (CC) diagram [159]. As Mn^{2+} substituted at In-site is a cation, hence we have shown optical transition from q=0 state to q=1 state (see Figure 5.14(h)). Here, absorption peak occurs at 2.82 eV i.e, in agreement with the experimental value.

5.4 Conclusion

We have systematically investigated the structural and optoelectronic properties of (un)defected 2D hybrid $(C_3H_5NH_3)_2PbI_4$, using first principles calculations. The spin-orbit splitting of conduction band is noticeable, which leads to a decrement in the bandgap. Therefore, SOC effect has been duly considered in all the calculations to determine accurate optical properties of mixed conformers. The 2D perovskite material CPPI is a wide bandgap semiconductor with a poor absorption spectrum. We have tuned the bandgap of CPPI system by substituting less toxic alternatives Ge and Sn in place of toxic element Pb, and observed the enhancement in the optoelectronic properties of the system. Similarly, we can tune the bandgap and enhance the optoelectronic properties in the case of compounds CBPI, CPEPI, and CHXPI. We have observed that complete removal of toxic Pb from CPPI is possible using Sn, whereas only partial replacement of Pb is possible with Ge. Moreover, the mixed conformers with Sn are more stable and have higher PCE in comparison to the conformers with Ge. Thus, we conclude that Sn substitution is more favorable in comparison to Ge substitution to replace toxic lead from CPPI. Lead-free 2D halide perovskite $(C_3H_5NH_3)_2SnI_4$ has highest efficiency with enhanced stability, which is useful for PV devices. Pristine and mixed configurations exhibit large exciton binding energy. The electron-phonon coupling is smaller than conventional lead halide perovskites. These results give more promise for experimental realization of more these type of new lead-free 2D perovskites for optoelectronic devices. We have concluded that lattice contracts and expands when Mn^{2+} doped substitutionally and interstitially, respectively in lead free hybrid 2D RP $(PEA)_4NaInCl_8$. Moreover, several red shifted peaks are absorbed for the doped systems owing to the Mn^{2+} d-d transition.

CHAPTER 6

Exciton and polaron dominated photo-physical phenomena in Ruddlesden popper phases of chalcogenide perovskites

6.1 Introduction

Perovskites with general chemical formula ABX_3 have found great attention in dielectric, optoelectronics, and solar cell applications due to their superb ferroelectric, piezoelectric, superconductive and photovoltaic properties [257, 258, 259]. During the last decade, in the field of solar cell applications, hybrid lead-halide perovskites namely, $CH_3NH_3PbX_3$ and $CH(NH_2)_2PbX_3$ (X = Cl, Br and I) have achieved great success owing to their small band gap, long carrier mobility, low manufacturing cost and high power conversion efficiency [260, 261, 262, 263, 264, 265, 266]. However, due to the presence of organic molecules, the stability of perovskites is affected towards heat, light and moisture, thereby degrading their efficiency with time in the practical world [173]. Moreover, presence of toxic lead in these materials makes them hazardous for the environment [174]. These shortcomings have hindered their practical applications.

In search of alternative perovskites that can alleviate the limitations of lead-halide perovskites, chalcogenide perovskites with S or Se-anion have been proposed for photovoltaic applications [267]. Several prototypical chalcogenide perovskites (viz. $SrHfS_3$ [268], $AZrS_3$ (A = Sr, Ca, Ba) [269, 270, 271], along with their related phases) have been synthesized successfully. Amongst them, $BaZrS_3$ consists of earth-abundant elements and is having moderate band gap ($\sim$1.82 eV [272]) ideal for photovoltaics. Moreover, it also exhibits ambipolar doping [273] and is stable against different environmental conditions [274]. In order to optimize the solar cell absorption, doping at Ba/Zr-sites have been attempted in this material [275, 271, 276]. However, such doped/alloyed configurations seem to lack stability [277]. Thin films of $BaZrS_3$ are also reported, which has directed the research towards its new phases named as Ruddlesden-Popper (RP) phases [278]. Tremendous efforts have been invested to tune the electrical and optical properties [272]. The RP phases as an imitative of the perovskite structure are evolving as a semiconductor for optoelectronic applications [279, 280]. Their general formula is $A_{n+1}B_nX_{3n+1}$, where perovskite structure blocks of unit cell thickness "n" are separated by rock salt layer AX along [001] direction. Alternate perovskite blocks are displaced in in-plane direction by half of the unit cell. The RP phases are included in the broad category of "2D perovskites" owing to their layered structural arrangement (see Figure 6.2). Note that several studies assigning to the layered perovskites as "2D perovskites" exist in the literature, where periodic stacking of perovskite layers result in a bulk structure. Their material properties can be tuned either by substitution or dimensional reduction [200, 221, 281]. Due to quantum confinement effects [282], considerable change in bulk physical properties (such as bulk modulus, elastic modulus, charge carrier properties and optical properties) can be seen on reducing the dimension of material [283, 11]. Research in this field is highly evolving [280, 284, 285, 10]. In optoelectronic materials exciton formation greatly influence the charge separation properties and hence, excitonic parameter such as exciton binding energy (E_B) acts as an important descriptor for optoelectronic applications. Solar cell performance depends upon the fraction of thermally dissociated excitons into electrons and holes, giving rise to the free-charge carriers. In addition, the concept of polarons has been used to explain multiple photo-physical phenomena in these materials [286]. Polaronic effects have been suggested to play an important role in the excitation dynamics and carrier transport. The separation of free charge is also influenced by the carrier mobility. Hence understanding the effect of electron-phonon coupling in terms of polaron mobility is important. A systematic study on the excitonic and polaronic effect in the RP phases of $BaZrS_3$ is hitherto unknown. The present Letter, therefore, explores the excitonic properties along with polaronic effect in RP phases of $Ba_{n+1}Zr_nS_{3n+1}$ (n=[1-3]) under the framework of Many Body Perturbation Theory. The electron-phonon coupling is also taken care of using Fröhlich model to compute the polaron mobility.

6.2 Methodology

We have executed a systematic study to explore the optical, electronic and excitonic properties using Density Functional Theory (DFT) [11, 10] and beyond approaches under the framework of Many Body Perturbation Theory [287, 288, 159]. All calculations are performed with Projected Augmented Wave (PAW) potentials as implemented in Vienna *Ab initio* Simulation Package (VASP) [244, 289]. The PAW potential of elements viz., Ba, Zr and S contain ten, twelve and six valence electrons, respectively. $Ba_{n+1}Zr_nS_{3n+1}$ (n=[1-3]) RP phases are tetragonal structure having space group I4/mmm [139]. All the structures are optimized using Generalized Gradient Approximation (GGA) as implemented in PBE [33] exchange-correlation (ϵ_{xc}) functional until the forces are smaller than 0.001 eV/Å. The Γ-centered 2×2×2 k-mesh sampling is employed for optimization calculations (optimized structures are shown in Figure 6.2). The electronic self-consistency loop convergence is set to 0.01 meV, and the kinetic energy cutoff is set to 600 eV for plane wave basis set expansion. To explore the optical properties and excitonic effects, Bethe-Salpeter Equation (BSE) is solved. Initially, we have used light 4×4×1 k-mesh for energy calculation (see Figure 6.1(a)). The convergence criteria for the number of occupied and unoccupied bands in BSE calculations is shown in Figure 6.1(b)). In order to have improved spectral features with denser k-mesh, we have employed the model-BSE (mBSE) [290] approach. Following this, we have performed Density Functional Perturbation Theory (DFPT) [291] with k-mesh 12×12×1, to discern the role of ionic contribution to dielectric function along with electronic contribution. Note that for GW and BSE calculations, we have used converged NBANDS i.e., 800. Lastly, by employing Fröhlich model approach [256], we have studied polaron effect in our systems. All the calculations are very well validated and benchmarked to test the convergence details, which are given in SI to ensure that the numbers are devoid of numerical error.

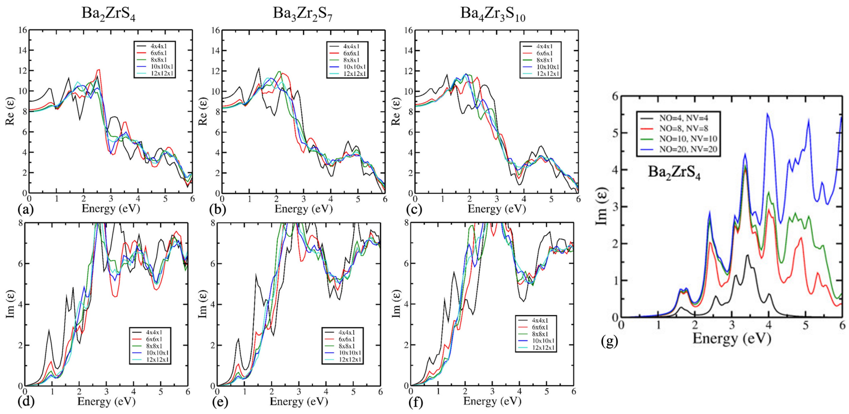

Figure 6.1: (a) Real (Re(ε)) and imaginary (Im(ε)) part of dielectric function for $Ba_{n+1}Zr_nS_{3n+1}$ (n=[1-3]) RP phases using PBE exchange-correlation ϵ_{xc} functional. (b) Variation of imaginary part (Im(ε)) of dielectric function with number of occupied (NO) and unoccupied (NV) bands using BSE for Ba_2ZrS_4.

6.3 Results

The exciton binding energy is defined as the energy required to decouple the exciton into individual electron (e) and hole (h) pair. Theoretically, the exciton binding energy (E_B) is calculated by taking the difference of the energy of bounded electron-hole (e-h) pair (i.e., BSE gap) and unbounded e-h pair (i.e., GW gap). In order to determine the optical response of $Ba_{n+1}Zr_nS_{3n+1}$ (n=[1-3]) RP phases, we have calculated the imaginary part of dielectric function (Im (ϵ)). Initially, we have benchmarked the exchange-correlation (ϵ_{xc}) functional for our system. As it is already known that single shot GW (G_0W_0) calculation strongly depends on the starting point, we need to validate the suitable starting point for G_0W_0 calculation. Note that spin-orbit coupling (SOC) effect is negligible in these systems (see Figure 6.3). Hence, we have excluded SOC in our calculations. The band gap of Ba_2ZrS_4, $Ba_3Zr_2S_7$ and $Ba_4Zr_3S_{10}$ are quite underestimated using PBE and the values are 0.61 eV, 0.42 eV and 0.34 eV, respectively. On the other hand, the same with default parameters (viz. exact exchange = 25% and screening parameter 0.2 $Å^{-1}$) of HSE06 are 1.39 eV, 1.18 eV and 1.08 eV, respectively. The HSE06 numbers are in good agreement with the experimental findings [272]. Further, the peak position, which is underestimated by PBE is improved by performing G_0W_0 by taking both PBE and HSE06 as a starting point, which shifts the peak to 2.11 eV (see Figure 6.6(a)) and 2.17 eV, respectively. Notably, the quasiparticle gaps computed using G_0W_0@PBE and G_0W_0@HSE06 are overestimated in comparison to the experimental band gap, as they do not take into account the exciton binding energy. Since, BSE takes into account the excitonic effect (which is ignored in G_0W_0 calculation), the results get improved when we solve the BSE to obtain optical band gap. Therefore, we have performed BSE@G_0W_0@PBE and BSE@G_0W_0@HSE06 to incorporate e-h interactions. By performing BSE@G_0W_0@PBE and BSE@G_0W_0@HSE06, we find the optical peak position of Ba_2ZrS_4 is respectively 1.71 eV (1.33 eV [272]) (see Figure 6.6(a)) and 1.85 eV (see Figure 6.4). Since, the former is more close to the experimental value, we have preferred to compute GW/BSE on top of the PBE Kohn-Sham orbitals as starting point. Similarly, we have performed G_0W_0@PBE and BSE@G_0W_0@PBE calculations to capture the optical and excitonic effect for $Ba_3Zr_2S_7$ and $Ba_4Zr_3S_{10}$, respectively. As per the previous analysis, we report the BSE peak position for $Ba_3Zr_2S_7$ and $Ba_4Zr_3S_{10}$ as 1.49 eV (1.28 eV [272]) and 1.43 eV, respectively, whereas the G_0W_0@PBE peak is obtained at 1.82 eV and 1.69 eV, respectively (see Figure 6.6(a-c)). Note that Figure 6.6(a-c) correspond to the average of opti-

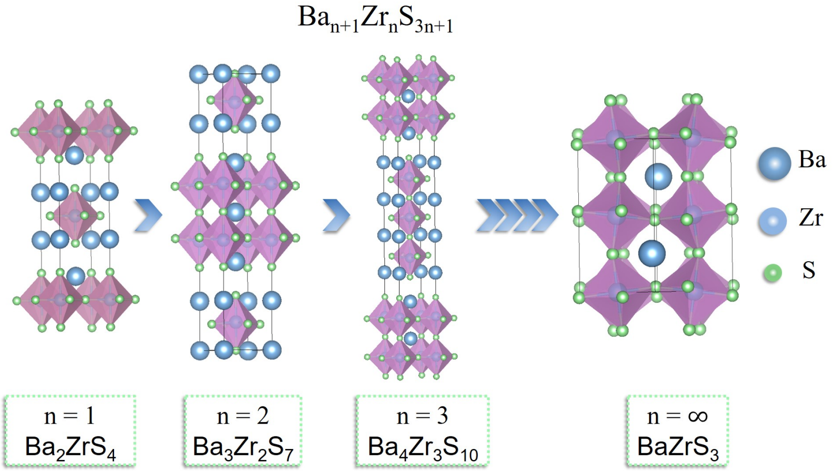

Figure 6.2: Optimized crystal structure of $Ba_{n+1}Zr_nS_{3n+1}$ (n=[1-3]) Ruddlesden-Popper phases (RP phases).

cal response in x, y and z directions. However, Figure 6.6 (d-f) and Figure 6.6 (g-i) show the directional optical response of the RP phases along E||xy and E||z direction, respectively (see discussion later).

It should be noted here that these numbers are highly dependent on the k-mesh and it's very challenging (even with the fastest supercomputers) to converge the BSE calculation to obtain the excitonic peak for computing E_B with absolute accuracy. In Figure 6.6, occurrence of red-shifted peak in BSE@G_0W_0@PBE than G_0W_0@PBE signifies the excitonic effect in the considered RP phases. The computed E_B of first bright exciton of Ba_2ZrS_4, $Ba_3Zr_2S_7$ and $Ba_4Zr_3S_{10}$ RP phases are found to be 0.40 eV, 0.33 eV and 0.26 eV, respectively. However, the discrepancy in the BSE peak position from the experimental value [272] may lead to some unprecedented error in the E_B values. Unfortunately, we have already ensured the highest possible k-mesh to compute the BSE@G_0W_0@PBE calculations. Involving a denser k-mesh is not feasible for the superstructures of RP phases for computing G_0W_0@PBE and BSE@G_0W_0@PBE – solely due to computational limitation. Therefore, this poses constrains to estimate the accurate E_B for the given systems using BSE@G_0W_0@PBE.

To compute exciton energy and E_B precisely, one needs to accurately calculate the optical spectra or optical gap using conventional BSE@G_0W_0 approach. However, there is inconsistency observed in BSE exciton peak, due to insufficient number of k-points. We can not afford higher k-mesh (viz. $\sim 8\times8\times1$) due to computational limitations even with the fastest supercomputers. This results in the incorrect E_B value. Therefore, to overcome this issue, a less expensive but robust model-BSE (mBSE) approach was proposed. In this model, the convergence of the optical spectra as a function of the number of k-mesh is performed. This method is generally based on two approximations:

(i) Using Eq. 6.1 the RPA static screening W is replaced by a simple analytical model. Here, the dielectric function is replaced by the local model function:

$$\varepsilon^{-1}_{\mathrm{G,G}}(|\mathrm{q+G}|) = 1 - (1 - \varepsilon^{-1}_{\infty})\exp(-\frac{|\mathrm{q+G}|^2}{4\lambda^2}) \tag{6.1}$$

where, ε_{∞} is the static ion-clamped dielectric function in the high frequency limit. $\varepsilon^{-1}_{\infty}$ is calculated either from DFPT or $\mathrm{G_0W_0}$. q and G are the wave vector and lattice vector of the reciprocal cell, respectively. λ is the screening length parameter, calculated by fitting ε^{-1} at small wave vectors with respect to |q+G| (see Figure 6.3 (a-c)). The parameters obtained for the $\mathrm{Ba_{n+1}Zr_nS_{3n+1}}$ (n=[1-3]) RP phases are collected in Table 6.1. In Figure 6.3 (d-f) the k-mesh convergence is also shown. Note that using BSE@$\mathrm{G_0W_0}$@PBE computing the same beyond $4 \times 4 \times 1$ k-mesh is not possible. A more detailed with even denser k-mesh convergence is also shown in Figure 6.4. Seeing it, we can say $8 \times 8 \times 1$ k-mesh is almost a converged one keeping in mind the computational cost for $10 \times 10 \times 1$ k-mesh and very minor shift of the peak w.r.t $8 \times 8 \times 1$ k-mesh.

Table 6.1: The calculated inverse of static ion-clamped dielectric function $\varepsilon^{-1}_{\infty}$ and the screening length parameter λ (Å^{-1}) used in mBSE (Eq. 6.5) for $\mathrm{Ba_{n+1}Zr_nS_{3n+1}}$ (n=[1-3]) RP phases.

$\mathrm{Ba_{n+1}Zr_nS_{3n+1}}$	$\varepsilon^{-1}_{\infty}$ (PBE)	λ (PBE)
$\mathrm{Ba_2ZrS_4}$	0.14	1.17
$\mathrm{Ba_3Zr_2S_7}$	0.15	1.19
$\mathrm{Ba_4Zr_3S_{10}}$	0.15	1.17

Now to validate the accuracy of mBSE@$\mathrm{G_0W_0}$@PBE w.r.t BSE@$\mathrm{G_0W_0}$@PBE, in Figure 6.5, we have plotted that the imaginary part of the dielectric function calculated with BSE@$\mathrm{G_0W_0}$@PBE as well as mBSE@$\mathrm{G_0W_0}$@PBE. We find the latter (mBSE@$\mathrm{G_0W_0}$@PBE) matches pretty well with the former (BSE@$\mathrm{G_0W_0}$@PBE). Seeing the spectra, we can say that the excitonic feature (i.e first peak) is also very well preserved by mBSE method. Notably, both the calculations are performed using 4×4×1 k-mesh with the same starting point since we couldn't afford BSE@$\mathrm{G_0W_0}$@PBE beyond this k-mesh. But with mBSE@$\mathrm{G_0W_0}$@PBE we

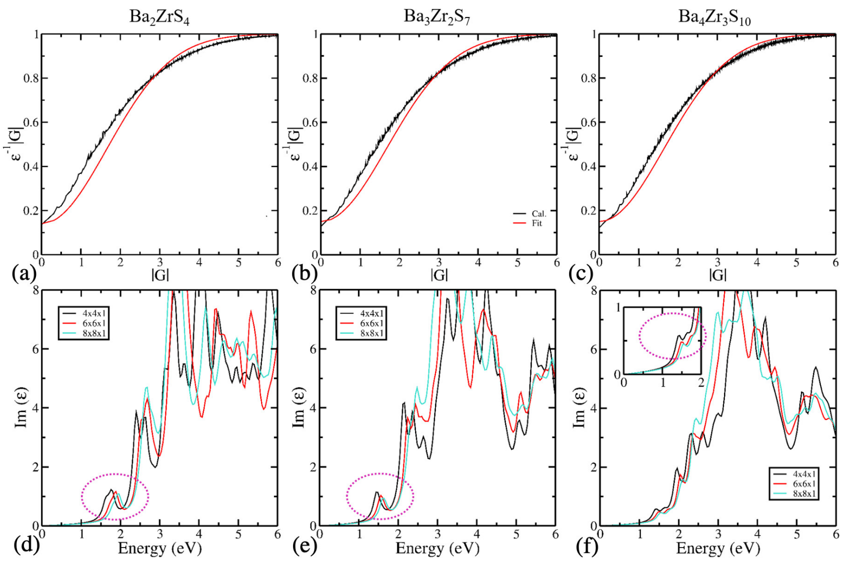

Figure 6.3: Variation of inverse of the dielectric function ε^{-1} with respect to |q+G| for (a) Ba_2ZrS_4, (b) $Ba_3Zr_2S_7$, and (c) $Ba_4Zr_3S_{10}$, respectively. The red curve is obtained by fitting based on Eq. (5). The mBSE calculated spectra with different k-mesh for (d) Ba_2ZrS_4, (e) $Ba_3Zr_2S_7$ and (f) $Ba_4Zr_3S_{10}$, respectively.

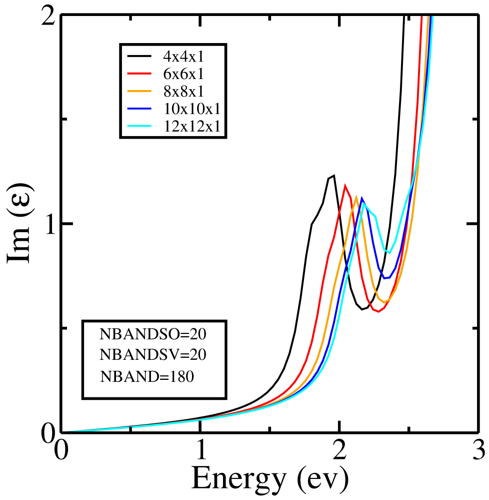

Figure 6.4: Model-BSE (mBSE) calculation with dense k-mesh and low NBANDS for Ba_2ZrS_4. Here, NBANDSO and NBANDSV correspond to number of occupied and vacant orbitals, respectively.

can do computation until 12×12×1 as shown in Figure 6.4.

As per the mBSE calculation, it is seen that a denser k-mesh sampling indeed red-shifts the BSE peak (see mBSE calculations in section V in SI). The E_B values are updated respectively to be 0.33 eV, 0.29 eV and 0.23 eV for n=[1-3] of $Ba_{n+1}Zr_nS_{3n+1}$ (with maximum possible error of ±0.03 eV as detailed in the SI section V). These numbers fall well within the range of E_B estimated via state-of-the-art method comprising of Wannier-Mott and Density Functional Perturbation Theory (DFPT) approach as explained later. The first two excitons are bright excitons in the considered RP phases and several dark excitons also exist below the second bright exciton of these systems. From the above studies, it's also noted the order of E_B of $Ba_{n+1}Zr_nS_{3n+1}$ follows a trend viz. n = 1 > n = 2 > n = 3 > n = ∞ (i.e., bulk $BaZrS_3$ [292]). Moreover, for Ba_2ZrS_4 (i.e. n = 1 RP phase) the difference between the direct and indirect band gap is ∼0.1 eV, which increases to ∼0.3 eV in case of n = 2, 3 RP phases. The optimal value of the band gap and relatively smaller difference between direct and indirect values for n = 1 RP phase, may suggest this to be ideal for solar cell application. Next, we have computed other

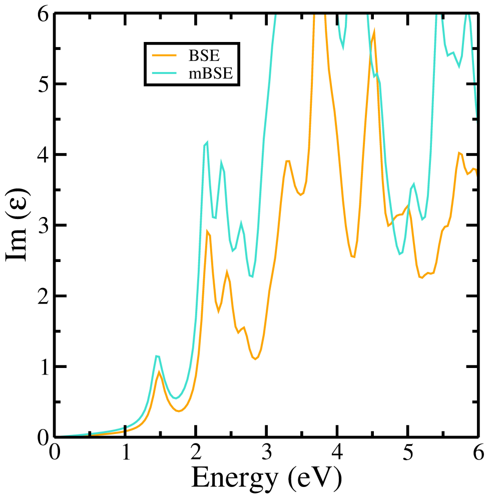

Figure 6.5: Imaginary part (Im (ε)) of the dielectric functional for $Ba_3Zr_2S_7$ using BSE and mBSE.

excitonic parameters. The excitonic lifetime (τ) is inversely proportional to the probability of wavefunction for electron-hole pair at zero seperation ($|\phi_n(0)|^2$). The excitonic temperature can be calculated by using relation that $E = k_BT$, where E, k_B and T correspond to energy, Boltzmann constant and temperature, respectively. The exciton radius (r_{exc}) is determined as follows:

$$r_{exc} = \frac{m_0}{\mu}\varepsilon_{eff}n^2 r_{Ry} \tag{6.2}$$

where m_0, μ, ε_{eff} and n are the free electron mass, reduced mass, static effective dielectric constant, and exciton energy level, respectively. r_{Ry} is the Bohr radius for 2D system i.e., half of the Bohr radius for 3D system. Hence, in our case $r_{Ry} = 0.0529/2 = 0.0265$ nm. Using excitonic radius we can calculate the probability of wavefunction for e-h at zero separation as follows:

$$|\phi_n(0)|^2 = \frac{1}{\pi(r_{exc})^3 n^3} \tag{6.3}$$

The excitonic parameters (computed using mBSE approach) are tabulated in Table 6.2. We find the probability of wavefunction for e-h pair at zero separation ($|\phi_n(0)|^2$) decreases on increasing

Table 6.2: Excitonic parameters for RP phases (calculated using mBSE@G_0W_0@PBE).

Excitonic parameters	Ba_2ZrS_4	$Ba_3Zr_2S_7$	$Ba_4Zr_3S_{10}$
E_B (eV)	0.33	0.29	0.23
T_{exc} (K)	3804	3364	2669
r_{exc} (nm)	0.34	0.37	0.55
$\lvert\phi_n(0)\rvert^2(10^{27}m^{-3})$	8.10	6.28	1.91
$\frac{1}{\lvert\phi_n(0)\rvert^2}(10^{-27}m^3)$	0.12	0.20	0.52

n in $Ba_{n+1}Zr_nS_{3n+1}$. Hence, the lifetime τ is expected to get increased with increasing n in $Ba_{n+1}Zr_nS_{3n+1}$ i.e., $\tau_{n=3} > \tau_{n=2} > \tau_{n=1}$. Note that the trend in the exciton lifetime can also be further verified from mBSE peaks. This is estimated from the Full Width at Half Maxima (FWHM) of the first peak of Im(ε). In Figure 6.7, we have shown the broadening of excitonic peak, which is well in agreement with previous experiments [272]. Therefore, the qualitative trend of exciton lifetime for $Ba_{n+1}Zr_nS_{3n+1}$ (n=[1-3]) is $\tau_{n=3} > \tau_{n=2} > \tau_{n=1}$ – which is very much inline as per our findings as in Table 6.2. Here broadening has shown the contribution due to the e-h interaction and it does not include the electron-phonon coupling effect. The latter is important especially for layered systems. But since the trend matches well with the experiment [272] it's therefore expected that it will remain same even after the inclusion of electron-phonon coupling. The role of electron-phonon coupling is discussed in greater details later but on a different context.

$Ba_{n+1}Zr_nS_{3n+1}$ (n=[1-3]) RP phases have tetragonal structure and exhibit optical anisotropy. Hence, it is required to study their optical and excitonic properties along E||xy (i.e., in-plane along x- or y-direction) and E||z (i.e., out-of-plane along z-direction) direction. We have observed anisotropy in Ba_2ZrS_4, $Ba_3Zr_2S_7$ and $Ba_4Zr_3S_{10}$ which can greatly affect their performance in practical application. Therefore, it is of paramount importance to understand the anisotropic effect in the optical and excitonic properties of $Ba_{n+1}Zr_nS_{3n+1}$ (n=[1-3]) RP phases. In Figure 6.6 (d-i), we have shown optical and excitonic contribution of $Ba_{n+1}Zr_nS_{3n+1}$ (n=[1-3]) RP phases along different directions viz. x, y and z. Employing Shockley-Queisser (SQ) criterion [206] for the solar cell and other optoelectronic devices, we can remark that $Ba_{n+1}Zr_nS_{3n+1}$ (n=[1-3]) RP phases are optically active in in-plane (i.e., along x- and y-direction) and optically inactive in out-of-plane (i.e., z-direction). These systems possess similar optical as well as ex-

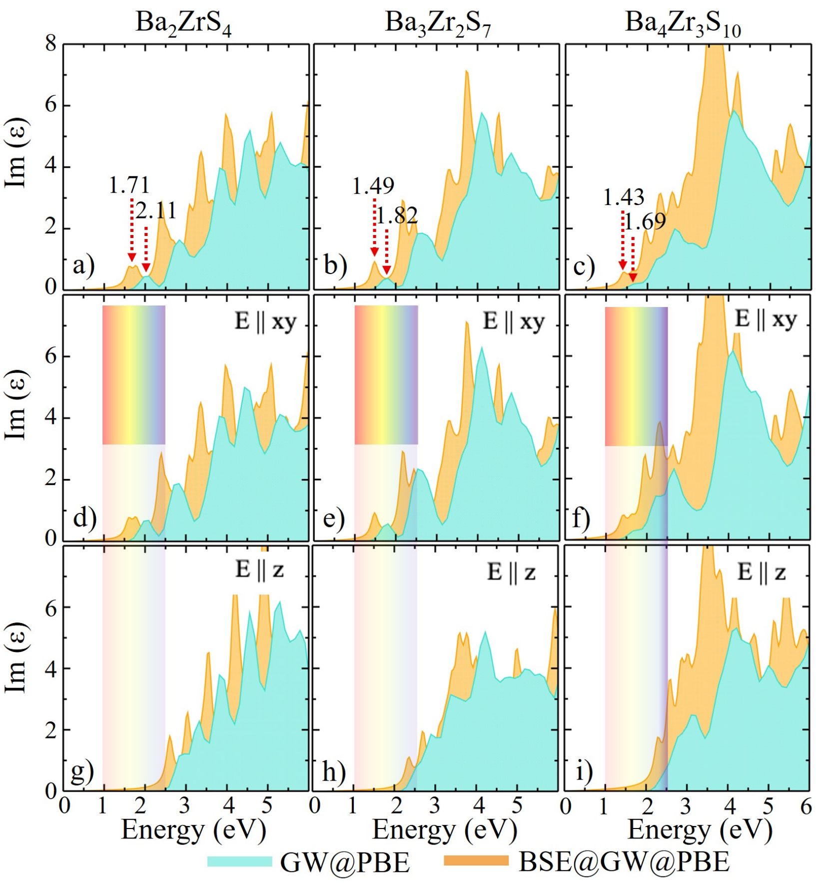

Figure 6.6: Imaginary part (Im (ϵ)) of the dielectric function for (a) Ba_2ZrS_4, (b) $Ba_3Zr_2S_7$, (c) $Ba_4Zr_3S_{10}$ using single shot GW (G_0W_0) and BSE. Im(ε) of dielectric function for (d) Ba_2ZrS_4 (e) $Ba_3Zr_2S_7$ and (f) $Ba_4Zr_3S_{10}$ along E || xy direction and Im(ε) of dielectric function for (g) Ba_2ZrS_4 (h) $Ba_3Zr_2S_7$ and (i) $Ba_4Zr_3S_{10}$ along E || z direction, using G_0W_0 and BSE. Here, coloured region is indicating the energy window that lies in visible region of electromagnetic spectra.

citonic properties along x- and y-direction (see Figure 6.6(d-f)). However, along z-direction, their optical and excitonic spectra are not only blue-shifted but also the feature of G_0W_0 and BSE peaks are quite different than that in case of in-plane direction (see Figure 6.6(g-i)). It is well known that exciton lifetime is inversely proportional to the width of the exciton peak. Hence, change in the feature of exciton peak greatly influences the excitonic parameters as well in different directions. The d-orbital contribution in valence band maximum (VBM) and conduction band minimum (CBm) could be responsible for the optical anisotropy in these systems. In bulk $BaZrS_3$, we have observed that Ba(6s), Zr(4d) and S(2p) orbitals are hybridized in the VBM. It is basically dominated by $2p_x$, $2p_y$, $2p_z$ orbitals of S element. The CBm of bulk $BaZrS_3$, consists hybridized orbitals of S($2p_x$, $2p_y$, $2p_z$) and Zr($4d_{xy}$, $4d_{yz}$, $4d_{xz}$, $4d_{z^2}$). Now, in case of Ba_2ZrS_4, the VBM hybridization is same as that of bulk $BaZrS_3$. However, in CBm,

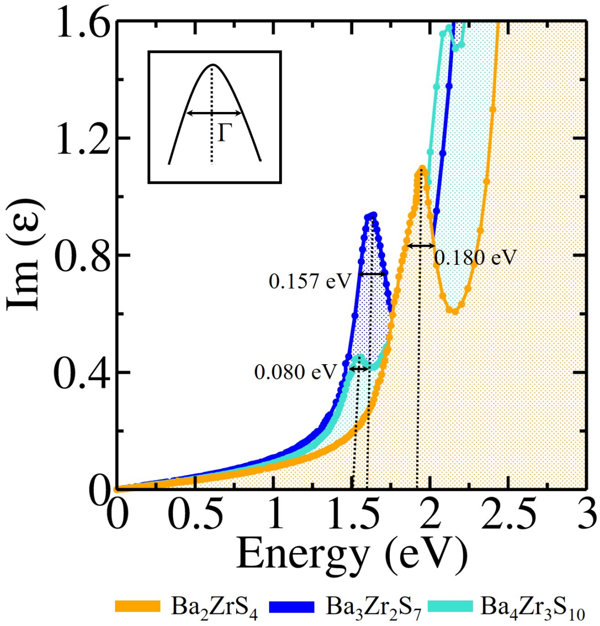

Figure 6.7: Full width at half maximum (FWHM) of exciton peak using mBSE@G_0W_0@PBE approach with dense k-mesh. Broadening of exciton peak is mainly due to electron-hole interaction. Here, Γ corresponds to the FWHM.

d_{xy} is strongly hybridized with S(2p)/Ba(6s)-orbitals and d_{yz}, d_{xz} are weakly hybridized. The hybridized orbitals obtained from the mixing of d_{yz}, d_{xz} and other orbitals of S and Ba are of higher energy. One the other hand orbitals that include d_{xy} are of lower energy. This results in polarization dependent optical gap. As CBm is contributed by d_{xy}, the optical transitions are allowed only for in-plane polarized light and not for out-of-plane polarized light. We have used Wannier-Mott model [253] for a simple screened Coulomb potential. Recently, it's reported that excitons of the RP phases of $MAPbX_3$ are known to be strongly influenced by the quantum confinement effects in the z-direction, exhibiting a quasi-2D character [293, 294]. In the present case as well, we notice the difference in the xy and z-direction spectrum, which signifies overall weak hybridization along z-direction. [1] For n = 1, 2 it's expected more to follow the 2D Wannier-Mott model. However for n = 3 or above the numbers generated via 3D

---

[1] In Ref. [294] we also note that with increasing number of layers, there is deviation from ideal 2D nature. This has been attributed to the screened Coulomb potential. In view of this due to unavailability of experiments, we have performed our calculation using Wannier-Mott model for 3D excitons as well. Despite for low dimensional systems it's expected that the excitons follow the 2D model, there are reports, where sometimes it shows deviation from ideal 2D nature. This has been attributed to the screened Coulomb potential. Due to this ambiguity it's called quasi-2D nature. Therefore, for n = 1, 2 it's expected more to follow the 2D Wannier-Mott model, for n = 3 or above the numbers generated via 3D Wannier-Mott may also seem to be relevant. In view of this, due to unavailability of experimental inputs in this system, we have provided theoretical values using either approaches.

Wannier-Mott may also seem to be relevant. Therefore, as per Wannier-Mott excitons in a 2D layered systems, the $\mathrm{E_B}$ for screened interacting e-h pair is given by:

$$\mathrm{E_B} = \frac{1}{(n-\frac{1}{2})^2}\left(\frac{\mu}{\epsilon_{\text{eff}}^2}\right)\mathrm{R}_\infty \tag{6.5}$$

where, μ is the reduced mass in term of rest mass of electron, ϵ_{eff} is the effective dielectric constant (which includes electronic as well as ionic contribution to dielectric constant) and R_∞ is the Rydberg constant. The reduced mass of $\mathrm{Ba_2ZrS_4}$, $\mathrm{Ba_3Z_2S_7}$ and $\mathrm{Ba_4Zr_3S_{10}}$ in term of electron rest mass are 0.32, 0.26 and 0.23, respectively. However, in the above expression, ϵ_{eff} is still unknown for these systems. It is already reported that lattice relaxation can influence the exciton binding energy [295]. For example, if ω_{LO} corresponds to longitudinal optical phonon frequency and $\mathrm{E_B} << \hbar\omega_{\text{LO}}$, one needs to consider the effect of lattice relaxation. Therefore, for ϵ_{eff}, a value intermediate between the static electronic dielectric constant at high frequency i.e., ϵ_e and the static ionic dielectric constant at low frequency i.e., ϵ_i should be considered. However, if $\mathrm{E_B} >> \hbar\omega_{\text{LO}}$, the effect of lattice relaxation can be ignored as in such cases $\epsilon_{\text{eff}} \to \epsilon_e$, where ϵ_e is the static value of dielectric constant at high frequency that mainly consists of electronic contribution. In Figure 6.8(a-c) and Figure 6.8(d-f), we have shown the electronic and ionic contribution to the dielectric function respectively, where ionic contribution is computed using DFPT approach. Notably, electronic contribution is computed using BSE approach. The static real part of ionic dielectric constant for $\mathrm{Ba_2ZrS_4}$, $\mathrm{Ba_3Z_2S_7}$ and $\mathrm{Ba_4Zr_3S_{10}}$ are $39.35, 31.19 and 57.59$, respectively. As per Figure 6.7, a considerable increase in the static

---

According to this model the $\mathrm{E_B}$ for 3D system is given by:

$$\mathrm{E_B} = \left(\frac{\mu}{\epsilon_{\text{eff}}^2}\right)(\mathrm{R}_\infty) \tag{6.4}$$

where, μ, ϵ_{eff} and R_∞ are the reduced mass, effective dielectric constant and Rydberg constant, respectively.

Table 6.3: Electronic and ionic contribution to the dielectric constant for $\mathrm{Ba_{n+1}Zr_nS_{3n+1}}$ (n=[1-3]) RP phases, where ϵ_e and ϵ_i correspond to the static value of electronic and ionic dielectric constant, respectively. $\mathrm{E_{Bu}}$ and $\mathrm{E_{Bl}}$ correspond to upper and lower bound of exciton binding energy, respectively.

$\mathrm{Ba_{n+1}Zr_nS_{3n+1}}$	ϵ_e	$\mathrm{E_{Bu}}$ (meV)	ϵ_i	$\mathrm{E_{Bl}}$ (meV)
$\mathrm{Ba_2ZrS_4}$	8.94	56.00	39.25	2.9
$\mathrm{Ba_3Zr_2S_7}$	8.32	50.14	31.19	3.49
$\mathrm{Ba_4Zr_3S_{10}}$	8.51	63.45	57.59	1.39

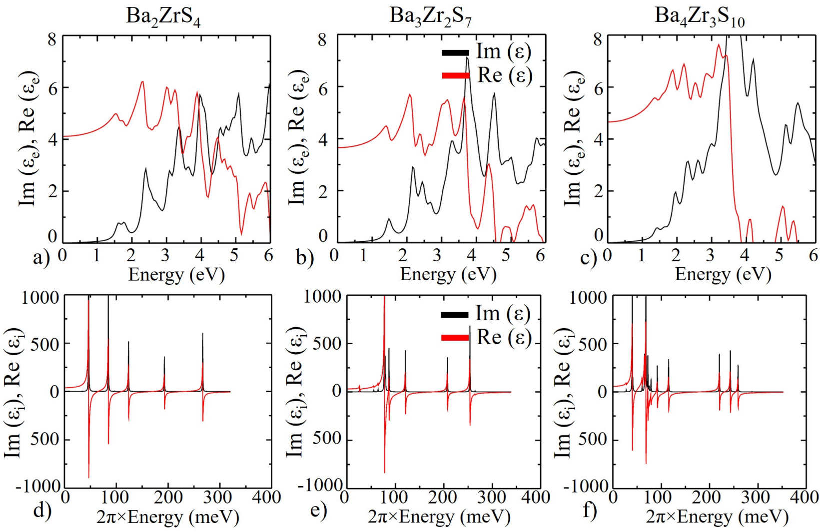

Figure 6.8: Electronic (Im (ε_e) and Re (ε_e)) (a)-(c) and ionic (Im (ε_i) and Re (ε_i)) (d)-(f) contribution to dielectric function for Ba_2ZrS_4, $Ba_3Zr_2S_7$ and $Ba_4Zr_3S_{10}$. Red and black color correspond to real (Re(ε)) and imaginary (Im(ε)), respectively.

low frequency of ionic dielectric constant is attributed to the occurrence of optically active phonon modes below 10 meV. This shows the ionic nature of the RP phases. Using electronic and ionic contribution of the dielectric constant and equation 6.5, we have calculated the upper and lower bound for the E_B (see Table6.4). The effective value of the dielectric constant and hence, the binding energy lies in between these upper and lower bounds listed in Table6.4. Note that in Table6.4, the static values of electronic and ionic dielectric constant for the considered RP phases are comparable with that of $APbX_3$ (A = MA, FA; X= I, Br) perovskites [296, 297]. Hence, we can say their optical response resembles with that of $APbX_3$ perovskites. Despite there was slight discrepency in the BSE peak position, we still can compare the E_B obtained after taking difference of G_0W_0 and BSE peaks and the same as summarized in Table6.4 using 2D Wannier-Mott model. We find the order of divergence of the upper bound value follows n = 1 > n = 2 > n = 3. This clearly implies that order of significance of ionic contribution to dielectric constant is n = 1 > n = 2 > n = 3. It means for bulk $BaZrS_3$ ionic contribution to dielectric constant must be negligible, which is in good agreement with recent report regarding bulk chalcogenide [292]. Recently, Ming *et al.* have reported the effect of strain on the band gap and octahedron rotation for Ba_2ZrS_4 [298]. According to their report, a significant change in the band gap and octahedron rotation is observed with the application of strain. However, in our case of Ba_2ZrS_4 RP phases, monotonic change in the band gap (but not as large as in case of Ming *et al.* [298]) has been observed on applying upto ±7% strain along b-axis and

Table 6.4: Electronic and ionic contribution to the dielectric constant for $Ba_{n+1}Zr_nS_{3n+1}$ (n=[1-3]) RP phases, where ϵ_e and ϵ_i correspond to the static value of electronic and ionic dielectric constant, respectively. E_{Bu} and E_{Bl} correspond to upper and lower bound of exciton binding energy, respectively.

$Ba_{n+1}Zr_nS_{3n+1}$	ϵ_e	E_{Bu} (eV)	ϵ_i	E_{Bl} (meV)
Ba_2ZrS_4	4.11	1.06	39.25	2.9
$Ba_3Zr_2S_7$	3.65	1.03	31.19	3.49
$Ba_4Zr_3S_{10}$	4.89	0.70	57.59	0.95

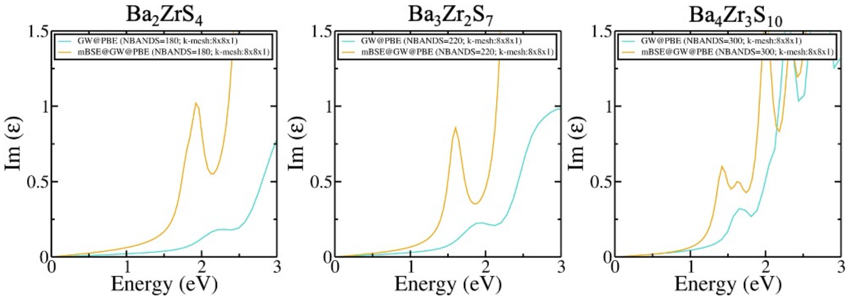

Figure 6.9: Capturing excitonic peak and estimation of E_B for the RP phases of $Ba_{n+1}Zr_nS_{3n+1}$ (n=[1-3]) using mBSE@G_0W_0@PBE method.

c-axis (see Figure 6.10). The effect on the band gap along b- and a-direction are symmetric.

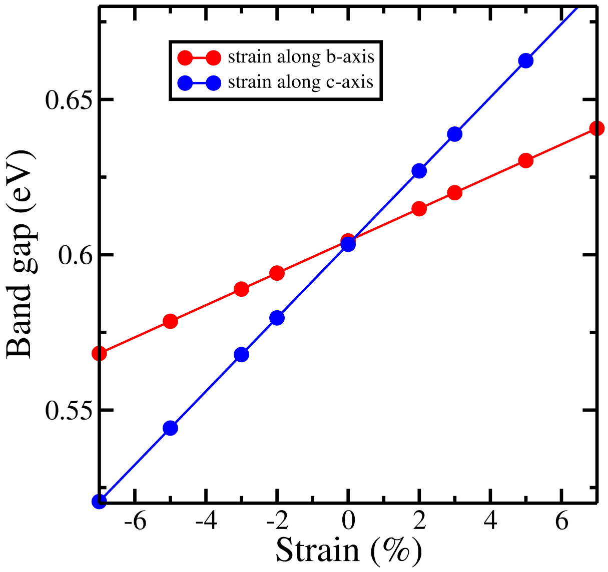

Figure 6.10: Variation of the bandgap with strain along different axis.

Further, the effect of strain on the band gap in out-of-plane direction is more significant than in in-plane direction. We have also noticed slight octahedral tilt under the application of strain along b-axis. In case of strain along c-axis, a small rotation of octahedron about c-axis has been observed. Here, we have calculated the elastic modulus of the RP phases that is given by

$$C_{2D} = \left(\frac{1}{A}\right)\frac{\delta^2 E}{\delta\varepsilon^2} \tag{6.6}$$

where A, ε and E correspond to the area of a unit cell, strain and total energy, respectively. We have observed that elastic modulus of the 2D RP phases is larger than previously reported 2D RP phases [298]. In order to compute carrier mobility, we have used deformation potential model [299, 300, 301, 302]. According to this model, the mobility of charge carrier is defined as:

$$\mu_{DP} = \frac{e\hbar^3 C_{2D}}{k_B T m^* m_d E_l^2} \tag{6.7}$$

where T is the temperature, m* is the effective mass of charge carrier and *e* is the elementary charge of electron. m_d correspond to the density-of-state effective mass that is defined as $m_d = \sqrt{m_x m_y}$. E_l is the deformation potential (for more details regarding calculation of C_{2D} and E_l see section VIII in SI). In Table 6.5, we have listed the values of C_{2D}, E_l and μ_{DP} for electron and hole of $Ba_{n+1}Zr_nS_{3n+1}$ (n=[1-3]) RP phases. As elastic modulus increases down the column (see Table 6.5), we can say that softness of the RP phases decreases on increasing the value of n in $Ba_{n+1}Zr_nS_{3n+1}$ (n=[1-3]). Mobility of electron also decreases on increasing n in $Ba_{n+1}Zr_nS_{3n+1}$ (n=[1-3]).

Table 6.5: Elastic modulus, deformation potential and predicted carrier mobility of $Ba_{n+1}Zr_nS_{3n+1}$ (n=[1-3]) RP phases.

$Ba_{n+1}Zr_nS_{3n+1}$	C_{2D} (eV Å^{-2})	E_l (eV)	μ_{DP} (cm^2 V^{-1} s^{-1})
Ba_2ZrS_4 (e)	20.02	6.36	5217.77
Ba_2ZrS_4 (h)	20.02	6.61	862.43
$Ba_3Z_2S_7$ (e)	23.77	6.41	3731. 67
$Ba_3Zr_2S_7$ (h)	23.77	6.39	57.92
$Ba_4Zr_3S_{10}$ (e)	24.11	6.72	2694.99
$Ba_4Zr_3S_{10}$ (h)	24.11	6.73	37.06

After analyzing the specific free volume (for details see section IX in SI), we find that study of electron-phonon coupling is important in these materials. Also, the presence of polarization in the RP phases lays emphasis on the polaron study. We have examined the electron-phonon

Table 6.6: Polaron parameters for $Ba_{n+1}Zr_nS_{3n+1}$ (n=[1-3]) RP phases.

width=0.70

$Ba_{n+1}Zr_nS_{3n+1}$	$1/\epsilon^*$	α	m_P/m^*	l_P (Å)	μ_P ($cm^2V^{-1}s^{-1}$)
Ba_2ZrS_4	0.09	1.84	1.39	354.30	164.75
$Ba_3Z_2S_7$	0.08	2.36	1.53	307.12	117.20
$Ba_4Zr_3S_{10}$	0.10	1.77	1.37	292.49	76.39

interaction in our system by the mesoscopic model, viz. Fröhlich's model [254, 303, 255] for the polarons. The dressed "quasiparticles", formed due to screened interaction of electron and hole by the lattice, are known as polarons. Fröhlich introduced a parameter to describe theoretically the momentum of electron in the field of polar lattice vibration. This parameter is known as dimensionless Fröhlich coupling constant [304, 254, 303].

$$\alpha = \frac{1}{\epsilon^*}\sqrt{\frac{R_y}{ch\omega_{LO}}}\sqrt{\frac{m^*}{m_e}} \tag{6.8}$$

where coupling constant α quantifies the electron-phonon coupling, m^* is the effective mass of electron, m_e is the rest mass of the electron, h is Planck's constant, c is the speed of light, ω_{LO} (in [cm^{-1}] units) is the optical phonon frequency, $1/\epsilon^*$ is the ionic screening parameter ($1/\epsilon^*$ = $1/\epsilon_\infty$ - $1/\epsilon_{static}$ where, ϵ_{static} and ϵ_∞ are static and high frequency dielectric constant) and R_y is the Rydberg energy. We have observed that electron-phonon coupling constant of considered RP phases (Table6.6), are smaller than that of their bulk $BaZrS_3$ [292]. Further, using the extended form of Fröhlich's polaron theory, given by Feynman, the effective mass of polaron (m_P) [303] is defined as:

$$m_P = m^*\left(1 + \frac{\alpha}{6} + \frac{\alpha^2}{40} + ...\right) \tag{6.9}$$

where m^* is the effective mass calculated from the band structure calculations (see section VII in SI). The polaron radii [305] can be calculated as follows:

$$l_P = \sqrt{\frac{h}{2cm^*\omega_{LO}}} \tag{6.10}$$

Polaron mobility according to the Hellwarth polaron model is defined as follows:

$$\mu_P = \frac{(3\sqrt{\pi}e)}{2\pi c\omega_{LO}m^*\alpha}\frac{\sinh(\beta/2)}{\beta^{5/2}}\frac{w^3}{v^3}\frac{1}{K} \tag{6.11}$$

where, $\beta = \mathrm{hc}\omega_{\mathrm{LO}}/k_{\mathrm{B}}\mathrm{T}$, *w* and *v* correspond to temperature dependent variational parameters. *K* is a function of *v*, *w*, and β [255] i.e., defined as follows:

$$K(a,b) = \int_0^\infty du[u^2 + a^2 - b\cos(vu)]^{-3/2}\cos(u) \tag{6.12}$$

Here, a^2 and b are calculated as:

$$a^2 = (\beta/2)^2 + \frac{(v^2 - w^2)}{w^2 v}\beta coth(\beta v/2) \tag{6.13}$$

$$b = \frac{(v^2 - w^2)}{w^2 v}\frac{\beta}{\sinh(\beta v/2)} \tag{6.14}$$

We have used lowest frequency of LO phonon i.e, 1.34, 1.46 and 1.36 THz for Ba_2ZrS_4, $Ba_3Zr_2S_7$ and $Ba_4Zr_3S_{10}$, respectively for our calculation (see Figure 6.8(d-f)). μ_{P} gives the upper limit of the charge carrier mobility, under the assumption that charge carrier (electron) interact only with the optical phonon. A significant change in the mobility of charge carrier can be seen on comparing the mobility of electron without including its interaction with the optical phonon (see Table 6.5) and with including interaction with the optical phonon (see Table 6.6). Here in Table 6.6, ionic screening is indicative of the ionicity for a system. On comparing our results with the hybrid inorganic-organic halide perovskites (ionic screening of $MAPbI_3$, $MAPbBr_3$ and $MAPbCl_3$ are 0.17, 0.18 and 0.22, respectively [305]), we can say that Ba_2ZrS_4, $Ba_3Zr_2S_7$ and $Ba_4Zr_3S_{10}$ are less ionic than $MAPbX_3$ (X = Cl, Br, I). Also, the obtained coupling constant is comparable or larger than $MAPbX_3$ (see Table 6.6). The lowering of mobility of charge carriers on the inclusion of LO phonon modes indicate that optical phonon modes are dominating over the acoustical phonon modes in these materials. Note that, in the absence of experimental data, these results may help as guideline for further research. Moreover, for qualitative analysis, our results are very informative to understand the charge transport properties of these RP phases. From Table6.6, we can clearly see that on increasing n in $Ba_{n+1}Zr_nS_{3n+1}$ (n=[1-3]) i.e., down the column the polaron mobility decreases and for bulk $BaZrS_3$ [270] phase it is very small. In view of this, the considered RP phases are expected to be better optical material than their bulk phase.

6.4 Conclusions

In conclusion, we have reported the electronic and excitonic properties of the RP phases of $Ba_{n+1}Zr_nS_{3n+1}$ (n=[1-3]) using Many Body Perturbation Theory. The exciton binding energy decreases on increasing the thickness of the perovskite layer. Double peak character is observed in the first excitonic peak calculated in in-plane direction of Ba_2ZrS_4. The difference between direct and indirect band gap increases with increasing n in $Ba_{n+1}Zr_nS_{3n+1}$ (n=[1-3]), thereby, making the band gap becomes more indirect. Using Wannier-Mott approach, we have obtained the upper and lower bound of E_B, from the electronic and ionic contribution of the dielectric constant, respectively. We have observed that significance of ionic contribution to dielectric function decreases on increasing n in $Ba_{n+1}Zr_nS_{3n+1}$. The charge carrier mobility is maximum in Ba_2ZrS_4, as computed by employing deformation potential of the same. Further, amongst $Ba_{n+1}Zr_nS_{3n+1}$ and bulk $BaZrS_3$, the electron-phonon coupling constant is relatively smaller for former RP phases. From our polaron study, we conclude that the optical phonon modes are dominating as compared to the acoustical phonon modes for these systems. A large discrepancy is noticed in the mobility of charge carriers (which includes the effect of acoustical phonon modes only in electron-phonon coupling) and polaron mobility (which includes the effect of optical phonon modes in addition to the acoustic modes in electron-phonon coupling). It shows the dominating character of optical phonon modes in the electron-phonon coupling and must be studied to understand charge transport properties of RP phases. Finally, from the perspective of device applications, these RP phases are expected to be promising optoelectronic materials.

CHAPTER 7

Role of defects and surrounding on the catalytic activity of the catalyst in energy fuel and bio-mass conversion

7.1 Introduction

Any chemical substance that stimulates the chemical reaction without undergoing any change in its composition is known as catalyst. In order to control any chemical reaction or process under practically attainable environmental conditions, the catalysts act as workhorses. In our daily life, catalysts have huge impact, for example catalysts are used in fuel cells, CO_2 capture, water purification, bio-mass conversion, and air pollution remediation, etc. In this chapter, we have discussed role of defects and surrounding ligands on the catalytic activity of the catalysts.

7.2 SO_3 decomposition over silica-modified β-SiC supported $CuFe_2O_4$ catalyst: atomistic insights

There are various ways to produce hydrogen through water-splitting. One of the potential way is sulfur-iodine (S-I) thermochemical water-splitting cycle. The S-I cycle involves several reaction steps, where SO_3 decomposition is most endothermic in nature. $CuFe_2O_4$ dispersed over treated or untreated β-SiC is used for SO_3 decomposition. Here, using DFT approach, we have studied the role of O-vacancy in enhansing the catalytic activity of the $CuFe_2O_4$ catalyst.

7.2.1 Computational details

Spin-polarized density functional theory (DFT) calculations are carried out using the projected augmented wave (PAW) pseudopotential as implemented in the Vienna ab initio Simulation Package (VASP) [244, 289]. All the modeled geometries are optimized using Perdew-Burke-Ernzerholf (PBE) exchange-correlation (ϵ_{xc}) functional within generalized gradient approximation (GGA) [33]. In all of the calculations, electronic self-consistency has been attained with an energy tolerance of 105 eV. For high precision calculations, we have used a cutoff energy of 500 eV for the plane-wave basis set. For obtaining the optimized ground-state structure, HellmanFeynman forces have been converged with a limit of 0.001 eV/Åby conjugate gradient (CG) minimization. The Brillouin zone is sampled at the Γ point for all the DFT calculations. We have employed a hybrid functional (HSE06) to compute the change in Gibbs free energy for adsorption and dissociation of SO_3 molecule on top of the supported cluster. The change in Gibbs free energy (ΔG) for different reaction steps are calculated as follows:

$\Delta G_1 = G_{catalyst-SO3} - G_{SO3} - G_{catalyst}$

$\Delta G_2 = G_{SO2-catalyst-O} - G_{catalyst-SO3}$

Where Gcatalyst, G_{SO3}, $G_{catalyst+SO3}$ and $G_{SO2-catalyst-O}$ correspond to the total energy of the catalyst (supported nanoparticles i.e, $CuFe_2O_4/\beta$-SiC(T) and $CuFe_2O_4/\beta$-SiC (UT)), the adsorbate in the gas phase and the adsorbate adsorbed on the catalyst, adsorbate dissociated on the catalyst, respectively. To have qualitative understanding of the bonding nature of adsorbed configurations, electron density difference analysis is carried out. Electron density difference ($\Delta\rho$) is calculated as:

$\Delta\rho = \rho(\text{catalyst} + SO_3) - \rho(SO_3) - \rho(\text{catalyst})$

To locate the transition states (TSs) along the minimum energy path the climbing-image nudged elastic band (Cl-NEB) method is used [306]. We have extracted nano cluster $CuFe_2O_4$-np of 5 Åradius from its bulk tetragonal crystal $CuFe_2O_4$ (space group $I4_1$/amd). Note that throughout the paper we have used $CuFe_2O_4$ notation for the nano cluster $CuFe_2O_4$-np. Similarly, 5 Ånano cluster of Fe_2O_3 is extracted from its bulk phase. Note that we have used the 111 facet of "β-SiC" phase to build the computational model of SiC to support $CuFe_2O_4$. A Layer of SiO_2 consisting of 84 is stacked over SiC support to represent our experimental model system viz. β-SiC (T). To prevent interaction among periodic images a vacuum region is set to 20 Å.

7.2.2 Result

In order to get insight to our experimental results, first we have modeled our supercell consisting of the substrate (SiO_2/SiC) of 222 atoms plus catalyst ($CuFe_2O_4$) bonded over it and denote this sytem with $CuFe_2O_4/\beta$-SiC (T). Similarly, we have simulated a supercell consisting of substrate (SiC) of 187 atoms and catalyst on top of it and denote this system with $CuFe_2O_4/\beta$-SiC (UT). Figure 7.1, shows the change in Gibbs free energy (ΔG) for adsorption (in first step) and dissociation (in second step) of SO_3 on top of $CuFe_2O_4/\beta$-SiC (T) and $CuFe_2O_4/\beta$-SiC (UT), respectively. Here, adsorption and dissociation of SO_3 both are exothermic processes. The change in free energy for both the above mentioned processes is more negative in case of the treated substrate. This shows the high catalytic activity and stability of the $CuFe_2O_4/\beta$-SiC (T). Further, to get insight into the reaction mechanism, the activation barrier is estimated using nudge elastic band (NEB) method. Notably, performing NEB calculation with support (consisting of more than 200 atoms) is computationally very challenging. Hence, to estimate the activation barrier for SO_3 dissociation, we have eliminated the effect of support. In Figure 7.2(a,b), we have shown reaction profile of dissociation of SO_3 on the surface of catalyst. We have estimated the activation barrier at two different sites (a) Fe-O-Cu site and (b) O-vacancy site (i.e., Fe-O-vacancy-Cu). A significant change in the activation barrier for the adsorption of SO_3 at O-vacancy site than other site is observed. This indicates that O-vacancies at the surface of catalyst facilitate the decomposition of SO_3. In order to understand interaction of SO_3 molecule and catalyst, we have plotted the atom projected density of states (see

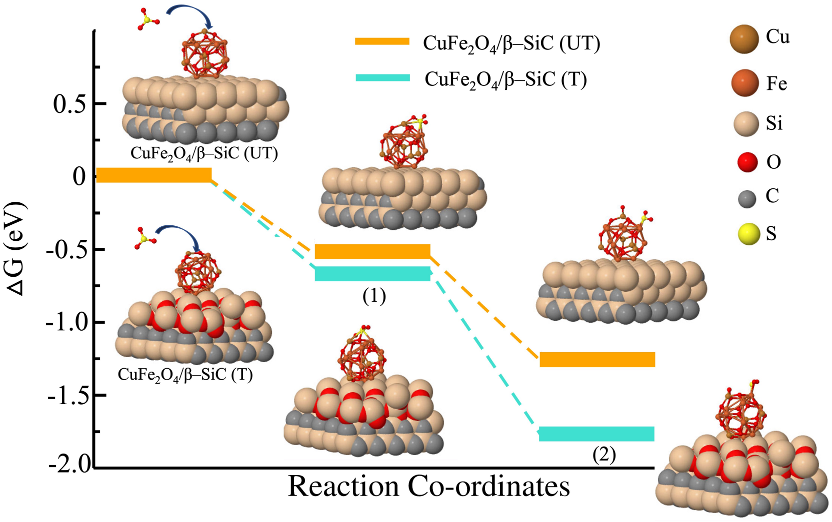

Figure 7.1: Free energy profile for adsorption and dissociation of SO_3 on the surface of $CuFe_2O_4/\beta$-SiC (UT) and $CuFe_2O_4/\beta$-SiC (T) catalyst, respectively.

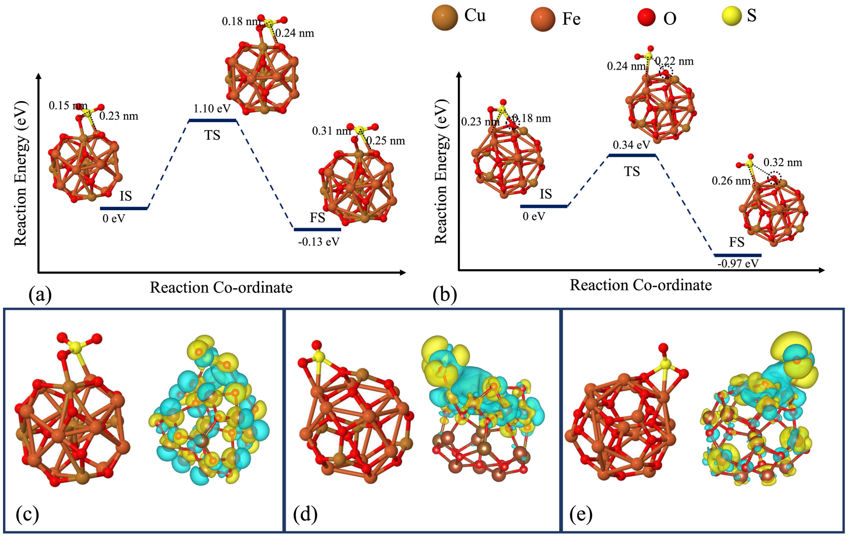

Figure 7.2: Reaction profile for the decomposition of SO_3 with initial state (IS), transition state (TS) and final state (FS) on (a) $CuFe_2O_4$ cluster and (b) $CuFe_2O_4$ cluster with oxygen vacancy. Structure and charge density difference contours for SO_3 adsorbed on top of cluster (c) $CuFe_2O_4$, (d) $CuFe_2O_4$ with O-vacancy) and (e) Fe_2O_3 with O-vacancy. In charge density difference plots cyan and yellow colour correspond to the negative and positive charge, respectively.

Figure 7.3). The isolated phase SO_3 exhibits discrete and sharp peaks in the pDOS spectrum, HOMO level is contributed by O atoms and LUMO is contributed by unoccupied states of S and O (see Figure 7.3(a). However, after adsorption of SO_3 on top of catalyst the S states get dispersed, broader and shifted to higher energy. Such shift owing to charge transfer from catalyst to SO_3 molecule, which results in elongation and weakening of one of S-O bond. This is evident from the S states appearing near Fermi level is an evident for the charge transfer from the cluster to SO_3. Therefore, if more S states are appearing near the Fermi level, more the charge transfer from cluster to SO_3 and more elongation of the S-O bond. For example, more S states are observed near fermi level when SO_3 is adsorbed at O-vacancy of $CuFe_2O_4$ (see Figure 7.3(c)) than SO_3 is adsorbed at Fe-O-Cu site of $CuFe_2O_4$. As a result, the S-O bond length for SO_3 adsorbed at O-vacancy and Fe-O-Cu site of $CuFe_2O_4$ are 0.18 and 0.15 nm, respectively. To depict this charge transfer we have also plotted the charge difference density for different configurations. Charge is more localized for SO_3 adsorbed at O-vacancy than at Fe-O-Cu site (see Figure 7.3(c,d)). As it is clear that charge transfer plays a significant role in the elongation and dissociation of S-O bond. This criteria, is more than sufficient to predict catalytic activity of any cluster. For SO_3 adsorbed at O-vacancy of $CuFe_2O_4$, more S states near fermi level are observed than SO_3 adsorbed at O-vacancy of Fe_2O_3 cluster (see Figure 7.3(c,d).

Similarly, on comparing charge density difference of SO_3 adsorbed at O-vacancy of $CuFe_2O_4$ and Fe_2O_3 (see Figure 7.3(d,e)), we discern that charge is more localized for $CuFe_2O_4$ catalyst. Hence, O-vacancy in $CuFe_2O_4$ catalyst are more favorable for SO_3 decomposition rather than O-vacancy in Fe_2O_3 catalyst.

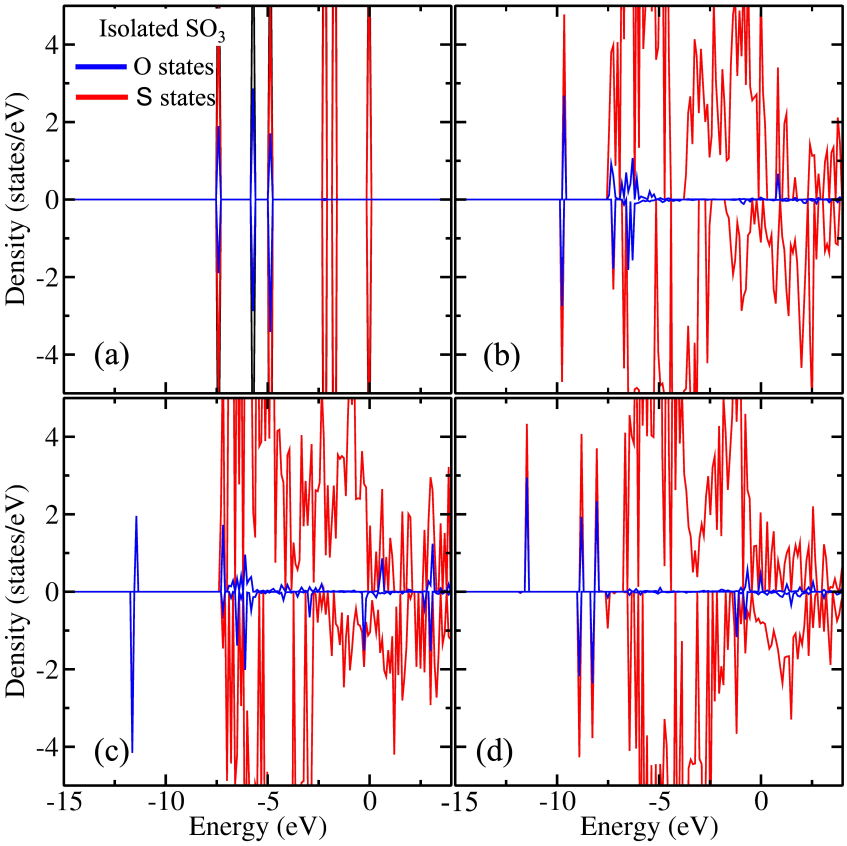

Figure 7.3: Partial density of states (pDOS) for (a) isolated SO_3, SO_3 adsorbed over the cluster (b) $CuFe_2O_4$, (c) $CuFe_2O_4$ with O-vacancy and (d) Fe_2O_3 with O-vacancy. Here, blue and red color correspond to S and O states, respectively.

7.3 Partial hydogenation of the xylose/glucose into useful sweateners using single Ru-atom catalyst surrounded by different ligands.

In solid catalysis, the atomically disperesed metal-single-atoms have evolved as a frontier owing to their distinctive electronic properties. Although, metal-single-atoms have achived great success in the solid catalysis, the biomass conversion using metal-single-atoms is still a challenging task in absence of inadequate metal-support interactions and poor yield. In our work, theoretically, we have studied role of different ligands surrounded single-Ru-atoms on the catalytic activities of the single-Ru-atoms in partial hydrogenation of the xylose/glucose.

7.3.1 Computational

Density functional theory (DFT) calculations were performed with Projector augmented wave (PAW) Pseudopotential[5,6] as implemented in Vienna ab initio Simulation Package (VASP). In all the calculations, the generalized gradient approximation (GGA) was used with the Perdew-Burke-Ernzerof (PBE) exchange-correlation functional. We have also validated results using more advanced hybrid functionals (viz. HSE06). For highly-accurate calculations, the cut-off energy of 500 eV was preferred for the plane-wave basis set. The electronic self-consistency was attained with an energy tolerance of 0.001 meV. For obtaining fully relaxed electronic configurations, Hellman-Feynmann forces were converged with a limit of 0.005 eV/Åusing conjugate gradient (CG) minimization. The Γ-centered 1x1x1 k-grid sampling is employed for the optimization of electronic configurations. To obtain the partial charges of all the atoms in different electronic configurations the Hirshfeld model was used. The adsorption energy (E_{ad}) of the adsorbate (glucose/xylose) is computed taking the difference of respective ground state energies, i.e.

$E_{ad} = E_{catalyst+glucose/xylose} - E_{glucose/xylose} - E_{catalyst}$

Where, $E_{catalyst}$, $E_{glucose/xylose}$, and $E_{catalyst+glucose/xylose}$ correspond to the total energy of the catalyst (Ru atom surrounded by different ligands), adsorbate (glucose/xylose) and the adsorbate adsorbed on the catalyst. Notably, the more negative is the E_{ad}, more is the adsorption strength. To have a qualitative understanding of the charge distribution, electron density difference analysis is carried out. Electron density difference $\Delta\rho = \rho$(Ru-atom + ligands surrounding Ru) – ρ(Ru-atom) – ρ(ligands surrounding Ru).

7.3.2 Results

DFT calculations were performed to explore the catalytic activity of Ru-atoms surrounded by different ligands, namely triphenylphosphine, triphenylamine, and catechol. For this purpose, the adsorption energy strengths were calculated for the adsorption of xylose and glucose on the surface of Ru-atoms surrounded by different ligands. From Figure 7.4(a), we can see that adsorption energy (E_{ad}) is maximum for Ru-PPh i.e. when Ru-atoms are surrounded by ligand containing P. On the other hand, adsorption energies are less negative for Ru-AmPh and Ru-

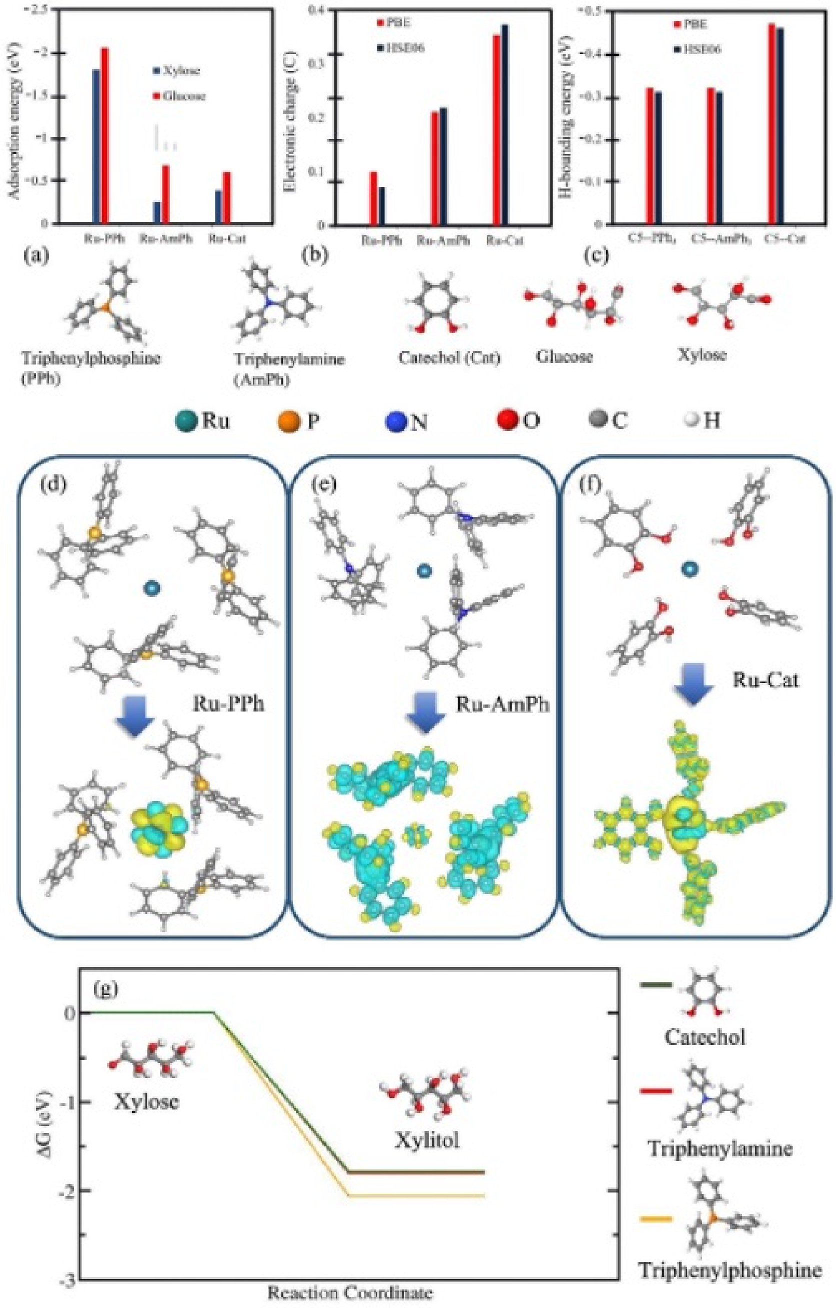

Figure 7.4: (a) Variation in the enumerated adsorption energy strength for glucose and xylose on the Ru-atom surrounded by different ligands. (b) The calculated Hirshfeld charge for the Ru atom in Ru-PPh, Ru-AmPh, and Ru-Cat, respectively. (c) The computed H-bonding energies between xylose (C5) and PPh, AmPh, and Cat, respectively. Energy minimized structures of (d) Ru-PPh-MesoSi, (e) Ru-AmPh, and (f) Ru-Cat along with their respective electron density difference plots; and (g) the change in Gibbs free energy for the partial hydrogenation of xylose to xylitol in the presence of different ligands (using PBE exchange–correlation functional); in the electron density difference plot, the cyan and the yellow colors correspond to the negative and positive charge densities, respectively..

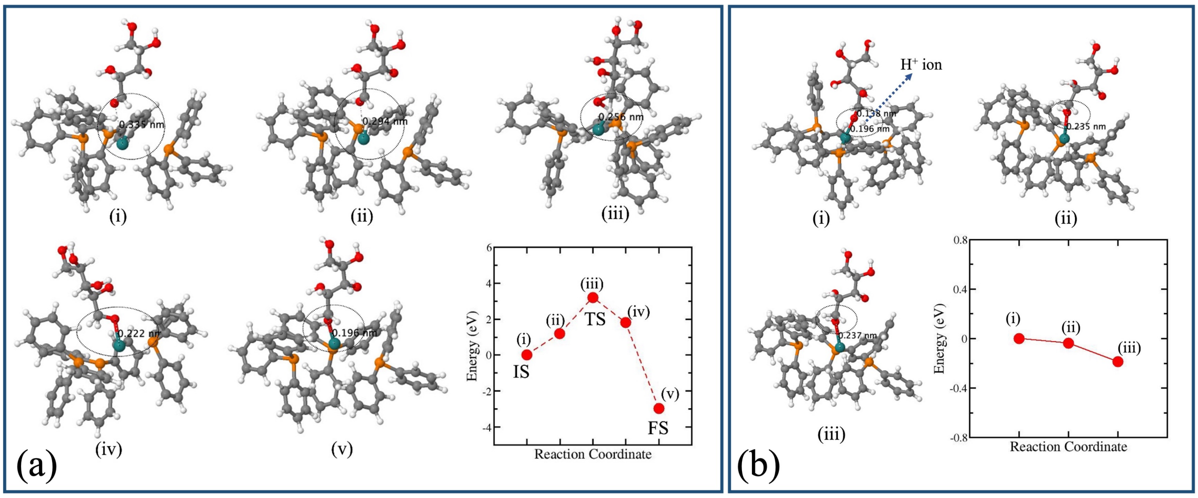

Figure 7.5: (a) Reaction profile for the adsorption and partial hydrogenation of the carbonyl group of the xylose with initial state (SI), transition state (TS) and final state (FS) on the single Ru atom surrounded by triphenylphosphine (Ru-PPh-MesoSi). (b) Reaction profile for the desorption of xylitol from the single Ru atom surrounded by triphenylphosphine (Ru-PPh-MesoSi).

Cat, this conveys that the catalytic performance of Ru-atoms for the hydrogenation of C5 and C6 sugar degrades in the presence of ligands containing N and O. DFT calculation shows that adsorption free energy of glucose/xylose on Ru-atoms increases on increasing the electronic charges on Ru-atoms, this indicates that electronic charge on Ru-atoms favours high activity (see Figure 7.4(b)). Hence, we can say that in the hydrogenation of C5/C6 sugars, the charge on Ru-atoms plays an important role and is consistent with the experimental results. However, the observed trend of the adsorption energy can also be related to the ligands surrounding Ru-atoms rather than the charge. The ligands could interact with the carbonyl group of the xylose/glucose during the catalytic process through the aromatic rings to intensify the activity. The computed interaction energies of xylose with triphenylphosphine, triphenylamine and catechol are -0.31 eV, -0.31 eV and -0.46 eV, respectively (see Figure 7.4(c)). Here, the strong interaction of catechol with sugars can cause difficulty in the desorption of the hydrogenated sugars from the catalysts. On the other hand, triphenylamine and triphenylphosphine ligands having suitable interaction strength with sugars acted as binding sites to induce the adsorption of sugars on Ru-atoms, leading to efficient hydrogenation of sugars into sweeteners. From Figure 7.4, we can see that both amine and phosphine ligands possess the same interaction energy with the sugars, however, the adsorption energy is different.

This shows that the charge on “Ru atoms” plays a crucial role in the hydrogenation of sugars into sweeteners. It is also validated through the electron density difference plot of Ru-PPh, Ru-AmPh, and Ru-Cat as shown in Figure 7.4(d-f). Charge density is highly localized at Ru-single-atom in the case of Ru-PPh (see Figure 7.4(d)). However, for Ru-AmPh and Ru-Cat charge density is distributed throughout the system and hence degrades the catalytic activity of Ru-single-atoms (see Figure 7.4(d-f)). Therefore, as per the theoretical analysis, it states that the electronic and geometric factors are controlling the activity of metal single atoms for the hydrogenation of bulky sugars. Low activity of Ru/C can be correlated by lacking such functionality of the support. Thus, we see the conjunction between the Ru-single-atoms and the neighbouring aromatic rings of triphenylphosphine govern as adsorption and desorption sites, facilitating xylose and glucose hydrogenation reaction. Moreover, it is known that the adsorption strength of substrate, electronic charge and geometry of the ligands - all together are collectively important in the partial hydrogenation of the xylose [307]. As for instance, the partial hydrogenation takes place if the adsorbate gets adsorbed into the substrate and in fact more negative adsorption energy is favourable for subsequent hydrogenation. Hence, the yield of the desired products are indirectly dependent on the adsorption strength of the substrates. Moreover, if there is more charge-transfer from the ligand to the Ru-atom, then it weakens the "Ru-H" bond and it can easily donate the H-atom to the adsorbate. Regarding this, we have also calculated the change in Gibbs free energy of formation (G) for the partial hydrogenation of xylose to xylitol in the presence of different ligands (see Figure 7.4(g)). Here, more negative value of G shows the ease of reaction i.e., hydrogenation. Hence, from Figure 7.4(g), we can discern that partial hydrogenation of xylose is more favorable in the presence of triphenylphosphine ligands. This can be explained from the charge transfer analysis. Not only G values, we also proved that partial hydrogenation depends on the interaction energy with the substrate, and the more the interaction energy of ligand, the harder will be the desorption of products from the catalyst, and hence the loss of selectivity in products is thus obvious, as agreed with our experimental results in Fig. 5c j. To have complete energy profile of the reaction, we have also performed NEB calculation for the partial hydrogenation of xylose on single Ru-atom surrounded by triphenlyphosphine ligands (see Figure 7.5 and 7.5).

After all, our findings firmly justifies the role of charge density, adsorption energy of substrate and the effect of ligand geometry (steric effect) in partial hydrogenation reaction. The effect of ligand is also profoundly applied towards un-functionalized carbon surface for controlled hydrodeoxygenation reaction [308]. Henceforth, a tailorable adsorption selectivity of substrates is shown through an important ligand effect on Ru-sites.

Energy profile for hydrogenation of the xylose to xylitol, using NEB approach We have done NEB for xylose adsorption and partial hydrogenation of carbonyl group over the Ru single atom surrounded by the triphenylphosphine ligands (the most promising catalyst i.e., Ru-PPh-MesoSi). In Figure 7.5(a), from ist initial state (SI) to iiird transition state (TS) the distance between the oxygen of the carbonyl group of xylose and the Ru atom decreases. At TS reaction step the H initially bonded with Ru atom interacts with the carbonyl group and in the ivth reaction step this H makes bond with C atom of the carbonyl group of the xylose and O atom is bonded with the Ru atom. In vth reaction step i.e., final state (FS) the bond length of Ru and O atom decreases, and this configuration is of minimum energy. Here, in Figure 7.5(a), partial hydrogenation of the xylose has been shown from ist reaction step to the vth reaction step. Further, in Figure 7.5(b), we have shown reaction steps for the complete hydrogenation of xylose and desorption of the xylitol form the Ru atom. In Figure 7.5(b), in first reaction step (i), the H^+ ion from the formic acid and NEt3 system [307, 309, 310] interacts with oxygen adsorbed on the Ru atom. In step ii, oxygen atom makes bound with H+ ion and it's bond with Ru atom becomes weak. In step iii the bond length of O and Ru atom increases, this shows that Ru-O bond is breaking. Here, steps ii and iii show the desorption of xylitol from the Ru atom. Also, from the energies of the i, ii and iii reaction steps, we conclude that after complete hydrogenation of xylose to xylitol desorption is energetically favorable reaction.

7.4 Conclusion

O-Vacancy in the catalyst facilitates the dissociation of the SO3 molecule due to more charge localization at O-vacancy in the catalyst. The charge is more localized at O-vacancy in the CuFe2O4 catalyst than in Fe2O3 CuFe2O4 nano-clusters are more suitable for SO3 dissociation than Fe2O3 nano-clusters. Catalytic performance of the Ru single atoms for the hydrogenation of C5 and C6 sugar degrades in the presence of ligands containing N and O. Large electronic charge on Ru single atom favours high activity. Electronic and geometric factors controls the activity of the metal single atoms for the hydrogenation of the bulky sugars.

CHAPTER 8

Summary

In conclusion, we have investigated the thermodynamic stability of point defects in LISICON using DFT simulations. We have found that the thermodynamically most stable configurations are $Li_{56-x}Si_{14-y}P_y \boxtimes_x O_{56}$ (x=y), where x and $y \in [0,4]$. To get insights on improved ionic conductivity, AIMD calculations are carried out. For both pristine and doped systems, the diffusion of Li-ions rises with temperature. We have also demonstrated that the Li-ion diffusion in LISICON increases when point defects (Li-$\boxtimes$, P, Al, and Ge substitutional impurities) are introduced at a certain temperature. The anisotropy in our system is shown by the jumps (vibrations) of Li-ions, which are in the order of plane ac $>$ ab $>$ bc. Furthermore, the impurities polarize the system, which causes bond softening and, as a result, a decrease in the activation barrier, which makes Li-ion hopping simpler. Our findings show that adding different point defects to LISICON increases its ionic conductivity. In case of double perovskite materials, we have given a complete analysis of alloying $Cs_2AgBiCl_6$ double perovskites with M(I), M(II), and M(III) cations. Here, we have demonstrated the significance of SOC in such systems by comparing the optical characteristics obtained using HSE06 and HSE06+SOC. To correctly estimate the band gap and band-edge locations in such systems, SOC plays a crucial role. The Goldschmidt tolerance factor and octahedral factor describe the structural stability and we have observed that all the mixed sublattices are structurally stable. The enthalpies of decomposition are negative, demonstrating the alloyed system's thermodynamic stability. We have reported that partial replacement of Au can be used instead of 100% Au at Ag site to improve the optical characteristics of $Cs_2AgBiCl_6$. We have demonstrated that band gap increases for replacement at Bi-sites as Sb concentration rises.We have shown that for substitution at Bi-sites with Sb, the band gap shrinks by up to 75% when the concentration of Sb is increased. The entire removal of Bi, however, results in a rapid rise in band gap for 100% substitution. When alkali metals (Na/K) are completely substituted at Ag-sites, the band gap increases abruptly. We have also shown that band gap reduction makes partial Au replacement (between 25% and 75%), an efficient way to improve optical characteristics. Additionally, we have seen that the stability declines as replacement levels at Ag- or Bi-sites rise. Therefore, we have come to the conclusion that partial replacement of Au and Sb at Ag- and Bi-sites, respectively, will be more economical, stable, and effective to improve the optical characteristics. We have concluded that in double perovskites, alloying with M(II) cations not only enhance the thermodynamic stability, but also enhance the power conversion efficiency. Furthermore, we have thoroughly examined the structural and optoelectronic characteristics of (un)defected 2D hybrid $(C_3H_5NH_3)_2PbI_4$. The conduction band's spin-orbit splitting is apparent, which causes the band gap to decrease. Therefore, to accurately calculate the optical characteristics of mixed conformers, SOC effect has been properly taken into account in all computations. Wide bandgap semiconductor CPPI, made of 2D perovskite, has a subpar absorption spectrum. We have adjusted the band gap of the CPPI system by replacing the hazardous element Pb with the less hazardous alternatives, Ge and Sn, and we have seen an improvement in the system's optoelectronic capabilities. The band gap may also be adjusted and the optoelectronic characteristics improved in the case of the compounds CBPI, CPEPI, and CHXPI. We have shown that utilising Sn allows for the entire removal of harmful Pb from CPPI, but using Ge only allows for the partial replacement of toxic Pb. In addition, compared to conformers with Ge, mixed conformers with Sn are more stable and have greater PCE. Thus, we have drawn the conclusion that, when replacing harmful lead from CPPI, Sn replacement is preferable than Ge substitution. The most efficient and stable 2D halide perovskite $(C_3H_5NH_3)_2SnI_4$ is suitable for photovoltaic (PV) devices. Excessive exciton binding energy is present in both pure and mixed forms. Compared to traditional lead halide perovskites, the electron-phonon coupling is lower. These materials exhibit low electron-phonon coupling than the conventional lead halide perovskites. It is observed that on replacing Pb with Sn, the effective masses of the charge carriers increase, and as a result charge carrier mobility decreases. This degrades the practical performance of Sn substituted conformers. Hence, in search for suitable optoelectronic solar cell material, we focused on layered type Ruddlesden-Popper phases of the chalcogenide perovskites. Using MBPT, we have reported the electronic and excitonic characteristics of the RP phases of $Ba_{n+1}Zr_nS_{3n+1}$ (n=[1-3]). As the perovskite layer becomes thicker, the exciton binding energy drops. The first excitonic peak computed in the direction of Ba_2ZrS_4 has a double peak nature. With rising n in $Ba_{n+1}Zr_nS_{3n+1}$ (n=[1-3]), the difference between the direct and indirect band gaps grows, making the band gap more indirect. We have determined the upper and lower bounds of E_B using the Wannier-Mott technique, based on the electronic and ionic contributions to the dielectric constant, respectively. We have demonstrated using the Wannier-Mott technique that ionic contribution to the dielectric constant may result in a reduction in E_B. However, compared to traditional lead halide perovskites, the ionic contribution is not as strong. In $Ba_{n+1}Zr_nS_{3n+1}$, we have noticed that the importance of the ionic contribution to the dielectric function diminishes as n increases. According to calculations made using the deformation potential of Ba_2ZrS_4, the charge carrier mobility is at its highest in this material. Additionally, the electron-phonon coupling constant is substantially less for former RP phases compared to bulk $BaZrS_3$ and $Ba_{n+1}Zr_{n+1}S_{3n+1}$. Our polaron investigation leads us to the conclusion that for these systems, optical phonon modes predominate over acoustical phonon modes. There is a significant difference between charge carrier mobility (which solely takes into account the influence of acoustical phonon modes in electron-phonon interaction) and polaron mobility (which includes the effect of optical phonon modes in addition to the acoustic modes in electron-phonon coupling). To comprehend the charge transport characteristics of RP phases, it must be investigated since it demonstrates the dominant nature of optical phonon modes in the electron-phonon connection. Finally, these RP phases are anticipated to be attractive optoelectronic materials from the standpoint of device applications. In conclusion, we have found that catalytic activity of catalysts is greatly affected by the presence of point defects and the surrounding. Overall, defects play crucial role in modulating various properties such as ion transport properties, electronic properties, optical properties, activation barrier of chemical reactions, and many other physical and chemical properties of the advanced energy materials. Hence, special attention must be paid to the defects existing in the materials developed. Our future efforts are to find and create more advanced energy materials using more advanced methodologies.

CHAPTER A

Appendix

Double perovskites materials

A.1 Band gap, tolerance factor, octahedral factor and enthalpy of decomposition of different configurations

Table A.1: Tolerance and octahedral factor of different conformers

Conformers	Tolerance factor (t)	Octahedral factor (μ)
$Cs_8Ag_4Bi_4Cl_{24}$	0.90	0.60
$Cs_8Ag_3Au_1Bi_4Cl_{24}$	0.89	0.62
$Cs_8Ag_2Au_2Bi_4Cl_{24}$	0.88	0.63
$Cs_8Ag_1Au_3Bi_4Cl_{24}$	0.87	0.65
$Cs_8Au_4Bi_4Cl_{24}$	0.87	0.66
$Cs_8Ag_3Cu_1Bi_4Cl_{24}$	0.91	0.58
$Cs_8Ag_2Cu_2Bi_4Cl_{24}$	0.93	0.55
$Cs_8Ag_1Cu_3Bi_4Cl_{24}$	0.95	0.52
$Cs_8Cu_4Bi_4Cl_{24}$	0.96	0.50
$Cs_8Ag_3In_1Bi_4Cl_{24}$	0.91	0.58
$Cs_8Ag_2In_2Bi_4Cl_{24}$	0.93	0.55
$Cs_8Ag_1In_3Bi_4Cl_{24}$	0.94	0.53
$Cs_8In_4Bi_4Cl_{24}$	0.96	0.51
$Cs_8Ag_3K_1Bi_4Cl_{24}$	0.89	0.62

$Cs_8Ag_2K_2Bi_4Cl_{24}$	0.88	0.63
$Cs_8Ag_1K_3Bi_4Cl_{24}$	0.87	0.65
$Cs_8K_4Bi_4Cl_{24}$	0.87	0.66
$Cs_8Ag_3Na_1Bi_4Cl_{24}$	0.90	0.59
$Cs_8Ag_2Na_2Bi_4Cl_{24}$	0.91	0.58
$Cs_8Ag_1Na_3Bi_4Cl_{24}$	0.92	0.58
$Cs_8Na_4Bi_4Cl_{24}$	0.92	0.57
$Cs_8Ag_3Ti_1Bi_4Cl_{24}$	0.91	0.58
$Cs_8Ag_2Ti_2Bi_4Cl_{24}$	0.92	0.56
$Cs_8Ag_1Ti_3Bi_4Cl_{24}$	0.93	0.54
$Cs_8Ti_4Bi_4Cl_{24}$	0.95	0.52
$Cs_8Ag_4Cr_1Bi_3Cl_{24}$	0.91	0.59
$Cs_8Ag_4Cr_2Bi_2Cl_{24}$	0.92	0.57
$Cs_8Ag_4Cr_3Bi_1Cl_{24}$	0.93	0.55
$Cs_8Ag_4Cr_4Cl_{24}$	0.94	0.54
$Cs_8Ag_4Ga_1Bi_3Cl_{24}$	0.92	0.57
$Cs_8Ag_4Ga_2Bi_2Cl_{24}$	0.93	0.55
$Cs_8Ag_4Ga_3Bi_1Cl_{24}$	0.95	0.52
$Cs_8Ag_4Ga_4Cl_{24}$	0.97	0.49
$Cs_8Ag_4In_1Bi_3Cl_{24}$	0.91	0.59
$Cs_8Ag_4In_2Bi_2Cl_{24}$	0.92	0.57
$Cs_8Ag_4In_3Bi_1Cl_{24}$	0.93	0.55
$Cs_8Ag_4In_4Cl_{24}$	0.94	0.54
$Cs_8Ag_4Sb_1Bi_3Cl_{24}$	0.91	0.58
$Cs_8Ag_4Sb_2Bi_2Cl_{24}$	0.92	0.56
$Cs_8Ag_4Sb_3Bi_1Cl_{24}$	0.93	0.55
$Cs_8Ag_4Sb_4Cl_{24}$	0.94	0.53
$Cs_8Ag_4Sc_1Bi_3Cl_{24}$	0.91	0.58
$Cs_8Ag_4Sc_2Bi_2Cl_{24}$	0.92	0.56
$Cs_8Ag_4Sc_3Bi_1Cl_{24}$	0.93	0.54
$Cs_8Ag_4Sc_4Cl_{24}$	0.95	0.52

$Cs_8Ag_4Tl_1Bi_3Cl_{24}$	0.91	0.60
$Cs_8Ag_4Tl_2Bi_2Cl_{24}$	0.91	0.58
$Cs_8Ag_4Tl_3Bi_1Cl_{24}$	0.92	0.57
$Cs_8Ag_4Tl_4Cl_{24}$	0.92	0.56
$Cs_8Ag_4Y_1Bi_3Cl_{24}$	0.90	0.59
$Cs_8Ag_4Y_2Bi_2Cl_{24}$	0.91	0.58
$Cs_8Ag_4Y_3Bi_1Cl_{24}$	0.92	0.58
$Cs_8Ag_4Y_4Cl_{24}$	0.92	0.57
$Cs_8Ag_3Cd_2Bi_3Cl_{24}$	0.91	0.58
$Cs_8Ag_3Co_2Bi_3Cl_{24}$	0.93	0.55
$Cs_8Ag_3Cu_2Bi_3Cl_{24}$	0.93	0.55
$Cs_8Ag_3Ge_2Bi_3Cl_{24}$	0.93	0.55
$Cs_8Ag_3Mn_2Bi_3Cl_{24}$	0.93	0.54
$Cs_8Ag_3Ni_2Bi_3Cl_{24}$	0.94	0.54
$Cs_8Ag_3Sn_2Bi_3Cl_{24}$	0.90	0.61
$Cs_8Ag_3V_2Bi_3Cl_{24}$	0.92	0.56
$Cs_8Ag_3Zn_2Bi_3Cl_{24}$	0.93	0.55
$Cs_8Ag_3Rh_2Bi_3Cl_{24}$	0.93	0.55

Table A.2: Band gap and enthalpy of decomposition of different conformers (double perovskites) for M(III) substitution

Conformers	PBE (eV)	PBE +SOC (eV)	HSE06 +SOC (eV)	HSE06 (eV)	ΔH_D (PBE+SOC) (eV)	ΔH_D (HSE06+SOC) (eV)
$Cs_8Ag_4Cr_1Bi_3Cl_{24}$	1.47	1.34	2.37	-	-9.19	-11.25
$Cs_8Ag_4Cr_2Bi_2Cl_{24}$	1.10	1.03	2.06	2.43	-8.96	-11.77
$Cs_8Ag_4Cr_3Bi_1Cl_{24}$	0.78	0.77	2.73	2.86	-8.65	-12.29
$Cs_8Ag_4Cr_4Cl_{24}$	0.80	0.79	2.81	2.94	-8.27	-12.81
$Cs_8Ag_4Ga_1Bi_3Cl_{24}$	1.91	1.55	2.52	-	-9.20	-10.84
$Cs_8Ag_4Ga_2Bi_2Cl_{24}$	1.57	1.38	2.45	-	-8.98	-
$Cs_8Ag_4Ga_3Bi_1Cl_{24}$	2.17	2.03	3.11	-	-8.71	-10.17
$Cs_8Ag_4Ga_4Cl_{24}$	1.31	1.27	2.62	-	-8.33	-9.70
$Cs_8Ag_4In_1Bi_3Cl_{24}$	1.91	1.61	2.58	-	-9.43	-
$Cs_8Ag_4In_2Bi_2Cl_{24}$	1.52	1.37	2.40	-	-9.47	-11.30
$Cs_8Ag_4In_3Bi_1Cl_{24}$	2.04	1.97	3.07	-	-9.16	-
$Cs_8Ag_4In_4Cl_{24}$	1.19	1.17	2.56	-	-9.46	-11.38
$Cs_8Ag_4Sb_1Bi_3Cl_{24}$	1.80	1.44	2.31	-	-9.30	-10.94
$Cs_8Ag_4Sb_2Bi_2Cl_{24}$	1.71	1.37	2.22	-	-9.23	-10.76
$Cs_8Ag_4Sb_3Bi_1Cl_{24}$	1.68	1.34	2.20	-	-9.16	-10.59
$Cs_8Ag_4Sb_4Cl_{24}$	1.69	1.64	2.57	-	-9.09	-
$Cs_8Ag_4Sc_1Bi_3Cl_{24}$	2.13	1.70	-	-	-9.27	-
$Cs_8Ag_4Sc_2Bi_2Cl_{24}$	2.18	1.69	-	-	-9.15	-
$Cs_8Ag_4Sc_3Bi_1Cl_{24}$	2.71	2.14	-	-	-9.01	-
$Cs_8Ag_4Sc_4Cl_{24}$	3.32	3.29	-	-	-8.84	-
$Cs_8Ag_4Tl_1Bi_3Cl_{24}$	0.65	0.62	-	-	-	-
$Cs_8Ag_4Tl_2Bi_2Cl_{24}$	0.45	0.42	-	-	-	-
$Cs_8Ag_4Tl_3Bi_1Cl_{24}$	0.83	0.82	0.45	0.42	-	-
$Cs_8Ag_4Tl_4Cl_{24}$	0.40	0.39	-	-	-	-
$Cs_8Ag_4Y_1Bi_3Cl_{24}$	2.11	1.74	-	-	-9.28	-
$Cs_8Ag_4Y_2Bi_2Cl_{24}$	2.28	1.80	-	-	-9.19	-
$Cs_8Ag_4Y_3Bi_1Cl_{24}$	2.87	2.21	-	-	-9.11	-
$Cs_8Ag_4Y_4Cl_{24}$	3.73	3.69	-	-	-9.01	-

A.2 Path of decomposition of $Cs_2AgBiCl_6$ into binary/ternary compounds on alloying with monovalent, trivalent and divalent configurations

- 1. $Cs_8Ag_4Bi_4Cl_{24} = 4AgCl + 2CsCl + 2Cs_3Bi_2Cl_9$
- 2. $Cs_8Ag_4Bi_4Cl_{24} = 3AgCl + Cs_2AgCl_3 + 2Cs_3Bi_2Cl_9$
- 3. $Cs_8Ag_3M(II)_2Bi_3Cl_{24} = 8CsCl + 2M(II)Cl_2 + 4AgCl + 4BiCl_3$
- 4. $Cs_8Ag_3M(II)_2Bi_3Cl_{24} = 2CsM(II)Cl_3 + 3Cs_3Bi_2Cl_9 + 3AgCl + 3CsCl$

Table A.3: Band gap and enthalpy of decomposition of different conformers (double perovskites) for M(I) substitution

Conformers	PBE (eV)	PBE +SOC (eV)	HSE06 +SOC (eV)	HSE06 (eV)	ΔH_D (PBE+SOC) (eV)	ΔH_D (HSE06+SOC) (eV)
$Cs_8Ag_4Bi_4Cl_{24}$	2.06	1.67	2.60	3.15	-9.36	-11.11
$Cs_8Ag_3Au_1Bi_4Cl_{24}$	1.15	0.88	1.79	2.17	-9.18	-10.90
$Cs_8Ag_2Au_2Bi_4Cl_{24}$	1.02	0.76	1.62	2.01	-9.00	-10.70
$Cs_8Ag_1Au_3Bi_4Cl_{24}$	0.96	0.69	1.54	1.94	-8.80	-10.49
$Cs_8Au_4Bi_4Cl_{24}$	1.46	0.70	1.54	1.95	-8.62	-10.28
$Cs_8Ag_3Cu_1Bi_4Cl_{24}$	1.27	1.07	2.23	2.61	-9.26	-10.97
$Cs_8Ag_2Cu_2Bi_4Cl_{24}$	1.20	1.00	2.12	2.54	-9.15	-10.83
$Cs_8Ag_1Cu_3Bi_4Cl_{24}$	1.15	0.94	2.01	2.49	-9.04	-10.69
$Cs_8Cu_4Bi_4Cl_{24}$	1.13	0.89	1.95	2.48	-8.92	-10.54
$Cs_8Ag_3In_1Bi_4Cl_{24}$	0.45	0.07	0.39	1.22	-9.25	-11.01
$Cs_8Ag_2In_2Bi_4Cl_{24}$	0.30	0.13	0.11	1.10	-9.14	-10.90
$Cs_8Ag_1In_3Bi_4Cl_{24}$	0.14	0.23	0.17	0.98	-9.02	-10.80
$Cs_8In_4Bi_4Cl_{24}$	0.29	0.55	0.46	-	-8.89	-10.71
$Cs_8Ag_3K_1Bi_4Cl_{24}$	2.07	1.71	-	-	-10.37	-
$Cs_8Ag_2K_2Bi_4Cl_{24}$	2.15	1.80	-	-	-10.37	-
$Cs_8Ag_1K_3Bi_4Cl_{24}$	2.32	1.97	-	-	-10.86	-
$Cs_8K_4Bi_4Cl_{24}$	4.18	3.31	-	-	-11.34	-
$Cs_8Ag_3Na_1Bi_4Cl_{24}$	2.06	1.69	-	-	-9.36	-
$Cs_8Ag_2Na_2Bi_4Cl_{24}$	2.16	1.78	-	-	-9.36	-
$Cs_8Ag_1Na_3Bi_4Cl_{24}$	2.35	1.96	-	-	-9.36	-
$Cs_8Na_4Bi_4Cl_{24}$	3.12	3.09	-	-	-9.35	-
$Cs_8Ag_3Ti_1Bi_4Cl_{24}$	0.20	0.02	0.05	0.40	-9.10	-11.04
$Cs_8Ag_2Ti_2Bi_4Cl_{24}$	0.03	0.01	-	-	-8.88	-11.57
$Cs_8Ag_1Ti_3Bi_4Cl_{24}$	0.05	0.01	0.06	-	-8.71	-11.91
$Cs_8Ti_4Bi_4Cl_{24}$	0.04	0.01	0.02	-	-8.56	-12.51

Table A.4: Band gap and enthalpy of decomposition of different conformers (double perovskites) for M(II) substitution

Conformers	PBE (eV)	PBE +SOC (eV)	HSE06 +SOC (eV)	HSE06 (eV)	ΔH_D (PBE+SOC) (eV)	ΔH_D (HSE06+SOC) (eV)
$Cs_8Ag_3Cd_2Bi_3Cl_{24}$	1.12	1.08	1.96	2.14	-9.12	-10.76
$Cs_8Ag_3Co_2Bi_3Cl_{24}$	0.77	0.71	2.01	-	-8.24	-11.79
$Cs_8Ag_3Cu_2Bi_3Cl_{24}$	Metal	Metal	-	-	-8.87	-
$Cs_8Ag_3Ge_2Bi_3Cl_{24}$	1.06	0.56	1.27	2.12	-9.18	-11.50
$Cs_8Ag_3Mn_2Bi_3Cl_{24}$	1.00	0.77	2.02	2.31	-9.56	-13.20
$Cs_8Ag_3Mo_2Bi_3Cl_{24}$	Metal	Metal	-	-	-8.31	-
$Cs_8Ag_3Ni_2Bi_3Cl_{24}$	0.79	0.07	1.64	1.73	-8.70	-11.63
$Cs_8Ag_3Sn_2Bi_3Cl_{24}$	1.05	0.41	1.06	2.07	-9.17	-10.87
$Cs_8Ag_3V_2Bi_3Cl_{24}$	1.90	0.31	0.77	1.26	-8.87	-11.74
$Cs_8Ag_3Zn_2Bi_3Cl_{24}$	1.04	0.93	1.87	2.05	-8.80	-10.43
$Cs_8Ag_3Rh_2Bi_3Cl_{24}$	0.50	0.19	1.32	1.76	-9.38	-11.99

Table A.5: The formula and space group of different secondary phases which include binary and ternary compounds

Formula	Space group	#	Formula	Space group	#
AgCl	Fm-3m	225	$CsAgCl_2$	P4/nmm	129
AuCl	I4-1/amd	141	$CsAuCl_2$	P4/nmm	129
$BiCl_3$	Pnma	62	CsCl	Pm-3m	221
$CdCl_2$	R-3m	166	$CsCdCl_3$	Pm-3m	221
$CoCl_2$	C2/m	12	$CsCoCl_3$	P6-3/mmc	194
$CrCl_3$	C2/m	12	$CsCuCl_3$	Cmcm	63
Cs_2AgCl_3	Pnma	62	$CsCuCl_2$	P4/nmm	129
Cs_2AuCl_3	Pnma	62	$CsGeCl_3$	R3m	160
Cs_2CuCl_3	Pnma	62	$CsNiCl_3$	P6-3/mmc	194
Cs_2ZnCl_3	Pnma	62	$CsSnCl_3$	P2-1/c	14
$Cs_3Bi_2Cl_9$	P6-3/mmc	194	CuCl	F-43m	216
$Cs_3Cr_2Cl_9$	P6-3/mmc	194	$CuCl_2$	C2/m	12
$Cs_3Ga_2Cl_9$	P-3m1	164	$GeCl_2$	P2-1/c	14
$Cs_3In_2Cl_9$	R-3c	167	InCl	Cmcm	63
$Cs_3Sb_2Cl_9$	P-3m1	164	$InCl_3$	P6-3/mmc	194
$Cs_3Sc_2Cl_9$	R-3c	167	KCl	Fm-3m	225
$Cs_3Tl_2Cl_9$	P6-3/mmc	194	$MnCl_2$	P-3m1	164
$Cs_3Y_2Cl_9$	P-3m1	164	$MoCl_2$	Cmcm	64
NaCl	Fm-3m	225	$NiCl_2$	R-3m	166
$RhCl_2$	P4-2/mnm	136	$SbCl_3$	Pnma	62
$ScCl_3$	R-3	148	$SnCl_2$	Pmma	62
$TcCl_2$	P-3m1	164	TiCl	R-3m	166
$TiCl_3$	P-31m	162	TlCl	Pm-3m	221
VCl_2	P-3m1	164	YCl_3	C2/m	12
$YbCl_2$	P4-2/mm	136	ZnCl	I-42d	122

Bibliography

[1] David J Singh and Lars Nordstrom. *Planewaves, Pseudopotentials, and the LAPW method*. Springer Science & Business Media, 2006.

[2] Saba Niaz, Taniya Manzoor, and Altaf Hussain Pandith. Hydrogen storage: Materials, methods and perspectives. *Renewable and Sustainable Energy Reviews*, 50:457–469, 2015.

[3] Weidong Xiao, William G Dunford, and Antoine Capel. A novel modeling method for photovoltaic cells. In *2004 IEEE 35th Annual Power Electronics Specialists Conference (IEEE Cat. No. 04CH37551)*, volume 3, pages 1950–1956. IEEE, 2004.

[4] Mathew Aneke and Meihong Wang. Energy storage technologies and real life applications–a state of the art review. *Applied Energy*, 179:350–377, 2016.

[5] R Chenni, M Makhlouf, T Kerbache, and A Bouzid. A detailed modeling method for photovoltaic cells. *Energy*, 32(9):1724–1730, 2007.

[6] Zvonimir Glasnovic and Jure Margeta. The features of sustainable solar hydroelectric power plant. *Renewable energy*, 34(7):1742–1751, 2009.

[7] Vinodkumar Etacheri, Rotem Marom, Ran Elazari, Gregory Salitra, and Doron Aurbach. Challenges in the development of advanced li-ion batteries: a review. *Energy & Environmental Science*, 4(9):3243–3262, 2011.

[8] Aleksandr Vasil'evich Bobylev. Exact solutions of the boltzmann equation. In *Akademiia Nauk SSSR Doklady*, volume 225, pages 1296–1299, 1975.

[9] PM Voyles, DA Muller, JL Grazul, PH Citrin, and H-JL Gossmann. Atomic-scale imaging of individual dopant atoms and clusters in highly n-type bulk si. *Nature*, 416(6883):826–829, 2002.

[10] P Hohenberg and W Kohn. Inhomogeneous electron gas phys. rev. 136. *B864*, 1964.

[11] Walter Kohn and Lu Jeu Sham. Self-consistent equations including exchange and correlation effects. *Physical review*, 140(4A):A1133, 1965.

[12] Zhen-Kun Tang, Zhi-Feng Xu, Deng-Yu Zhang, Shu-Xian Hu, Woon-Ming Lau, and Li-Min Liu. Enhanced optical absorption via cation doping hybrid lead iodine perovskites. *Scientific reports*, 7(1):7843, 2017.

[13] Rishikanta Mayengbam, SK Tripathy, and Gopinath Palai. First-principle insights of electronic and optical properties of cubic organic–inorganic mage x pb (1–x) i3 perovskites for photovoltaic applications. *The Journal of Physical Chemistry C*, 122(49):28245–28255, 2018.

[14] Zhen-Kun Tang, Ya-Nan Zhu, Zhi-Feng Xu, and Li-Min Liu. Effect of water on the effective goldschmidt tolerance factor and photoelectric conversion efficiency of organic–inorganic perovskite: insights from first-principles calculations. *Physical Chemistry Chemical Physics*, 19(23):14955–14960, 2017.

[15] Diwen Liu, Qiaohong Li, Jinyu Hu, Rongjian Sa, and Kechen Wu. Photovoltaic performance of lead-less hybrid perovskites from theoretical study. *The Journal of Physical Chemistry C*, 123(20):12638–12646, 2019.

[16] Satyawan Nagane, Dibyajyoti Ghosh, Robert LZ Hoye, Baodan Zhao, Shahab Ahmad, Alison B Walker, M Saiful Islam, Satishchandra Ogale, and Aditya Sadhanala. Lead-free perovskite semiconductors based on germanium–tin solid solutions: structural and optoelectronic properties. *The Journal of Physical Chemistry C*, 122(11):5940–5947, 2018.

[17] Dongwen Yang, Wenmei Ming, Hongliang Shi, Lijun Zhang, and Mao-Hua Du. Fast diffusion of native defects and impurities in perovskite solar cell material ch3nh3pbi3. *Chemistry of Materials*, 28(12):4349–4357, 2016.

[18] Max Born and Robert Oppenheimer. Zur quantentheorie der molekeln. *Annalen der physik*, 389(20):457–484, 1927.

[19] John C Slater. A simplification of the hartree-fock method. *Physical review*, 81(3):385, 1951.

[20] Graeme Henkelman and Hannes Jónsson. Improved tangent estimate in the nudged elastic band method for finding minimum energy paths and saddle points. *The Journal of chemical physics*, 113(22):9978–9985, 2000.

[21] Charlotte Froese Fischer. General hartree-fock program. *Computer physics communications*, 43(3):355–365, 1987.

[22] Axel D Becke. A new mixing of hartree–fock and local density-functional theories. *The Journal of chemical physics*, 98(2):1372–1377, 1993.

[23] Vladimir Fock. Näherungsmethode zur lösung des quantenmechanischen mehrkörperproblems. *Zeitschrift für Physik*, 61(1-2):126–148, 1930.

[24] John C Slater. Note on hartree's method. *Physical Review*, 35(2):210, 1930.

[25] Enrico Fermi. Eine statistische methode zur bestimmung einiger eigenschaften des atoms und ihre anwendung auf die theorie des periodischen systems der elemente. *Zeitschrift für Physik*, 48(1-2):73–79, 1928.

[26] Llewellyn H Thomas. The calculation of atomic fields. In *Mathematical Proceedings of the Cambridge Philosophical Society*, volume 23, pages 542–548. Cambridge University Press, 1927.

[27] Paul AM Dirac. Note on exchange phenomena in the thomas atom. In *Mathematical Proceedings of the Cambridge Philosophical Society*, volume 26, pages 376–385. Cambridge University Press, 1930.

[28] Mel Levy. Electron densities in search of hamiltonians. *Phys. Rev. A*, 26:1200–1208, Sep 1982.

[29] Elliott H. Lieb. Density functionals for coulomb systems. *International Journal of Quantum Chemistry*, 24(3):243–277, 1983.

[30] Richard M Martin and Richard Milton Martin. *Electronic structure: basic theory and practical methods*. Cambridge university press, 2004.

[31] Neil W Ashcroft, N David Mermin, et al. Solid state physics [by] neil w. ashcroft [and] n. david mermin., 1976.

[32] David M Ceperley and Berni J Alder. Ground state of the electron gas by a stochastic method. *Physical review letters*, 45(7):566, 1980.

[33] John P Perdew, Kieron Burke, and Matthias Ernzerhof. Generalized gradient approximation made simple. *Phys. Rev. Lett.*, 77(18):3865, 1996.

[34] David Sholl and Janice A Steckel. *Density functional theory: a practical introduction*. John Wiley & Sons, 2011.

[35] Aliaksandr V Krukau, Oleg A Vydrov, Artur F Izmaylov, and Gustavo E Scuseria. Influence of the exchange screening parameter on the performance of screened hybrid functionals. *The Journal of chemical physics*, 125(22):224106, 2006.

[36] John P Perdew, Matthias Ernzerhof, and Kieron Burke. Rationale for mixing exact exchange with density functional approximations. *J. Chem. Phys.*, 105(22):9982–9985, 1996.

[37] Lars Hedin. On correlation effects in electron spectroscopies and the gw approximation. *Journal of Physics: Condensed Matter*, 11(42):R489, 1999.

[38] G. Kresse and J. Furthmüller. Efficiency of ab-initio total energy calculations for metals and semiconductors using a plane-wave basis set. *Computational Materials Science*, 6(1):15 – 50, 1996.

[39] G. Kresse and D. Joubert. From ultrasoft pseudopotentials to the projector augmented-wave method. *Phys. Rev. B*, 59:1758–1775, Jan 1999.

[40] P. E. Blöchl. Projector augmented-wave method. *Phys. Rev. B*, 50:17953–17979, Dec 1994.

[41] Hendrik J Monkhorst and James D Pack. Special points for brillouin-zone integrations. *Physical review B*, 13(12):5188, 1976.

[42] Volker Blum, Ralf Gehrke, Felix Hanke, Paula Havu, Ville Havu, Xinguo Ren, Karsten Reuter, and Matthias Scheffler. Ab initio molecular simulations with numeric atom-centered orbitals. *Comput. Phys. Commun.*, 180(11):2175–2196, 2009.

[43] Alex Willand, Yaroslav O Kvashnin, Luigi Genovese, Álvaro Vázquez-Mayagoitia, Arpan Krishna Deb, Ali Sadeghi, Thierry Deutsch, and Stefan Goedecker. Norm-conserving pseudopotentials with chemical accuracy compared to all-electron calculations. *The Journal of chemical physics*, 138(10):104109, 2013.

[44] David Vanderbilt. Soft self-consistent pseudopotentials in a generalized eigenvalue formalism. *Physical review B*, 41(11):7892, 1990.

[45] Peter E Blöchl. Projector augmented-wave method. *Physical review B*, 50(24):17953, 1994.

[46] Bi-Ching Shih, Yu Xue, Peihong Zhang, Marvin L Cohen, and Steven G Louie. Quasiparticle band gap of zno: High accuracy from the conventional g 0 w 0 approach. *Physical review letters*, 105(14):146401, 2010.

[47] Jiří Klimeš, Merzuk Kaltak, and Georg Kresse. Predictive g w calculations using plane waves and pseudopotentials. *Physical Review B*, 90(7):075125, 2014.

[48] Torbjörn Björkman, Andris Gulans, Arkady V Krasheninnikov, and Risto M Nieminen. van der waals bonding in layered compounds from advanced density-functional first-principles calculations. *Physical review letters*, 108(23):235502, 2012.

[49] Mark S Hybertsen and Steven G Louie. First-principles theory of quasiparticles: calculation of band gaps in semiconductors and insulators. *Physical review letters*, 55(13):1418, 1985.

[50] Mark S Hybertsen and Steven G Louie. Electron correlation in semiconductors and insulators: Band gaps and quasiparticle energies. *Physical Review B*, 34(8):5390, 1986.

[51] Rex W Godby, Michael Schlüter, and LJ Sham. Self-energy operators and exchange-correlation potentials in semiconductors. *Physical Review B*, 37(17):10159, 1988.

[52] Lars Hedin. New method for calculating the one-particle green's function with application to the electron-gas problem. *Physical Review*, 139(3A):A796, 1965.

[53] Ferdi Aryasetiawan and Olle Gunnarsson. The gw method. *Reports on Progress in Physics*, 61(3):237, 1998.

---

[54] Noa Marom, Minjung Kim, and James R. Chelikowsky. Structure selection based on high vertical electron affinity for tio_2 clusters. *Phys. Rev. Lett.*, 108:106801, Mar 2012.

[55] Edwin E Salpeter and Hans Albrecht Bethe. A relativistic equation for bound-state problems. *Physical Review*, 84(6):1232, 1951.

[56] Murray Gell-Mann and Francis Low. Bound states in quantum field theory. *Physical Review*, 84(2):350, 1951.

[57] LJ Sham and TM Rice. Many-particle derivation of the effective-mass equation for the wannier exciton. *Physical Review*, 144(2):708, 1966.

[58] W Hanke and LJ Sham. Many-particle effects in the optical excitations of a semiconductor. *Physical Review Letters*, 43(5):387, 1979.

[59] Gordon Baym and Leo P Kadanoff. Conservation laws and correlation functions. *Physical Review*, 124(2):287, 1961.

[60] G Strinati. Dynamical shift and broadening of core excitons in semiconductors. *Physical Review Letters*, 49(20):1519, 1982.

[61] Giovanni Onida, Lucia Reining, RW Godby, R Del Sole, and Wanda Andreoni. Ab initio calculations of the quasiparticle and absorption spectra of clusters: the sodium tetramer. *Physical review letters*, 75(5):818, 1995.

[62] X Leng, F Jin, M Wei, and Y Ma. Wiley interdiscip. rev.: Comput. mol. sci. 6, 532–550 (2016).

[63] Ig Tamm. relativistic interaction of elementary particles. *In selected papers*, pages pages 157–174.

[64] Gerald D Mahan. Condensed matter in a nutshell. In *Condensed Matter in a Nutshell*. Princeton University Press, 2010.

[65] Charles Kittel and Ching-yao Fong. *Quantum theory of solids*. Wiley, 1987.

[66] Mark Fox. Optical properties of solids, 2002.

[67] Paul Adrien Maurice Dirac. The quantum theory of the emission and absorption of radiation. *Proceedings of the Royal Society of London. Series A, Containing Papers of a Mathematical and Physical Character*, 114(767):243–265, 1927.

[68] Fred L Wilson. Fermi's theory of beta decay. *American Journal of Physics*, 36(12):1150–1160, 1968.

[69] Richard Fitzpatrick. *Maxwells Equations and the Principles of Electromagnetism*. Laxmi Publications, Ltd., 2010.

[70] William Jones and Norman Henry March. *Theoretical solid state physics*, volume 35. Courier Corporation, 1985.

[71] Richard Phillips Feynman. Forces in molecules. *Physical review*, 56(4):340, 1939.

[72] Xuemei Lang, Shuanshi Fan, and Yanhong Wang. Intensification of methane and hydrogen storage in clathrate hydrate and future prospect. *Journal of Natural Gas Chemistry*, 19(3):203–209, 2010.

[73] C Liu, YY Fan, M Liu, HT Cong, HM Cheng, and Ms S Dresselhaus. Hydrogen storage in single-walled carbon nanotubes at room temperature. *Science*, 286(5442):1127–1129, 1999.

[74] A Peles, JA Alford, Zhu Ma, Li Yang, and MY Chou. First-principles study of na al h 4 and na 3 al h 6 complex hydrides. *Physical Review B*, 70(16):165105, 2004.

[75] Jorge Íñiguez, T Yildirim, TJ Udovic, M Sulic, and CM Jensen. Structure and hydrogen dynamics of pure and ti-doped sodium alanate. *Physical Review B*, 70(6):060101, 2004.

[76] Santanu Chaudhuri and James T Muckerman. First-principles study of ti-catalyzed hydrogen chemisorption on an al surface: a critical first step for reversible hydrogen storage in naalh4. *The Journal of Physical Chemistry B*, 109(15):6952–6957, 2005.

[77] W Lohstroh and M Fichtner. Rate limiting steps of the phase transformations in ti-doped na al h 4 investigated by isotope exchange. *Physical Review B*, 75(18):184106, 2007.

[78] Vassilis Daioglou, Andre PC Faaij, Deger Saygin, Martin K Patel, Birka Wicke, and Detlef P van Vuuren. Energy demand and emissions of the non-energy sector. *Energy & Environmental Science*, 7(2):482–498, 2014.

[79] Christoph Hank, André Sternberg, Nikolas Köppel, Marius Holst, Tom Smolinka, Achim Schaadt, Christopher Hebling, and Hans-Martin Henning. Energy efficiency and economic assessment of imported energy carriers based on renewable electricity. *Sustainable Energy & Fuels*, 2020.

[80] Don B Fox, Daniel Sutter, and Jefferson W Tester. The thermal spectrum of low-temperature energy use in the united states. *Energy & Environmental Science*, 4(10):3731–3740, 2011.

[81] S. Bhattacharya, Guotao Wu, Chen Ping, Y. P. Feng, and G. P. Das. Lithium calcium imide [li2ca(nh)2] for hydrogen storage: Structural and thermodynamic properties. *The Journal of Physical Chemistry B*, 112(36):11381–11384, 2008. PMID: 18710276.

[82] Amrita Bhattacharya and Saswata Bhattacharya. Exploring n-rich phases in lixny clusters for hydrogen storage at nanoscale. *J. Phys. Chem. Lett.*, 6(18):3726–3730, 2015. PMID: 26722747.

[83] Hui Zeng, Jingjing Xie, Hao Xie, Bao-Lian Su, Menghu Wang, Hang Ping, Weimin Wang, Hao Wang, and Zhengyi Fu. Bioprocess-inspired synthesis of hierarchically porous nitrogen-doped tio2 with high visible-light photocatalytic activity. *J. Mater. Chem. A*, 3:19588–19596, 2015.

[84] Sainan Liu, Zhenyang Cai, Jiang Zhou, Anqiang Pan, and Shuquan Liang. Nitrogen-doped tio2 nanospheres for advanced sodium-ion battery and sodium-ion capacitor applications. *J. Mater. Chem. A*, 4:18278–18283, 2016.

[85] Michel Armand and J-M Tarascon. Building better batteries. *Nature*, 451(7179):652, 2008.

[86] Bruno Scrosati and Jürgen Garche. Lithium batteries: Status, prospects and future. *Journal of power sources*, 195(9):2419–2430, 2010.

[87] Martin Winter and Ralph J Brodd. What are batteries, fuel cells, and supercapacitors? *Chemical reviews*, 105(3):1021–1021, 2005.

[88] Amer Hammami, Nathalie Raymond, and Michel Armand. Lithium-ion batteries: Runaway risk of forming toxic compounds. *Nature*, 424(6949):635, 2003.

[89] JM Tarascon and M Armand. Issues and challenges facing rechargeable lithium batteries nature 414. 2001.

[90] Michel Armand and J-M Tarascon. Building better batteries. *Nature*, 451(7179):652, 2008.

[91] Noriaki Kamaya, Kenji Homma, Yuichiro Yamakawa, Masaaki Hirayama, Ryoji Kanno, Masao Yonemura, Takashi Kamiyama, Yuki Kato, Shigenori Hama, Koji Kawamoto, et al. A lithium superionic conductor. *Nature materials*, 10(9):682–686, 2011.

[92] Jang Wook Choi and Doron Aurbach. Promise and reality of post-lithium-ion batteries with high energy densities. *Nature Reviews Materials*, 1(4):1–16, 2016.

[93] Yuki Kato, Satoshi Hori, Toshiya Saito, Kota Suzuki, Masaaki Hirayama, Akio Mitsui, Masao Yonemura, Hideki Iba, and Ryoji Kanno. High-power all-solid-state batteries using sulfide superionic conductors. *Nature Energy*, 1(4):1–7, 2016.

[94] Takao Inoue and Kazuhiko Mukai. Are all-solid-state lithium-ion batteries really safe?–verification by differential scanning calorimetry with an all-inclusive microcell. *ACS applied materials & interfaces*, 9(2):1507–1515, 2017.

[95] Le Shi and Tianshou Zhao. Recent advances in inorganic 2d materials and their applications in lithium and sodium batteries. *Journal of Materials Chemistry A*, 5(8):3735–3758, 2017.

[96] Tobias Binninger, Aris Marcolongo, Matthieu Mottet, Valéry Weber, and Teodoro Laino. Comparison of computational methods for the electrochemical stability window of solid-state electrolyte materials. *Journal of Materials Chemistry A*, 2020.

[97] Vinodkumar Etacheri, Rotem Marom, Ran Elazari, Gregory Salitra, and Doron Aurbach. Challenges in the development of advanced li-ion batteries: a review. *Energy & Environmental Science*, 4(9):3243–3262, 2011.

[98] Michal Osiak, Hugh Geaney, Eileen Armstrong, and Colm O'Dwyer. Structuring materials for lithium-ion batteries: advancements in nanomaterial structure, composition, and defined assembly on cell performance. *Journal of Materials Chemistry A*, 2(25):9433–9460, 2014.

[99] Paul Albertus, Susan Babinec, Scott Litzelman, and Aron Newman. Status and challenges in enabling the lithium metal electrode for high-energy and low-cost rechargeable batteries. *Nature Energy*, 3(1):16–21, 2018.

[100] Yayuan Liu, Yangying Zhu, and Yi Cui. Challenges and opportunities towards fast-charging battery materials. *Nature Energy*, 4(7):540–550, 2019.

[101] Jeffrey G Smith and Donald J Siegel. Low-temperature paddlewheel effect in glassy solid electrolytes. *Nature Communications*, 11(1):1–11, 2020.

[102] Michel Armand and J-M Tarascon. Building better batteries. *Nature*, 451(7179):652, 2008.

[103] Noriaki Kamaya, Kenji Homma, Yuichiro Yamakawa, Masaaki Hirayama, Ryoji Kanno, Masao Yonemura, Takashi Kamiyama, Yuki Kato, Shigenori Hama, Koji Kawamoto, et al. A lithium superionic conductor. *Nature materials*, 10(9):682, 2011.

[104] Christian Masquelier. Solid electrolytes: Lithium ions on the fast track. *Nature materials*, 10(9):649, 2011.

[105] Eliana Quartarone and Piercarlo Mustarelli. Electrolytes for solid-state lithium rechargeable batteries: recent advances and perspectives. *Chemical Society Reviews*, 40(5):2525–2540, 2011.

[106] Jeffrey W Fergus. Ceramic and polymeric solid electrolytes for lithium-ion batteries. *Journal of Power Sources*, 195(15):4554–4569, 2010.

[107] Longwei Liang, Xuan Sun, Jinyang Zhang, Jinfeng Sun, Linrui Hou, Yang Liu, and Changzhou Yuan. Sur-/interfacial regulation in all-solid-state rechargeable li-ion batteries based on inorganic solid-state electrolytes: advances and perspectives. *Materials Horizons*, 6(5):871–910, 2019.

[108] Juchuan Li, Cheng Ma, Miaofang Chi, Chengdu Liang, and Nancy J Dudney. Solid electrolyte: the key for high-voltage lithium batteries. *Advanced Energy Materials*, 5(4):1401408, 2015.

[109] Fuminori Mizuno, A Hayashi, K Tadanaga, and M Tatsumisago. New, highly ion-conductive crystals precipitated from li_2s–p_2s_5 glasses. *Advanced Materials*, 17(7):918–921, 2005.

[110] Longwei Liang, Xuan Sun, Jinyang Zhang, Jinfeng Sun, Linrui Hou, Yang Liu, and Changzhou Yuan. Sur-/interfacial regulation in all-solid-state rechargeable li-ion batteries based on inorganic solid-state electrolytes: advances and perspectives. *Materials Horizons*, 6(5):871–910, 2019.

[111] Noriaki Kamaya, Kenji Homma, Yuichiro Yamakawa, Masaaki Hirayama, Ryoji Kanno, Masao Yonemura, Takashi Kamiyama, Yuki Kato, Shigenori Hama, Koji Kawamoto, et al. A lithium superionic conductor. *Nature materials*, 10(9):682–686, 2011.

[112] Yan Wang, William Davidson Richards, Shyue Ping Ong, Lincoln J Miara, Jae Chul Kim, Yifei Mo, and Gerbrand Ceder. Design principles for solid-state lithium superionic conductors. *Nature materials*, 14(10):1026–1031, 2015.

[113] Ramaswamy Murugan, Venkataraman Thangadurai, and Werner Weppner. Fast lithium ion conduction in garnet-type $li_7la_3zr_2o_{12}$. *Angewandte Chemie International Edition*, 46(41):7778–7781, 2007.

[114] Qi Liu, Zhen Geng, Cuiping Han, Yongzhu Fu, Song Li, Yan-bing He, Feiyu Kang, and Baohua Li. Challenges and perspectives of garnet solid electrolytes for all solid-state lithium batteries. *Journal of Power Sources*, 389:120–134, 2018.

[115] Jae-Kwang Kim, Young Jun Lim, Hyojin Kim, Gyu-Bong Cho, and Youngsik Kim. A hybrid solid electrolyte for flexible solid-state sodium batteries. *Energy & Environmental Science*, 8(12):3589–3596, 2015.

[116] Youichi Shimizu, Yasunori Azuma, and Satoko Michishita. Sol–gel synthesis of nasicon discs from aqueoussolution. *Journal of Materials Chemistry*, 7(8):1487–1490, 1997.

[117] Supriya Roy and P Padma Kumar. Influence of cationic ordering on ion transport in nasicons: Molecular dynamics study. *Solid State Ionics*, 253:217–222, 2013.

[118] M Guin and F Tietz. Survey of the transport properties of sodium superionic conductor materials for use in sodium batteries. *Journal of power sources*, 273:1056–1064, 2015.

[119] Youichi Shimizu, Yasunori Azuma, and Satoko Michishita. Sol–gel synthesis of nasicon discs from aqueoussolution. *Journal of Materials Chemistry*, 7(8):1487–1490, 1997.

[120] Woo Ju Kwon, Hyeongil Kim, Kyu-Nam Jung, Woosuk Cho, Sung Hyun Kim, Jong-Won Lee, and Min-Sik Park. Enhanced li+ conduction in perovskite $\mathrm{li}_{3x}\mathrm{la}_{2/3-x}\square_{1/3-2x}\mathrm{tio}_3$ solid-electrolytes via microstructural engineering. *Journal of Materials Chemistry A*, 5(13):6257–6262, 2017.

[121] Ryoji Kanno and Masahiro Murayama. Lithium ionic conductor thio-lisicon: The $\mathrm{li}_2\mathrm{sges}_2\mathrm{p}_2\mathrm{s}_5$ system. *Journal of the electrochemical society*, 148(7):A742–A746, 2001.

[122] Christian Masquelier. Solid electrolytes: Lithium ions on the fast track. *Nature materials*, 10(9):649, 2011.

[123] Iek-Heng Chu, Han Nguyen, Sunny Hy, Yuh-Chieh Lin, Zhenbin Wang, Zihan Xu, Zhi Deng, Ying Shirley Meng, and Shyue Ping Ong. Insights into the performance limits of the $\mathrm{li}_7\mathrm{p}_3\mathrm{s}_{11}$ superionic conductor: a combined first-principles and experimental study. *ACS applied materials & interfaces*, 8(12):7843–7853, 2016.

[124] Marcela Calpa, Nataly Carolina Rosero-Navarro, Akira Miura, and Kiyoharu Tadanaga. Instantaneous preparation of high lithium-ion conducting sulfide solid electrolyte $\mathrm{li}_7\mathrm{p}_3\mathrm{s}_{11}$ by a liquid phase process. *RSC advances*, 7(73):46499–46504, 2017.

[125] GB Kunshina, IV Bocharova, and VI Ivanenko. Preparation of the $\mathrm{li}_{1.5}\mathrm{al}_{0.5}\mathrm{ge}_{1.5}(\mathrm{po}_4)_3$ solid electrolyte with high ionic conductivity. *Inorganic Materials: Applied Research*, 8(2):238–244, 2017.

[126] Stefan Adams and R Prasada Rao. Structural requirements for fast lithium ion migration in $\mathrm{li}_{10}\mathrm{gep}_2\mathrm{s}_{12}$. *Journal of Materials Chemistry*, 22(16):7687–7691, 2012.

[127] Yuki Kato, Satoshi Hori, Toshiya Saito, Kota Suzuki, Masaaki Hirayama, Akio Mitsui, Masao Yonemura, Hideki Iba, and Ryoji Kanno. High-power all-solid-state batteries using sulfide superionic conductors. *Nature Energy*, 1(4):16030, 2016.

[128] Alexander Kuhn, Oliver Gerbig, Changbao Zhu, Frank Falkenberg, Joachim Maier, and Bettina V Lotsch. A new ultrafast superionic li-conductor: ion dynamics in $\mathrm{li}_{11}\mathrm{si}_2\mathrm{ps}_{12}$ and comparison with other tetragonal lgps-type electrolytes. *Physical Chemistry Chemical Physics*, 16(28):14669–14674, 2014.

[129] Philipp Bron, Sebastian Johansson, Klaus Zick, Jorn Schmedt auf der Gunne, Stefanie Dehnen, and Bernhard Roling. $Li_{10}snp_2s_{12}$: an affordable lithium superionic conductor. *Journal of the American Chemical Society*, 135(42):15694–15697, 2013.

[130] Sebastian Wenzel, Simon Randau, Thomas Leichtweiß, Dominik A Weber, Joachim Sann, Wolfgang G Zeier, and Jurgen Janek. Direct observation of the interfacial instability of the fast ionic conductor $li_{10}gep_2s_{12}$ at the lithium metal anode. *Chemistry of Materials*, 28(7):2400–2407, 2016.

[131] Justin M Whiteley, Jae H Woo, Enyuan Hu, Kyung-Wan Nam, and Se-Hee Lee. Empowering the lithium metal battery through a silicon-based superionic conductor. *Journal of the Electrochemical Society*, 161(12):A1812–A1817, 2014.

[132] JF Whitacre and WC West. Crystalline li_3po_4/li_4sio_4 solid solutions as an electrolyte for film batteries using sputtered cathode layers. *Solid State Ionics*, 175(1-4):251–255, 2004.

[133] Syed Bahari Ramadzan Syed Adnan, Nor Sabirin Mohamed, and KA Norwati. Li_4sio_4 prepared by sol-gel method as potential host for lisicon structured solid electrolytes. *International Journal of Physical and Mathematical Sciences*, 5(2):183–186, 2011.

[134] RD Shannon, BE Taylor, AD English, and T Berzins. New li solid electrolytes. In *International Symposium on Solid Ionic and Ionic-Electronic Conductors*, pages 783–796. Elsevier, 1977.

[135] WH Baur and T Ohta. The crystal structure of $li_{3.75}si_{0.75}p_{0.25}o_4$ and ionic conductivity in tetrahedral structures. *Journal of Solid State Chemistry*, 44(1):50–59, 1982.

[136] Yue Deng, Christopher Eames, Jean-Noel Chotard, Fabien Lalere, Vincent Seznec, Steffen Emge, Oliver Pecher, Clare P Grey, Christian Masquelier, and M Saiful Islam. Structural and mechanistic insights into fast lithium-ion conduction in li_4sio_4–li_3po_4 solid electrolytes. *Journal of the American Chemical Society*, 137(28):9136–9145, 2015.

[137] Yuki Sakurai, Atsushi Sakuda, Akitoshi Hayashi, and Masahiro Tatsumisago. Preparation of amorphous li_4sio_4–li_3po_4 thin films by pulsed laser deposition for all-solid-state lithium secondary batteries. *Solid State Ionics*, 182(1):59–63, 2011.

[138] BJ Neudecker and W Weppner. Li_9sialo_8: a lithium ion electrolyte for voltages above 5.4 v. *Journal of the electrochemical society*, 143(7):2198–2203, 1996.

[139] Yue Deng, Christopher Eames, Benoit Fleutot, Renald David, Jean-Noel Chotard, Emmanuelle Suard, Christian Masquelier, and M Saiful Islam. Enhancing the lithium ion conductivity in lithium superionic conductor (lisicon) solid electrolytes through a mixed polyanion effect. *ACS applied materials & interfaces*, 9(8):7050–7058, 2017.

[140] Robert G Parr. Density functional theory of atoms and molecules. In *Horizons of Quantum Chemistry*, pages 5–15. Springer, 1980.

[141] Peter E Blöchl. Projector augmented-wave method. *Physical review B*, 50(24):17953, 1994.

[142] Georg Kresse and Jürgen Hafner. Ab initio molecular-dynamics simulation of the liquid-metal–amorphous-semiconductor transition in germanium. *Physical Review B*, 49(20):14251, 1994.

[143] Georg Kresse and Jürgen Furthmüller. Efficient iterative schemes for ab initio total-energy calculations using a plane-wave basis set. *Physical review B*, 54(16):11169, 1996.

[144] Tao Tang, Piheng Chen, Wenhua Luo, Deli Luo, and Yu Wang. Crystalline and electronic structures of lithium silicates: A density functional theory study. *Journal of nuclear materials*, 420(1-3):31–38, 2012.

[145] John P Perdew, John A Chevary, Sy H Vosko, Koblar A Jackson, Mark R Pederson, Dig J Singh, and Carlos Fiolhais. Atoms, molecules, solids, and surfaces: Applications of the generalized gradient approximation for exchange and correlation. *Physical Review B*, 46(11):6671, 1992.

[146] Jochen Heyd, Gustavo E. Scuseria, and Matthias Ernzerhof. Hybrid functionals based on a screened coulomb potential. *The Journal of Chemical Physics*, 118(18):8207–8215, 2003.

[147] Péter Pulay. Convergence acceleration of iterative sequences. the case of scf iteration. *Chemical Physics Letters*, 73(2):393–398, 1980.

[148] Denis J Evans and Brad Lee Holian. The nose–hoover thermostat. *The Journal of chemical physics*, 83(8):4069–4074, 1985.

[149] Amrita Bhattacharya and Saswata Bhattacharya. Unraveling the role of vacancies in the potentially promising thermoelectric clathrates $\mathrm{Ba_8Zn}_x\mathrm{Ge}_{46-x-y}\square_y$. *Phys. Rev. B*, 94:094305, Sep 2016.

[150] Saswata Bhattacharya, Daniel Berger, Karsten Reuter, Luca M. Ghiringhelli, and Sergey V. Levchenko. Theoretical evidence for unexpected o-rich phases at corners of mgo surfaces. *Phys. Rev. Materials*, 1:071601, Dec 2017.

[151] Jochen Heyd, Gustavo E Scuseria, and Matthias Ernzerhof. Hybrid functionals based on a screened coulomb potential. *The Journal of chemical physics*, 118(18):8207–8215, 2003.

[152] Michael K Bates, Qingying Jia, Huong Doan, Wentao Liang, and Sanjeev Mukerjee. Charge-transfer effects in ni–fe and ni–fe–co mixed-metal oxides for the alkaline oxygen evolution reaction. *ACS Catal.*, 6(1):155–161, 2015.

[153] Cong Liu, Thomas R Cundari, and Angela K Wilson. Co2 reduction on transition metal (fe, co, ni, and cu) surfaces: In comparison with homogeneous catalysis. *J. Phys. Chem. C*, 116(9):5681–5688, 2012.

[154] Yun Hang Hu and Eli Ruckenstein. Binary mgo-based solid solution catalysts for methane conversion to syngas. *Catal. Rev.*, 44(3):423–453, 2002.

[155] Xingfeng He, Yizhou Zhu, Alexander Epstein, and Yifei Mo. Statistical variances of diffusional properties from ab initio molecular dynamics simulations. *npj Computational Materials*, 4(1):18, 2018.

[156] Aris Marcolongo and Nicola Marzari. Ionic correlations and failure of nernst-einstein relation in solid-state electrolytes. *Physical Review Materials*, 1(2):025402, 2017.

[157] Yohei Okada, Masahiro Ikeda, and Masaru Aniya. Non-arrhenius ionic conductivity in solid electrolytes: A theoretical model and its relation with the bonding nature. *Solid State Ionics*, 281:43–48, 2015.

[158] John Christopher Bachman, Sokseiha Muy, Alexis Grimaud, Hao-Hsun Chang, Nir Pour, Simon F Lux, Odysseas Paschos, Filippo Maglia, Saskia Lupart, Peter Lamp, et al. Inorganic solid-state electrolytes for lithium batteries: mechanisms and properties governing ion conduction. *Chemical reviews*, 116(1):140–162, 2015.

[159] Pooja Basera, Shikha Saini, and Saswata Bhattacharya. Self energy and excitonic effect in (un) doped tio 2 anatase: a comparative study of hybrid dft, gw and bse to explore optical properties. *Journal of Materials Chemistry C*, 7(45):14284–14293, 2019.

[160] Marvin A Kraft, Sean P Culver, Mario Calderon, Felix Bocher, Thorben Krauskopf, Anatoliy Senyshyn, Christian Dietrich, Alexandra Zevalkink, Jurgen Janek, and Wolfgang G Zeier. Influence of lattice polarizability on the ionic conductivity in the lithium superionic argyrodites $\mathrm{li}_6\mathrm{ps}_5\mathrm{x}$ (x= cl, br, i). *Journal of the American Chemical Society*, 139(31):10909–10918, 2017.

[161] Jarvist M Frost, Keith T Butler, Federico Brivio, Christopher H Hendon, Mark Van Schilfgaarde, and Aron Walsh. Atomistic origins of high-performance in hybrid halide perovskite solar cells. *Nano letters*, 14(5):2584–2590, 2014.

[162] Nicholas De Marco, Huanping Zhou, Qi Chen, Pengyu Sun, Zonghao Liu, Lei Meng, En-Ping Yao, Yongsheng Liu, Andy Schiffer, and Yang Yang. Guanidinium: a route to enhanced carrier lifetime and open-circuit voltage in hybrid perovskite solar cells. *Nano letters*, 16(2):1009–1016, 2016.

[163] Yongfei Zhang, Yongqi Liang, Yajuan Wang, Fengwan Guo, Licheng Sun, and Dongsheng Xu. Planar fapbbr_3 solar cells with power conversion efficiency above 10%. *American Chemical Society Energy Letters*, 3(8):1808–1814, 2018.

[164] Qi Dong, Lei Lei, Juliana Mendes, and Franky So. Operational stability of perovskite light emitting diodes. *Journal of Physics: Materials*, 3(1):012002, jan 2020.

[165] E Gagaoudakis, A Panagiotopoulos, T Maksudov, M Moschogiannaki, D Katerinopoulou, G Kakavelakis, G Kiriakidis, V Binas, E Kymakis, and K Petridis. Self-powered, flexible and room temperature operated solution processed hybrid metal halide p-type sensing element for efficient hydrogen detection. *Journal of Physics: Materials*, 3(1):014010, jan 2020.

[166] Jiwei Ma, Aurélien Habrioux, Yun Luo, Guadalupe Ramos-Sanchez, Laura Calvillo, Gaetano Granozzi, Perla B. Balbuena, and Nicolas Alonso-Vante. Electronic interaction between platinum nanoparticles and nitrogen-doped reduced graphene oxide: effect on the oxygen reduction reaction. *J. Mater. Chem. A*, 3:11891–11904, 2015.

[167] Tom J. Savenije, Carlito S. Ponseca, Lucas Kunneman, Mohamed Abdellah, Kaibo Zheng, Yuxi Tian, Qiushi Zhu, Sophie E. Canton, Ivan G. Scheblykin, Tonu Pullerits, Arkady Yartsev, and Villy Sundström. Thermally activated exciton dissociation and recombination control the carrier dynamics in organometal halide perovskite. *The Journal of Physical Chemistry Letters*, 5(13):2189–2194, 2014.

[168] Pooja Basera, Manish Kumar, Shikha Saini, and Saswata Bhattacharya. Reducing lead toxicity in the methylammonium lead halide mapbi_3: Why sn substitution should be preferred to pb vacancy for optimum solar cell efficiency. *Physical Review B*, 101:054108, 2020.

[169] Min Ji Hong, Scott R Svadlenak, Konstantinos A Goulas, and John G Labram. Thermal stability of mobility in methylammonium lead iodide. *Journal of Physics: Materials*, 3(1):014003, nov 2019.

[170] K. Xerxes Steirer, Philip Schulz, Glenn Teeter, Vladan Stevanovic, Mengjin Yang, Kai Zhu, and Joseph J. Berry. Defect tolerance in methylammonium lead triiodide perovskite. *ACS Energy Letters*, 1(2):360–366, 2016.

[171] Xiaofan Zhang, Bingyan Zhang, Zhixiang Zuo, Mingkui Wang, and Yan Shen. N/si co-doped oriented single crystalline rutile tio2 nanorods for photoelectrochemical water splitting. *J. Mater. Chem. A*, 3:10020–10025, 2015.

[172] Nicholas P. Chadwick, Emily N. K. Glover, Sanjayan Sathasivam, Sulaiman N. Basahel, Shaeel A. Althabaiti, Abdulrahman O. Alyoubi, Ivan P. Parkin, and Claire J. Carmalt. Photo-activity and low resistivity in n/nb co-doped tio2 thin films by combinatorial aacvd. *J. Mater. Chem. A*, 4:407–415, 2016.

[173] Byung-wook Park and Sang Il Seok. Intrinsic instability of inorganic–organic hybrid halide perovskite materials. *Advanced Materials*, 31(20):1805337, 2019.

[174] Aslihan Babayigit, Anitha Ethirajan, Marc Muller, and Bert Conings. Toxicity of organometal halide perovskite solar cells. *Nature Materials*, 15(3):247, 2016.

[175] Michael Kulbak, David Cahen, and Gary Hodes. How important is the organic part of lead halide perovskite photovoltaic cells? efficient cspbbr_3 cells. *The Journal of Physical Chemistry Letters*, 6(13):2452–2456, 2015.

[176] Jia Liang, Caixing Wang, Yanrong Wang, Zhaoran Xu, Zhipeng Lu, Yue Ma, Hongfei Zhu, Yi Hu, Chengcan Xiao, Xu Yi, et al. All-inorganic perovskite solar cells. *Journal of the American Chemical Society*, 138(49):15829–15832, 2016.

[177] Yeonsig Nam, Jong Hyeon Lim, Kyoung Chul Ko, and Jin Yong Lee. Photocatalytic activity of tio2 nanoparticles: a theoretical aspect. *J. Mater. Chem. A*, 7:13833–13859, 2019.

[178] Anna Iwaszuk, P. A. Mulheran, and Michael Nolan. Tio2 nanocluster modified-rutile tio2 photocatalyst: a first principles investigation. *J. Mater. Chem. A*, 1:2515–2525, 2013.

[179] Mingzheng Ge, Chunyan Cao, Jianying Huang, Shuhui Li, Zhong Chen, Ke-Qin Zhang, S. S. Al-Deyab, and Yuekun Lai. A review of one-dimensional tio2 nanostructured materials for environmental and energy applications. *J. Mater. Chem. A*, 4:6772–6801, 2016.

[180] Zhao-Qi Li, Chong-Jiao Mo, Yao Guo, Nan-Nan Xu, Qin-Yu Zhu, and Jie Dai. Discrete supertetrahedral cuins nanoclusters and their application in fabrication of cluster-sensitized tio2 photoelectrodes. *J. Mater. Chem. A*, 5:8519–8525, 2017.

[181] Yao Cai, Wei Xie, Yin Ting Teng, PC Harikesh, Biplab Ghosh, Patrick Huck, Kristin A Persson, Nripan Mathews, Subodh G Mhaisalkar, Matthew Sherburne, et al. High-throughput computational study of halide double perovskite inorganic compounds. *Chemistry of Materials*, 31(15):5392–5401, 2019.

[182] Na Chen, Tong Cai, Wenhao Li, Katie Hills-Kimball, Hanjun Yang, Meidan Que, Yasutaka Nagaoka, Zhenyang Liu, Dong Yang, Angang Dong, et al. Yb-and mn-doped lead-free double perovskite $\mathrm{cs}_2\mathrm{agbix}_6$ (x= cl–, br–) nanocrystals. *American Chemical Society Applied Materials & Interfaces*, 11(18):16855–16863, 2019.

[183] Dan Han, Tao Zhang, and Shiyou Chen. High-throughput first-principles screening of layered magnetic double perovskites cs4msb2x12 for spintronic applications. *Journal of Physics: Condensed Matter*, 32(22):225705, mar 2020.

[184] Jun Xing, Hai Bo Jiang, Jian Fu Chen, Yu Hang Li, Long Wu, Shuang Yang, Li Rong Zheng, Hai Feng Wang, P. Hu, Hui Jun Zhao, and Hua Gui Yang. Active sites on hydrogen evolution photocatalyst. *J. Mater. Chem. A*, 1:15258–15264, 2013.

[185] Jie Zhou, Han Wu, Chun-Yi Sun, Cheng-Ying Hu, Xin-Long Wang, Zhen-Hui Kang, and Zhong-Min Su. Ultrasmall c-tio2x nanoparticle/g-c3n4 composite for co2 photoreduction with high efficiency and selectivity. *J. Mater. Chem. A*, 6:21596–21604, 2018.

[186] Raman Singh Lamba, Pooja Basera, Saswata Bhattacharya, and Sameer Sapra. Band gap engineering in $\mathrm{cs_2(na_x ag_{1-x})bicl_6}$ double perovskite nanocrystals. *The Journal of Physical Chemistry Letters*, 10(17):5173–5181, 2019.

[187] T Thao Tran, Jessica R Panella, Juan R Chamorro, Jennifer R Morey, and Tyrel M McQueen. Designing indirect–direct bandgap transitions in double perovskites. *Materials Horizons*, 4(4):688–693, 2017.

[188] Wan Deng, Zun-Yi Deng, Jiawei He, Mingzi Wang, Zi-Xuan Chen, Su-Huai Wei, and Hong-Jian Feng. Synthesis of $\mathrm{cs_2agsbcl_6}$ and improved optoelectronic properties of $\mathrm{cs_2agsbcl_6}$/$\mathrm{tio_2}$ heterostructure driven by the interface effect for lead-free double perovskites solar cells. *Applied Physics Letters*, 111(15):151602, 2017.

[189] George Volonakis, Amir Abbas Haghighirad, Rebecca L Milot, Weng H Sio, Marina R Filip, Bernard Wenger, Michael B Johnston, Laura M Herz, Henry J Snaith, and Feliciano Giustino. $\mathrm{cs_2inagcl_6}$: a new lead-free halide double perovskite with direct band gap. *The Journal of Physical Chemistry Letters*, 8(4):772–778, 2017.

[190] Federico Locardi, Matilde Cirignano, Dmitry Baranov, Zhiya Dang, Mirko Prato, Filippo Drago, Maurizio Ferretti, Valerio Pinchetti, Marco Fanciulli, Sergio Brovelli, et al. Colloidal synthesis of double perovskite $\mathrm{cs_2agincl_6}$ and mn-doped $\mathrm{cs_2agincl_6}$ nanocrystals. *Journal of the American Chemical Society*, 140(40):12989–12995, 2018.

[191] Xin-Gang Zhao, Ji-Hui Yang, Yuhao Fu, Dongwen Yang, Qiaoling Xu, Liping Yu, Su-Huai Wei, and Lijun Zhang. Design of lead-free inorganic halide perovskites for solar

cells via cation-transmutation. *Journal of the American Chemical Society*, 139(7):2630–2638, 2017.

[192] Weiwei Meng, Xiaoming Wang, Zewen Xiao, Jianbo Wang, David B Mitzi, and Yanfa Yan. Parity-forbidden transitions and their impact on the optical absorption properties of lead-free metal halide perovskites and double perovskites. *The Journal of Physical Chemistry Letters*, 8(13):2999–3007, 2017.

[193] Jochen Heyd, Gustavo E Scuseria, and Matthias Ernzerhof. Hybrid functionals based on a screened coulomb potential. *The Journal of Chemical Physics*, 118(18):8207–8215, 2003.

[194] Gabriel R Schleder, Antonio C M Padilha, Carlos Mera Acosta, Marcio Costa, and Adalberto Fazzio. From DFT to machine learning: recent approaches to materials science–a review. *Journal of Physics: Materials*, 2(3):032001, may 2019.

[195] Saswata Bhattacharya and G. P. Das. *First-Principles Design of Complex Chemical Hydrides as Hydrogen Storage Materials*, chapter 20, pages 424–439. Taylor and Francis Group, 2013.

[196] G Kresse and J Hafner. 14251); g. kresse, j. furthmüller. *Physical Review B*, 54:11169, 1996.

[197] Eric T McClure, Molly R Ball, Wolfgang Windl, and Patrick M Woodward. Cs2agbix6 (x= br, cl): new visible light absorbing, lead-free halide perovskite semiconductors. *Chemistry of Materials*, 28(5):1348, 2016.

[198] Shikha Saini, Pooja Basera, Manish Kumar, Preeti Bhumla, and Saswata Bhattacharya. Metastability triggered reactivity in clusters at realistic conditions: a case study of n-doped (TiO2) n for photocatalysis. *Journal of Physics: Materials*, 4(1):015001, nov 2020.

[199] Amrita Bhattacharya and Saswata Bhattacharya. Unraveling the role of vacancies in the potentially promising thermoelectric clathrates $\mathrm{ba}_8\mathrm{zn}_x\mathrm{ge}_{46-x-y}\square_y$. *Phys. Rev. B*, 94:094305, Sep 2016.

[200] Deepika Gill, Manish Kumar, Pooja Basera, and Saswata Bhattacharya. Understanding the ionic diffusivity in the (meta) stable (un) doped solid-state electrolyte from first-principles: A case study of lisicon. *The Journal of Physical Chemistry C*, 124(32):17485, 2020.

[201] Saswata Bhattacharya, Daniel Berger, Karsten Reuter, Luca M Ghiringhelli, and Sergey V Levchenko. Theoretical evidence for unexpected o-rich phases at corners of mgo surfaces. *Physical Review Materials*, 1(7):071601, 2017.

[202] Gregor Kieslich, Shijing Sun, and Anthony K Cheetham. An extended tolerance factor approach for organic–inorganic perovskites. *Chemical science*, 6(6):3430–3433, 2015.

[203] Chonghea Li, Xionggang Lu, Weizhong Ding, Liming Feng, Yonghui Gao, and Ziming Guo. Formability of abx_3 (x= f, cl, br, i) halide perovskites. *Acta Crystallographica Section B: Structural Science*, 64(6):702–707, 2008.

[204] Jiban Kangsabanik, Vipinraj Sugathan, Anuradha Yadav, Aswani Yella, and Aftab Alam. Double perovskites overtaking the single perovskites: A set of new solar harvesting materials with much higher stability and efficiency. *Physical Review Materials*, 2(5):055401, 2018.

[205] Qingde Sun, Hangyan Chen, and Wan-Jian Yin. Do chalcogenide double perovskites work as solar cell absorbers: a first-principles study. *Chemistry of Materials*, 31(1):244–250, 2018.

[206] William Shockley and Hans J Queisser. Detailed balance limit of efficiency of p-n junction solar cells. *Journal of Applied Physics*, 32(3):510–519, 1961.

[207] Christopher N Savory, Aron Walsh, and David O Scanlon. Can pb-free halide double perovskites support high-efficiency solar cells? *American Chemical Society Energy Letters*, 1(5):949–955, 2016.

[208] Hamid M Ghaithan, Zeyad A Alahmed, Saif MH Qaid, Mahmoud Hezam, and Abdullah S Aldwayyan. Density functional study of cubic, tetragonal, and orthorhombic cspbbr3 perovskite. *ACS omega*, 5(13):7468–7480, 2020.

[209] Manjari Jain, Arunima Singh, Pooja Basera, Manish Kumar, and Saswata Bhattacharya. Understanding the role of sn substitution and pb- in enhancing the optical properties and

solar cell efficiency of ch (nh 2) 2 pb 1- x- y sn x y br 3. *Journal of Materials Chemistry C*, 8(30):10362–10368, 2020.

[210] Liping Yu and Alex Zunger. Identification of potential photovoltaic absorbers based on first-principles spectroscopic screening of materials. *Physical Review Letters*, 108(6):068701, 2012.

[211] Marina R Filip, Samuel Hillman, Amir Abbas Haghighirad, Henry J Snaith, and Feliciano Giustino. Band gaps of the lead-free halide double perovskites $\mathrm{cs_2biagcl_6}$ and $\mathrm{cs_2biagbr_6}$ from theory and experiment. *The Journal of Physical Chemistry Letters*, 7(13):2579–2585, 2016.

[212] Henry J Snaith. Perovskites: the emergence of a new era for low-cost, high-efficiency solar cells. *The journal of physical chemistry letters*, 4(21):3623–3630, 2013.

[213] Jun Hong Noh, Sang Hyuk Im, Jin Hyuck Heo, Tarak N Mandal, and Sang Il Seok. Chemical management for colorful, efficient, and stable inorganic–organic hybrid nanostructured solar cells. *Nano letters*, 13(4):1764–1769, 2013.

[214] Jonas Stenberg. Perovskite solar cells. *UMEA UNIVERSITY: Master in Energy Engineering*, 2017.

[215] Wan-Jian Yin, Tingting Shi, and Yanfa Yan. Unique properties of halide perovskites as possible origins of the superior solar cell performance. *Advanced Materials*, 26(27):4653–4658, 2014.

[216] Akihiro Kojima, Kenjiro Teshima, Yasuo Shirai, and Tsutomu Miyasaka. Organometal halide perovskites as visible-light sensitizers for photovoltaic cells. *Journal of the American Chemical Society*, 131(17):6050–6051, 2009.

[217] Michael M Lee, Joël Teuscher, Tsutomu Miyasaka, Takurou N Murakami, and Henry J Snaith. Efficient hybrid solar cells based on meso-superstructured organometal halide perovskites. *Science*, 338(6107):643–647, 2012.

[218] Martin A Green, Anita Ho-Baillie, and Henry J Snaith. The emergence of perovskite solar cells. *Nature photonics*, 8(7):506–514, 2014.

[219] Michael Grätzel. The light and shade of perovskite solar cells. *Nature materials*, 13(9):838–842, 2014.

[220] Pooja Basera, Manish Kumar, Shikha Saini, and Saswata Bhattacharya. Reducing lead toxicity in the methylammonium lead halide $\mathrm{MAPbI_3}$: Why sn substitution should be preferred to pb vacancy for optimum solar cell efficiency. *Physical Review B*, 101(5):054108, 2020.

[221] Deepika Gill, Preeti Bhumla, Manish Kumar, and Saswata Bhattacharya. High-throughput screening to modulate electronic and optical properties of alloyed $\mathrm{Cs_2AgBiCl_6}$ for enhanced solar cell efficiency. *Journal of Physics: Materials*, 4(2):025005, 2021.

[222] Manjari Jain, Arunima Singh, Pooja Basera, Manish Kumar, and Saswata Bhattacharya. Understanding the role of sn substitution and pb-$\boxtimes$ in enhancing the optical properties and solar cell efficiency of $\mathrm{ch(nh_2)_2pb_{1-x-y}sn_x\boxtimes_y br_3}$. *Journal of Materials Chemistry C*, 8:10362–10368, 2020.

[223] Giorgio Schileo and Giulia Grancini. Lead or no lead? availability, toxicity, sustainability and environmental impact of lead-free perovskite solar cells. *Journal of Materials Chemistry C*, 9(1):67–76, 2021.

[224] Fabio Chiarella, Andrea Zappettini, Francesca Licci, Ivo Borriello, Giovanni Cantele, Domenico Ninno, Antonio Cassinese, and Ruggero Vaglio. Combined experimental and theoretical investigation of optical, structural, and electronic properties of $\mathrm{CH_3NH_3SnX_3}$ thin films ($\mathrm{X = Cl, Br}$). *Physical Review B*, 77(4):045129, 2008.

[225] Daniel Adjei Agyeman, Kyeongse Song, Seung Ho Kang, Mi Ru Jo, Eunbi Cho, and Yong-Mook Kang. An improved catalytic effect of nitrogen-doped tio2 nanofibers for rechargeable li–o2 batteries; the role of oxidation states and vacancies on the surface. *J. Mater. Chem. A*, 3:22557–22563, 2015.

[226] David G Billing and Andreas Lemmerer. Inorganic–organic hybrid materials incorporating primary cyclic ammonium cations: The lead iodide series. *CrystEngComm*, 9(3):236–244, 2007.

[227] Victor Moritz Goldschmidt. Die gesetze der krystallochemie. *Naturwissenschaften*, 14(21):477–485, 1926.

[228] Minghao Wang, Wei Wang, Ben Ma, Wei Shen, Lihui Liu, Kun Cao, Shufen Chen, and Wei Huang. Lead-free perovskite materials for solar cells. *Nano-Micro Letters*, 13(1):1–36, 2021.

[229] Liu Liang, Lu Wencong, and Chen Nianyi. On the criteria of formation and lattice distortion of perovskite-type complex halides. *Journal of Physics and Chemistry of Solids*, 65(5):855–860, 2004.

[230] Jia Zhang and Bin Hu. Revealing photoinduced bulk polarization and spin-orbit coupling effects in high-efficiency 2d/3d pb-sn alloyed perovskite solar cells. *Nano Energy*, 76:104999, 2020.

[231] Chuangye Ge, YZB Xue, Liang Li, Bin Tang, and Hanlin Hu. Recent progress in 2d/3d multidimensional metal halide perovskites solar cells. *Frontiers in Materials*, 7:380, 2020.

[232] Deepika Gill, Arunima Singh, Manjari Jain, and Saswata Bhattacharya. Exploring exciton and polaron dominated photophysical phenomena in ruddlesden–popper phases of $\mathrm{Ba_{n+1}Zr_nS_{3n+1}}$ (n = 1–3) from many body perturbation theory. *The Journal of Physical Chemistry Letters*, 12(28):6698–6706, 2021.

[233] Boubacar Traore, Laurent Pedesseau, Linda Assam, Xiaoyang Che, Jean-Christophe Blancon, Hsinhan Tsai, Wanyi Nie, Constantinos C Stoumpos, Mercouri G Kanatzidis, Sergei Tretiak, et al. Composite nature of layered hybrid perovskites: assessment on quantum and dielectric confinements and band alignment. *ACS nano*, 12(4):3321–3332, 2018.

[234] Tingwei Zhou, Ming Wang, Zhigang Zang, Xiaosheng Tang, and Liang Fang. Two-dimensional lead-free hybrid halide perovskite using superatom anions with tunable electronic properties. *Solar Energy Materials and Solar Cells*, 191:33–38, 2019.

[235] Rayan Chakraborty and Angshuman Nag. Dielectric confinement for designing compositions and optoelectronic properties of 2d layered hybrid perovskites. *Physical Chemistry Chemical Physics*, 23(1):82–93, 2021.

---

[236] Laurent Pedesseau, Daniel Sapori, Boubacar Traore, Roberto Robles, Hong-Hua Fang, Maria Antonietta Loi, Hsinhan Tsai, Wanyi Nie, Jean-Christophe Blancon, Amanda Neukirch, et al. Advances and promises of layered halide hybrid perovskite semiconductors. *ACS nano*, 10(11):9776–9786, 2016.

[237] Pablo P Boix, Shweta Agarwala, Teck Ming Koh, Nripan Mathews, and Subodh G Mhaisalkar. Perovskite solar cells: beyond methylammonium lead iodide. *The Journal of Physical Chemistry Letters*, 6(5):898–907, 2015.

[238] Makhsud I Saidaminov, Omar F Mohammed, and Osman M Bakr. Low-dimensional-networked metal halide perovskites: the next big thing. *ACS Energy Letters*, 2(4):889–896, 2017.

[239] Jun Hu, Liang Yan, and Wei You. Two-dimensional organic–inorganic hybrid perovskites: a new platform for optoelectronic applications. *Advanced Materials*, 30(48):1802041, 2018.

[240] Carmen Ortiz-Cervantes, Paulina Carmona-Monroy, and Diego Solis-Ibarra. Two-dimensional halide perovskites in solar cells: 2d or not 2d? *ChemSusChem*, 12(8):1560–1575, 2019.

[241] Kshetra Mohan Dehury, Pawan K Kanaujia, Mohammad Adnan, Manish Kumar, Saswata Bhattacharya, and G Vijaya Prakash. Structure-dependent (non) linear optical excitons in primary cyclic ammonium ($\mathrm{C_nH_{2n-1}NH_2}$; n = 3–8)-based inorganic–organic hybrid semiconductor series. *The Journal of Physical Chemistry C*, 125(12):6821–6831, 2021.

[242] Amrita Bhattacharya and Saswata Bhattacharya. Exploring n-rich phases in lixny clusters for hydrogen storage at nanoscale. *The Journal of Physical Chemistry Letters*, 6(18):3726–3730, 2015. PMID: 26722747.

[243] Manish Kumar, Manjari Jain, Arunima Singh, and Saswata Bhattacharya. Sublattice mixing in cs2agincl6 for enhanced optical properties from first-principles. *Applied Physics Letters*, 118(2):021901, 2021.

[244] Georg Kresse and Jürgen Furthmüller. Efficiency of ab-initio total energy calculations for metals and semiconductors using a plane-wave basis set. *Computational materials science*, 6(1):15–50, 1996.

[245] Kannan Pradeesh, K Nageswara Rao, and G Vijaya Prakash. Synthesis, structural, thermal and optical studies of inorganic-organic hybrid semiconductors, $\mathrm{R-PbI_4}$. *Journal of Applied Physics*, 113(8):083523, 2013.

[246] Qingde Sun and Wan-Jian Yin. Thermodynamic stability trend of cubic perovskites. *Journal of the American Chemical Society*, 139(42):14905–14908, 2017.

[247] Markus Becker, Thorsten Klüner, and Michael Wark. Formation of hybrid $\mathrm{ABX_3}$ perovskite compounds for solar cell application: first-principles calculations of effective ionic radii and determination of tolerance factors. *Dalton Transactions*, 46(11):3500–3509, 2017.

[248] W Travis, ENK Glover, Hugo Bronstein, DO Scanlon, and RG Palgrave. On the application of the tolerance factor to inorganic and hybrid halide perovskites: a revised system. *Chemical Science*, 7(7):4548–4556, 2016.

[249] Pooja Basera, Shikha Saini, and Saswata Bhattacharya. Self energy and excitonic effect in (un)doped tio2 anatase: a comparative study of hybrid dft, gw and bse to explore optical properties. *Journal of Materials Chemistry C*, 7:14284–14293, 2019.

[250] Liping Yu, Robert S Kokenyesi, Douglas A Keszler, and Alex Zunger. Inverse design of high absorption thin-film photovoltaic materials. *Advanced Energy Materials*, 3(1):43–48, 2013.

[251] Manish Kumar, Arunima Singh, Deepika Gill, and Saswata Bhattacharya. Optoelectronic properties of chalcogenide perovskites by many-body perturbation theory. *The Journal of Physical Chemistry Letters*, 12(22):5301–5307, 2021. PMID: 34061540.

[252] Sven Rühle. Tabulated values of the shockley–queisser limit for single junction solar cells. *Solar Energy*, 130:139–147, 2016.

[253] Michael J Waters, Daniel Hashemi, and John Kieffer. Semiclassical model for calculating exciton and polaron pair energetics at interfaces. *Materials Science and Engineering: B*, 261:114657, 2020.

[254] Herbert Fröhlich. Electrons in lattice fields. *Advances in Physics*, 3(11):325–361, 1954.

[255] Robert W Hellwarth and Ivan Biaggio. Mobility of an electron in a multimode polar lattice. *Physical Review B*, 60(1):299, 1999.

[256] Jarvist Moore Frost. Calculating polaron mobility in halide perovskites. *Physical Review B*, 96(19):195202, 2017.

[257] B Jaffe, WR Cook, and H Jaffe. Piezoelectric ceramics academic press london. In *JCPDS 71-2171*. Piezoelectric Ceramics Academic Press: London; 1971.

[258] Sekai Tombe, Getachew Adam, Herwig Heilbrunner, Dogukan Hazar Apaydin, Christoph Ulbricht, Niyazi Serdar Sariciftci, Christopher J. Arendse, Emmanuel Iwuoha, and Markus C. Scharber. Optical and electronic properties of mixed halide (x = i, cl, br) methylammonium lead perovskite solar cells. *J. Mater. Chem. C*, 5:1714–1723, 2017.

[259] Shujun Zhang, Fei Li, Xiaoning Jiang, Jinwook Kim, Jun Luo, and Xuecang Geng. Advantages and challenges of relaxor-pbtio$_3$ ferroelectric crystals for electroacoustic transducers–a review. *Prog. Mater. Sci.*, 68:1–66, 2015.

[260] Felix Deschler, Michael Price, Sandeep Pathak, Lina E Klintberg, David-Dominik Jarausch, Ruben Higler, Sven Huttner, Tomas Leijtens, Samuel D Stranks, Henry J Snaith, et al. High photoluminescence efficiency and optically pumped lasing in solution-processed mixed halide perovskite semiconductors. *J. Phys. Chem. Lett.*, 5(8):1421–1426, 2014.

[261] Dong Shi, Valerio Adinolfi, Riccardo Comin, Mingjian Yuan, Erkki Alarousu, Andrei Buin, Yin Chen, Sjoerd Hoogland, Alexander Rothenberger, Khabiboulakh Katsiev, et al. Low trap-state density and long carrier diffusion in organolead trihalide perovskite single crystals. *Science*, 347(6221):519–522, 2015.

[262] Kevin G. Stamplecoskie, Joseph S. Manser, and Prashant V. Kamat. Dual nature of the excited state in organic–inorganic lead halide perovskites. *Energy Environ. Sci.*, 8:208–215, 2015.

[263] Yu Bi, Eline M Hutter, Yanjun Fang, Qingfeng Dong, Jinsong Huang, and Tom J Savenije. Charge carrier lifetimes exceeding 15 μs in methylammonium lead iodide single crystals. *J. Phys. Chem. Lett.*, 7(5):923–928, 2016.

[264] Parthiban Ramasamy, Da-Hye Lim, Bumjin Kim, Seung-Ho Lee, Min-Sang Lee, and Jong-Soo Lee. All-inorganic cesium lead halide perovskite nanocrystals for photodetector applications. *Chem. Commun.*, 52:2067–2070, 2016.

[265] Tomas Leijtens, Kevin Bush, Rongrong Cheacharoen, Rachel Beal, Andrea Bowring, and Michael D. McGehee. Towards enabling stable lead halide perovskite solar cells; interplay between structural, environmental, and thermal stability. *J. Mater. Chem. A*, 5:11483–11500, 2017.

[266] Nila Nandha K. and Angshuman Nag. Synthesis and luminescence of mn-doped $cs_2agincl_6$ double perovskites. *Chem. Commun.*, 54:5205–5208, 2018.

[267] Yi-Yang Sun, Michael L Agiorgousis, Peihong Zhang, and Shengbai Zhang. Chalcogenide perovskites for photovoltaics. *Nano Lett.*, 15(1):581–585, 2015.

[268] Kota Hanzawa, Soshi Iimura, Hidenori Hiramatsu, and Hideo Hosono. Material design of green-light-emitting semiconductors: Perovskite-type sulfide $srhfs_3$. *J. Am. Chem. Soc.*, 141(13):5343–5349, 2019.

[269] Chi-Shen Lee, Katja M Kleinke, and Holger Kleinke. Synthesis, structure, and electronic and physical properties of the two $srzrs_3$ modifications. *Solid State Sci.*, 7(9):1049–1054, 2005.

[270] Arnab Majumdar, Adebayo A Adeleke, Sudip Chakraborty, and Rajeev Ahuja. Emerging piezochromism in lead free alkaline earth chalcogenide perovskite $azrs_3$ (a= mg, ca, sr and ba) under pressure. *J. Mater. Chem.C*, 8(46):16392–16403, 2020.

[271] Samanthe Perera, Haolei Hui, Chuan Zhao, Hongtao Xue, Fan Sun, Chenhua Deng, Nelson Gross, Chris Milleville, Xiaohong Xu, David F Watson, et al. Chalcogenide perovskites–an emerging class of ionic semiconductors. *Nano Energy*, 22:129–135, 2016.

[272] Wei Li, Shanyuan Niu, Boyang Zhao, Ralf Haiges, Zhiqiang Zhang, Jayakanth Ravichandran, and Anderson Janotti. Band gap evolution in ruddlesden-popper phases. *Phys. Rev. Mater.*, 3(10):101601, 2019.

[273] Weiwei Meng, Bayrammurad Saparov, Feng Hong, Jianbo Wang, David B Mitzi, and Yanfa Yan. Alloying and defect control within chalcogenide perovskites for optimized photovoltaic application. *Chem. Mater.*, 28(3):821–829, 2016.

[274] Vikash Kumar Ravi, Seong Hoon Yu, Parikshit Kumar Rajput, Chandrani Nayak, Dibyendu Bhattacharyya, Dae Sung Chung, and Angshuman Nag. Colloidal bazrs$_3$ chalcogenide perovskite nanocrystals for thin film device fabrication. *Nanoscale*, 13(3):1616–1623, 2021.

[275] Xiucheng Wei, Haolei Hui, Samanthe Perera, Aaron Sheng, David F Watson, Yi-Yang Sun, Quanxi Jia, Shengbai Zhang, and Hao Zeng. Ti-alloying of bazrs$_3$ chalcogenide perovskite for photovoltaics. *ACS omega*, 5(30):18579–18583, 2020.

[276] Korina Kuhar, Andrea Crovetto, Mohnish Pandey, Kristian S Thygesen, Brian Seger, Peter CK Vesborg, Ole Hansen, Ib Chorkendorff, and Karsten W Jacobsen. Sulfide perovskites for solar energy conversion applications: computational screening and synthesis of the selected compound lays$_3$. *Energy Environ. Sci.*, 10(12):2579–2593, 2017.

[277] Qingde Sun, Hangyan Chen, and Wan-Jian Yin. Do chalcogenide double perovskites work as solar cell absorbers: a first-principles study. *Chem. Mater.*, 31(1):244–250, 2018.

[278] Corrado Comparotto, Alexandra Davydova, Tove Ericson, Lars Riekehr, Marcos V Moro, Tomas Kubart, and Jonathan Scragg. Chalcogenide perovskite bazrs$_3$: Thin film growth by sputtering and rapid thermal processing. *ACS Appl. Energy Mater.*, 3(3):2762–2770, 2020.

[279] Jia Song, De Ning, Bernard Boukamp, Jean-Marc Bassat, and Henny JM Bouwmeester. Structure, electrical conductivity and oxygen transport properties of ruddlesden–popper phases $\mathrm{ln}_{n+1}\mathrm{ni}_n\mathrm{o}_{3n+1}$ (ln= la, pr and nd; n= 1, 2 and 3). *J. Mater. Chem. A*, 8(42):22206–22221, 2020.

[280] Dibyajyoti Ghosh, Debdipto Acharya, Laurent Pedesseau, Claudine Katan, Jacky Even, Sergei Tretiak, and Amanda J Neukirch. Charge carrier dynamics in two-dimensional hybrid perovskites: Dion–jacobson vs. ruddlesden–popper phases. *J. Mater. Chem. A*, 8(42):22009–22022, 2020.

---

[281] Jian Qiu, Yingdong Xia, Yiting Zheng, Wei Hui, Hao Gu, Wenbo Yuan, Hui Yu, Lingfeng Chao, Tingting Niu, Yingguo Yang, et al. 2d intermediate suppression for efficient ruddlesden–popper (rp) phase lead-free perovskite solar cells. *ACS Energy Lett.*, 4(7):1513–1520, 2019.

[282] Michael G Stanford, Philip D Rack, and Deep Jariwala. Emerging nanofabrication and quantum confinement techniques for 2d materials beyond graphene. *NPJ 2D Mater. Appl.*, 2(1):1–15, 2018.

[283] Jin-Wook Lee, Jeong-Hyuk Im, and Nam-Gyu Park. Quantum confinement effect of cdse induced by nanoscale solvothermal reaction. *Nanoscale*, 4(20):6642–6648, 2012.

[284] Xiangxin Tian, Yongzhuan Zhang, Rongkun Zheng, Di Wei, and Jingquan Liu. Two-dimensional organic–inorganic hybrid ruddlesden–popper perovskite materials: preparation, enhanced stability, and applications in photodetection. *Sustainable Energy & Fuels*, 4(5):2087–2113, 2020.

[285] Yuran Yu, Zhuo Wang, and Guosheng Shao. Theoretical tuning of ruddlesden–popper type anti-perovskite phases as superb ion conductors and cathodes for solid sodium ion batteries. *J. Mater. Chem. A*, 7(17):10483–10493, 2019.

[286] Myeongkee Park, Amanda J Neukirch, Sebastian E Reyes-Lillo, Minliang Lai, Scott R Ellis, Daniel Dietze, Jeffrey B Neaton, Peidong Yang, Sergei Tretiak, and Richard A Mathies. Excited-state vibrational dynamics toward the polaron in methylammonium lead iodide perovskite. *Nat. Commun.*, 9(1):1–9, 2018.

[287] Hong Jiang, Patrick Rinke, and Matthias Scheffler. Electronic properties of lanthanide oxides from the gw perspective. *Phys. Rev. B*, 86(12):125115, 2012.

[288] F Fuchs, C Rödl, A Schleife, and F Bechstedt. Efficient o(n_2) approach to solve the bethe-salpeter equation for excitonic bound states. *Phys. Rev. B*, 78(8):085103, 2008.

[289] Georg Kresse and Daniel Joubert. From ultrasoft pseudopotentials to the projector augmented-wave method. *Phys. Rev. B*, 59(3):1758, 1999.

[290] Menno Bokdam, Tobias Sander, Alessandro Stroppa, Silvia Picozzi, DD Sarma, Cesare Franchini, and Georg Kresse. Role of polar phonons in the photo excited state of metal halide perovskites. *Sci. Rep.*, 6(1):1–8, 2016.

[291] M Gajdoš, K Hummer, G Kresse, J Furthmüller, and F Bechstedt. Linear optical properties in the projector-augmented wave methodology. *Phys. Rev. B*, 73(4):045112, 2006.

[292] Manish Kumar, Arunima Singh, Deepika Gill, and Saswata Bhattacharya. Optoelectronic properties of chalcogenide perovskites by many-body perturbation theory. *J. Phys. Chem. Lett.*, 12:5301–5307, 2021.

[293] Yeongsu Cho and Timothy C Berkelbach. Optical properties of layered hybrid organic–inorganic halide perovskites: A tight-binding gw-bse study. *J. Phys. Chem. Lett.*, 10(20):6189–6196, 2019.

[294] Qiong Wang, Chuanpeng Jiang, Pengpeng Zhang, and Thomas W Hamann. Overcoming bulk recombination limits of layered perovskite solar cells with mesoporous substrates. *J. Phys. Chem. C*, 122(25):14177–14185, 2018.

[295] Christoph Freysoldt, Blazej Grabowski, Tilmann Hickel, Jörg Neugebauer, Georg Kresse, Anderson Janotti, and Chris G Van de Walle. First-principles calculations for point defects in solids. *Rev. Mod. Phys.*, 86(1):253, 2014.

[296] Pooja Basera, Arunima Singh, Deepika Gill, and Saswata Bhattacharya. Capturing excitonic effects in lead iodide perovskites from many-body perturbation theory. *arXiv:2008.03381*, page **2020**.

[297] Manjari Jain, Deepika Gill, Preeti Bhumla, Pooja Basera, and Saswata Bhattacharya. Theoretical insights to excitonic effect in lead bromide perovskites. *Appl. Phys. Lett.*, 118(19):192103, 2021.

[298] Chen Ming, Ke Yang, Hao Zeng, Shengbai Zhang, and Yi-Yang Sun. Octahedron rotation evolution in 2d perovskites and its impact on optoelectronic properties: the case of ba–zr–s chalcogenides. *Mater. Horiz.*, 7(11):2985–2993, 2020.

[299] Frank Szmulowicz and Frank L Madarasz. Deformation-potential-theory calculation of the acoustic-phonon-limited conductivity and hall mobilities for p-type silicon. *Phys. Rev. B*, 27(4):2605, 1983.

[300] Shin-ichi Takagi, Akira Toriumi, Masao Iwase, and Hiroyuki Tango. On the universality of inversion layer mobility in si mosfet's: Part i-effects of substrate impurity concentration. *IEEE Trans. Electron Devices*, 41(12):2357–2362, 1994.

[301] Samantha Bruzzone and Gianluca Fiori. Ab-initio simulations of deformation potentials and electron mobility in chemically modified graphene and two-dimensional hexagonal boron-nitride. *Appl. Phys. Lett.*, 99(22):222108, 2011.

[302] Jingsi Qiao, Xianghua Kong, Zhi-Xin Hu, Feng Yang, and Wei Ji. High-mobility transport anisotropy and linear dichroism in few-layer black phosphorus. *Nat. Commun.*, 5(1):1–7, 2014.

[303] Richard Phillips Feynman. Slow electrons in a polar crystal. *Phys. Rev.*, 97(3):660, 1955.

[304] Ivan Biaggio, Robert W Hellwarth, and Jouni P Partanen. Band mobility of photoexcited electrons in $\mathrm{bi}_{12}\mathrm{sio}_{20}$. *Phys. Rev. Lett.*, 78(5):891, 1997.

[305] Michael Sendner, Pabitra K Nayak, David A Egger, Sebastian Beck, Christian Müller, Bernd Epding, Wolfgang Kowalsky, Leeor Kronik, Henry J Snaith, Annemarie Pucci, et al. Optical phonons in methylammonium lead halide perovskites and implications for charge transport. *Mater. Horiz.*, 3(6):613–620, 2016.

[306] Graeme Henkelman, Blas P Uberuaga, and Hannes Jónsson. A climbing image nudged elastic band method for finding saddle points and minimum energy paths. *The Journal of chemical physics*, 113(22):9901–9904, 2000.

[307] Qing-Yuan Bi, Xian-Long Du, Yong-Mei Liu, Yong Cao, He-Yong He, and Kang-Nian Fan. Efficient subnanometric gold-catalyzed hydrogen generation via formic acid decomposition under ambient conditions. *Journal of the American Chemical Society*, 134(21):8926–8933, 2012.

[308] Haitao Yu, Yang Xu, Kaden Havener, Meng Zhang, Li Zhang, Wenjin Wu, and Kun Huang. Temperature-controlled selectivity of hydrogenation and hydrodeoxygenation of biomass by superhydrophilic nitrogen/oxygen co-doped porous carbon nanosphere supported pd nanoparticles. *Small*, 18(16):2106893, 2022.

[309] Quang Thang Trinh, Bhadravathi Krishnamurthy Chethana, and Samir H Mushrif. Adsorption and reactivity of cellulosic aldoses on transition metals. *The Journal of Physical Chemistry C*, 119(30):17137–17145, 2015.

[310] Prince N Amaniampong, Quang Thang Trinh, Karine de Oliveira Vigier, Duy Quang Dao, Ngoc Han Tran, Yingqiao Wang, Matthew P Sherburne, and Francois Jerome. Synergistic effect of high-frequency ultrasound with cupric oxide catalyst resulting in a selectivity switch in glucose oxidation under argon. *Journal of the American Chemical Society*, 141(37):14772–14779, 2019.